Investigating the pathophysiology of *KCNJ13* and *USH2A* retinopathies using zebrafish models

Maria Toms

Institute of Ophthalmology, University College London (UCL)

Submitted to UCL for the degree of Doctor of Philosophy

Supervisors: Prof Andrew Webster, Dr Mariya Moosajee

May 2018

Declaration

I, Maria Toms, confirm that the work presented in this thesis is my own. Where information has been derived from other sources, I confirm that this has been indicated in the thesis.

Abstract

Inherited retinal diseases (IRDs) encompass a large group of clinically and genetically heterogeneous diseases that affect approximately 1 in 3000 people, representing an important cause of severe visual loss in the human population. In the past two decades, significant contributions towards our understanding of these disorders has included the identification of over 250 causative genes. In this thesis, the pathophysiology of IRDs associated with *KCNJ13* and *USH2A* was investigated using relevant zebrafish models.

Mutations in *KCNJ13* are associated with Leber congenital amaurosis, the most severe IRD subtype that causes blindness in childhood. *KCNJ13* encodes the Kir7.1 channel, a potassium channel expressed on the apical retinal pigment epithelium (RPE). Longitudinal assessment of the *kcnj13* mutant zebrafish (*obelix*^{td15}) revealed a late onset retinal degeneration at 12 months with retinovascular abnormalities, and a corresponding decline of visual function. Ultrastructural examination of the *obelix*^{td15} RPE uncovered changes in phagosome clearance and mitochondrial growth prior to notable degeneration which indicate that the disease may be a primary phagosome failure with a secondary failure in mitochondrial physiology. In addition, gene and protein expression changes consistent with altered mitochondrial activity and retinal stress were observed. The alterations in the RPE are reminiscent of those seen in age-related macular degeneration and highlight potential therapeutic targets for *KCNJ13* retinopathy.

USH2A mutations are the most common cause of Usher Syndrome, characterised by combined retinitis pigmentosa and sensorineural deafness. *USH2A* encodes the large transmembrane protein, usherin, expressed in the photoreceptors and cochlear hair cells. CRISPR/Cas9 gene targeting was used to create an *ush2a* mutant zebrafish line, which showed a slowly progressive photoreceptor degeneration from 6 months with mislocalisation of rhodopsin. Developmental abnormalities in the neuromast and inner ear hair cells were also identified in *ush2a* larvae. The findings suggest that

ush2a is involved in rhodopsin trafficking and rod photoreceptor maintenance in the zebrafish retina, as well as playing a role in mechanosensory system development. Overall, the *ush2a* zebrafish phenotype showed consistency with the clinical phenotype in *USH2A* patients, indicating the value of this model for gaining further insight into the disease pathophysiology.

Acknowledgements

I gratefully acknowledge the continuous support and guidance from my supervisor, Dr Mariya Moosajee, who has always believed in my abilities and encouraged me to achieve an ever-higher standard of work. I would also like to thank my supervisor Prof Andrew Webster for the enthusiasm and expertise he has provided throughout my PhD. I am grateful for the support of my fellow laboratory team members, especially that of Dhani Tracey-White, Dr Rose Richardson and Dr Nick Owen, who have all contributed their time and experience towards my studies. I would like to acknowledge Dr Matthew Hayes and Dr Thomas Burgoyne from the Electron Microscopy lab for their outstanding work.

This research would not have been possible without the support of funding bodies, including the Academy of Medical Sciences and National Institute for Health Research.

And finally, I am grateful to my partner and family for their constant love and encouragement. In particular, Dr Graham ‘Greyhound’ Toms has always gone above and beyond to support me.

Awards and Publications

Papers:

Toms M, Bitner-Glindzicz M, Webster A, Moosajee M. Usher syndrome: a review of the clinical phenotype, genes and therapeutic strategies. *Expert Review of Ophthalmology*. 2015;10(3):241-56.

Toms M, Tracey-White D, Muhundhakumar D, Sprogyte L, Dubis AM, Moosajee M. Spectral Domain Optical Coherence Tomography: An *In Vivo* Imaging Protocol for Assessing Retinal Morphology in Adult Zebrafish. *Zebrafish*. 2017;14(2):118-25.

Toms M, Burgoyne T, Tracey-White D, Richardson R, Dubis AM, Webster A, Futter C, Gorin MB, Moosajee, M. Phagosomal and mitochondrial alterations in RPE contribute to *KCNJ13* retinopathy – submitted to *The Journal of Clinical Investigation*.

Awards:

National Institute for Health Research (NIHR) Rare Diseases Translational Research Collaboration's Eye Theme International Research Secondment.

European Paediatric Ophthalmological Society (EPOS) Meeting Travel Award.

School of Life and Medical Sciences Student Conference Grant.

Presentations:

Toms, M., Tracey-White D, Richardson R, Burgoyne T, Moosajee M. *KCNJ13*-related severe early onset retinal degeneration associated with a mitochondrial pathophysiology – paper presentation at European Paediatric Ophthalmological Society (EPOS) annual meeting 2017.

Toms, M., Tracey-White D, Richardson R, Burgoyne T, Moosajee M. *KCNJ13*-related LCA associated with a mitochondrial aging pathophysiology – paper presentation at The UK Eye Genetics Group (UKEGG) & The International Society for Genetic Eye Diseases & Retinoblastoma (ISGEDR) meeting 2017.

Toms, M., Tracey-White D, Richardson R, Burgoyne T, Moosajee M. Leber Congenital Amaurosis: A mitochondrial pathophysiology underlying *KCNJ13*-related retinal degeneration – poster presentation at British & Irish Paediatric Ophthalmology & Strabismus Association (BIPOSA) annual meeting 2017.

Toms, M, Hayes, M, Webster AR, Moosajee M. Loss of *ush2a* causes rhodopsin mislocalisation and adult onset photoreceptor degeneration in a zebrafish model of Usher syndrome – paper presentation at The Association for Research in Vision and Ophthalmology (ARVO) annual meeting 2018.

Table of contents

List of figures

List of tables

Abbreviations

µl	microlitre
µm	micrometre
aa	amino acid
ASO	antisense oligonucleotides
ATP	adenosine triphosphate
bp	base pair
COOH	carboxyl
cpd	cycles per degree
CRISPR/ Cas9	clustered regularly interspaced short palindromic repeats/ CRISPR-associated protein
DAPI	4′,6-Diamidino-2-phenylindole dihydrochloride
DFNA	autosomal dominant non-syndromic deafness
DFNB	autosomal recessive non-syndromic deafness
DNA	deoxyribonucleic acid
cDNA	complementary DNA
dsDNA	double-stranded DNA
dpf	days post-fertilisation
EDTA	ethylenediaminetetraacetic acid
ELM	external limiting membrane
ENU	*N*-ethyl-*N*-nitrosourea
ERG	electroretinogram
GCL	ganglion cell layer
GFAP	glial fibrillary acidic protein
HDR	homology directed repair
hpf	hours post-fertilisation
IHC	inner hair cells
INL	inner nuclear layer
IPL	inner plexiform layer
iPSC	induced pluripotent stem cells
IRD	inherited retinal diseases
IS	inner segments
K^+	potassium ions
lamEGF	laminin epidermal growth factor
LCA	Leber congenital amaurosis
LTLD	lower tip link density
MET	mechanotransduction
$MgCl_2$	magnesium chloride
mpf	months post-fertilisation
NH2	amino
NHEJ	non-homologous end joining
nl	nanolitre
obe^{td15}	*obelix^{td15}*
OHC	outer hair cells
ON	optic nerve
ONL	outer nuclear layer
OPL	outer plexiform layer
OS	outer segments
PAM	protospacer adjacent motif
PBS	phosphate-buffered saline
PBS-T	phosphate-buffered saline with 0.1% tween
PCR	polymerase chain reaction
RT-PCR	reverse transcription PCR
qRT-PCR	quantitative RT-PCR
PDZ	postsynaptic density 95; discs large; zonula occludens- 1
PMC	periciliary membrane complex
PRC	periciliary ridge complex
PTU	phenylthiourea
PFA	paraformaldehyde
RNA	ribonucleic acid
mRNA	messenger RNA
sgRNA	single guide RNA
ROS	reactive oxygen species
RP	retinitis pigmentosa
RPE	retinal pigment epithelium
rpm	revolutions per minute
TUNEL	terminal deoxynucleotidyl transferase dUTP nick end labelling
SD-OCT	spectral domain optical coherence tomography
SDS	sodium dodecyl sulphate
SEM	standard error of the mean
SSC	saline sodium citrate
SVD	snowflake vitreoretinal degeneration
TALENs	transcription activator-like effector nucleases
TCA	trichloroacetic acid
UTLD	upper tip link density
UV	ultraviolet
VEGF	vascular endothelial growth factor
VIP	volume intensity projection
WT	wild-type
ZFNs	zinc finger nucleases

1 Introduction

Inherited retinal diseases (IRDs) are a heterogenous group of diseases affecting approximately 1 in 3000 people that collectively cause progressive retinal degeneration with resultant sight loss. In the United Kingdom, they are the commonest cause of visual impairment (blind) certification in working age adults (1) and the second most common cause in children (2). Since the initial mapping of the *RHO* gene in a form of retinitis pigmentosa in 1990, over 250 IRD causative mutations have been identified (3). The blinding nature of these conditions highlights the need for therapeutic innovation. Significant progress has been made towards our understanding of the molecular and cellular mechanisms underlying a range of IRDs, which has been achieved largely through the use of animal models and has culminated in several completed and ongoing human clinical trials. Although mice have been commonly used for modelling retinal disease, zebrafish have emerged as attractive non-mammalian alternatives due to multiple advantages, including cost-efficiency and genetic manipulability (4). The ease at which mutant models for specific disease gene variants can now be generated using modern gene editing techniques will facilitate the further expansion of knowledge surrounding IRD pathomechanisms and assist the development of new treatment strategies for various IRDs.

1.1 The retina

1.1.1 Organisation and function of the mature vertebrate retina

The retina is a laminated multicellular tissue of neuroectodermal origin, approximately 0.2 mm thick in humans, lining the inner surface of the posterior segment of the eye **(Figure 1-1**) (5). This structure is essential for our visual perception and is specialised in receiving, converting and amplifying visual signals. These are sent via the optic nerve to the visual centres of the brain in the form of coded electrical impulses, allowing an image

Figure 1-1. Basic structure of the eye and organisation of the retinal cells.
(A) The retina lines the posterior segment of the eye. The retinal pigment epithelium (RPE) lies between the retina and the choroid (a vascularised connective tissue). The fovea of the retina is specialised for maximum visual acuity. Light focused onto the retina is translated into neural response by the retinal cells and relayed to the brain via the optic nerve. (B) Retinal cell organisation. (C) Cross-section of the human retina showing layers. (D) Structure of the rod and cone photoreceptors. Adapted from (5, 6). G, ganglion cell; A, amacrine cell; B, bipolar cell; H, horizontal cell; R, rod cell; C, cone cell; M, Müller cell. OS, outer segments; IS, inner segments; ONL, outer nuclear layer; OPL, outer plexiform layer; INL, inner nuclear layer; IPL, inner plexiform layer; GCL, ganglion cell layer.

of the surrounding environment to be formed. The retina is composed of five major classes of nerve cells: photoreceptor, bipolar, horizontal, ganglion and amacrine cells (7). As each cell class has several subtypes, this is a simplified view of the complex and diverse circuitry of the retina. The cell bodies and connections of the retinal neurons are arranged in a stereotypic multilayered structure observed across species. Two major laminae, the outer plexiform layer (OPL) and the inner plexiform layer (IPL), contain the synaptic connections while the cell bodies are restricted to the ganglion cell layer (GCL), inner nuclear layer (INL) and outer nuclear layer (ONL). The INL contains the cell bodies of the bipolar, horizontal and amacrine cells and the ONL comprises the photoreceptor cell bodies. In addition to the neural components, a single type of glial cell (the Müller glia) spans the retina, providing important structural and functional support for the neurons.

Within the photoreceptor layer, there are two types of cells: rods and cones (5). Rod cells are the more abundant cell type and are sensitive to low light levels. Their visual pigment is known as rhodopsin. Humans typically possess three types of cone cells, each containing a particular opsin that is sensitive to light of certain wavelengths, enabling colours to be visualised. They are defined as S-cones (short wavelength), M-cones (medium wavelength) or L-cones (long wavelength). The ratio of rods to cones and the number of cone cell types varies between species and is largely dependent whether an animal is diurnal or nocturnal (8). In many species, including humans, the rods and cones are unevenly distributed across the retina. The primate retina has a central region of approximately 5-6 mm in diameter known as the macula, which is specialised for high acuity vision (6). The fovea is an ~700-µm-diameter foci at the centre of this region and contains cone cells only (5).

The photoreceptor cells are arranged in a defined layer and their outer segments are in direct contact with the retinal pigment epithelium (RPE), which is a monolayer of neuroepithelial cells necessary for the normal function and survival of the photoreceptors (8, 9). The pigmented nature of the RPE is caused by melanosomes, melanin-containing organelles that absorb scattered light, protecting the retina from phototoxic damage. These cells are also required for phagocytosis of parts of the outer segments, removing toxic by-products from phototransduction. Furthermore, the RPE plays an essential role in the visual cycle by replenishing the photoreceptors with re-isomerised chromophore molecules. Other functions of the RPE include the maintenance of the outer blood-retina barrier, and the active transport of metabolites, nutrients and waste products between the choriocapillaris and the photoreceptor cells (9).

The first step in retinal processing of visual information is the conversion of light to chemical and electrical signals, which is carried out by the photoreceptor cells (5). Light enters the eye through the cornea and pupil and is focused onto the retina by the refractive power of the cornea and lens, where it passes through the entire thickness of the neural retina until it impinges on the photoreceptors in the outermost layer. Morphologically, photoreceptor cells can be segmented into different parts: a synaptic end that faces the bipolar cells, the cell body that contains the nucleus, an inner segment where protein synthesis occurs and a large outer segment where phototransduction takes place (**Figure 1-1D**). The outer segments are densely packed with membranes containing forms of opsin, the visual pigment, covalently bound to the light-sensitive chromophore, 11-cis retinal. When photons are captured by the opsin molecules, the chromophore isomerises and the phototransduction cascade is initiated; this complex chain of events involves G-protein activation and the closing of cation channels, causing a hyperpolarisation of the membrane potential that ultimately results in a decreased secretion of the neurotransmitter glutamate at the photoreceptor synaptic terminals.

Once the light information is converted into a neural response, the photoreceptor cells use glutamate to pass the signal onto bipolar interneurons in the OPL, where it is then relayed to the inner retina (7). Horizontal cells also contact the bipolar cells and modulate signal transmission from the photoreceptors. Bipolar cells can be divided into two major classes, rod and cone bipolar cells, based on which photoreceptor cell type they predominantly synapse with. In addition, bipolar cells form two functional subclasses: Those that depolarise (ON) and those that hyperpolarise (OFF) to increments in light intensity. Rod bipolar cells are ON-bipolar cells, whereas cone bipolar cells can either be ON- or OFF-type.

In the inner retina, cone bipolar cells synapse with the retinal ganglion cells and amacrine interneurons [2]. Amacrine cells are vital modulators of signal transmission, which they achieve by providing feedforward inhibition onto ganglion cells or controlling neurotransmitter release from the bipolar cells by feedback inhibition. Inhibition is mediated largely by two fast neurotransmitters, γ-aminobutyric acid (GABA) and glycine. Both horizontal and amacrine cells play a key role in the horizontal redistribution of the visual signal in the retina, which is essential for the integration of components of a visual pattern. Light information leaves the retina via the retinal ganglion cells, whose axons converge to form the optic nerve, through which the signal will reach the higher visual centres of the brain for processing.

1.1.2 Development of the retina

Ocular development is a complex process characterised by an ongoing series of inductive signals and timely action of transcription factors, resulting in the initial establishment of the major eye components, and the coordinated differentiation of these structures (10). In humans, eye development is first evident at around 22 days of

embryonic development with the appearance of the optic pits and is not completed until several months after birth (11).

During embryogenesis, the eye is derived from three tissues: neuroectoderm which gives rise to the neural retina, RPE, optic stalk, iris dilator and sphincter muscles, and ciliary body; surface ectoderm, which forms the lens and subsequently the conjunctival and corneal epithelia; and mesenchyme which originates from the neural crest cells forming the corneal endothelium and stroma, iris stroma, ciliary muscles and vasculature, and sclera (4). Retinal development begins with the specification of the eye field during late gastrulation, marked by the expression of the homeobox gene *RAX* by cells within the single eye field located centrally in the developing forebrain (10). Other prominent markers are *PAX6* and *LHX2*, which are heavily involved in patterning the eye fields. The splitting of the eye field occurs in parallel with the establishment of the midline, which is the main function of Sonic hedgehog (Shh). During neurulation, two lateral optic pits become apparent as the first signs of the developing eyes. The eyes develop as a consequence of inductive interactions between the surface ectoderm and evaginations of the diencephalon (forebrain), known as the optic vesicles (**Figure 1-2**). These are connected to the developing central nervous system by the optic stalk which later develops into the optic nerve. The optic vesicles induce the epithelium to produce a lens placode, which ultimately pinches off to form the lens. The cornea eventually forms as a result of inductive interactions between the lens vesicle and the overlying surface ectoderm.

During the lens formation process, the ectoderm stimulates the optic vesicle to invaginate and form a bilayered optic cup, which will give rise to the retina and RPE (10). The outer layer of the optic cup remains thin and differentiates into the RPE, which is located

Figure 1-2. Human embryonic ocular development.
(A) The neuroectodermal optic vesicle grows towards the surface ectoderm around 27 days of gestation, signalling between the two embryonic tissues leads to thickening of the surface ectoderm to form a lens placode. (B) The distal portion of the optic vesicle invaginates so that the presumptive neural retina is apposed to the presumptive RPE in a double-walled cup structure. The optic cup grows circumferentially. The inner layer differentiates into the neural retina from 28–35 days of gestation. The outer layer of the optic cup gives rise to the RPE. The lens develops concomitantly with the retina. Formation of the optic fissure, a transient opening in the ventral surface of the optic cup, enables the vasculature to enter and supply the developing eye. (C) The lens placode invaginates to become the lens pit, which deepens and closes before pinching off from the surrounding surface ectoderm (yellow) as the lens vesicle by 35 days of gestation. The optic fissure fuses by this timepoint. (D) Cells of the central lens placode migrate to the posterior lens vesicle and elongate to form primary lens fibre cells (blue), filling the lens vesicle lumen by 50 days of gestation. Cells of the peripheral lens placode migrate to the anterior lens vesicle forming the anterior epithelium (orange). The cornea (yellow) develops when the surface ectoderm closes after detachment of the lens vesicle from the surface ectoderm. From (4).

between the vascular choroid and photoreceptor layer of the retina, forming part of the blood-retina barrier (6). There is a close interdependence between the photoreceptors, RPE and choroid (which nourishes them), and a dysfunction in one of these components can cause secondary dysfunction in the others. As the RPE forms, the inner layer of the optic cup thickens and begins a long process of differentiation into the different cell types of the neural retina (10). The outer lips of the optic cup, where the developing neural and pigmented retinas meet, will transform into the iris and ciliary body (12).

Within the developing retina, the generation of appropriate cell types, numbers and distributions depend on many cell intrinsic and extrinsic factors, including time of cell genesis, that act together to specify cell fate (10). In vertebrates, the retinal cell differentiation follows an evolutionary conserved temporal order that occurs in partially overlapping waves. Generally, the ganglion cells are generated first, followed by horizontal and cone cells, amacrine cells, rods, bipolar cells and, finally, Müller glia (13). There are two major gradients of differentiation, the first of which moves vertically from the inner to the outer layers of the retina, while the second travels horizontally and is based on the outward spread of the vertical gradient from the centre towards the periphery of the retina (10). The horizontal gradient begins with the differentiation of the ganglion cells, and later leads to the definition of the INL and ONL. The IPL and OPL become more defined as cells within the nuclear layers send out processes. Numerous extrinsic signalling molecules are thought to contribute to the patterning of the vertebrate retina, including members of the Wnt, bone morphogenetic protein (BMP), Notch, fibroblast growth factor (FGF) and hedgehog signalling families (13, 14).

Once all cell types of the neural retina have been generated, a series of developmental events allow the formation and maintenance of connections between the various retinal cell types and between the retina and the brain (11). As development progresses, the

optic stalk connecting the optic cup to the diencephalon becomes invaded by neuronal processes originating from the retinal ganglion cells, becoming the optic nerve. This further develops into the optic tract to reach the appropriate regions of the brain. Within the retina, the cellular components progressively organise into precise networks through the expression of neurotransmitters and the extension of neuronal processes, necessary for intercellular communication. Once the neuronal circuitry of the retina and optic pathway is established, the retina is able to begin receiving and processing visual information. During human embryogenesis, visually-evoked potentials can be recorded by 30 weeks of gestation, suggestive of a level of functional integrity at this point (4).

1.1.3 Inherited retinal diseases

Numerous coordinated genetic interactions underlie the correct formation and maintenance of the retina, and visual impairment may result in cases where a necessary molecular factor is congenitally defective or non-functional. Inherited retinal diseases (IRDs) are a large group of heterogenous disorders affecting approximately 1 in 3000 people, for which over 250 causative genes have been identified (3, 15). Depending on the severity of the mutations, the cell type that is primarily affected by the mutation, and the function of the protein that is encoded by the corresponding gene, IRDs can be divided into different clinical subtypes with a varying age of onset, rate of progression and clinical features (6, 8). The most severe subtype of IRD is Leber congenital amaurosis, with an onset of symptoms in the first year of life and resulting in complete blindness in childhood. Other subtypes include retinitis pigmentosa (RP; a rod-cone dystrophy), macular dystrophy, cone-rod dystrophy, cone dystrophy, achromatopsia or congenital stationary night blindness, that all display a large degree of clinical and genetic heterogeneity. In addition, there are some other subtypes of IRD that are caused by mutations in only a single gene, e.g. choroideremia (caused by mutations in *CHM*)

and Best disease (caused by mutations in *BEST1*). In recent years, there has been a move towards the use of gene-based definitions rather than phenotype-based clinical subtypes for retinopathies, due to the vast heterogeneity and phenotypic variability among the IRDs. By focusing on genotype, we can further understand gene function, disease mechanisms and develop targeted treatments.

RP is the most common cause of IRD in the human population, with an estimated prevalence of approximately 1 in every 4000 people (6). It typically presents with impaired night vision and peripheral vision (due to rod dysfunction), progressing eventually to loss of central vision due to cone cell degeneration. The age of onset varies greatly depending on the type of RP, with a range from early childhood to late adulthood (16). The diagnosis can be made based upon the clinical symptoms, the typical findings when examining the retina, visual field testing, and electroretinography (ERG). Fundus examination may show some degree of optic nerve pallor, retinal vessel attenuation, and bone spicule pigmentation in the periphery.

More than 60 genes have been linked to RP, and many causative genes encode key players in phototransduction signalling, the visual cycle, and photoreceptor fate determination (3). The most common single genes that cause RP are *RPGR* (10–20% of cases), *RHO* (8–10% of cases), and *USH2A* (~3% of cases) (6). In addition to isolated cases, RP is a feature of more than 30 different syndromes in which non-ocular signs are also present, and these syndromes account for 20–30% of all RP cases. Examples of such disorders include Usher syndrome, Bardet-Biedl syndrome and Joubert syndrome. These syndromic forms of RP are often ciliopathies, as the genes underlying them encode proteins that participate in ciliary complexes not exclusively found in the retinal photoreceptors (which possess a specialised cilium) and therefore exhibit additional non-retinal symptoms. Some of the genes mutated in these syndromes can

also underlie non-syndromic RP. Although the more severe (i.e. protein-truncating) mutations might be more often causative for syndromic forms, a genotype–phenotype correlation is not always clear.

While significant progress has been made towards developing effective treatments, there are currently no established standard treatment modalities for patients with RP or other IRDs, with the exception of patients with *RPE65* mutations (17). From a therapeutic perspective, the eye has several key advantages including its accessibility and its immune-privileged nature that is ensured by the blood-retina barrier, which would allow a robust delivery of therapeutic molecules that remain within the eye. The most effective therapeutic approach is influenced by the stage of the disease. When the photoreceptor or RPE cells are still structurally intact, gene therapy appears to be the most promising therapeutic strategy, typically involving viral delivery of the wild-type cDNA of the defective gene to the retina via subretinal injections. This strategy has already shown potential in patients with *RPE65* mutations, choroideremia and RP, and there are several ongoing clinical trials (17, 18). Spark Therapeutics gained FDA approval for their *RPE65* gene therapy, Luxturna, in December 2017. However, if the RPE or photoreceptor cells are fully degenerated, alternative strategies need to be employed such as cell replacement therapy (19) or, at a very advanced stage of the disease, retinal implants (20). Ideally, it would be preferable to treat IRDs as early as possible when the majority of cells are still intact, e.g. with gene therapeutic approaches. As this requires the development of therapies tailored to each gene, suitable cellular and animal models that mimic the molecular and clinical defects observed in patients are necessary to further understand the underlying disease mechanisms and assess therapeutic efficacy and safety.

1.1.4 The zebrafish as a model system

In recent years, the zebrafish has become highly useful model system in which to study the molecular details of vertebrate development and disease. These small freshwater teleost fish offer many advantages as an experimental model; fertilisation and subsequent development are external, and embryonic transparency allows the visualisation of morphogenetic movements and organogenesis with a standard dissecting microscope. Development is rapid in the zebrafish; by 24 hours post-fertilisation (hpf) all of the major organ systems have formed and by 3 days post-fertilisation (dpf) the zebrafish is a free swimming larva (21). Other practical advantages of studying zebrafish is the ability to maintain high numbers in a relatively small space, their rapid sexual maturation (~3 months) and the production of large numbers of eggs; one breeding pair can produce up to 200 fertilised eggs. Additionally, several large-scale mutagenesis screens and the availability of modern techniques for gene editing in zebrafish have provided a powerful resource in which to study *in vivo* gene function. The genetic and experimental accessibility of this organism has underpinned its success as a model of the visual system.

Zebrafish retinal development and anatomy

Due to a striking level of conservation in ocular anatomy among the vertebrate species, the zebrafish retina is comparable to that of humans. As already described in the human retina, the zebrafish retina contains seven major cell types: six neurons (photoreceptor, bipolar, horizontal, ganglion and amacrine cells) and the Müller glia (21). In contrast to rodents, the zebrafish is diurnal and in addition to rod photoreceptors they possess a number of diverse cone cell subtypes, which can be divided into four classes based upon spectral sensitivity and morphology – blue, green, red and ultraviolet (UV) cones. The zebrafish photoreceptor outer segments are arranged in distinct tiered layers according to subtype, as follows (innermost to outermost): UV cones (short single cones), blue

cones (long single cones), red-green double cones and rods (22). The zebrafish retina demonstrates the typical multi-layered structure observed across other vertebrate species (**Figure 1-3**).

During zebrafish development, eye and lens morphogenesis and differentiation of the retinal layers exhibit a high level of consistency with that of other vertebrates (21). The components of the eye originate from the three embryonic tissues as already described. Following specification of the eye field, inductive interactions and cell movement allow development of the zebrafish eyes from cell masses that evaginate from the forebrain. The optic cups are formed at around 22 hpf. Within the inner layer of the optic cup, which is to become the neural retina, differentiation of the ganglion cell layer is observed at around 32 hpf. Neurogenesis of the remaining retinal cell types follows approximately in the direction from the inner to the outer retina. By 48 hpf, lamination can be observed across most of the zebrafish retina. Differentiation of the photoreceptor cells proceeds by 50 hpf, marked by the expression of rhodopsin and red cone opsin. In zebrafish, the UV cones are the first cone cells to mature and red-green double cones are the last to complete development. Between 72-96 hpf, all the major classes of retinal cell types can be identified in the zebrafish retina and behavioural responses indicative of ocular function, such as visually-evoked startle responses, begin to be observed.

The zebrafish retinal ultrastructure

The retinal ultrastructure has been described in some detail in both larval and adult zebrafish (22, 23). In the outer retina, the photoreceptors show a typical ordered tier arrangement with rods easily distinguished from cones based on outer segment morphology, mitochondrial composition and synaptic ultrastructure (23). Generally, the zebrafish photoreceptors have many characteristics similar to other species. One feature that is unique to teleost fish is the cone accessory outer segment, which is a cytoplasmic

Figure 1-3. The zebrafish eye and retinal structure in comparison to human.
(A) Zebrafish retinal histology at 5 days post-fertilisation (dpf). (B) Comparison of the human and zebrafish adult retinal histology. (C) Comparison of human and zebrafish eye structure and retinal layer thickness measurements. GCL, ganglion cell layer; IPL, inner plexiform layer; INL, inner nuclear layer; OPL, outer plexiform layer; ONL, outer nuclear layer; ON, optic nerve; RNFL, retinal nerve fibre layer; IS, inner segments; IS, outer segments; RPE, retinal pigment epithelium. Adapted from (4, 24, 25).

structure that protrudes from the connecting cilium and runs alongside the photoreceptor outer segment (26) (**Figure 1-4**). Although the function of this structure remains unclear, it may provide structural support to the outer segment (27) and be involved in exchange of metabolites between RPE and cones (26, 27). Moreover, in response to changes in light conditions and to circadian signals during light/dark adaptation of the teleost retina, reversible retinomotor movements take place that result in contraction and elongation of rods and cones to expose the outer segment optimally to incoming light (28). It has been suggested that by anchoring the cones to the RPE, the accessory outer segment may preserve the highly organised arrangement of the various cone subtypes in the fish retina (27).

The RPE is also an essential component of the teleost retinomotor response (29). The zebrafish RPE is a monolayer of cells with large apical projections that interdigitate with the photoreceptor outer segments, filled with melanosomes (pigment) that absorb harmful backscattered light (**Figure 1-4**). In adult zebrafish, the melanosomes migrate into the apical projections with constant speed and reach the fully light-adapted state approximately 1 hour after the onset of light, and this migration is reversed in the dark (28, 29). This response serves to protect the rod visual pigment from overstimulation in light conditions, which is necessary in the absence of pupillary reflexes in lower vertebrates. Another crucial light-dependent process performed by the RPE is phagocytosis, in which portions of the photoreceptor outer segments are phagocytosed by the RPE on a daily basis and the resulting phagosomes are required to move from the apical to the basal region in order to mature and acquire the capacity to fuse with lysosomes for degradation (30). Outer segment shedding is triggered by the onset of light. Defects in phagosome processing are associated with several negative outcomes, such as lipid accumulation, oxidative stress and mitochondrial dysfunction (31-34), and have been found in models of several retinal diseases (35-39). While phagosomes have

Figure 1-4. Features of the adult zebrafish retinal ultrastructure.
(A) The inner and outer segment (RIS, ROS) of a rod photoreceptor showing mega-mitochondria (M) in the inner segment ellipsoid. From (23). (B) The inner and outer segment (CIS, COS) of a cone photoreceptor where the accessory outer segment (AOS) can be seen protruding from the connecting cilium (CC). From (26). (C) A retinal pigment epithelium (RPE) cell with nucleus (N), phagocytised fragments (phagosomes, P) of shed photoreceptor outer segments. Mitochondria (M) and melanosomes (melanin pigment granules, MP) are visible. A nucleated red blood cell (RBC) is in a blood vessel (V) in the choriocapillaris. From (23). All scale bars = 1 μm.

been observed in the zebrafish RPE ultrastructure (23), there has been limited characterisation of their activity in zebrafish.

The outer retina has the greatest metabolic demand in the body, owing largely to the photoreceptor activity, and therefore has an enriched mitochondrial population to meet the high-energy needs of these cells to ensure function and survival (40). The main role of mitochondria is to provide energy in the form of ATP, in addition to numerous other tasks which include regulation of apoptosis stress response pathways and calcium levels. Within the zebrafish retinal ultrastructure, significantly enlarged mitochondria with elevated ATP production can be viewed in the photoreceptor inner segment ellipsoids (41, 42) (**Figure 1-4**). These so-called mega-mitochondria are thought to be necessary to supply the high energy consumption of the photoreceptors. Abundant mitochondria are also required in the highly metabolically active RPE cells and mitochondrial dysfunction has been linked to retinal disease (43), however there has not been in-depth examination of these organelles in the zebrafish RPE.

Zebrafish models of retinal disease

The zebrafish has provided an effective system for genetic analysis of ocular development and function. The zebrafish genome is well curated and it has been found that approximately 70% of human protein coding genes have at least one zebrafish orthologue, with 84% of known human disease-causing genes having a zebrafish counterpart (44). Many mutations in the zebrafish genome have been associated with phenotypes of visual dysfunction that have parallels with human disease, including models of RP and choroideremia (4, 24, 45). Previous forward genetic screens, using chemical and insertional based mutagenesis, have aided the identification of many genes involved in different aspects of retinal development and physiology, including

cellular specification and morphogenesis, retinal lamination and photoreceptor cell function (46-49). For instance, one large-scale mutagenesis screen by Malicki et al (1996) uncovered 49 mutations affecting various elements of retinal development, which were divided into six categories based on phenotype, including retinal patterning and photoreceptor survival (47). Visual mutants have been identified using both morphological analysis and visual behaviour assays, such as the optokinetic response (49).

Gene editing in zebrafish

In recent years, the development of modern genome editing techniques, which include zinc finger nucleases (ZFNs) (50, 51), TALENs (transcription activator-like effector nucleases) (52, 53) and CRISPR (clustered regularly interspaced short palindromic repeats) (54), have made precise and efficient targeted mutagenesis possible. All three methods are based on the activity of nucleases which use either protein (ZFNs and TALENs) or RNA (CRISPR) based sequence specificity domains and non-specific nuclease domains that create a double strand break (DSB) in the DNA at the target site. Two major DNA repair pathways termed ‘non-homologous end joining’ (NHEJ) and ‘homology directed repair’ (HDR) are activated to repair a DSB (55). NHEJ tends to be imprecise thus leading to insertions or deletions (indels) at the break site, where they either cause frameshift or non-frameshift mutations that often result in a non-functional protein (knockouts). Alternatively, by providing a donor template to guide precise repair of the DSB, HDR can be used for targeted knock-in of specific sequences, desired transgenes, or dominant negative missense mutations at the endogenous locus.

ZFNs were the first of the genome-editing nucleases to be applied successfully in zebrafish for targeted gene knockout (50, 51). ZFNs create hybrid proteins that consist of the catalytic domain of a non-specific endonuclease, Fok1 and a custom-designed,

sequence-specific, DNA binding domain containing three or more (up to six) zinc finger motifs which bind DNA. To reduce the risk of off-target effects, the Fok1 nuclease can be designed as a heterodimer that only cleaves DNA if the left and the right zinc fingers position the two Fok1 subunits appropriately to generate an active enzyme. Although this system can be designed for high specificity, the widespread adoption of ZFNs by the zebrafish community has been hindered by their high cost, difficult assembly protocols, unknown efficiency, and limited flexibility of design (56). In subsequent years, TALENs and CRISPR have emerged as faster, cheaper, and more efficient approaches.

Similar to ZFNs, TALENs are hybrid proteins consisting of a sequence-specific DNA binding domain (derived from the transcription activator-like effectors, TALEs) and the catalytic domain of the Fok1 endonuclease (57). The DNA binding domain of TALEs consists of multiple sequence repeats, each 33–35 amino acids long and identical to others except for residues 12 and 13, termed the repeat variable di-residue (RVD). Each version of the repeat binds to a specific DNA nucleotide and this specificity is determined by the amino acid composition of RVD. TALENs provide high degree of specificity for the target locus with relatively simple rules for the custom protein design and the theoretical potential for off-target mutagenesis is similar to ZFNs. TALENs have proven to be a more efficient and cost-effective platform compared to ZFNs with the potential to target any desired sites in the zebrafish genome at moderate throughput (52, 53, 58).

The CRISPR/CRISPR-associated protein (Cas) type II system was first discovered as an adaptive immune system in archaea and bacteria (55, 59). In this system, the endonuclease Cas9 is directed to specific genomic loci by CRISPR RNA (crRNA) and trans-activating CRISPR RNA (tracrRNA), which recognises target sequences in the genome. Cas9 generates a DSB at the 20-nt target site which has a protospacer adjacent motif (PAM) sequence just adjacent to it, which is ‘NGG’ for the most popular Cas9 from

Streptococcus pyogenes. On average, NGG occurs every 8 bases in the genome. The most advantageous feature of CRISPR is the easy programmability of the single guide RNA (sgRNA, fusion of crRNA and tracrRNA into one component) to target any desired region, which is achieved by altering the 20-nt target sequence contained in the sgRNA. In recent years, CRISPR has emerged as a highly popular gene editing tool of choice due to its high efficiency, cost-effectiveness and simplicity of use. However, the risk of off-target mutagenesis associated with this system has caused concern and been shown to be significant *in vitro* (60). Such levels of off-target activity have not been detected *in vivo*, and CRISPR has been used in zebrafish to achieve high germline mutation transmission rates with low off-target mutagenesis (61-67).

In addition to the various available gene modification strategies, transient gene knockdown is also possible in zebrafish using antisense technologies, which has allowed rapid validation of the pathogenicity of genetic mutations discovered in human patients, including those associated with RP (68, 69). Morpholino oligonucleotides are injected into the zebrafish embryo typically at the one-cell stage and bind to specific mRNA transcripts, either blocking translation or mRNA splicing of the gene of interest. Gene expression can be knocked down for up to 5 days. Although caution should be taken when conducting morpholino experiments, as limitations include the risk of off-target effects and difficulty in reproducibility, with appropriate controls this method can be a quick and effective way to study gene function in wild-type zebrafish.

The accessibility of relatively inexpensive and straightforward genetic techniques is facilitating the production of numerous zebrafish models for a range of retinal diseases. These resources will be invaluable for gaining insight into the underlying pathological details of various disorders and providing preclinical models for assessing the efficacy

and safety of potential treatment strategies.

1.2 Leber congenital amaurosis

Leber congenital amaurosis (LCA, MIM #614186) is the most severe form of IRD, typically causing severe visual impairment at birth or within the first year of life. Although LCA is a rare condition, with a worldwide prevalence of approximately 3 in 100,000 newborns (70), it is still a significant cause of blindness, affecting 20% of children in schools for the blind. Furthermore, it accounts for ⩾5% of all inherited retinopathies.

1.2.1 Clinical characteristics

LCA was first described in 1869 by German ophthalmologist Theodor Leber and now encompasses a group of severe early infantile onset rod–cone disorders (71). The disorder is characterised by the following clinical features: profound and early visual loss, sensory nystagmus (oscillations of the eye), amaurotic pupils and absent electrical signals on an ERG. Symptoms can present as early as 6 weeks, in the form of nystagmus or absence of fixation in the eyes (72). Fundus examination may be normal at presentation, but a variety of abnormal fundus appearances may be present or develop over time, including disc pallor, vessel attenuation or mild peripheral pigmentary retinopathy (71). There may also be disc drusen, optic disc oedema or pseudopapilloedema, a flecked retina, maculopathy or nummular pigmentation. There is a significant degree of phenotypic variability in patients with LCA, with characteristics such as photophobia, refractive error and nyctalopia (night blindness) and the presence of associated ocular features, such as cataracts and keratoconus, varying considerably between patients (72). It has been recognised that in some cases the retinal phenotype can suggest the underlying molecular defect, and these phenotype-genotype

correlations may aid in determining the causative gene.

1.2.2 Genes & proteins

LCA is a highly heterogenous disorder and typically shows monogenic and autosomal recessive inheritance. According to RetNet, 26 causative genes have been identified in patients with LCA to date, accounting for approximately 70% of cases (71). *GUCY2D*, *CEP290*, *CRB1*, *RDH12* and *RPE65* are the LCA genes most frequently mutated. *GUCY2D* was the first gene to be associated with LCA and accounts for approximately 10-20% of cases (71, 73). It encodes retinal guanylate cyclase-1, known to play a role in photoreceptor recovery following phototransduction. Other proteins encoded by LCA genes participate in a variety of retinal pathways, including the retinoid cycle, photoreceptor ciliary transport and photoreceptor outer segment development and disc morphogenesis (71). While a significant proportion of patient cases remain unsolved, modern sequencing technology has facilitated the discovery of several rarer and lesser studied genes associated with LCA, including *KCNJ13*.

KCNJ13

KCNJ13 (MIM #603208) is a three-exon gene located on chromosome 2q37 which encodes a low-conductance inwardly rectifying potassium channel (Kir) that functions as a homotetramer (74-76). The basic structure of a Kir channel is made up of two transmembrane α helices with cytoplasmic NH2 and COOH termini, separated by an extracellular pore-forming loop that acts as a selectivity filter (**Figure 1-5**) (77). The Kir7.1 channel is expressed in a range of tissues, including the intestine, kidney, retina and RPE (75, 76, 78-80). In the RPE, Kir7.1 is localised to the apical membrane at the interface with the photoreceptor outer segments, where it facilitates potassium ion (K^+) efflux to the subretinal space in order to offset a decrease in levels in response to light

A

B

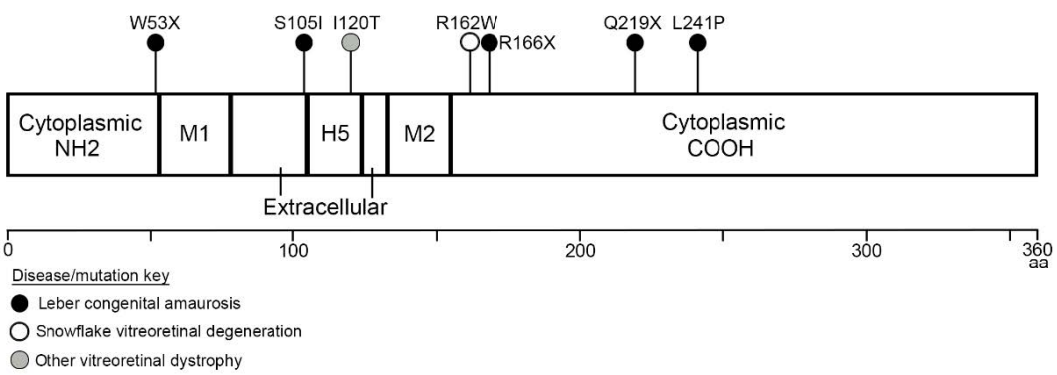

Figure 1-5. Structure of Kir7.1 channel and location of identified mutations.
(A) The Kir7.1 channel is made up of two transmembrane α helices (M1 and M2) with cytoplasmic NH2 and COOH termini, separated by an extracellular pore-forming loop that acts as a selectivity filter (H5). Adapted from (81). (B) Linear structure of Kir7.1 protein with mapped mutations colour-coded according to their associated disease.

exposure (82). Additionally, K^+ transport provides the driving force for controlled fluid flow across the blood–retina barrier formed by the RPE (76, 83). Kir7.1 shows co-localisation with the Na^+/K^+ pump, suggesting that it is involved in K^+ recycling required to keep up with high rates of epithelial ion transport (80).

Mutations in *KCNJ13* were initially identified in three individuals with LCA from two separate families (81). Affected siblings in family A were homozygous for a nonsense mutation, p.Arg166*, while the affected member of family B was found to possess a homozygous missense variant, p.Leu241Pro. All three cases showed early onset visual loss with progressive degeneration of both rod and cone cells, and grossly abnormal retinal appearances which included heavy pigmentation, macular atrophy, nummular pigmented lesions (**Figure 1-6**). Subsequently, a further nonsense mutation, p.Trp53*, was discovered in an LCA patient showing arteriolar abnormalities, macular pigmentation, and bilateral RPE anomalies upon retinal examination (84). Most recently, an individual identified as compound heterozygous for missense and nonsense *KCNJ13* mutations, p.Ser105Ile and p.Gln219*, was diagnosed with LCA with distinct clumpy pigment deposits in the macula, nummular pigment deposits in the macular periphery and retinal vessel attenuation (85). A further missense mutation in *KCNJ13*, p.Arg162Trp, has been associated with a separate ocular disorder, autosomal dominant snowflake vitreoretinal degeneration (SVD, MIM #193230), which features fibrillar degeneration of the vitreous humour, early-onset cataract, minute crystalline deposits in the retina (79). Homozygous missense mutations (p.Ile120Thr) have been identified in patients with a distinct congenital vitreoretinal dystrophy associated with juvenile or early-adult-onset cataracts (86). It is unknown why different mutations cause such phenotypic variability seen in *KCNJ13* patients and mutation-specific modelling will be necessary to examine this further. See **Figure 1-5B** for a visual summary of all *KCNJ13* mutations.

Figure 1-6. Retinal imaging of patients and unaffected family members carrying *KCNJ13* mutations.
(A) Colour photographs of right fundi of patient A-2 (aged 34) and patient A-3 (aged 32) in family A as well as left fundus of patient B-3 in family B (aged 33). Normal left fundus of 39-year old unaffected p.Arg66* carrier (A-1, family A) is also shown. (B) Infrared image and linear spectral domain optical coherence tomography scans of right (1, 2) and left (3, 4) retina of patient B-3 in family B. Right retina of 64-year-old unaffected mother (B-1) is shown for comparison (5). From (81).

1.2.3 Animal models

Various animal models are available for the LCA genes, which have aided in furthering our understanding of the disease pathology. Mouse models for *GUCY2D* (87), *RPE65* (88), *CRB1*(89), *RDH12* (90) have been well characterised and used for successful preclinical gene replacement studies (71). Canine models harbouring mutations in *RPE65* (91) and *RPGRIP1* (92) have also been valuable for proof-of-principle therapeutic studies. Several zebrafish mutants or morphants have been examined for the LCA genes, generally showing obvious developmental defects in the retina (93-96). *CRB1* orthologues have been well characterised in both drosophila and zebrafish, which effectively recapitulate the mammalian phenotype (93, 97).

For *KCNJ13*, two mouse models have been independently generated. Homozygous *Kcnj13* null mutant mice showed cleft palate and moderate retardation in lung development, suffering early postnatal mortality by P0 (98) Examination of the retinal phenotype in *Kcnj13* mosaic mice produced using CRISPR/Cas9 revealed that in regions where RPE cells were lacking Kir7.1, the overlying photoreceptors showed a corresponding degeneration (99). Furthermore, it was found that wild-type RPE cells could rescue neighbouring photoreceptor cells that overlay mutant RPE. ERG a- and b-waves were also reduced in the *Kcnj13* mosaic mice. A further investigation in which Kir7.1 was suppressed in the eyes of wild-type mice showed that loss of channel function caused reduced ERG a-, b- and c-wave amplitudes, while the Kir7.1 blocker had no effect on the *ex vivo* isolated mouse retina ERG where the RPE was not attached to the isolated retina preparation (100). Overall, mouse studies confirm the essential role of RPE-based Kir7.1 function in retinal photoreceptor function and maintenance. *kcnj13* mutant zebrafish (*obelix*) have been identified by their defective skin pattern formation, displaying broader stripes than wild-type fish (101). In this mutant, the melanophores were found to not respond correctly to the melanosome dispersion signal derived from

the sympathetic neurons and this resulted in aberrant melanosome aggregation (102). However, the RPE or retina were not investigated.

1.2.4 Therapeutic studies

The severe blinding nature of LCA has made this condition of key interest for gene therapy development, culminating in several completed or ongoing clinical trials for viral vector delivery of *RPE65* (103-106). The success of such trials has led to the development of the recently FDA-approved Luxturna gene therapy for *RPE65* patients, produced by Spark Therapeutics. Promising preclinical studies also make gene therapy a likely option for *GUCY2D*, *RDH12, CEP290*, *RPGRIP1* and *AIPL1* (71). Other potential therapeutic strategies include the use of CRISPR/Cas9-mediated gene editing, antisense oligonucleotide-mediated splicing defect correction and stem cell-derived RPE implantation. The vast heterogeneity of LCA highlights the need for numerous gene-specific animal and cellular models, for further understanding the specific pathomechanisms of each subtype to enable appropriate gene-tailored treatment.

1.2.5 Summary

Extensive study of the LCA retinal pathophysiology has resulted in well-characterised roles for the most common LCA genes and promising therapeutic advancements for affected patients. This is not the current situation for rarer and more recently identified such as *KCNJ13*, an RPE-localised ion channel gene not directly involved in the photoreceptor morphogenesis, transport or visual pathways, making it dissimilar to many other LCA genes. Examination of the *Kcnj13* mouse demonstrated its essential role in photoreceptor maintenance but was limited by early lethality of the homozygous-null mice. Further investigation using appropriate models will aid in unveiling the disease mechanisms underlying *KCNJ13*-related retinopathy.

1.3 Usher syndrome

Usher syndrome represents a group of inherited disorders characterised by dual sensory impairment of the audiovestibular and visual systems. It is named after Charles Usher, a British ophthalmologist who demonstrated the hereditary nature of this disease in 1914 (107). Usher syndrome is the most common human syndrome involving combined visual and hearing loss, accounting for more than half of deaf–blindness cases (108, 109). It has an estimated prevalence of between 3 and 6 in 100,000 people worldwide (110-114). Furthermore, it represents 5% of all congenital deafness cases and 18% of retinitis pigmentosa (RP) cases (110, 113). Usher syndrome is both clinically and genetically heterogeneous, and is divided into three distinct clinical subtypes associated with a number of genetic loci. To date, there is no available cure for this disease.

1.3.1 Clinical characteristics

Usher syndrome was first described in 1858 by German ophthalmologist Albrecht von Graefe, and is characterised by the combination of sensorineural hearing loss with progressive retinal degeneration in the form of RP (115). It is categorised into three clinical subtypes according to severity of hearing loss and the presence or absence of vestibular dysfunction (116). Usher syndrome type 1 (Usher 1) is the most severe subtype in which patients exhibit profound congenital hearing loss with vestibular dysfunction. It accounts for approximately 25–44% of all Usher syndrome cases (117). Children with Usher 1 show delayed motor development and usually do not walk before the age of 18 months (116). Speech acquisition may also be disrupted if the deafness is not corrected (118). In Usher syndrome type 2 (Usher 2), hearing loss is congenital, moderate to severe, and vestibular function is normal. It is the most common form of the disorder, representing over half of all cases (117). Usher syndrome type 3 (Usher 3) is rare in most populations, accounting for approximately 2% of all cases. Usher 3 patients

display progressive hearing loss with variable vestibular function. Possibly due to regional founder effects, this subtype is much more common in Finland, where it accounts for 40% of Usher syndrome cases (119). It is also particularly prevalent among Ashkenazi Jewish people (120).

RP develops in all three Usher subtypes, typically first presenting as night blindness (nyctalopia) and loss of peripheral vision caused by rod photoreceptor degeneration (121). It eventually progresses to cone cell degeneration and central vision loss, which results in patients becoming registered sight impaired or severely sight impaired (blind). Clinical features may also include abnormal retinal pigmentation, such as peripheral bone spicules, arterial narrowing, and optic nerve pallor, and the development of cataracts. Progression with time is evident symptomatically with a reduction in field, and later loss of acuity. Objectively, this is characterised by a reduction in fundus autofluorescence, thinning of the outer retina on optical coherence tomography, and constriction of field size on perimetry testing. ERG is a sensitive investigation and can show reduction of amplitudes and increased latency in the early stages of the disease. It is a useful test to perform in an infant born with profound deafness to determine the likelihood of underlying Usher 1, even before visual dysfunction is otherwise noted. White light photography (colour images) and autofluorescence images of an adult with Usher 2 are shown in **Figure 1-7**. Although there is much overlap, Usher 1 patients generally have an earlier onset of symptoms and age of diagnosis compared with Usher 2 patients, with Usher 1 presenting in the first decade and Usher 2 in the second or later (122). Usher 3 patients show variable onset of RP but it usually starts from around the age of 20 years (118).

There is variation of clinical expression within each Usher subtype, and overlapping and

Figure 1-7. Clinical imaging of a 55-year-old male with Usher syndrome type 2. Fundus photograph of (A) right and (B) left eye demonstrating an *USH2A* retinopathy. Fundus autofluorescence (FAF) imaging of corresponding (C) right and (D) left eye. A hyperautofluorescent ring on FAF and preserved photoreceptor inner segment ellipsoid line in the area within the hyperautofluorescent ring can be noted. Images provided by Professor Andrew Webster.

atypical presentations have been described for all three. Cases that are not easily classifiable under a certain type could be categorised as atypical Usher syndrome.

1.3.2 Genes & proteins

Usher syndrome is inherited in an autosomal recessive manner. Since the discovery of the first Usher gene in 1995, at least 10 causative genes have been identified for the disease (**Table 1-1**). Among these, there are six Usher 1 genes, three Usher 2 genes, and one Usher 3 gene.

For several Usher genes, there appears to be a genotype–phenotype correlation, and different mutations in most Usher genes have been linked to other disorders, including non-syndromic RP and non-syndromic hearing loss (123-134). Autosomal dominant and autosomal recessive forms of non-syndromic deafness are typically abbreviated as DFNA and DFNB, respectively, and subtypes are numbered in the order they were described (DFNB2, DFNB18, DFNB23, etc.). Mutations in most Usher genes can also lead to atypical forms of Usher syndrome.

The Usher genes encode a number of structurally and functionally distinct proteins, most expressed as multiple splice and protein variants. Many of the proteins are broadly expressed in a range of mammalian tissues, including the brain, olfactory epithelium, kidney, lung, intestine, ovary and testes (135-140). All the Usher proteins are expressed in the inner ear and retina, where they perform essential functions in hearing and vision.

Usher syndrome 1 genes

Currently, there are nine loci known to be involved in Usher 1. The genes identified for

Table 1-1. Usher syndrome loci, genes, proteins, additional associated diseases and animal models.
RP: Retinitis pigmentosa

Usher type	Usher locus	Gene symbol	Chromosomal location	Protein	Predicted function	Associated diseases	Mouse models	Zebrafish models	References
Usher 1	USH1B	*MYO7A*	11q13.5	Myosin VIIa	Motor protein	DFNB2; DFNA11	*Shaker1*	*mariner*	(123, 141-144)
	USH1C	*USH1C*	11p15.1	Harmonin	PDZ scaffold protein	DFNB18	*Deaf circler; Ush1c*$^{-/-}$; *harmonin-PDZ2*^{AAA}*; Ush1c* knock-in	*ush1c*^{fh298}	(125, 145-152)
	USH1D	*CDH23*	10q21–q22	Cadherin-23	Cell adhesion protein	DFNB12	*Waltzer*	*sputnik*	(126, 153, 154)
	USH1E	Unknown	21q21						(155)
	USH1F	*PCDH15*	10q21–q22	Protocadherin-15	Cell adhesion protein	DFNB23	*Ames waltzer*	*orbiter*	(124, 156, 157)
	USH1G	*USH1G*	17q24-q25	SANS	Scaffold protein	Non-syndromic deafness	*Jackson shaker*		(132, 158)
	USH1H	Unknown	15q22-23						(159)
	USH1J	*CIB2*	15q23-q25.1	CIB2	Ca^{2+} and integrin binding protein	DFNB48	*Cib2*^{F91S}, *Cib2*^{tm1a} *CIB2*$^{-/-}$		(127, 160, 161)
	USH1K	Unknown	10p11.21-q21.1						(162)
Usher 2	USH2A	*USH2A*	1q41	Usherin	Cell adhesion protein	Non-syndromic RP	*Ush2a*$^{-/-}$		(163-165)
	USH2C	*GPR98*	5q14-q21	GPR98 (or VLGR1, Mass1	G-protein coupled receptor	Non-syndromic deafness	*Gpr98*$^{-/-}$; *Gpr98*/del7TM		(133, 166-168)
	USH2D	*WHRN*	9q32-q34	Whirlin	PDZ scaffold protein	DFNB31	*Whirler*; *whirlin*$^{-/-}$		(169, 170)
Usher 3	USH3A	*CLRN1*	3q21-q25	Clarin-1	Transmembrane protein	Non-syndromic RP	*Clrn*$^{-/-}$*; Clrn1*^{N48K} KO-TgAC1	*clrn*$^{-/-}$	(134, 171-176)

six of these loci are as follows: *MYO7A* (*USH1B*) (141), *USH1C* (145, 146), *CDH23* (*USH1D*) (153), *PCDH15* (*USH1F*) (156), *USH1G* (158), and *CIB2* (*USH1J*) (127). The *USH1A* locus, originally described in 1992, was subsequently withdrawn due to the finding that six of the nine French families examined in the original study carry mutations in *MYO7A* (177). The *USH1E*, *USH1H*, and *USH1K* loci have been mapped to chromosomes 21q21, 15q22–23, and 10p11.21–q21.1, respectively (155, 159, 162), but the genes are yet to be identified.

MYO7A is the most frequently mutated and well-characterised gene associated with Usher 1 (141, 178). It codes for myosin VIIa, an unconventional motor protein. In addition to a motor domain and five IQ motifs responsible for binding actin, ATP and myosin light chain, myosin VIIa possesses a complex tail region containing various protein–protein interaction domains. It is generally believed that myosin VIIa plays a role in transporting cargo along actin filaments, using ATP hydrolysis to drive movement. It has also been suggested that the protein is required to generate tensions in the cytoskeleton, based on the finding that it is a slow motor that stays bound to actin for extended periods (179).

In addition to Usher 1, different mutations in *MYO7A* have been associated with dominant and recessive non-syndromic hearing loss (DFNA11 and DFNB2, respectively) (143, 180). Mutations that allow some residual motor protein function are thought to cause the milder non-syndromic phenotypes, whereas more severe truncating mutations cause Usher 1 (181). A study of a large Usher 1 patient population with *MYO7A* mutations found extensive variability in the clinical phenotype but did not report a significant genotype–phenotype correlation (182). A milder retinal phenotype was associated with a splice site change (c.133-2A>G), previously

reported to cause DFNB2 (142).

The protein encoded by *USH1C* is known as harmonin (145, 146). This gene is also associated with non-syndromic recessive deafness, DFNB18 (125, 183). Several isoforms have been reported, each containing multiple PDZ (postsynaptic density 95; discs large; zonula occludens- 1) domains (184). PDZ domains are protein modules that interact with the C-terminal sequences of other proteins and are typically involved in the assembly of supramolecular complexes (185). Harmonin may form homodimers (186), and certain isoforms are thought to be capable of binding F-actin (187). Altogether, the properties of harmonin support a key role in organising multiprotein complexes and anchoring to the cytoskeleton.

SANS, the protein produced by *USH1G*, is a further putative scaffolding protein involved in Usher 1 (158). Mutations in SANS are rare, and some have been found to cause atypical Usher syndrome with normal vestibular function (188, 189). SANS possesses several domains capable of mediating protein–protein interactions, including a PDZ-binding motif at its C-terminus (137). It has also been shown to form homomeric structures via its central domain (186). SANS is believed to be another key organiser of protein networks involved in Usher syndrome.

CDH23 and *PCDH15* code for transmembrane cell–cell adhesion proteins cadherin-23 and protocadherin-15, respectively (153, 156). Both genes produce several splice variants and protein. isoforms, which show time- and tissue-dependent expression in the retina and inner ear (190-192). Most of the isoforms of both proteins possess cytoplasmic domains containing PDZ-binding motifs, a transmembrane domain and an extracellular region composed of numerous cadherin (EC) repeats (193). The cadherin domains contain Ca^{2+}-binding motifs, through which the two proteins are

thought to interact with each other to enable Ca^{2+}-mediated cell adhesion in the inner ear hair cells. There appears to be a genotype–phenotype correlation in *CDH23* and *PCDH15*; missense mutations are primarily associated with non-syndromic deafness (DFNB12 or DFNB23), whereas frameshift, nonsense and splice site mutations cause Usher 1 (124, 126, 194, 195).

CIB2 is a relatively recently discovered Usher gene found to underlie both USH1J and DFNB48 (127). It encodes a calcium- and integrin-binding protein containing three helix–loop–helix (EF-hand) domains that change conformation upon binding of calcium, and are thought to mediate intracellular calcium signalling and cellular calcium homeostasis (196). It has been suggested that CIB2 may act as a calcium buffer to maintain optimal Ca^{2+} concentrations in the inner ear hair cells, essential for auditory processes (197). In addition, as it possesses an integrin-binding motif, CIB2 might participate in Ca^{2+}-dependent linkages between the cytoskeleton and plasma membrane. A recent study has disputed *CIB2* as an Usher syndrome causative gene by reporting biallelic loss of function variants in patients with non-syndromic hearing loss and no retinal symptoms (198).

Usher syndrome 2 genes

Three genes underlying Usher 2 have been identified so far, which are *USH2A* (163), *GPR98* (*USH2C*) (166), and *WHRN* (*USH2D*) (130). The *USH2B* locus was withdrawn after the finding that mutations in the *GPR98* and *PDE6B* genes were responsible for the disease phenotypes of the Tunisian family originally studied (199).

USH2A is the most prevalent causative gene in Usher syndrome patients worldwide (138, 163, 200-202). It is a 72 exon gene encoding the protein usherin, for which a short secreted variant (~170 kDa) and a very large transmembrane variant (~600

kDa) have been reported (138, 163). Full length usherin possesses domains common to extracellular matrix proteins and cell adhesion proteins, including several laminin domains and fibronectin III repeats as well as a transmembrane region followed by an intracellular domain with a PDZ-binding domain at its C-terminal end. RT-PCR and immunofluorescence analysis of expression has detected the presence of usherin in many tissues, particularly the vascular and structural basement membranes, although early studies did not distinguish between the two isoforms (138, 140, 203, 204). The long isoform has been detected predominantly in the retina and developing cochlea (138, 165). Usherin may play roles in cellular adhesion, transport and maintaining the function of the basement membranes of the photoreceptors and cochlear hair cells.

USH2A has a diverse mutation spectrum, which includes nonsense, frameshift, missense, and splice-affecting mutations, as well as deletions and duplications (**Figure 1-8**). The most common mutation found in *USH2A*, and the single most frequent molecular defect causing Usher syndrome, is a single base pair (bp) deletion in exon 13 (p.Glu767Serfs*21) (178, 205), which would cause a frameshift mutation if translated, but has also been shown to be associated with exon splicing (206). Mutation of *USH2A* is associated with a significant proportion of non-syndromic RP, and specific mutant alleles are more common among such patients and families (164). A clinical and molecular survey of patients with *USH2A*-associated RP confirmed the presence of 'retinal disease-specific' alleles that are rarely reported in Usher 2 families, the most common being p.Cys759Phe (207). Such 'retinal-disease specific' alleles appear to be distinct from those causing Usher syndrome, the latter class including most alleles that would be expected to produce no viable protein (e.g., those causing premature truncation). In the case of a genotype that includes one 'retinal disease-specific' allele *in trans* with an Usher allele, non-syndromic RP is manifested. The study led to the proposal of a model of allelic hierarchy, in which the

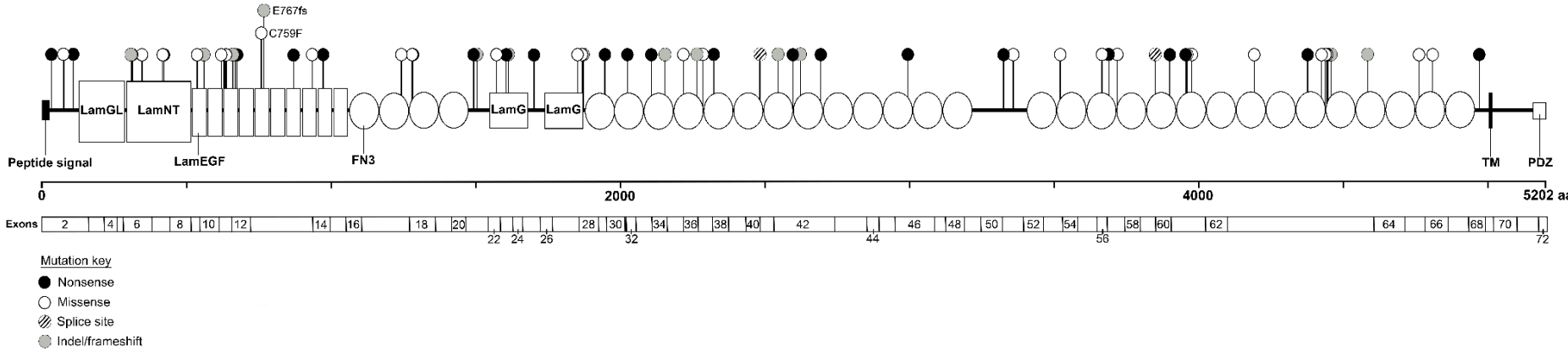

Figure 1-8. Domain structure of the *USH2A* protein with mapped mutations.
The *USH2A* protein (usherin) is a 5202 amino acid protein consisting of the following conserved domains: a laminin globular-like domain (LamGL), an N-terminal laminin domain (LamNT), laminin-type epidermal growth factor-like domains (LamEGF), fibronectin III domains (FN3), a transmembrane domain (TM) and a PDZ-binding domain. Mapped mutations are from a cohort of Moorfields Eye Hospital patients with *USH2A*-related Usher syndrome (unpublished data). p.Glu767Serfs (E767fs) and p.Cys759Phe (C759F) are the most common mutations associated with Usher syndrome 2 and *USH2A* non-syndromic retinitis pigmentosa, respectively.

presence of at least one ‘retinal disease-specific’ allele in a patient with *USH2A*-related retinopathy resulted in preservation of hearing. A further study on *USH2A* genotype-phenotype correlations found that the presence of two truncating mutations was associated with Usher syndrome patients, and the presence of at least one truncating mutation was related with earlier visual decline (208). More severe and progressive hearing impairment has also been associated with a combination of two truncating mutations in *USH2A* (209).

GPR98 (also commonly known as *very large G protein-coupled receptor 1*, *VLGR1*, or *monogenic audiogenic seizure susceptibility 1*, *MASS1*) encodes the largest known (6306 amino acid) cell surface receptor, mutations in which underlie *USH2C* (129, 166). G protein-coupled receptors are seven transmembrane receptors that communicate through heterotrimeric G proteins and other signalling pathways to transduce extracellular signals into intracellular physiological changes (210). GPR98 is in the adhesion G protein-coupled receptor subfamily, members of which are characterised by very large extracellular N-termini featuring various adhesion domains capable of mediating cell–cell and cell–matrix interactions (211). GPR98 is typically regarded as an orphan receptor, and the mechanism of GPR98-regulated signalling and its role in Usher syndrome remain elusive. It was been reported that the receptor undergoes autoproteolysis into α and β subunits, the latter of which is able to signal independently via coupling with the G protein α_i subunit ($G\alpha_i$) (212). Previously, the receptor has been found to be able to sense extracellular calcium and activate protein kinases A and C via the $G\alpha_s$ and $G\alpha_q$ subunits (213).

The least common Usher 2 causative gene, *WHRN*, produces the cytoskeletal scaffold protein whirlin (130). There are multiple transcripts of whirlin and two predominantly expressed variants (long and short) (169, 214). N-terminal mutations

that affect the long isoform are found in *USH1D* patients (130, 215), whereas mutations in the C-terminal region manifest as DFNB31 (170, 216). The full length protein contains a proline-rich region and three PDZ domains, all thought to be protein interaction modules. As whirlin is the nearest homologue of the *USH1C* protein harmonin, it is believed to be another key assembler of protein complexes essential to visual and hearing function (214).

Usher syndrome 3 genes

CLRN1 (or *USH3A*) is the only gene currently confirmed for Usher 3 (171, 217). It codes for the four-transmembrane-domain protein, clarin-1. Two prevalent mutations, p.Tyr176* and p.Asn48Lys, account for most cases of Usher 3 in Finnish and Ashkenazi Jewish patients, respectively (120, 218). It is otherwise a highly uncommon disorder. Clarin-1 belongs to a superfamily of four-transmembrane-domain proteins (TM4SF), which includes the claudin and tetraspanin families (219). Structural and sequence homology to the cerebellar synapse protein stargazin suggests a role for clarin-1 in the photoreceptor and hair cell synapses (171) and supporting reports have indicated that the protein is involved in synaptic development and maintenance (220, 221). In addition, it has been found to associate with tubulin and post-trans-Golgi vesicles in mouse hair cell cultures, implicating a function in vesicle transport (222). Clarin-1 may also be involved in actin cytoskeleton regulation as it was demonstrated in cell culture studies that the protein forms microdomains in the plasma membrane, affects F-actin organisation and induces lamellipodia formation (223).

Other Usher syndrome-related genes

In addition to the known Usher causative genes, a further gene *PDZ domain-containing 7* (*PDZD7*) has been reported to act as a disease modifier and contributor to a digenic form of Usher syndrome, suggested to dispute the traditional view of the

syndrome as a classic Mendelian disorder (224). A subsequent sequencing analysis study investigating nine Usher genes in a UK patient cohort did not find convincing evidence of digenic inheritance, indicating that this does not make a significant contribution to Usher syndrome (178). *PDZD7* mutations have also been identified as causative of non-syndromic hearing loss (225).

One study reported homozygous nonsense mutations in *CEP250* (encoding ciliary protein C-NAP1) linked to cases of atypical Usher syndrome, characterised by early onset hearing loss and mild RP (226). The same patients were also found to be heterozygous for a mutation in *C2orf71*, an additional ciliary protein gene known to cause recessive RP. Mutations in *CEP78* have been identified in patients with adult-onset cone-rod dystrophy and sensorineural deafness, also described as atypical Usher syndrome (227). A novel homozygous missense variant in *histidyl-tRNA synthetase* has also been reported in two patients with a phenotype compatible with Usher 3 (228).

1.3.3 Animal models

Mouse models

A number of spontaneous and transgenic animal models have been described for the Usher genes over the years. To date, there has been at least one mutant mouse model characterised for each Usher causative gene (118, 160). Most available models display a relatively faithful manifestation of the hearing and balance abnormalities found in Usher syndrome. Congenital deafness is a common feature of the Usher syndrome models, with characteristic head tossing and circling behaviour indicative of vestibular dysfunction observed in Usher 1 and Usher 3 mutants (except *Cib2* mice, where vestibular function is preserved). *Gpr98* knockouts are also

susceptible to audiogenic seizures (229).

Examination of the Usher mutant inner ear has revealed distinctive abnormalities in hair bundle architecture in these models. Hair bundles are the specialised mechanosensitive structures found on inner ear hair cells, consisting of well-organised stereocilia graded in height. Mice with mutations in Usher 1 orthologues have been found to possess abnormally developed hair bundles with fragmented and misorientated stereocilia (147, 160) with the exception of *CIB2* knockout mice where hair bundles develop normally and degenerate postnatally in the cochlea (161). Consistently, various mechanotransduction (MET) abnormalities have been observed in Usher 1 mutants (157, 160, 230-232). In *Gpr98*, *Ush2a*, and *Whrn* mutant mice, abnormal stereociliary organisation and defective MET responses have been reported in outer hair cell (OHC) but not in inner hair cell (IHC) bundles (165, 167-169, 233). An interesting exception is $Whrn^{wi/wi}$ mice, which show shortened stereocilia in both hair cell types as well as disorganised OHC bundles (170, 234, 235). $Clrn^{-/-}$ mice exhibit a similar phenotype to most of the Usher 2 models, showing defective OHC bundle morphology and MET responses, with normal IHC bundle development (172, 236). They also demonstrate progressively severe head tossing and circling behaviours and defective MET responses in the vestibular hair cells. Overall, the morphological and electrophysiological defects demonstrated by Usher mutant mice are indicative of an essential Usher protein role in correct hair bundle development and function.

In contrast to the close imitation of audiovestibular defects observed in Usher syndrome patients, the majority of the Usher mouse models do not mimic the retinal symptoms that are also characteristic of the disorder. Obvious widespread retinal cell degeneration and vision loss have been reported only in *Ush2a* and *Whrn* (long

isoform) knockout (165, 169) and *Ush1c* knock-in mice (in which the mouse *Ush1c* was replaced by a sequence cloned from Acadian Usher 1 patients) (148). A further Usher mouse model derived from a Kunming background (named $KM^{USH/USH}$) was discovered to have reduced expression of *Pde6b* and *Ush2a* and develop spontaneous RP (237). Among the mice that show no retinal degeneration, some *Myo7a*, *Cdh23*, *Pcdh15*, *Gpr98* and *Clrn* mutant strains show abnormal ERG responses, as well as the *Ush1c* knock-in mice, indicative of compromised photoreceptor function (148, 167, 238-241). Other distinctive retinal features have been observed in mice lacking myosin VIIa, which display increased opsin concentration in the photoreceptor connecting cilium (242) and aberrant positioning of the melanosomes and phagosomes in the RPE cells (243, 244). There is also a reduced concentration of RPE65 in the RPE, which is a key metalloenzyme in the retinoid visual cycle necessary for maintaining visual function (245). These findings are consistent with multiple transport-related roles of myosin VIIa in the retina. Although photoreceptor loss is not evident in *Ush2a* mutant mice until after a year of age, defective optomotor responses, cone opsin mislocalisation and Müller glia activation has been detected as early as day 70 postnatally (246).

The phenotypic discrepancy between Usher syndrome human patients and Usher mutant mice could be related to many factors, including the shorter lifespan of mice compared with humans, functional redundancy of Usher proteins in the murine retina and interspecies differences in light exposure and photoreceptor cell architecture (118, 247). One notable structural difference between primate and rodent photoreceptors is the presence of calyceal processes, which are absent or vestigial in mice (247). Calyceal processes are microvilli-like structures that form membrane–membrane connection sites between the outer segment of the photoreceptors and surrounding subcellular compartments. Usher 1 proteins have been found to co-

localise in these structures in primate photoreceptors. In addition to the lack of calyceal processes, murine cone photoreceptors were reported to show a different distribution pattern of the Usher 1 proteins, which was suggested to explain why the mouse models do not have a degenerative retinal phenotype. It has been found that continuous light exposure or short-term light/dark changes are able to induce retinal degeneration in *USH1B* and *USH2D* mouse models (248, 249) and therefore may be necessary to produce similar phenotypes in the other Usher syndrome models. However, contradictory findings have been reported by a separate study, which suggest that the retinas of *Myo7a*$^{-/-}$ mice are more resistant to light-induced damage compared with wild-type retinas (245). Recently, loss of *Ush1g* and *Ush1c* in albino mice was able to induce cone dysfunction and death (250).

Zebrafish models

The zebrafish has become an increasingly popular model for both auditory and visual studies in recent years, and a number of mutants and morphants have been described for orthologues of the Usher genes. Zebrafish possess two mechanosensory systems, the inner ear and the lateral line, both of which contain hair cells that are homologous to that of the mammalian inner ear (251). *myo7a*, *cdh23*, *pcdh15a* and *ush1c* mutant zebrafish have all been reported to show defects related to balance and hearing (144, 149, 154, 252). Consistent with the corresponding mouse models, the hair bundles of these Usher 1 mutant larvae show a disorganised splayed stereocilia arrangement and are functionally defective. In addition, knockdown of *cib2* expression in zebrafish larvae resulted in abnormal hair bundle development and reduced microphonic potentials of the lateral line neuromasts (127).

In the zebrafish retina, several Usher proteins have been localised to subsets of retinal cells other than the photoreceptors, including the Müller cells and amacrine cells (149, 253, 254). Visual symptoms have not been ubiquitously reported in the Usher 1 zebrafish models, and the most obvious retinal phenotypes have been observed in *myo7a*, *pcdh15b* and *ush1c* mutants/morphants (149, 252, 255). *myo7aa*$^{-/-}$ zebrafish were reported to show mild retinal degeneration by 10 days post-fertilisation (dpf), which was exacerbated by rearing in constant light conditions (255). Furthermore, ERG recordings revealed a significant decrease in both a- and b-wave amplitudes in these mutants. Zebrafish possess two orthologues of the *USH1F* gene, *pcdh15a* and *pcdh15b*, which were found to play independent roles in hearing and vision (252). Although mutations in *pcdh15a* cause deafness and vestibular dysfunction, knock down of *pcdh15b* expression caused improper photoreceptor outer segment organisation and reduced optokinetic and ERG responses. *ush1c* mutant zebrafish larvae were reported to have early progressive retinal cell degeneration with defective optokinetic responses (149). Furthermore, ERG recordings from *ush1c* morphants revealed a diminished b-wave to a-wave ratio.

Among the Usher 2 gene orthologues, morpholino knockdown of *ush2a*, and *gpr98* in combination with *pdzd7a*, showed increased photoreceptor cell death observed at 5 dpf (224). *pdzd7a* morphants also demonstrated abnormal hair bundle development, hearing defects and circle swimming behaviour indicative of vestibular dysfunction. Moreover, disrupting expression of *dfnb31a* and *dfnb31b* (zebrafish *WHRN* orthologues) resulted in reduced optokinetic responses (256). As morpholino knockdown of gene expression only lasts up to around 5 dpf, examination of germline mutants will be necessary to further investigate the Usher 2 genes in zebrafish at later stages of development.

Consistent with the other Usher genes examined in the zebrafish, blocking the expression of the USH3A protein orthologue, clarin-1, leads to functionally defective neuromast hair cells (220). Although hair bundle morphology was not affected in these morphants, the neuromasts of these morphants showed reduced MET channel activity, defective vesicular turnover, shortened kinocilia, and mislocalisation of the synaptic components. In contrast, *clrn1* mutants generated by ZFNs displayed aberrant hair bundle morphology with diminished function (174). In the same study, two transgenic zebrafish lines were produced either expressing human wild-type *CLRN1* or mutant *CLRN1* containing the missense mutation commonly found in Ashkenazi Jewish patients (*CLRN1*^{N48K}). The wild-type clarin-1 localised to the hair bundles, while the mutant protein mostly mislocalised to the cell body, with only a small amount reaching the hair bundle. Visual abnormalities have not been reported in either *clrn1* morphants or mutants.

1.3.4 The Usher interactome

Although the Usher genes are predicted to encode proteins with a range of individual functions, the similarities of clinical phenotype within different types of Usher syndrome supports the idea that all the Usher proteins are involved in a common cellular mechanism. The interactome model is a unifying theory that postulates the existence of dynamic Usher protein complexes in the inner ear and retina that perform vital roles in vision and hearing. Harmonin, SANS, and whirlin are proposed to be scaffolding proteins at the core of these multiprotein complexes, which consist of both Usher and non-Usher proteins. Support for this hypothesis has been gained through several biochemical assays which have revealed extensive *in vitro* interactions among Usher 1 and/or Usher 2 proteins (168, 186, 187, 214, 232, 257-261). For example, harmonin has been found to interact with all other Usher 1 proteins (except CIB2), as well as usherin and GPR98 (186, 187, 257, 262). Furthermore, the finding

that ablation of one Usher protein leads to mislocalisation or loss of at least one other Usher protein in the mouse inner ear and retina provides evidence that such interactions exist *in vivo* (147, 168, 187, 232, 259, 262-264), for example, normal cellular localisation of usherin and GPR98 is abolished in the whirlin knockout mouse (169).

As the Usher protein complexes have been localised to several subcellular locations in the ciliated sensory neurons of the inner ear and retina, Usher syndrome is considered a ciliopathy. Abnormalities that could be related to cilia defects, including slow sperm motility, bronchiectasis, and reduced beat frequency of the nasal cilia have been occasionally reported in some Usher syndrome patients (265-267). An investigation into olfactory function found that Usher 1 patients showed a greater age-related decline in olfaction, and older Usher 1 patients had significantly lower olfactory scores compared to healthy controls (268). Furthermore, various Usher proteins were shown to be expressed in the murine nasal epithelium, and electro-olfactogram readings from Usher 1 mutant mice were indicative of significantly different odour detection capabilities (269). However, the main sensory defects associated with Usher syndrome indicate the most prominent roles of the Usher complexes are in the cochlea and retina, where various studies have indicated involvement in cohesion, MET, synaptic maturation, and protein and organelle transport. Below is an outline of the key Usher protein networks in the inner ear and retina.

Usher complexes in the inner ear

The cochlear and vestibular hair cells are the sensory cells responsible for converting mechanical stimuli into electrical responses. In the inner ear, OHCs receive and mechanically amplify low-level sound-evoked vibrations entering the cochlea, whereas IHCs convert the amplified mechanical signals into electrical receptor

potentials which are relayed to the brain (270). Hair bundles, the mechanoreceptive organelles present on the apical surface of the hair cells, are composed of three to four rows of actin-filled stereocilia arranged in increasing height toward the kinocilium. The kinocilium, the genuine hair cell cilium, is a transient structure in hair cell development responsible for correct orientation of the developing stereocilia (271). Deflection of the stereocilia results in mechanical opening of MET channels located at the top of the hair cell stereocilia, inflow of cations into the hair cell causing membrane depolarisation and release of neurotransmitter from the ribbon synapse at the basal end of the cell (270).

There are a number of transient and permanent fibrous links that tether the stereocilia together in the developing and mature hair bundles (**Figure 1-9**) (272). In the developing hair bundle, these links are essential for the maintenance of hair bundle cohesion. Cadherin-23 and protocadherin-15 are interacting components of the transient lateral links and the kinociliary links, which form dense networks that interconnect the emerging stereocilia as well as the stereocilia to the kinocilium (147, 192, 273). In mice, these links usually appear by embryonic day 17.5 and disappear postnatally (272). Harmonin isoform b most likely anchors the links to the actin core of the stereocilium, whereas myosin VIIa and SANS ensure the correct localisation of harmonin-b in the bundle (147). All Usher 1 mouse mutants possess similar morphological hair bundle anomalies that support the existence of these complexes. These include fragmentation of the hair bundle from the earliest stage of hair bundle development onwards, along with a mispositioned kinocilium frequently not associated with a stereocilia cluster (147).

Around postnatal day 0 (P0), transient structures located near the base of the stereocilia, known as ankle links, begin to form (272). GPR98, usherin, and whirlin

Figure 1-9. Stereociliary links during hair bundle development and in the mature inner ear hair cell.
Cadherin-23 (CDH23) and protocadherin-15 (PCDH15) are components of the kinociliary links and transient lateral links that connect the emerging stereocilia and kinocilium (K) during embryogenesis. Postnatally, these links are replaced by ankle links (of which usherin and GPR98 form components) and apical lateral links. In the mature hair cell, the kinocilium disappears and adjacent stereocilia are connected by horizontal top connectors and tip links. Cadherin-23 and protocadherin-15 comprise the tip links. The upper tip link density (UTLD) and lower tip link density (LTLD) are the tip link sites of insertion on the stereocilia. SANS, harmonin-b and myosin VIIa localise at the UTLD.

(and PDZD7) have been found to co-localise in the ankle link region, and the proteins have been found to be mutually dependent for normal localisation in the hair cells (167-169, 214, 274). The individual proteins have been found to make distinct contributions to the ankle link assembly, with GPR98 playing the most essential role (263). It has been demonstrated that myosin VIIA is also crucial for the correct localisation of the Usher 2 proteins in the stereocilia (264). Usher 2 mouse mutants have a much milder stereociliary dysmorphic phenotype than Usher 1 models, which becomes apparent after birth (165, 167-169, 263, 275). The OHCs of these mice show abnormal U-shaped hair bundles, compared with the V-shaped staircase-like organisation observed in wild-type mice. Stereociliary morphological defects in Usher 2 mutant mice suggest roles for the ankle link complex in regulating IHC stereociliary growth and differentiation as well as OHC stereociliary rigidity and organisation during postnatal development (263).

In addition to their role in stereociliary development, the Usher 1 proteins are essential for the functioning of the mature hair bundle as they are the building blocks of the MET apparatus, the tip link (276). The tip link itself comprises of homodimers of cadherin-23 and protocadherin-15 interacting via their EC repeats, which form a link between adjacent stereocilia (261). Myosin VIIa, SANS, and harmonin are believed to form a complex in the upper tip link density, which is the point where the cadherin-23 C-terminal attaches to the taller stereocilium and is anchored to the actin core by harmonin-b (150, 262, 277). Disrupting *Cdh23*, *Pcdh15* or *Ush1g* in mice (157, 232) and *cdh23* in zebrafish (154) results in the absence of tip links, and the Usher 1 mouse mutants demonstrate MET abnormalities (150, 157, 230-232). The cytoplasmic domain of protocadherin-15 is anchored to the adjacent shorter stereocilia at the lower tip link density, the molecular composition of which is much less well characterised (276). CIB2 has been localised to the stereocilia, with increased

concentration near the tip, and functional studies in zebrafish have indicated an involvement in the MET response (127). Tip links are proposed to be coupled with MET channels, which are located at the base of the links, and may operate through a direct or indirect gating spring mechanism (270).

In both the inner ear and retina, several Usher proteins have been localised to the sensory cell ribbon synapses, although their function at these locations remains relatively unexplored. Variants of protocadherin-15, cadherin-23, harmonin, clarin-1, usherin, GPR98 and whirlin have all been reported in the synapses of the developing and mature hair cells (190, 214, 221, 254, 257, 278, 279). Protocadherin-15, cadherin-23, GPR98 and clarin-1 have been reported to interact and form a complex at the hair cell synapses (221). Defective protocadherin-15 or clarin-1 in mice results in delayed synaptic maturation, indicating a role for the complex in synaptogenesis. In addition, GPR98 has been found to interact with SNAP25, a component of the SNARE complex, suggesting involvement of the Usher proteins in vesicle docking and fusion (278). Harmonin isoform a is expressed at the base of hair cells and photoreceptors (183, 279) and has been reported to presynaptically associate with $Ca_v1.3$ Ca^{2+} channels in the mouse inner ear, highlighting a role in regulation of the electrical and calcium signals in the sensory cells (279, 280).

Usher complexes in the retina

In the retina, photoreceptors are the light-sensitive neurons that convert light energy into electrical signals. They possess an outer segment, which is packed with flat membrane disks that contain the proteins essential for phototransduction, and an inner segment in which the organelles necessary for metabolism and protein synthesis are located. The inner and outer segments are linked by a connecting cilium, through which the molecular components required for phototransduction are

transported. At the basal end of the cell is the cell body and synaptic terminus, necessary for signal transmission to the bipolar and horizontal cells.

Knowledge of the Usher protein functions in the retina is much more limited than that of the inner ear, largely due to the absence of obvious retinal phenotypes in most of the animal models examined. Although expression in other retinal cells (such as the RPE and Müller cells) has been observed for some Usher proteins (127, 149, 173, 253, 254, 281), they have been found to localise to several main locations within the photoreceptor cells, including the periciliary region and basal bodies near the connecting cilium, and the synaptic region (**Figure 1-10**) (282). In mouse and monkey photoreceptors, GPR98, usherin, and whirlin are expressed at the periciliary membrane complex (PMC), a specialised plasma membrane region near the connecting cilium, which is thought to be analogous to the periciliary ridge complex (PRC) in frog photoreceptors (247, 258). The amphibian PRC is a specialised domain for docking and fusion of transport vesicles. The three Usher 2 proteins have been found to form a network at the PMC in mouse photoreceptors and if any of the proteins are defective, formation of this Usher 2 complex is disrupted (169). SANS also localises at the connecting cilium region where it has been shown to interact with whirlin and provides a linkage to the microtubule transport machinery (258). Although certain mutations of *Ush2a* and *Whrn* cause retinal degeneration in mice, indicating the importance of the Usher 2 complex in photoreceptor survival, there is limited evidence that it is involved in protein trafficking through the connecting cilium. However, cone opsin and rhodopsin have been found to be mislocalised in *Ush2a* (165, 246) and *whirler* mice (249), respectively. The Usher protein that has the most well-characterised retinal functions in transport is myosin VIIa, which has been shown to be play a role in the trafficking of opsin and transducin through the connecting cilium (242, 248). Furthermore, it is required in the RPE for correct localisation of the

Figure 1-10. A rod photoreceptor with several key Usher protein cellular locations.
Photoreceptors are specialised ciliated sensory neurons consisting of an outer segment packed with membrane discs containing the photopigments, a connecting cilium with microtubules, an inner segment with organelles necessary for metabolism, a cell body containing the nucleus and a synaptic terminus. The calyceal processes are microvilli-like structures that connect the basal end of the inner segment to the surrounding cellular structures. In primate photoreceptors, the Usher (USH)1 proteins localise in these structures. The USH2 proteins are localised to the periciliary membrane complex, which may be involved in vesicle trafficking between the inner and outer segment. Myosin VIIa is highly expressed in the retinal pigment epithelium (RPE), where it is required for correct localisation of the melanosomes, phagosomes and the enzyme RPE65. All the USH proteins have been detected in the synaptic region, where they may be involved in synaptogenesis and maintenance. The exact localisation of CIB2 is yet to be determined.

melanosomes, phagosomes and the enzyme RPE65 (243-245). As observed in the cochlear hair cells, most of the Usher proteins have been localised to the synapses of the retinal photoreceptor cells, indicating a role in synaptogenesis and maintenance (137, 149, 184, 190, 214, 222, 257, 283, 284). Consistent with this idea, 'floating' ribbon synapses are observed in the zebrafish retina when *ush1c* expression is knocked down (149). In the mouse retina, whirlin shows an association with the $Ca_v1.3$ Ca^{2+} channels, which suggests an involvement in channel organisation and membrane fusion (283). Studies focusing on the Usher protein interactions in the neuronal synapses are necessary to further uncover their synaptic functions in the photoreceptors and hair cells.

In human, monkey, and frog photoreceptors, all Usher 1 proteins except CIB2 (not examined) have been localised to the calyceal processes (247). It has been suggested that they form an Usher 1 protein-mediated adhesion belt that connects the outer segment basal region to the surrounding structures. Although the role of the calyceal processes is still unknown, they have been proposed to be synonymous structures to hair cell stereocilia, raising the possibility of a mechanosensory-related role of the Usher 1 network in the retinal photoreceptors. Recent findings in *Xenopus* indicated that calyceal processes, together with their associated links, may control the sizing of rod disks and cone lamellae throughout their daily renewal (285).

1.3.5 Therapeutic studies

Although there is currently no effective treatment to cure Usher syndrome, various studies have made progress toward developing molecular and cell-based therapies for the disease. As cochlear implantation has proven to be an effective approach to ameliorate hearing loss in Usher 1 and Usher 3 patients (286, 287) and hearing aids

are a suitable strategy for Usher 2 patients, therapeutic studies have mostly focused on treating the retinal defects.

The retina is an attractive therapeutic target due to its immune-privileged nature and accessibility for the delivery of intraocular treatments. In recent years, significant focus has been drawn on the development of gene replacement therapy using viral vectors. Several investigations have employed the use of adeno-associated virus (AAV) vectors to restore expression of myosin VIIa in the RPE cells and photoreceptors of *Myo7a* mutant mice after subretinal injection (288-291). Two different studies have demonstrated that single AAV vectors carrying human *MYO7A* cDNA administered to the retinas of adult mutant mice were able to restore wild-type or higher than wild-type levels of functional myosin VIIa expression, which corrected opsin distribution in the photoreceptors and melanosome localisation in the RPE for several months post-injection (288, 289). Recovery from light desensitisation was also improved in these mice up to 6 months post-injection (288). Replacement of whirlin expression has also been achieved in the whirlin knockout mouse retina using a similar approach (292). Delivery of murine *Whrn* cDNA via AAV vectors at P18 was able to produce wild-type levels of whirlin expression and restore cellular localisation of usherin and GPR98 for up to 6 months. In *Clrn1*$^{-/}$ mice, AAV-based delivery has been used to express CLRN1 in the adult retina following subretinal or intravitreal injection (293).

Although these techniques have shown some success in rescuing the retinal molecular and cellular defects in these models, there are safety concerns over packing large cDNAs, such as *MYO7A* and *USH2A*, into single AAV vectors, which have a carrying capacity that is significantly smaller than these genes. To address this problem, some researchers have utilised dual AAV vectors, which reconstitute

the gene by splicing (trans-splicing), homologous recombination (overlapping), or a combination of both (hybrid) (289-291, 294). However, restoration of protein expression levels and phenotypic rescue has been reported to be less effective when using this approach (289, 290, 294). For instance, Lopes et al. (289) found that subretinal injection of *MYO7A* split between dual overlapping AAV vectors produced variable levels of protein expression in the *Myo7a* mutant mouse retina that were significantly less than those achieved from single 'oversized' AAV delivery. Furthermore, only a minority of retinal cells showed corrected opsin and melanosome localisation.

Alternatively, delivery of functional *MYO7A* to the *USH1B* mouse model retina via lentiviral-based vectors has proved successful (295, 296). An EIAV (equine infectious anaemia virus)-based lentiviral vector carrying the human *MYO7A* gene (UshStat) injected subretinally into neonatal mutant mice was able to restore photoreceptor function, determined by evaluating α-transducin translocation in photoreceptors in response to low light intensity levels, and protected the photoreceptors from light-induced degeneration (296). Although they offer the advantage of a larger carrying capacity than AAV vectors, lentiviral vectors have more limited efficiency and there is a potential risk of tumourigenicity as a result of insertional mutagenesis (297). Currently, there is an ongoing Phase I/II clinical trial being conducted by Oxford BioMedica to evaluate the safety of UshStat in USH1 patients with *MYO7A* mutations (https://clinicaltrials.gov/ct2/show/NCT01505062).

Although initial gene therapy studies for Usher syndrome focused on retinal function, subsequent investigations have examined the hearing and balance defects. Gene delivery using AAV vectors has achieved significant improvements in auditory and

vestibular hair cell function in mouse models of USH1C (298), USH1G (299), USH2D (300) and USH3 (176).

Studies using cell-based strategies have included an investigation in which forebrain-derived neural progenitor cells were transplanted into the retinas of *Ush2a* knockout mice at P80 (246). Functional deterioration of vision was prevented and mislocalisation of cone pigment was reversed for at least 10 weeks. Due to short follow-up time, it is unknown whether the transplant would have alleviated retinal degeneration, as photoreceptor loss only becomes evident in this model after 1 year. Retinal implantation of capsules containing human NTC-201 cells has been trialled in patients with isolated RP, Usher 2 and Usher 3 but showed no therapeutic benefit in the primary outcome variable (301). These cells release ciliary neurotrophic factor, which were previously found to reduce photoreceptor loss in animal models of retinal degeneration (302). Although the development of cell-based therapies to treat a range of medical conditions shows huge promise, evidence for the use of such strategies to specifically treat Usher syndrome is currently lacking.

Investigations using small molecules to treat Usher syndrome have included the use of translational read-through drugs, which are able to induce insertion of an amino acid at the site of premature stop codons, allowing read-through of nonsense mutations. These drugs, which include aminoglycosides and their derivatives, have been used to suppress *PCDH15* and *USH1C* patient nonsense mutations *in vitro*, in cell cultures and in retinal explants (303-307). Furthermore, *in vivo* administration of molecules NB54 and ataluren (PTC124) was able to restore expression of full-length harmonin in the mouse retina (307). As traditional read-through drugs have been found to be highly cytotoxic, considerable efforts over the past few years have focused on producing new generations of ‘designer’ aminoglycoside derivatives with

high efficiency and low cellular toxicity. Ataluren, a drug unrelated to aminoglycosides, has demonstrated relatively low toxicity with high read-through efficacy (307). Although read-through drugs offer several advantages, including viral vector-free delivery and no risk of mutagenesis by genome insertion, they are not appropriate for treating the proportion of Usher cases that are not caused by nonsense mutations. Another small molecule that has been of interest for Usher syndrome treatment, known as BioFocus 844 (BF844), was identified through cell-based high throughput screening as capable for stablilising Clarin-$1^{N48K,}$ (175). BF844 was shown to attenuate hearing loss and prevent deafness when administered to an Usher 3 knock-in mouse model.

Other molecular approaches include genome-editing, which can involve the use of synthetic nucleases that are capable of cutting around gene mutations and correcting the DNA error through homologous recombination with a normal DNA template (308). One study employed the use of two ZFNs to correct an *USH1C* point mutation and induce full-length harmonin expression in cultured cells (309). In recent years, the CRISPR/Cas9 system has become highly popular for gene editing due to its efficiency and ease of use, and may be an effective tool for correcting Usher mutations. This technique was used for successful *in vitro* mutation repair in *USH2A* patient fibroblasts harbouring homozygous c.2299delG mutations (310). Although specificity was high in this study, off-target toxicity is still a major concern in the use of genome-editing techniques and significant investigation is required to assess the feasibility of these techniques as a mode of treatment in patients.

A further therapeutic option is the use of antisense oligonucleotides (ASOs), which are short synthetic modified nucleic acids that bind RNA through base pairing, and can be designed to bind pre-mRNA at cryptic splice sites and therefore prevent

defective splicing. One study reported the use of ASOs to rescue both the hearing and vestibular defects in USH1C knock-in mice, which possess a cryptic splice site mutation that results in truncated harmonin protein (311). Peritoneal injection of ASO in neonatal mice was shown to partially correct defective pre-mRNA splicing of mutant *USH1C* transcripts, increasing protein expression, and improving cochlear hair cell morphology. A single systemic dose was able to restore hearing and vestibular function up to 6 and 9 months respectively, although it remains to be seen whether ASOs can also rescue the retinal phenotype in these mice. The same group have delivered ASOs to USH1C knock-in fetal mice *in utero* via intrauterine injection into the amniotic cavity and observed corrected splicing in the inner ear of postnatal mice, highlighting the potential of this therapy for treating congenital diseases prenatally (312). ASOs have also been used to correct a splicing defect caused by a deep intronic mutation in the *USH2A* gene (c.7595-2144A>G) which leads to insertion of a pseudoexon, in both patient-derived fibroblasts and a minigene splice assay (313).

1.3.6 Summary

Since the discovery of the first Usher gene over 20 years ago, considerable progress has been made in our understanding of the genetics of Usher syndrome. The Usher genes encode a number of proteins with various cellular functions, including scaffolding, adhesion, trafficking, and signalling. Extensive biochemical, cellular localisation and animal studies have been used to examine the molecular details underlying the Usher syndrome pathogenesis. Significant evidence indicates that the Usher proteins form multicomponent complexes in the inner ear hair cells, where they are essential for hair bundle development and maintenance. Roles in protein transport and synaptogenesis in the retina and inner ear have also been highlighted, although knowledge on these functions is less clear. Investigation into the Usher protein networks and their roles in the retina has proved a challenge, largely due to the lack

of Usher mouse models with obvious retinal phenotypes. A range of therapeutic studies have showed huge promise for the development of effective treatments for Usher syndrome-associated RP, although progress may currently be limited by the necessity for appropriate models with retinal degeneration.

1.4 Aims

Chapter Three: KCNJ13

In this chapter, the *KCNJ13*-related retinopathy will be investigated by:

i) Examining the conservation and expression of *kcnj13* in the zebrafish.

ii) Characterising the retinal phenotype of *kcnj13* zebrafish mutant, *obelix*^{td15}.

Chapter Four: USH2A

In this chapter, the *USH2A*-related retinopathy will be investigated by:

i) Examining the conservation and expression of *ush2a* in the zebrafish.

ii) Generating an *ush2a* mutant zebrafish using the CRISPR/Cas9 system.

iii) Characterising the retinal phenotype of *ush2a* mutant zebrafish.

2 Materials and Methods

2.1 Zebrafish husbandry

Wild-type AB (WT), *obelix*^{td15} (*obe*^{td15}) and *ush2a* zebrafish were generated by natural pair-wise matings of genotyped heterozygous or homozygous fish and were maintained at the University College London (UCL) Institute of Ophthalmology biomedical research unit or at the Bloomsbury campus zebrafish facility according to standard protocols (314) and UK Home Office guidelines. *obe*^{td15} and *ush2a* homozygous mutant fish were compared to age- and strain-matched fish, *obe*$^{+/+}$ and *ush2a*$^{+/+}$ respectively, which are referred to as WT. Genotyping primer sequences and conditions are listed in **Table 2-1**. Fish were maintained at 28.5˚C on a 14:10 hour light: dark cycle. Developing embryos were staged in hours post fertilisation (hpf) or days post fertilisation (dpf) as previously described (315). If being light or dark-reared, embryos were incubated in constant light or constant darkness using specialised light-controlled boxes up to 8 dpf. For terminal experimentation, zebrafish were anaesthetised in 0.2 mg/ml Tricaine (MS-222, Western Chemical Inc.) and euthanised under schedule 1. Eyes were harvested from adult zebrafish through enucleation. For wholemount imaging, zebrafish were imaged using a Nikon SM-1500 stereomicroscope with a Nikon digital sight DS-Fi2 system.

2.2 Patient evaluation

The study was approved by the local research ethics committee, and all investigations were conducted in accordance with the principles of the Declaration of Helsinki; informed consent was obtained from all participating individuals. Molecular genetic testing was performed on genomic DNA extracted from blood using an LCA next-generation sequencing (NGS) panel including *KCNJ13*, with Sanger sequencing to

confirm the mutations. Ophthalmic evaluation included slit lamp examination, fundus examination, spectral domain optical coherence tomography (SD-OCT) (Carl Zeiss Meditec, Inc., Dublin, CA) and fundus fluorescein angiography (FFA) with Optos imaging, as part of routine clinical care.

2.3 Total RNA extraction and RT-PCR

2.3.1 RNA extraction

Total RNA was isolated from whole WT zebrafish at various time points from 24 hpf to 14 dpf, or enucleated zebrafish eyes from 1 month post fertilisation (mpf) or above, using TRIzol reagent (Invitrogen). 50 larvae, or two eyes, were homogenised in 0.5 ml of TRIzol using a needle and syringe and incubated for 5 minutes at room temperature. Phase separation was achieved through the addition of 0.25 ml of chloroform and centrifugation at 12,000 × g for 15 minutes at 4 °C. 0.25 ml of 100% isopropanol was added to the aqueous phase and samples were incubated at room temperature for 10 minutes before centrifugation at 12,000 × g for 15 minutes at 4 °C to allow RNA precipitation. The RNA pellet was washed in 0.5 ml of 75% ethanol (centrifugation 7500 × g for 5 minutes at 4 °C), air-dried and incubated in 20 µl of RNase-free water for 10 minutes at 55˚C for re-suspension. To remove DNA contamination, samples were treated with TURBO DNase (Thermo Fisher) and cleaned up using phenol:chloroform extraction as follows: 85 µl of RNase-free water and 15 µl of ammonium acetate stop solution (mMESSAGE mMACHINE kit, Invitrogen) were added to each sample and RNA was extracted by adding an equal volume of phenol:chloroform, centrifugation at maximum speed for 4 minutes and recovery of the aqueous phase. The extraction was repeated twice. To precipitate the RNA, an equal volume of 100% isopropanol was added to the samples before incubation at -20 °C for at least 15 minutes. Samples were centrifuged at 4 °C for 15

minutes at maximum speed to pellet the RNA. The supernatant was removed and the RNA was re-suspended in 20 µl of RNase-free water. Samples were quantified using a NanoDrop 2000 Spectrophotometer (Thermo Scientific).

2.3.2 Reverse transcription (RT)

For each sample, 1 µg of RNA was used for cDNA synthesis using the SuperScript III First-Strand Supermix for qRT-PCR (Invitrogen). Converted samples were treated with *E.coli* RNase H (Invitrogen) to remove the remaining RNA template.

2.3.3 PCR

Amplification of a 538 bp *kcnj13* cDNA sequence or a 520 bp *ush2a* cDNA sequence was performed using MyTaq DNA polymerase (Bioline) with RT-PCR primers (Sigma-Aldrich) (see **Table 2-1** for primer sequences). *ef1α* primers were used as a control. The following PCR cycle conditions were used: incubation at 95˚C for 1 minute for initial denaturation, followed by 35 cycles of 95˚C for 15 seconds (denaturation); annealing temperature for 15 seconds and 72˚C for 15 seconds (extension). All RT-PCR primers were designed to span exon-exon boundaries. 8 µl of each sample were run on a 2% agarose gel containing SafeView Nucleic Acid Stain (ABM).

2.4 Wholemount *in situ* hybridisation using digoxygenin-labelled RNA probes

2.4.1 Riboprobe synthesis

The *ush2a* cDNA sequence was cloned into pGEM-T-Easy Vectors (Promega) by overnight incubation at 4 °C with T4 DNA Ligase (Promega). Transformation was

performed using One Shot TOP10 Competent Cells (Invitrogen), according to manufacturer's instructions. The transformation was incubated at 37 °C overnight on LB agar plates containing 100 µg/ml ampicillin. Single colonies were inoculated into 10 ml LB broth containing 100 µg/ml ampicillin and incubated overnight, shaking at 37 °C. Plasmid DNA was purified from each culture using a QIAprep Spin Miniprep Kit (Qiagen), according to manufacturer's protocol. Samples were Sanger sequenced to verify *ush2a* PCR product insert.

Prior to transcription, 1 µg of plasmid DNA was linearised using the appropriate restriction enzyme (NcoI or NdeI, Promega), depending on whether the sense or antisense probe was required. Samples were run on a 1% agarose gel to analyse digestion. The linearised templates were cleaned up using a phenol/chloroform extraction followed by ethanol precipitation using glycogen (Invitrogen). Riboprobes were transcribed using 1 µg of linear plasmid DNA as a transcription template. The DNA was incubated with 20 units of the relevant T7 or SP6 polymerase (Promega) in a 20 µl reaction containing 1X Transcription Buffer (Promega), 40 units of RNasin ribonuclease inhibitor (Promega), 10 mM dithiothreitol (DTT) (Promega) and 1X digoxigenin-UTP RNA labelling mix (Roche). The reaction was incubated at 37 °C for 2 hours. To remove the template DNA, 2 µl of RNase-free DNase I (Thermo Fisher) was added and the reaction was incubated for a further 30 minutes at 37 °C. The reaction was stopped by the addition of 2 µl of sterile 0.25 M EDTA. The labelled riboprobes were purified using ProbeQuant G-50 microcolumns (GE Healthcare) according to the manufacturer's protocol, followed by lithium chloride precipitation. The probes were re-suspended in hybridisation (Hyb+) mix (50% formamide, 5X sodium citrate [SSC], 50 µg/ml yeast RNA, 50 µg/ml heparin, 1% sodium dodecyl sulphate [SDS] in sterile water) and stored at -20 °C.

2.4.2 Embryo fixation

WT embryos used for wholemount *in situ* were raised in medium containing 0.2 mM phenylthiourea (PTU, Sigma-Aldrich) to prevent pigment formation. At 48 hpf, embryos were de-chorionated and fixed in 4% paraformaldehyde (PFA) in 1X phosphate-buffered saline (PBS) overnight at 4 °C. The following day, embryos were washed twice in 1XPBS/0.1% Tween-20 (Sigma-Aldrich) (PBS-T) for 5 minutes at room temperature before de-hydrating through a graded methanol series (25%, 50%, 75%, 100%, 5 minutes each) in PBS-T. Embryos were stored at -20 °C in 100% methanol for a minimum of 2 hours before use.

2.4.3 Pre-hybridisation treatment

At room temperature, embryos were re-hydrated through 5 minutes washes in successive dilutions of methanol (75%, 50%, 25%) in PBS-T, following by 4X 5 minute washes in PBS-T. Embryos were permeabilised by incubation with 10 µg/ml proteinase K in PBS-T for 20 minutes. After this digestion step, embryos were washed for 5 minutes in PBS-T before fixation in 4% PFA for 20 minutes. Embryos then received 4 washes of 5 minutes in PBS-T. This was followed by incubation in 300 µl of Hyb+ for a minimum of 2 hours in a heat block at 68 °C.

2.4.4 Hybridisation

The Hyb+ was removed and replaced with fresh mix containing approximately 200 ng of digoxigenin-labelled riboprobe. The embryos were incubated overnight in a hybridisation oven pre-heated to 68 °C with gentle shaking.

2.4.5 Post-hybridisation washes and antibody incubation

Embryos received the following washes at 68 °C: 4X 30 minutes in Hyb- (50% formamide, 5X SSC, 50 µg/ml heparin, 1% SDS in sterile water), 15 minutes in 2X SSC and 2X 15 minutes in 0.2X SSC. At room temperature, embryos were washed three times in PBS-T for 15 minutes. Following these washes, embryos were blocked in MABlock (maleic acid buffer + 2% Blocking reagent (Roche)) for a minimum of 1 hour at room temperature. Embryos were then incubated at 4 °C overnight in 300 µl of MABlock containing Anti-Digoxigenin-AP Fab fragments (Roche) diluted 1:5000.

2.4.6 Antibody detection

Following overnight incubation in antibody solution, embryos were rinsed in PBS-T before washing 4 times in PBS-T for 15 minutes. Embryos were then given 3 washes of 5 minutes in staining buffer (100 mM Tris, 50 mM $MgCl_2$, 100 mM NaCl, 0.1% Tween-20 and 1 mM levamisole, pH 9.5). Embryos were incubated in 500 µl of BM Purple detection buffer solution (Roche) at 4 °C in the dark until the desired level of staining was developed. To fix the colour, embryos were incubated in 4% PFA for 30 minutes. Before imaging, embryos were washed several times in PBS before serially dehydrating through a graded glycerol-PBS series. Embryos were imaged in 95% glycerol using a Nikon SMZ-1500 stereo microscope with Nikon Digital Sight DS-Fi2 system.

2.5 RNAscope assay

Enucleated adult zebrafish eyes (~6 mpf) or whole 6 dpf larvae were and fixed in 4% PFA/PBS at 4 °C overnight. After washing three times in PBS for 10 minutes, the eyes/larvae were incubated in 10%, 20% and 30% sucrose/PBS at 4 °C overnight each time. The samples were frozen embedded in Tissue-Tek O.C.T embedding

medium (VWR) using dry ice and 14 um sections were collected onto Superfrost PLUS slides (VWR) using a Leica CM1850 cryostat. The sectioned tissue was washed with PBS for 5 minutes to remove O.C.T, followed by boiling in RNAscope Target Retrieval reagent (Advanced Cell Diagnostics, ACD) for 5 minutes. Afterwards, slides were briefly washed with sterile water and incubated for 15 minutes at 40 °C with RNAscope Protease III reagent (ACD). Fluorescent *in situ* hybridisation staining was performed using the RNAscope Fluorescent Multiplex Detection kit (ACD) according to the user's manual. Briefly, sections were incubated with RNAscope probes for two hours at 40 °C for hybridisation, before the incubating with the following amplification solutions: AMP-1 (30 minutes), AMP-2 (15 minutes), AMP-3 (30 minutes) and AMP-4 ALT-B (15 minutes). All amplification steps took place at 40 °C and were separated by two minute washes in RNAscope wash buffer. The sections were counterstained with DAPI solution (ACD), mounted in Prolong Gold Antifade mountant (Thermo Fisher) and imaged using a Leica LSM 710 confocal microscope. The *kcnj13*, *ush2a*, *gpr98* and *dfnb31a* target probes and *odc1* and *dapB* control probes were designed and provided by ACD. For immunostaining, slides were washed in PBS immediately after the RNAscope assay before blocking and antibody staining as described in section 2.11.1

2.6 Disruption of *ush2a* in zebrafish using CRISPR/Cas9

2.6.1 sgRNA design and synthesis

A summary of the CRISPR process is shown in **Figure 2-1**. Firstly, CRISPR targets were identified using crispr.mit.edu and a high scoring guide sequence was selected (scoring system from 0 to 100, estimating the faithful on-target activity of each guide). The following 20 bp target sequence in *ush2a* exon 11 was chosen:

5’-AATATCTGGCTGCACGGTCC-3’

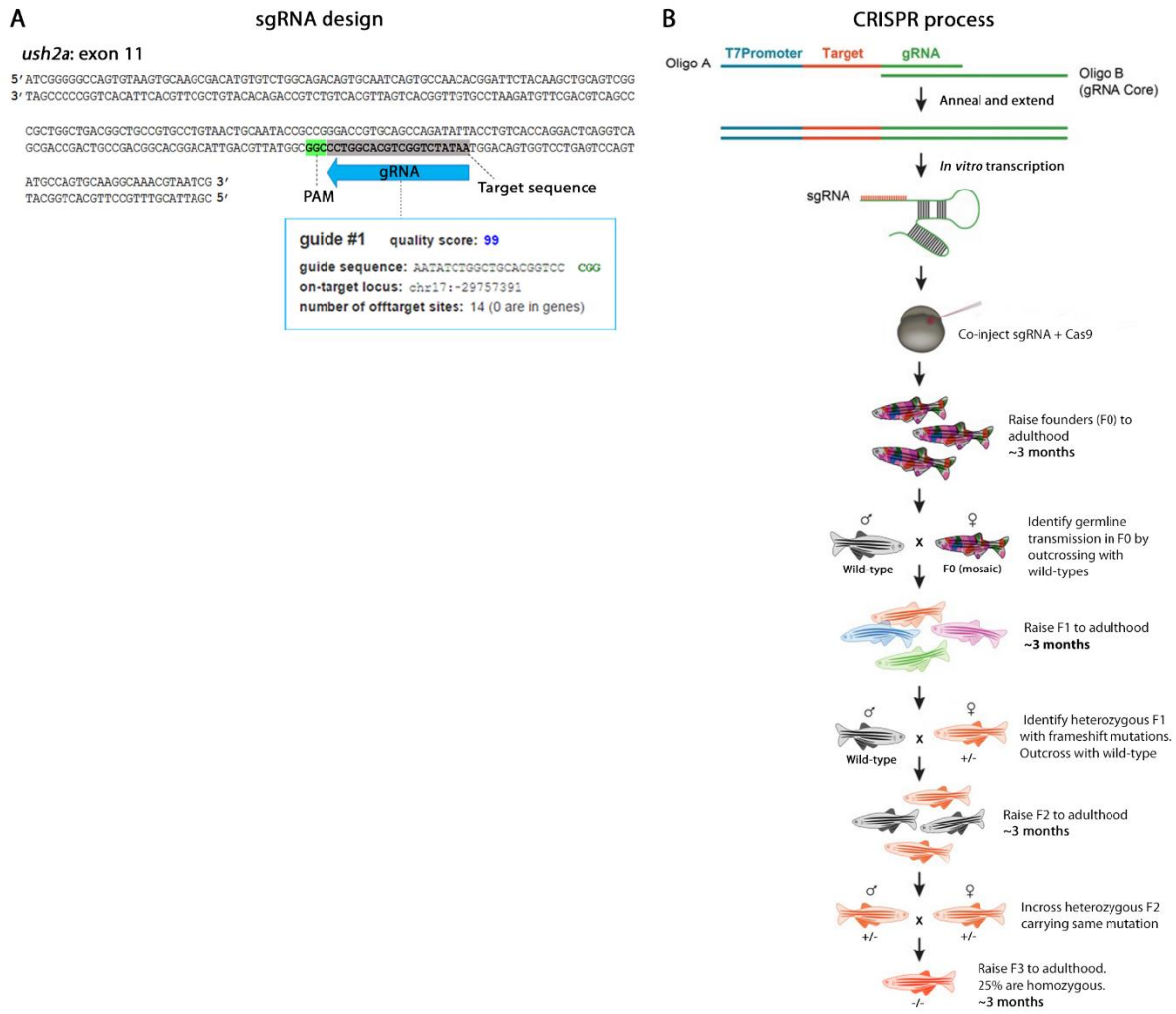

Figure 2-1. CRISPR design for targeted mutagenesis of *ush2a* and generation of the *ush2a* mutant line.
(A) Using an online CRISPR design tool (crispr.mit.edu), a high scoring 20 base pair gRNA sequence has been selected to target a specific DNA sequence in exon 11 of *ush2a*. The sgRNA uses the sequence as a guide to induce a double-strand break at a protospacer adjacent motif (PAM, '-NGG'). (B) To generate the sgRNA template, a gene-specific DNA oligo consisting of the T7 promoter, the gRNA target sequence and a 20 base pair sequence that overlaps with a generic sgRNA template (oligo A) is annealed with the constant reverse oligo B. The sgRNA is transcribed in *vitro* from this template and co-injected with Cas9 mRNA into the one-cell stage zebrafish embryos. *ush2a* homozygous mutant fish are generated through a series of outcross and incross breedings.

A cloning-free method similar to that reported in Gagnon et al. (2014) was used to synthesise the sgRNA (316). To generate the sgRNA template, a gene-specific DNA oligo consisting of the T7 promoter, the 20 bp target sequence and a 20 bp sequence that overlapped to a generic sgRNA template (constant reverse oligo) was designed as follows (Sigma-Aldrich):

5'-TAATACGACTCACTATA – GGN($_{20}$) **–** GTTTTAGAGCTAGAAATAGCAA-3'

The two guanines at the beginning of the target sequence are required for *in vitro* transcription and extra guanines were added as the target sequence did not already contain them. The sequence of the 80 bp constant reverse oligo was:

5'-

AAAAGCACCGACTCGGTGCCACTTTTTCAAGTTGATAACGGACTAGCCTTATTT

TAACTTGCTATTTCTAGCTCTAAAAC-3'

The gene-specific and constant reverse oligos were annealed in a thermocycler under the following conditions: 95˚C for 5 minutes, ramping down to 85˚C at -2˚C/second, ramping down to 25˚C at 0.1˚C/second and holding at 4 ˚C. The annealed oligos were then filled in using T4 DNA polymerase (New England BioLabs) incubated at 12˚C for 20 minutes. The dsDNA was cleaned up using the EZNA Cycle Pure Kit (Omega Bio-Tek). The dsDNA sample was run on a 2% agarose gel to verify a product of the correct size. Approximately 200 ng of template DNA was used for *in vitro* transcription of sgRNA using the HiScribe T7 High Yield RNA Synthesis Kit (New England BioLabs), according to manufacturer's instructions. 1 µl of TURBO DNase (ThermoFisher Scientific) was added and incubated at 37˚C for 20 minutes to remove the template DNA. Purification of sgRNA was performed using the RNeasy Mini Kit (Qiagen), according to manufacturer's instructions.

2.6.2 Cas9 mRNA synthesis

The Cas9 plasmid pT3Ts-nCas9n (Addgene #46757) was used as a template for Cas9 mRNA synthesis. The plasmid arrived as a bacterial stab which was streaked on an LB agar plates containing 100 µg/ml ampicillin and incubated overnight at 37 °C. Single colonies were inoculated into 10 ml LB broth containing 100 µg/ml ampicillin and incubated overnight, shaking at 37 °C. The plasmid was purified from the cultures using a QIAprep Spin Miniprep Kit according to the manufacturer's protocol and Sanger sequenced with T3 primers to verify identity. The plasmid was linearised by XbaI (Promega) and the mMESSAGE mMACHINE T3 Transcription Kit (ThermoFisher Scientific) was used to transcribe mRNA, according to manufacturer's instructions. A Poly(A) tail was added using the Poly(A) Tailing Kit (ThermoFisher Scientific), according to manufacturer's instructions. Purification of Cas9 mRNA was carried out using the RNeasy Mini Kit (Qiagen). Both sgRNA and Cas9 mRNA were stored at -80 °C.

2.6.3 Microinjection

All injections were performed on WT strain AB. A solution of 150 ng/µl Cas9 mRNA and 75 ng/µl sgRNA was co-injected into the cell of one-cell stage embryos, using a Picospritzer III intracellular microinjector (Parker). A dose volume of approximately 1 nl was used for injection.

2.6.4 Assessment of mutagenesis

To investigate the mutagenesis activity of the sgRNA, genomic DNA was extracted from injected embryos at 24 hpf before PCR amplification of the region containing the target site. To extract DNA, de-chorionated embryos were incubated for 3 hours at 50˚C in DNA extraction buffer consisting of: 10 mM Tris (pH 8.2), 300 mM NaCl, 0.5%

SDS, 200 µg/µl proteinase K, 10 mM EDTA. For precipitation of the DNA samples, two volumes of 100% ethanol were added and samples were incubated on ice for 30 minutes before centrifugation at maximum speed for 20 minutes. After removal of the supernatant, 100 µl of 70% ethanol was added and samples were centrifuged for a further 2 minutes. The liquid was removed and the pellets were air-dried for 5-10 minutes before re-suspension in 20 µl of TE buffer. An *ush2a* DNA sequence of 652 bp containing the CRISPR target site was PCR amplified from the samples using MyTaq DNA polymerase (Bioline) with the *ush2a* exon 11 primers (see **Table 2-1**). The cycle conditions used were: incubation at 95˚C for 1 minute for initial denaturation, followed by 35 cycles of 95˚C for 15 seconds (denaturation); 61˚C for 15 seconds (annealing) and 72˚C for 10 seconds (extension). Samples were analysed using Sanger sequencing.

2.6.5 Establishing CRISPR germline mutant lines

Injected embryos were raised to adulthood to generate 'founder' fish (F_0). To identify fish that were transmitting germline mutations, each founder was outcrossed with WT fish and genomic DNA from 10 pooled embryos was analysed for the presence of mutations through Sanger sequencing as already described. Founders that transmitted mutations were bred with WT fish and the heterozygous F1 progeny were raised to adulthood. Genomic DNA from F1 finclips was extracted and analysed using sequencing. F1 fish that were identified as possessing frameshift mutations were outcrossed with WT fish to generate F2 fish, which were raised to adulthood and sequenced using finclipping. F2 heterozygous fish carrying the same mutation were incrossed to produce F3 progeny, 25% of which were homozygous for the desired mutation. Homozygous fish and their WT siblings were used for subsequent breeding and phenotypic characterisation.

2.7 Retinal histology

For histological evaluation, enucleated eyes fixed in 4% PFA/PBS at 4 °C overnight. They were washed three times in PBS for 5 minutes and three times in sterile water for 10 minutes before dehydrating through a graded ethanol series (30%, 50%, 70%, 95% and two times in 100%, 2 minutes each). The samples were embedded using JB-4 embedding kit (Polysciences Inc.), according to manufacturer's instructions. Transverse retinal sections of 7 µm were cut using a Leica RM 2065 microtome, stained with 1% toluidine blue and mounted in DPX mountant (Fisher). Sections were imaged on a Leica DMRB with Jenoptik D-07739 Optical System. Retinal sections containing optic nerve were used for examination to ensure consistency in the retinal location between fish.

For flat-mounting of 12-month old WT and *obe*^{td15} retinas, lenses were removed from enucleated eyes before fixing in 4% PFA/PBS at 4 °C. Eyes were washed in PBS before flat-mounting onto microscope slides with Prolong Gold Antifade mountant. Flat-mounted retinas were imaged on Leica LSM 710 confocal microscope. Cone photoreceptors were visualised by autofluorescence.

2.8 Spectral domain optical coherence tomography (SD-OCT)

2.8.1 Imaging and animal equipment

In addition to histological analysis, SD-OCT was used to examine the adult zebrafish retina. Although histology is the established gold standard for analysing retinal structure, SD-OCT offers the advantage of rapid *in vivo* imaging, allowing longitudinal assessment and examination of additional features including the vasculature and cone mosaics. In this technique, single depth measurements are called an A-scan,

with series of depth scans along a single plane called B-scan, which creates an optical section. Series of densely sampled B-scans can be visualised *en face* to generate optical flat-mounts (volume intensity projections, VIP) for further analysis.

SD-OCT images of live adult zebrafish retinas were captured using the Bioptigen Envisu R2200 SDOIS (Bioptigen, Inc.) as described (317). The SD-OCT apparatus included a base system (host computer, SD-OCT engine with reference arm, and a handheld SD-OCT probe), imaging mount, and animal alignment stage (**Figure 2-2**). The probe was held in the mount in a vertical position directly above the alignment stage, where the zebrafish was placed and could be moved up and down. The alignment stage was able to move in the X or Z meridians. InVivoVue software (Bioptigen, Inc.) was used for creating and saving OCT image files. Before all SD-OCT imaging, zebrafish were anaesthetised in 0.2 mg/ml tricaine in tank system water. For imaging of the optic nerve, a custom rubber holder with projections to maintain position was used to hold the zebrafish in place. When imaging the photoreceptor mosaic, the zebrafish were laid on a grooved plasticine wedge placed in an immersion tank with attached tubing and syringe to control water level. A weighted strap was used to stabilise the fish.

2.8.2 Imaging of the optic nerve and retinal layers

For imaging the optic nerve and retinal lamination, the zebrafish was placed in the rubber holder and positioned at an angle relative to the probe as shown in **Figure 2-2B** and **C**. A 1.4x1.4mm perimeter protocol with 1000 A-scans per B-scan with 100 total scans was used. The bore of the SD-OCT probe was initially brought into very close proximity to the fish eye, and live imaging was commenced. Following this, the position of the probe relative to the animal stage could be finely adjusted until an

Figure 2-2. SD-OCT equipment setup.
(A) Overview of the SD-OCT equipment setup. (B, C) Orientation of SD-OCT probe relative to the fish for visualising the optic nerve. (D) Orientation of the probe relative to the submerged fish for acquisition of en face cone mosaic images. 1, handheld SD-OCT probe; 2, imaging mount; 3, animal alignment stage; 4, zebrafish; 5, fish holder; 6, immersion tank; 7, weighted strap. SD-OCT, spectral domain optical coherence tomography.

adequate image could be obtained and the optic nerve was located. This was achieved by moving the mounted probe up or down or adjusting the position of the platform with the fish holder. During the imaging process, drops of 0.2 mg/ml tricaine were regularly pipetted on the fish gills to maintain moisture and on the eye to prevent corneal desiccation and maintain image quality.

2.8.3 Imaging of the photoreceptor mosaic

When imaging the cone photoreceptor mosaic, the anaesthetised zebrafish was placed in the immersion tank containing 0.2 mg/ml tricaine in tank water solution and was perpendicular to the probe. A rectangular scanning protocol consisting of a 1x1mm perimeter with 400 A-scans per B-scan with 400 total B-scans was used for volume intensity projection (VIP) images of the fundus mosaic. The syringe attached to the tank was used to adjust the water level. The optimal water height (~1 mm above the cornea) determined the clarity and brightness of individual photoreceptors.

2.8.4 Image analysis

Previously, it has been shown that retinal thickness measurements taken from histological sections and SD-OCT scans are comparable (317). Here, retinal thickness measurements from SD-OCT B-scans were obtained manually either using the calipers tool on the InVivoVue software (*obe*^{td15} retinas) or using the Diver software (Bioptigen, Inc.) (*ush2a* retinas). Using Diver, 4 measurements were taken at a distance of approximately 400 μm from the optic nerve for each fish retina. For cone mosaic images, Voronoi domain analysis was used to assess the orderliness with which the receptor array tiles the retina (318, 319). In this kind of tiling, all points in the plane are partitioned into Voronoi domains, which represent all those points in the plane that are closer to a particular cell than to any other cell. The ideal sampling

of a mosaic is produced by hexagonally, six-sided arranged photoreceptor cells. In this study, photoreceptor cells were manually identified using ImageJ from *en face* SD-OCT scans which were extracted from the volume. Cell coordinates were analysed using using 'Voronoi' function in MATLAB (MathWorks). Percentage of six-sided cells and distribution of sidedness were assessed.

2.9 Optokinetic response analysis

Adult zebrafish were lightly anaesthetized in 0.2 mg/ml tricaine and placed in a custom-made foam holder supported by dissection pins in a 55 mm petri dish. The dish was filled with tank water and the fish were allowed to regain consciousness, then placed into a custom-made optokinetic device consisting of a 12 cm acrylic drum, revolutions per minute (rpm) adjustable rotating motor with laser tachometer and stereo microscope (Zeiss Stemi-2000C) c-mounted with a digital SLR camera (Nikon D5100). Each zebrafish was assessed with varying grating lengths (from 0.4 cm to 0.04 cm in 0.04 cm increments) at a consistent rpm speed (12 rpm) until the stripes could no longer be tracked by the zebrafish, following published protocols (320). Visual acuity was calculated as cycles per degree (cpd) using the following equation:
where **a** is the distance from the centre of the lens to the grating, and **h** is the length of one cycle of the smallest grating at which an optokinetic response was observed. As a positive control, three WT zebrafish at 6 mpf received an intravitreal injection of 0.1 ml of 10 µm ouabain to induce a chemical retinal degeneration, and were assessed at day 3 post-injection, a stage at which the retina is known to be ablated (321).

2.10 Vibrational startle reflex test

A tapping-induced vibrational startle reflex test was performed on 6 dpf zebrafish, similar to that described in (174). Individual larvae were placed in a Petri dish of tank water and left until they became motionless. When stationary, the side of the Petri dish was tapped with a pencil and zebrafish was classed as ‘responders’ or ‘non-responders’ depending on whether tapping induced a burst swim response.

2.11 Immunohistochemistry

2.11.1 Immunostaining of retinal cryosections

Fresh enucleated eyes or whole larvae were fixed with 4% PFA/PBS overnight at 4 °C before incubation in 30% sucrose/PBS for 6 hours at room temperature. The samples were mounted and frozen in TissueTek O.C.T using dry ice. 14 µm sections were cut using a Leica CM1850 cryostat and collected onto Superfrost PLUS slides. After air-drying for two hours, sections were washed in PBS/0.1% Triton-X (Sigma-Aldrich) before being blocked for 1 hour with 20% normal goat serum (Sigma-Aldrich) in PBS/0.1% Triton-X and incubated in primary antibody in antibody solution (1% normal goat serum in PBS/0.5% Triton-X) at 4 °C overnight (all antibodies used are listed in **Table 2-2**). After washing three times with PBS/0.5% Triton-X, the sections were incubated in appropriate secondary Alexa Fluor antibody (Thermo Fisher) diluted 1:500 in antibody solution for 2 hours at room temperature. Finally, the sections were counterstained and mounted using Prolong Diamond Antifade mountant + DAPI (Thermo Fisher). The slides were imaged using a Leica LSM 710 confocal microscope.

2.11.2 Wholemount hair cell immunostaining

Larval zebrafish at 6 dpf were fixed with 4% PFA/PBS overnight at 4 °C. Zebrafish were washed in PBS for 10 minutes and incubated in PBS/1% Triton-X for 4 days to dissolve the otoliths. The larvae were blocked in in 20% normal goat serum in PBS/1% Triton-X for one hour at room temperature before incubating with anti-acetylated tubulin (Sigma-Aldrich) diluted 1:500 in 1% normal goat serum in PBS/0.5% Triton-X overnight at 4 °C. The larvae were washed three times for 10 minutes in PBS/1% Triton-X before incubating for two hours at room temperature with Alexa Fluor 488 secondary antibody diluted 1:500 and Alexa Fluor 647 Phalloidin (Thermo Fisher) diluted 1:10 in 1% normal goat serum in PBS/0.5% Triton-X. The larvae were washed twice for 10 minutes in PBS/1% Triton-X before mounting in Prolong Gold Antifade Mountant on self-made multiwell microscope slides. Fluorescent hair cells were visualised using Zeiss LSM 700 AxioImage M.1 upright confocal microscope.

2.12 Terminal deoxynucleotidyl transferase dUTP nick end labelling (TUNEL) assay

Retinal cryosections were collected as described in section 2.11.1. Prior to TUNEL staining, retinal sections were fixed in 1% PFA/PBS for 10 minutes at room temperature. They were washed twice in PBS for 5 minutes before treatment with 2:1 ethanol/acetic acid for 5 minutes at -20˚C. Sections were given a further two 5 minute washes in PBS. The ApopTag® Plus Fluorescein In Situ Apoptosis Detection Kit (Millipore) was used to detect apoptosis in the retinal sections, according to manufacturer's instructions. Sections were mounted in Prolong Diamond Antifade mountant + DAPI. Images were taken on a Zeiss LSM 700 AxioImage M.1 upright microscope.

2.13 Transmission electron microscopy (TEM)

All fish were fully light-adapted upon collection (at midday) unless being dark-adapted, in which case they were incubated without light for 48 hours before collection. Enucleated *z*ebrafish eyes were fixed in 2% paraformaldehyde-2% glutaraldehyde prior to incubation with 1% osmium tetroxide-1% potassium ferrocyanide. Following dehydration in an ethanol series and propylene oxide, the zebrafish were embedded in epon resin. Using a Leica EM UC7 ultramicrotome, 100 nm sections were cut, collected on formvar-coated copper grids (EMS) and stained with lead citrate (-). Sections were examined on a Jeol 1010 TEM and imaged using a Gatan Orius SC1000B charge-coupled device camera. Mitochondria and phagosome numbers, and mitochondria size were analysed from TEM images using ImageJ software.

2.14 Adenosine triphosphate (ATP) assay

ATP was measured by luciferin–luciferase assay (Enliten ATP Assay System, Promega). The retina (including RPE) was dissected from enucleated eyes of WT and *obe*^{td15} fish and placed in Krebs solution. The samples were transferred to 2.5% trichoroacetic acid (TCA), then homogenised by sonication (3 X 10 seconds, XL-2000 Qsonica LLC) on ice. Cell debris was removed by centrifugation at 13,000 rpm for 30 minutes at 4 °C. The supernatant was collected and the TCA was neutralised with 1 M Tris–acetate buffer (pH 7.75, final TCA concentration 0.0625%). Protein concentration was measured using the BCA Protein Assay Kit (Pierce), a plate reader (Tecan Safire) and Magellan Software. To analyse ATP, 10 µl of the neutralised samples was added to 100 µl of luciferin–luciferase in fresh buffer and ATP levels were measured using a Glomax®-20/20 luminometer (Promega) and data was normalised to concentration of protein.

2.15 Western Blot

RPE and retinal tissue was isolated from enucleated WT and *obe*^{td15} zebrafish eyes and snap-frozen in liquid nitrogen. The samples were homogenised by sonication (3 × 10 s, XL-2000 Qsonica LLC) with cold RIPA lysis buffer (Pierce) containing 1X Protease Inhibitor Cocktail (Pierce) and 1X Phosphatase Inhibitor Cocktail (Pierce). Cell debris was removed by centrifugation at 13000 rpm for 15 minutes at 4 °C. Protein concentration was measured using the BCA Protein Assay Kit (Pierce), a plate reader (Tecan Safire) and Magellan Software. For each sample, 10 µg of protein was boiled at 95 °C for 5 minutes with 5 µl Nupage sample buffer and 2 µl Nupage reducing agent (Thermo Fisher). Proteins were separated on an Any kD SDS–polyacrylamide gel (BioRad) and transferred onto an Immun-Blot PVDF membrane (BioRad). The membrane was blocked for one hour at room temperature in blocking solution (5% dry milk/PBS-T) and incubated overnight at 4°C with primary rabbit anti-hsp60 antibody (Abcam) diluted 1:1000 in blocking solution. After washing 5 times in PBS-T, the membrane was incubated for one hour at room temperature with secondary anti-rabbit IgG HRP conjugate diluted 1:10,000 (Sigma-Aldrich). The membrane was washed 5 times in PBS-T before chemiluminescent detection using the Clarity™ ECL Western Blotting Substrate (Biorad) and the ChemiDoc MP Imaging system (Biorad). Using Restore Western Blot Stripping Buffer (Pierce), the membrane was stripped and re-probed with 1:5000 polyclonal anti-β-actin antibody (Sigma-Aldrich) as a loading control. ImageJ was used to determine the relative abundance of hsp60 compared with corresponding levels of control protein expression.

2.16 Quantitative RT-PCR (qRT-PCR)

RPE and retinal tissue was isolated from enucleated 6 mpf and 12 mpf WT and *obe*^{td15} zebrafish eyes. Total RNA was extracted using the RNeasy micro kit (Qiagen)

according to the manufacturer's instructions. RNA samples were DNase-treated using On-Column DNase I (Qiagen). Using 500 ng total RNA, cDNA was reverse transcribed using the Superscript III First-strand synthesis Supermix kit (Thermo Fisher), according to the manufacturer's instructions. For quantitative real-time PCR amplifications, gene expression was quantified using SYBR Select fluorescent dye (Thermo Fisher) in triplicate reactions for each sample. All qRT-PCR primers are listed in **Table 2-1**. The expression of each gene was normalised to the geometric mean of *β-actin*, *ribonucleoprotein L13a* and *ef1α* internal housekeeping genes. The StepOne Plus RealTime PCR System (Thermo Fisher) was used and reactions analysed using the Comparative CT experiment option in the StepOne software (Version 2.3).

2.17 Statistics

Data are shown as mean values ± SEM from *n* observations. Student's *t* tests were performed using SPSS software (IBM). $P<0.05$ was accepted to indicate statistical significance (*****).

Table 2-1. Primer sequences and conditions.

Gene primer	Sequence (5'-3')	Annealing temperature (˚C)	Product size (bp)
kcnj13 genotyping forward primer *kcnj13* genotyping forward primer	TCATCCTAATTTCCTCTCCACC TGTCGATGCTGAACTCCAGAG	63	463
kcnj13 RT-PCR forward primer *kcnj13* RT-PCR forward primer	TGGAGACGCAACTCACTATTG TATTGGATCTCGTCAGGCAG	64	538
ush2a RT-PCR forward primer *ush2a* RT-PCR reverse primer	TGATCCTCGTGTACAAAGTGG TGTACCTGATAGACTGTG	55	520
ef1α RT-PCR forward primer *ef1α* RT-PCR reverse primer	CAAGGGCTCCTTCAAGTACGCCTG GGCAGAATGGCATCAAGGGCA	58	561
ush2a exon 11 forward primer *ush2a* exon 11 reverse primer	GAGACCCATTCTGTTAAAGCACC TCCCAGTTTGGCATTGCAGATC	61	652
polg2 qRT-PCR forward primer *polg2* qRT-PCR reverse primer	GTGGAGGAAGTTTGCTTTAGGCCCG GGGTCCACAGTGTCTCCAGCGT	55	143
fis1 qRT-PCR forward primer *fis1* qRT-PCR reverse primer	ACAGACTTAAGGAGTATGAGAGAGC AATACCACCGACAATCGCCA	55	152
opa1 qRT-PCR forward primer *opa1* qRT-PCR reverse primer	GCCGGAAGTGTAGTTACCTG AGGTGGTCTCTGTGGGTTGT	55	150
pgk1 qRT-PCR forward primer *pgk1* qRT-PCR reverse primer	GTGGACGTGAAAGGAAAGCG TGCAGCCTTGATTCTCTGGTT	55	96
ldha qRT-PCR forward primer *ldha* qRT-PCR reverse primer	AGATGGTGGTTGACAGTGCAT TACCCAGAATGCAAGGCACA	55	195
sod1 qRT-PCR forward primer *sod1* qRT-PCR reverse primer	GGTGACAACACAAACGGCTG TGGCATCAGCGGTCACATTA	55	124
sod2 qRT-PCR forward primer *sod2* qRT-PCR reverse primer	ACAGCAAGCACCATGCAACA CAGCTCACCCTGTGGTTCTCC	55	200
bcl2a qRT-PCR forward primer *bcl2a* qRT-PCR reverse primer	GAGGTTGGGATGCCTTCGTG CCAAGCCGAGCACTTTTGTT	55	90
β-actin qRT-PCR forward primer *β-actin* qRT-PCR reverse primer	TGTACCCTGGCATTGCTGAC TGGAAGGTGGACAGGGAGGC	55	145
L13a qRT-PCR forward primer *L13a* qRT-PCR reverse primer	TCTGGAGGACTGTAAGAGGTATGC AGACGCACAATCTTGAGAGCAG	55	148
ef1α qRT-PCR forward primer *ef1α* qRT-PCR reverse primer	CTGGAGGCCAGCTCAAACAT ATCAAGAAGAGTAGTACCGCTAGCATTAC	55	87

Table 2-2. Antibodies used for immunohistochemistry

Antibody	Species	Supplier	Dilution
anti-ZRF1	Rabbit	Zebrafish International Resource Center	1:100
anti-RPE65	Rabbit	Abcam	1:500
1D4 (red opsin)	Mouse	Abcam	1:50
4D2 (rhodopsin)	Mouse	Abcam	1:100
anti-acetylated tubulin	Mouse	Abcam	1:200
Alexa Fluor 647 Phalloidin	-	Thermo Fisher	1:10

3 *KCNJ13* in the zebrafish

3.1 Results

3.1.1 Conservation of *kcnj13* in the zebrafish

The zebrafish *kcnj13* gene is a two-exon gene encoding the 362 aa Kir7.1 protein, an inwardly rectifying potassium channel consisting of two α helix transmembrane domains (M1 and M2) and a pore-forming loop (H5) (**Figure 3-1**). As zebrafish frequently have two orthologues of mammalian genes as a consequence of an additional round of whole genome duplication (44), *kcnj13* was assessed for duplicates; however, the zebrafish genome was found to contain one *kcnj13* gene. Using the NBCI BLASTP tool, the zebrafish Kir7.1 protein sequence was compared to the human and mouse orthologues, which were found to be 48% and 49% identical respectively. Clustal X was used to align the zebrafish, mouse and human protein sequences, showing that the M1, M2 and H5 domains are highly conserved between species.

Temporal expression of *kcnj13* in the WT zebrafish was examined using RT-PCR analysis (**Figure 3-2**). *kcnj13* was found to be expressed from 24 hpf and was detected in the adult eye (~6 mpf). ***ef1α*** was used as a control gene and showed consistent expression at all timepoints. RNAscope *in situ* hybridisation was used to determine spatial expression of *kcnj13* mRNA on adult retinal cryosections. Using this assay, individual *kcnj13* mRNA transcripts were visualised as spots of fluorescence throughout the inner and outer retina, distributed evenly through the GCL, INL, OPL, ONL/photoreceptors and RPE. Immunostaining with an RPE65 antibody confirmed localisation of *kcnj13* transcripts to the RPE. o*dc1* and *dapB* (bacterial gene) probes

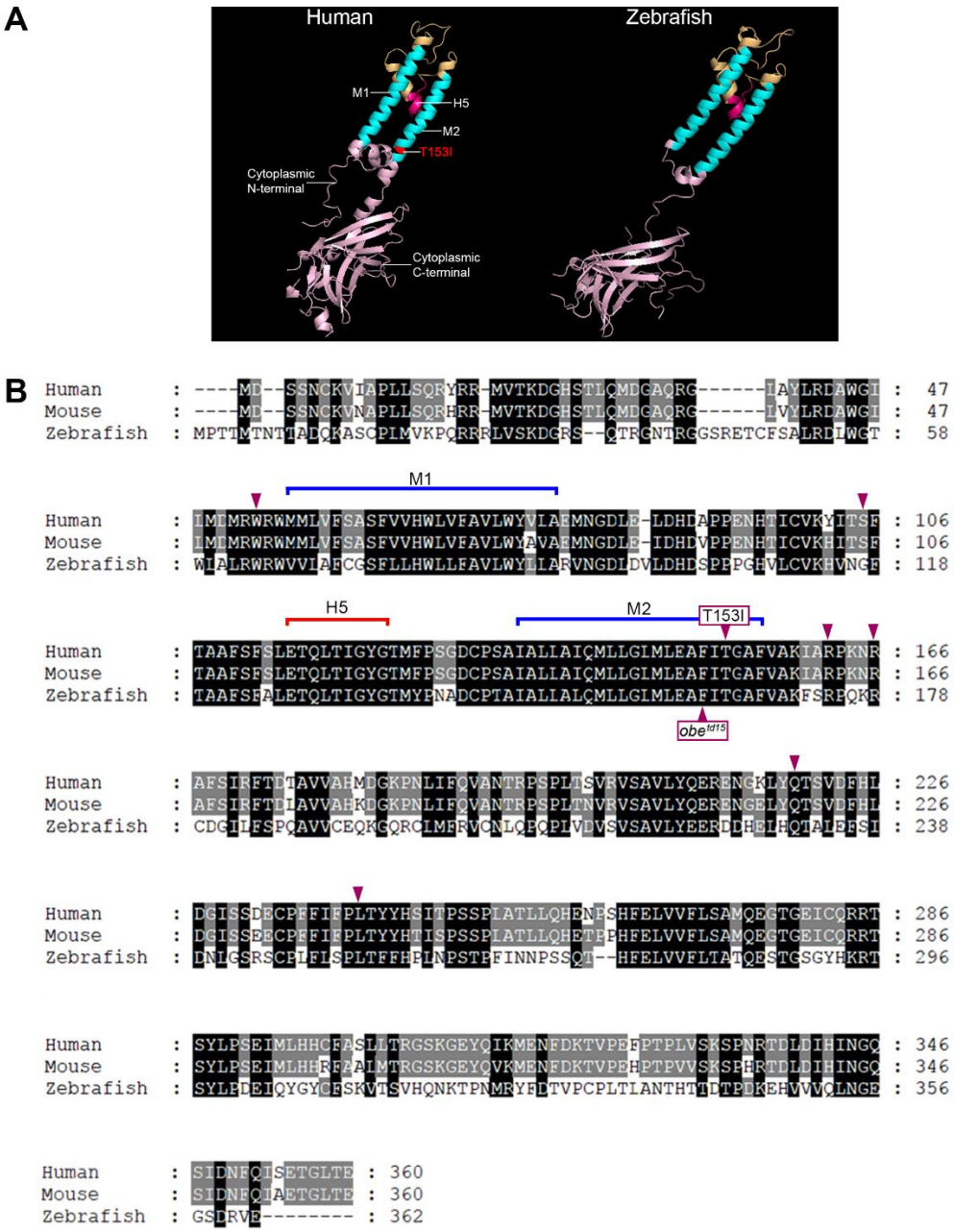

Figure 3-1. Kir7.1 protein structure and alignment of human, mouse and zebrafish Kir7.1 sequences.

(A) Human and zebrafish protein models showing predicted Kir7.1 monomer models. The models were generated using Phyre2; the crystal structures of Kir3.2 and Kir2.2 were used as templates for the human and zebrafish proteins, respectively. The unreported p.Thr153Ile (T153I) mutation is highlighted on the human Kir7.1 model. (B) Alignment of the human, mouse and zebrafish Kir7.1 protein sequences, aligned using Clustal X. The conserved domains are annotated as follows: transmembrane α helices, M1 & M2, and the pore-forming loop, H5. The positions of all mutations identified in *KCNJ13* patients are annotated with arrows above the human sequence. The mutation carried by the *obe*^{td15} zebrafish is labelled on the zebrafish sequence.

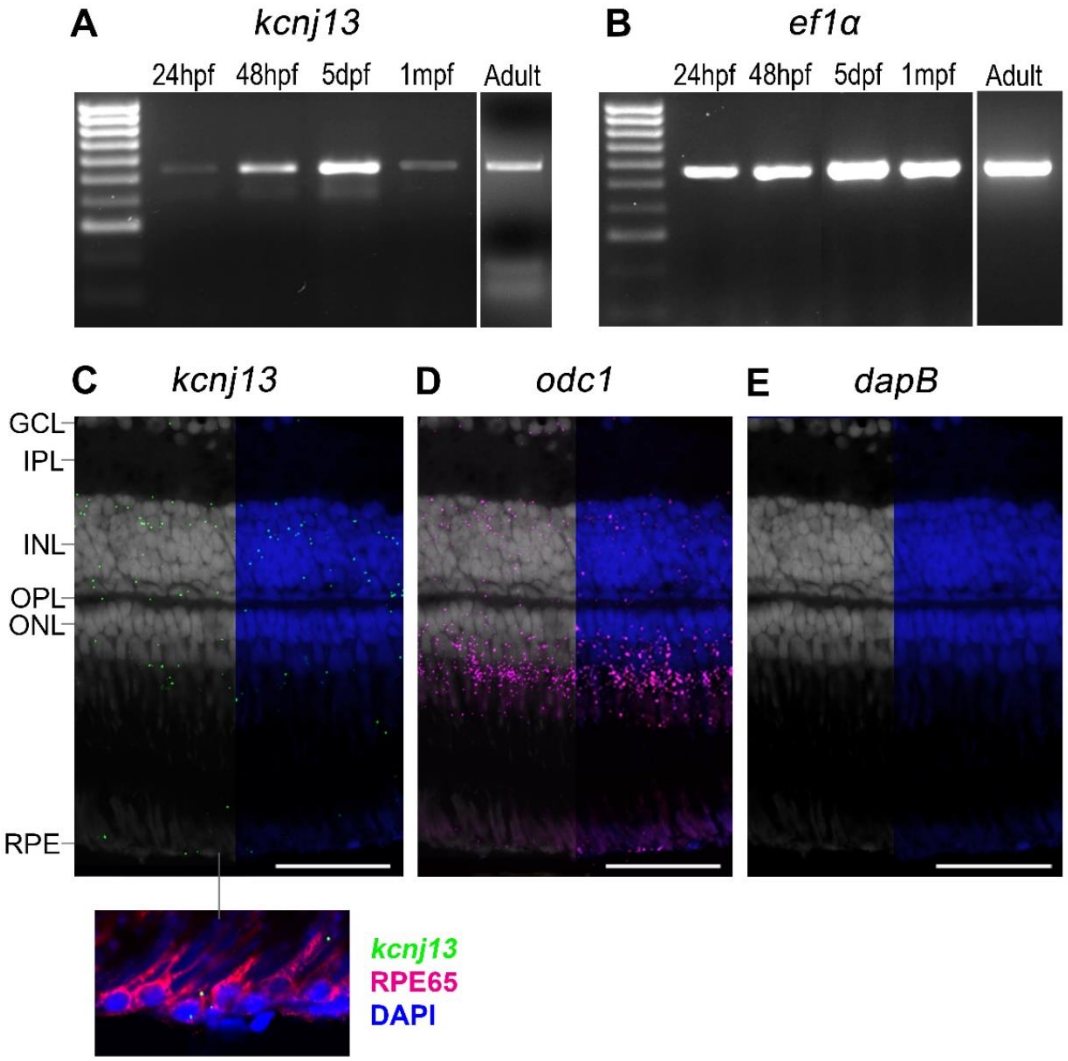

Figure 3-2. Expression of *kcnj13* in the zebrafish.
RT-PCR was used to detect expression of (A) *kcnj13* and (B) *ef1α* (control) in whole wild-type zebrafish larvae between 24 hours post-fertilisation (hpf) and 5 days post-fertilisation (dpf), and enucleated eyes of 1 month post-fertilisation (mpf) and adult (~6 mpf) zebrafish. RNAscope probes were used to detect expression of (C) *kcnj13*, (D) *odc1* (positive control) and (E) *dapB* (negative control) on adult zebrafish transverse retinal cryosections. Sections were counterstained with DAPI nucleic acid stain (blue). Immunostaining with anti-RPE65 (red) highlighted the RPE cells in (C). GCL, ganglion cell layer; IPL, inner plexiform layer; INL, inner nuclear layer; OPL, outer plexiform layer; ONL, outer nuclear layer; RPE, retinal pigment epithelium. Scale bar = 50 µm.

were used as positive and negative controls respectively. *odc1* was detected in all layers except the IPL. The *dapB* probe showed little or no fluorescence, corresponding to absent gene expression.

3.1.2 General morphology and retinal histology

The wholemount morphology of the homozygous *obe*^{td15} zebrafish was unremarkable until 1 mpf, when the characteristic broader stripe skin pigmentation was noted (**Figure 3-3A-B**) There were no gross ocular morphological differences between WT (*obe*$^{+/+}$) and *obe*^{td15} zebrafish at any timepoint. Sanger sequencing was used to confirm genotype, which verified the presence of the missense mutation c.502T>C (p.Phe168Leu) which is located in *kcnj13* exon 2, previously identified in (102).

Histological evaluation was used to compare the WT and *obe*^{td15} retinas between 1 mpf and 12 mpf (**Figure 3-3E-L**). The *obe*^{td15} retina showed normal development and was comparable to WT fish until 12 mpf, at which point the *obe*^{td15} retina showed extensive retinal degeneration with disruption of the photoreceptor layer and RPE, and overall thinning of all other retinal layers.

3.1.3 The use of SD-OCT to examine zebrafish retinal morphology

In addition to histological analysis, SD-OCT was used to examine the adult zebrafish retina. Comparison between transverse retinal histology sections and SD-OCT B-scans showed that live imaging can provide an accurate representation of the structural organisation of the zebrafish retina, with a level of detail akin to that obtained by histological methods (**Figure 3-4A**). It was possible to obtain high quality cross-sectional views of the adult zebrafish retina with clearly delineated layers,

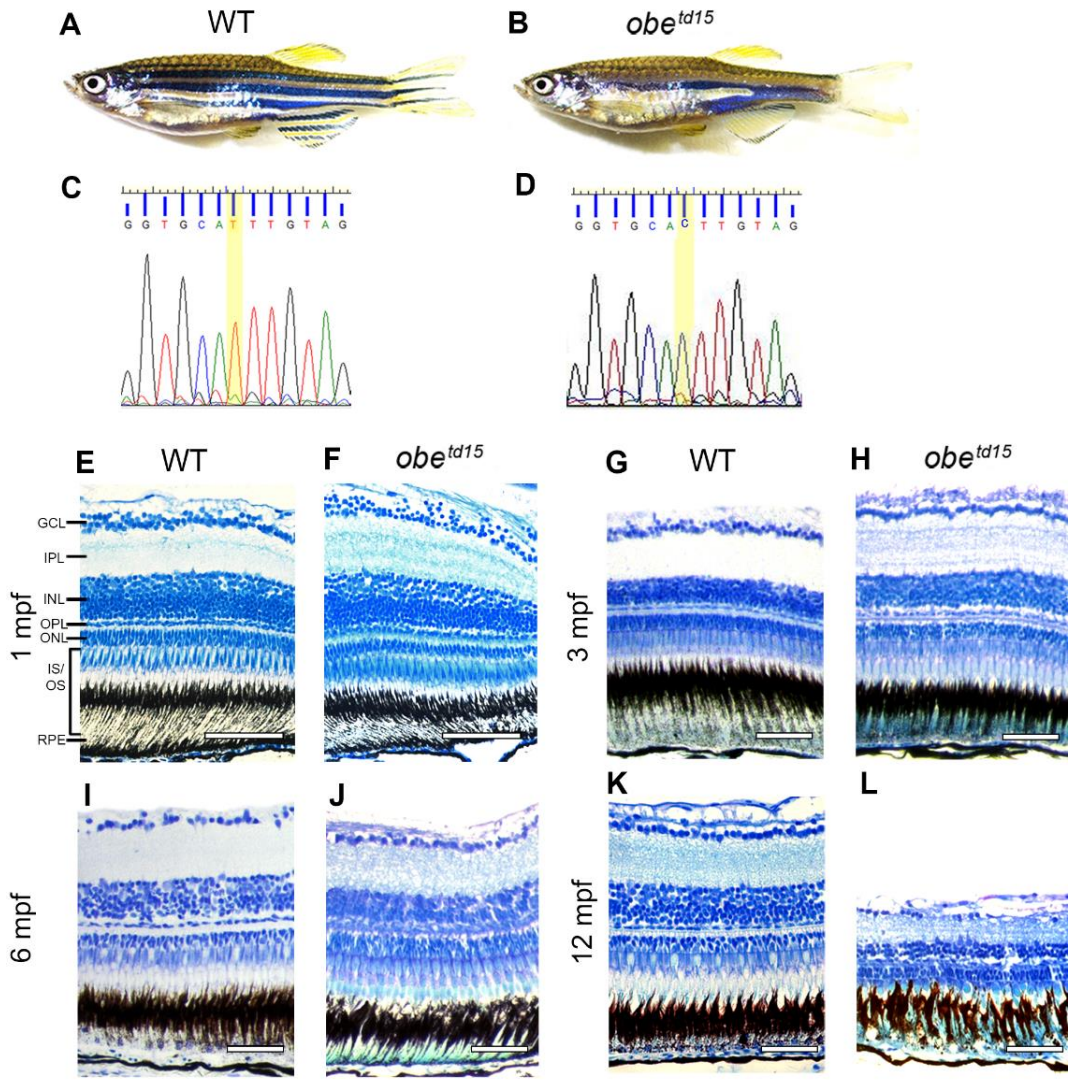

Figure 3-3. General morphology and retinal histology of *obe*^{td15} zebrafish. Wholemount imaging of adult wild-type (WT) (A) and *obe*^{td15} (B) zebrafish showed the defective pigmentation which causes broader stripes in the mutant. There were no gross ocular abnormalities in the *obe*^{td15} zebrafish. Sanger sequencing was used to confirm the WT (C) and *kcnj13* (D) sequence from finclip samples, which confirmed the missense change c.502T>C in the *obe*^{td15} homozygous fish. Transverse retinal sections with optic nerve were stained with 1% toluidine blue to compare the retinal histology of WT and *obe*^{td15} zebrafish at 1 month post-fertilisation (mpf) (E, F), 3 mpf (G, H), 6 mpf (I, J) and 12 mpf (K, L). Representative sections are shown from two retinas per timepoint for WT and mutant fish. GCL, ganglion cell layer; IPL, inner plexiform layer; INL, inner nuclear layer; OPL, outer plexiform layer; ONL, outer nuclear layer; IS/OS, photoreceptor inner/outer segments; RPE, retinal pigment epithelium. Scale bar = 50 µm.

Figure 3-4. The use of SD-OCT to visualise the zebrafish retina.
(A) SD-OCT retinal cross-sections were compared with the equivalent histology sections. (B-G) The zebrafish cone photoreceptor mosaic was imaged using SD-OCT. The zebrafish has four spectral cone subtypes (UV, blue, green, and red). B-scan cross-sectional view (B) with green lines that represent the area analysed in (C), which shows an *en face* projection of UV cone submosaic. B-scan cross-sectional view (D) with green lines that represent the area analysed in (E), which shows an *en face* projection of the red-green submosaic. (F) Schematic representation of the planar mosaic arrangement of cone photoreceptors in zebrafish. The four cone photoreceptor subtypes UV (magenta), blue, green, and red are in a highly stereotypical spatial arrangement, with alternating rows of red-green double cones and blue/UV single cones. (G) A merged image of the UV (magenta) and red-green (green) cone mosaics. (H, I) SD-OCT was used to image the optic nerve and retinal vasculature. The cross-sectional image shows the optic

nerve (bracket) (H) and the *en face* view shows convergence of the retinal blood vessels to the optic nerve region (arrow) (I). GCL, ganglion cell layer; IPL, inner plexiform layer; INL, inner nuclear layer; OPL, outer plexiform layer; ONL, outer nuclear layer; ELM, external limiting membrane; OS, outer segments; RPE, retinal pigment epithelium. VIP, volume intensity projection. Scale bar = 50 µm.

including the GCL, IPL, INL, OPL, ONL, external limiting membrane (ELM), photoreceptor outer segments and RPE.

Furthermore, the *en face* cone photoreceptor sublayers could be visualised using SD-OCT (**Figure 3-4B-G**). In the adult zebrafish retina, the four cone photoreceptor subtypes differing in their spectral sensitivity are arranged into a precise reiterated pattern (mosaic) with tiers. The well stereotyped mosaic organisation consists of alternating rows of red-green-sensitive double cones and UV- and blue-sensitive single cones. Using live imaging, it was demonstrated that by analysing specific regions within the photoreceptor layer on the B-scan retinal cross-section, it was possible to visualise the innermost and outermost cone tiers, the presumptive UV and red-green submosaics, on the corresponding *en face* VIP views. By merging these cone layers, a detailed image of the precisely organised adult zebrafish cone mosaic was constructed.

Using SD-OCT, the optic nerve and inner retinal vasculature could also be imaged and used to orientate the scans. The optic nerve, which can be used as a retinal landmark, appeared as a smudge-like interruption to the linear arrangement of the retinal layers (**Figure 3-4H-I**). In the *en face* projection, the inner retinal blood vessels could be visualised travelling outwards from the optic nerve region and branching toward the peripheral retina.

3.1.4 Retinal structure and cone mosaic organisation in *obe^{td15}* zebrafish

Cross-sectional B-scan images of WT and *obe^{td15}* confirmed histological changes showing that significant retinal thinning and loss of photoreceptor layers are apparent

at 12 mpf (**Figure 3-5**). Measurement of retinal thickness from SD-OCT images revealed that *obe*^{td15} retinas were similar in thickness at 3 and 6 mpf, while mean thickness at 12 mpf showed a significant reduction (35%), measuring at 139 ±13.5 μm compared to 214 ±4.5 μm in WT (n=5, $p<0.05$).

To assess the regularity of the *en face* UV cone mosaics, Voronoi diagrams, in which a Voronoi polygon is associated with each cone photoreceptor and colour-coded according to the number of sides it possesses, were derived from the cone mosaic images (**Figure 3-6**). The WT zebrafish retinas at each timepoint were dominated by regions of green-coded 6-sided polygons, indicating a regular triangular lattice. The other colours marked points of disruption in the hexagonally packed mosaics. It was found that there was loss of the regular mosaic of 6-sided polygons in *obe*^{td15} retinas at 12 mpf. At 3, 6 and 12 mpf, the mean percentage of cones with 6 neighbours in the *obe*^{td15} fish was 70.8 ±0.9%, 69.9 ±2.6% and 60.6 ±8.9%, respectively, compared to WT fish at the corresponding age; 77.8 ±1.7%, 70.3 ±2.5% and 74.1 ±2.2% respectively (n=5). The reduction in regularity with age exceeded the rate of loss of photoreceptors with normal ageing. It should be noted that several retinas were too severely affected to be included in the analysis due to an inability to distinguish the cones. Flat-mounted retinas from WT and mutant fish at 12 mpf showed patchy loss of cones and severe disruption of mosaic organisation *obe*^{td15} retinas when visualised using cone outer segment autofluorescence (**Figure 3-7**).

3.1.5 Retinal vasculature in *obe*^{td15} zebrafish

At 12 mpf, SD-OCT imaging revealed gross abnormalities in the appearance of the inner retinal vasculature of *obe*^{td15} zebrafish (**Figure 3-8**). Comparison of the WT and *obe*^{td15} central retinal vessels emerging from the optic nerve region show that the

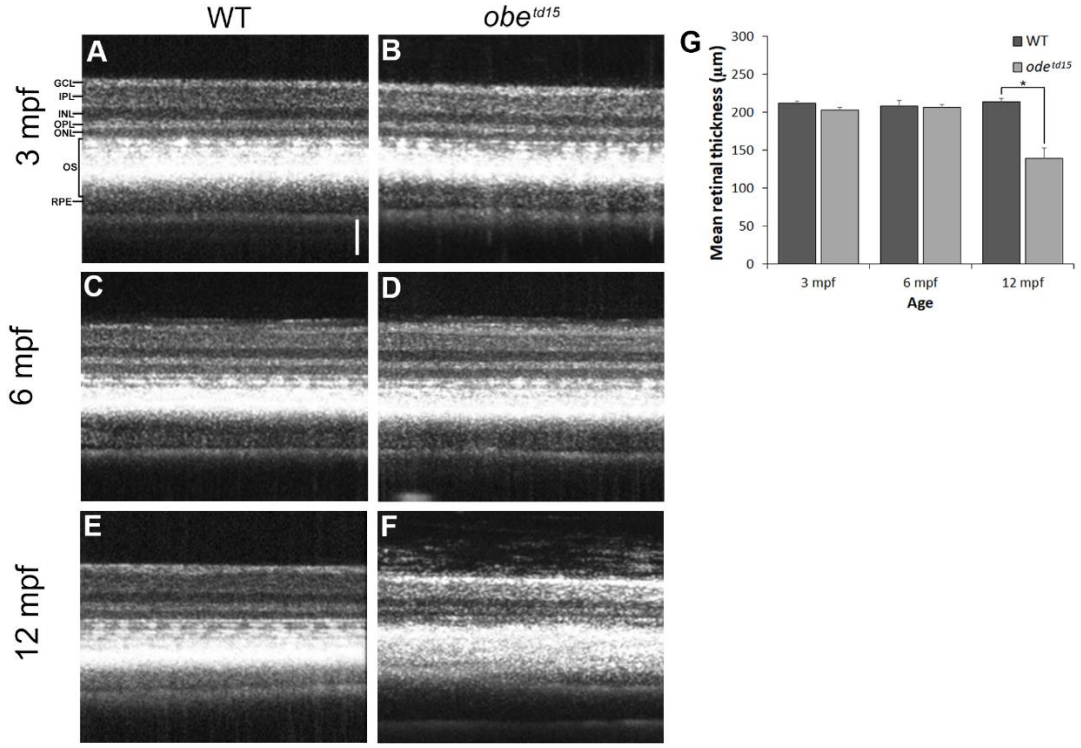

Figure 3-5. Longitudinal *in vivo* imaging of the *obe*^{td15} retinal structure.
SD-OCT was used to image the retinas in live wild-type (WT) and *obe*^{td15} zebrafish at 3 months post fertilisation (mpf) (A, B), 6 mpf (C, D) and 12 mpf (E, F). Bar chart (G) shows retinal thickness measurements (GCL-RPE) at each timepoint, measured using Bioptigen InVivoVue software (n=5 for each age, mean ± SEM). GCL, ganglion cell layer; IPL, inner plexiform layer; INL, inner nuclear layer; OPL, outer plexiform layer; ONL, outer nuclear layer; OS, outer segments; RPE, retinal pigment epithelium. Scale bar = 50 µm.

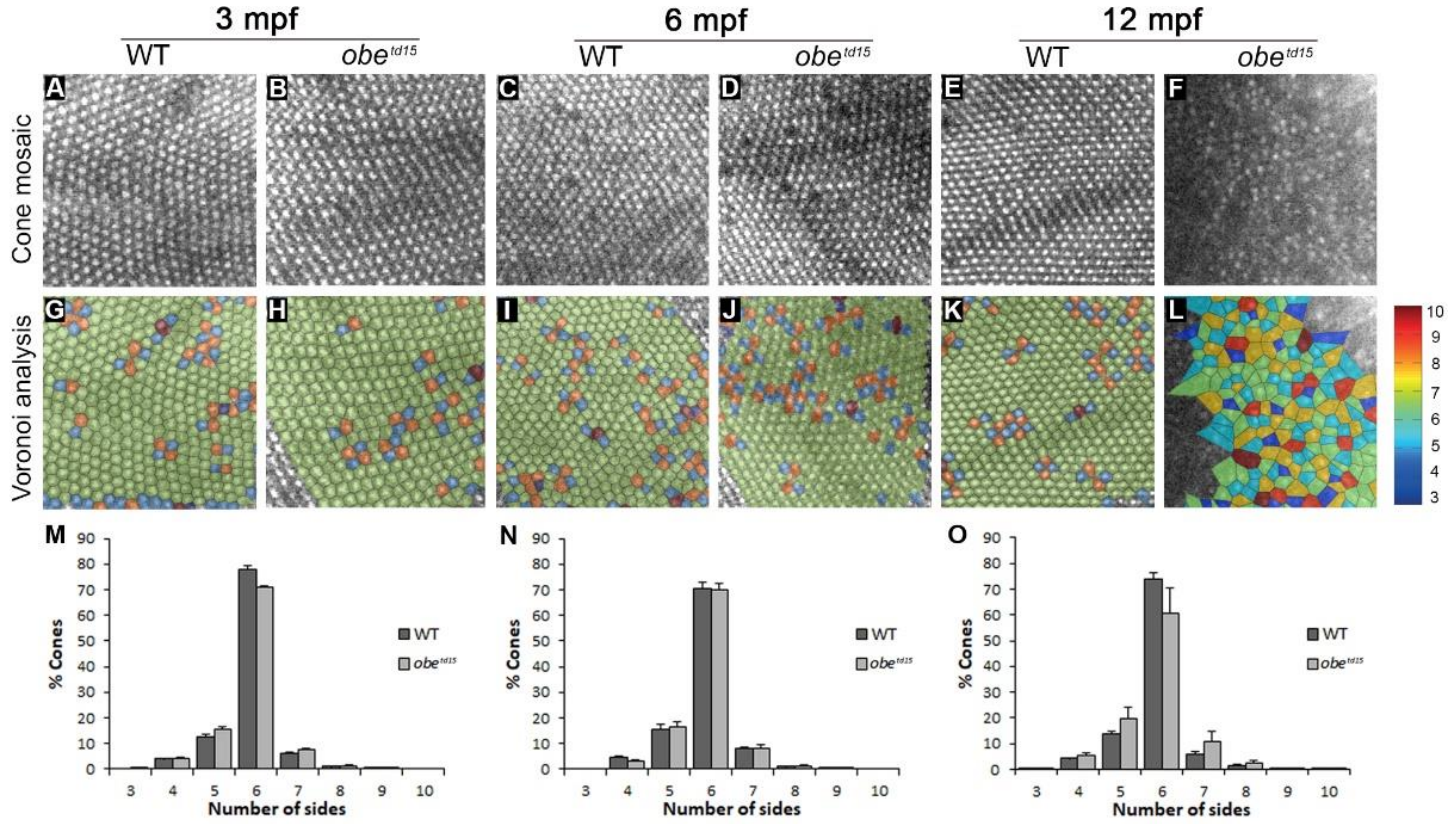

Figure 3-6. Cone mosaic organisation in *obe*^{td15} zebrafish.
SD-OCT was used at 3, 6 and 12 months post fertilisation (mpf) to image the *en face* cone photoreceptor mosaics (A-F) from which the corresponding Voronoi domain diagrams were produced (G-L) in which a Voronoi polygon is associated with each cone photoreceptor and colour-coded according to the number of sides it possesses (colour key shown on right). Bar charts show the mean percentage of three- to ten-sided Voronoi domains in wild-type (WT) and *obe*^{td15} zebrafish at (M) 3 mpf (N) 6 mpf and (O) 12 mpf (n=5 for each age, mean ± SEM).

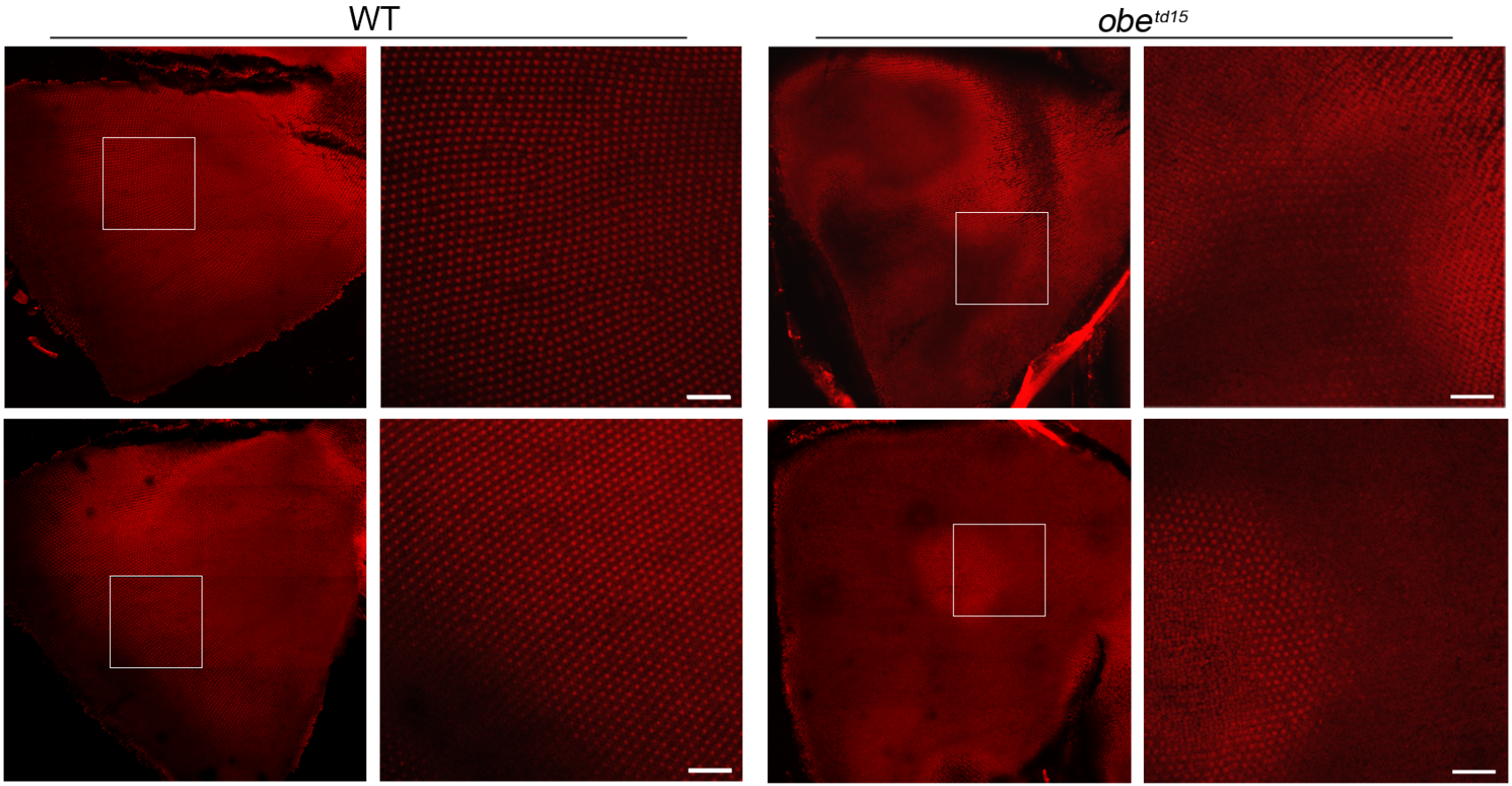

Figure 3-7. Cone mosaic imaging of flat-mounted *obe*^{td15} retinas.
The retinas of 12 months post fertilisation wild-type (WT) and *obe*^{td15} fish were flat-mounted and images of the cone autofluorescence were taken by confocal microscopy, demonstrating patchy loss and disruption of the cone mosaic (n=1). Scale bar = 50 µm.

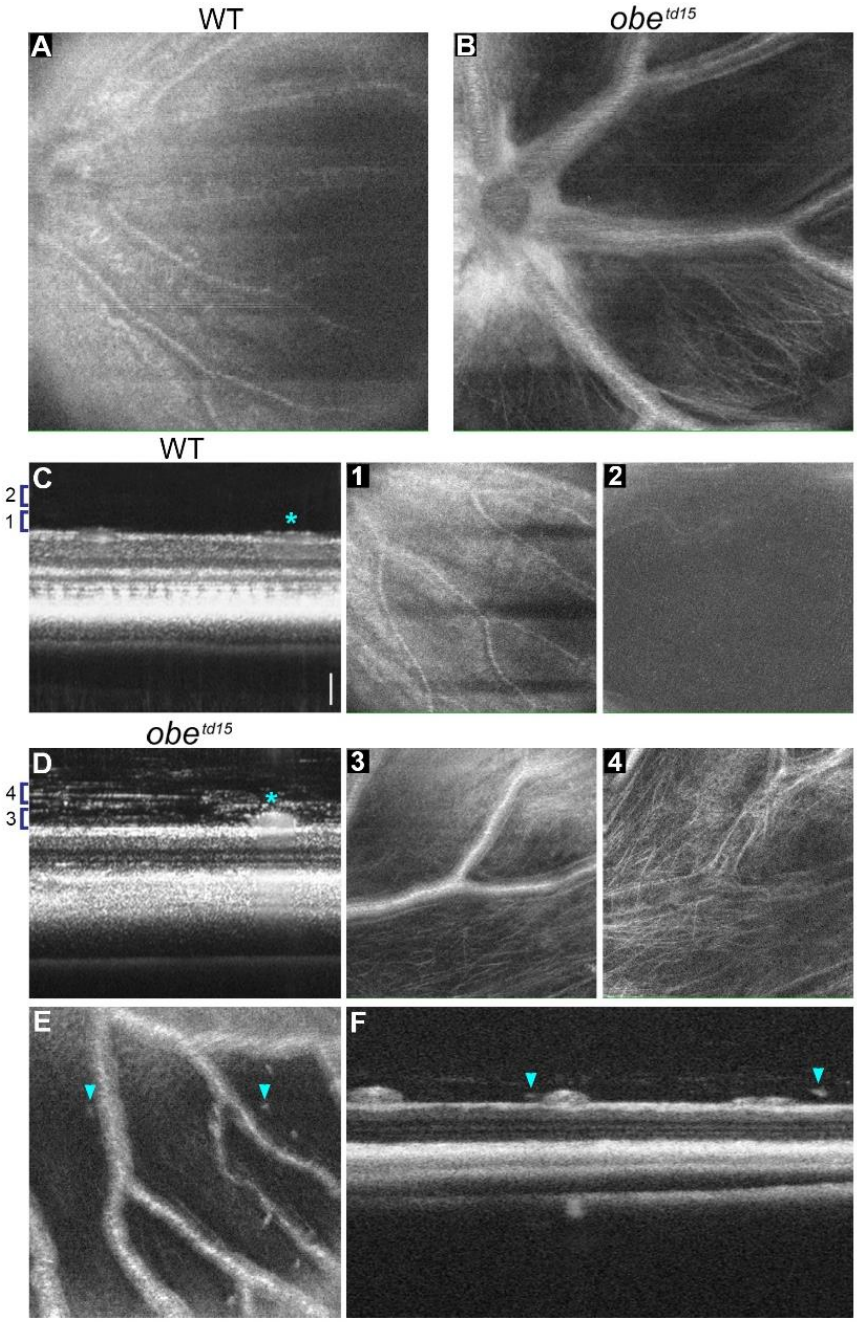

Figure 3-8. Retinal vasculature in *obe*^{td15} zebrafish.
SD-OCT *en face* images of the inner retinal vessels emerging from the optic nerve region in the wild-type (WT) (A) and *obe*^{td15} (B) fish at 12 months post-fertilisation, showing abnormal blood vessel appearance in the mutant retina. Cross-sectional B-scans from WT (C) and *obe*^{td15} (D) fish also demonstrate notable differences in vessel size (vessels indicated with *). Numbered brackets (1-4) on the cross-sections represent areas analysed at two different depths in the vitreous adjacent to the inner retina, shown on the corresponding *en face* images. Fibrous material was apparent at each depth in the *obe*^{td15} vitreous (3, 4) but was not seen on the WT images (1, 2). Hyper-reflective deposits were also noted in the vitreous of the *obe*^{td15} retina on both B-scan (E) and *en face* (F) images, indicated with arrows. Representative images are shown from 5 retinas per timepoint for WT and mutant fish.

vessels appeared to be abnormally enlarged and hyper-reflective in the *obe*^{td15} retina compared to WT, making them much more easily distinguishable on SD-OCT. The difference in vessel diameter was also apparent on the B-scan cross-sectional images where they appear as prominent spherical structures overlying the GCL in the *obe*^{td15} retina while relatively unremarkable in comparison on the WT images. Furthermore, examination of two regions in the vitreous at level of the vessels and just above the vessels on VIP images revealed the presence of fibrous material in the *obe*^{td15} vitreous which was not present in the WT. Spot-like hyper-reflective vitreal deposits were also noted on both B-scan and VIP views of the *obe*^{td15} retina.

3.1.6 Retinal vasculature in *KCNJ13* patients

Two previously unreported unrelated LCA families (both resulting from consanguineous marriages within the Persian Jewish community), each had two children who were diagnosed in infancy, with the same homozygous missense mutation (c.458C>T, p.Thr153Ile) in *KCNJ13* (**Table 3-1**). The mutation is located within the region coding for the conserved H2 α helix domain (**Figure 3-1**). Both families were investigated for retinovascular changes. In family A, both affected siblings developed retinal neovascularization with diffuse severe leakage and vitreous haemorrhages at age 17 on a background of characteristic *KCNJ13*-LCA (with area of nummular pigment at the level of the RPE, especially over the posterior pole, macular atrophy and optic disc pallor with retinal vessel attenuation). Patient A-1 and A-2 developed fibrosis along the arcades and optic disc, they received extensive pan-retinal photocoagulation (PRP) and two intravitreal injections of avastin. Following a vitreous haemorrhage in the left eye, Patient A-1 had a pars plana vitrectomy with secondary complications of cataracts requiring phacoemulsifcation followed by uveitic glaucoma resulting in posterior capsule opacification and membranectomy. Patient A-2 also developed retinal neovascularization and fibrosis that required extensive

Table 3-1. Leber congenital amaurosis (LCA) and snowflake vitreoretinal degeneration (SVD) patients with *KCNJ13* mutations examined in this study and previous publications. RVA, right visual acuity; LVA, left visual acuity; FFA, fundus fluorescein angiogram; CF, count fingers; NPL, no light perception; PRP, pan-retinal photocoagulation; logMAR, logarithm of the minimal angle of resolution. All patients had LCA except for where marked ▲SVD †other vitreoretinal dystrophy.

Patient	Age	Mutation	RVA	LVA	FFA
A-1	20	c.458C>T, p.Thr153Ile	CF	NPL	Retinal neovascularization, diffuse severe leakage (early leakage primarily associated with areas of prior fibrosis along arcades and disc), had extensive PRP.
A-2	18	c.458C>T, p.Thr153Ile	CF	1.2 logMAR	Right vitreous haemorrhage with diffuse severe leakage.
B-1	13	c.458C>T, p.Thr153Ile	1.3 logMAR	1.3 logMAR	Very mild leakage from the disc in both eyes but with no neovascularization elsewhere and no peripheral vessel leakage.
B-2	10	c.458C>T, p.Thr153Ile	CF	CF	No evidence of blood vessel leakage or neovascularization elsewhere.
Sergouniotis et al 2011 (81)					
Patient A-2	34	c.496C>T p.Arg166*	2.0 logMAR	2.0 logMAR	-
Patient A-3	32	c.496C>T p.Arg166*	1.78 logMAR	1.48 logMAR	-
Patient B-3	33	c.722T>C p.Leu241Pro	1.45 logMAR	1.45 logMAR	-
Pattnaik et al 2015 (84)	10	c.158G>A p.Trp53*	2.0 logMAR	CF	-
Perez-Roustit et al. 2017 (85)	31	c.314G.T p.Ser105Ile, c.655C.T p.Gln219*	1.0 logMAR	1.3 logMAR	-
▲**Hejtmancik et al. 2008** (79) **Lee et al. 2003** (322) 13 family members with SVD	12-85	c.484C>T p.Arg162Trp	See Table 1 in (322)	-	-

†Khan et al. 2015 (86)					
Case 1	12	c.359T>C p.Ile120Thr	Hand motion	0.7 logMAR	-
Case 2	33	c.359T>C p.Ile120Thr	1.3 logMAR	1.3 logMAR	-

PRP.

Subsequently, he had multiple haemorrhages in the right eye and required two vitrectomies and a membrane delamination and removal. Fundus fluorescein angiogram (FFA) was performed to investigate for ongoing retinal neovascularization and early and late leakage was seen in both patient (**Figure 3-9A-C**).

The two affected siblings in family B, both female and younger than the two affected males from family A, showed characteristic features of LCA. Patient B-1 (age 13) showed very mild leakage from the optic disc in both eyes, but no evidence of retinal neovascularization elsewhere on FFA. Patient B-2 (age 10) showed no retinovascular changes (**Figure 3-9D-F**). Biannual monitoring is underway. In the previously reported families diagnosed with *KCNJ13*-LCA, where affected patients are between 10 – 34 years, no reports of retinovascular changes have been described.

3.1.7 Visual function in *obe*^{td15} zebrafish

In order to determine the visual function of *obe*^{td15} zebrafish, optokinetic response testing was undertaken at 3, 6, and 12 mpf comparing WT fish to *obe*^{td15} and positive control WT fish injected with ouabain to induce a chemical retinal degeneration. The results show that the *obe*^{td15} zebrafish had a similar visual acuity to WT fish at 3 mpf (1.39 ±0.18 cpd in WT, 1.21 ±0.10 cpd in mutant fish) and at 6 mpf WT fish showed a greater but not significant increase in acuity (2.01 ±0.48 cpd in WT, 1.30 ±0.12 cpd in mutant fish) (**Figure 3-10**). At 12 mpf, the mean visual acuity of *obe*^{td15} zebrafish showed a significant decline and was measured as 0.46 ±0.09 cpd compared to 1.65 ±0.41 cpd in age-matched WT ($p<0.05$). A minimum of four WT and *obe*^{td15} zebrafish were assessed per timepoint. Optokinetic responses were not observed in ouabain-

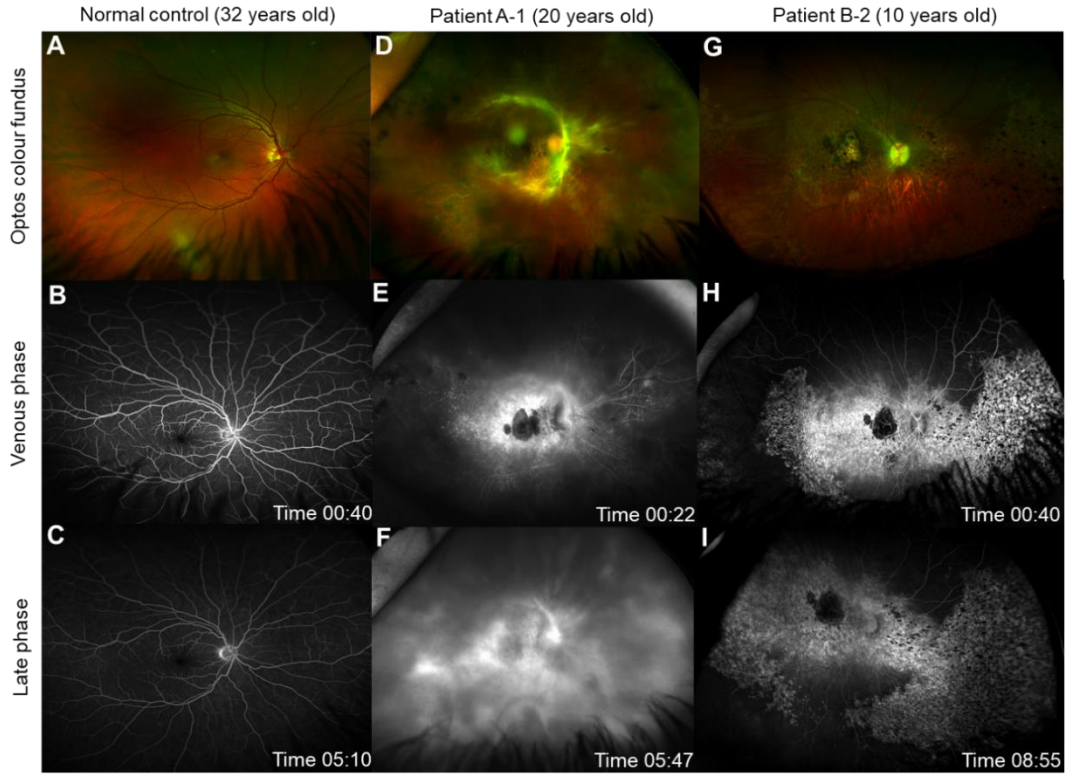

Figure 3-9. Retinal vasculature in *KCNJ13* patients.
Ultra-wide field fluorescein angiography (FFA) using Optos (Dunfermline, Scotland) of the right eye from two unrelated patients with a novel missense mutation (p.Thr153Ile) in *KCNJ13* compared to normal control male age 32 years (A-C). Panel Patient A-1, 20 years old, (D) colour fundus images showing vasoproliferative response around the arcades, widespread pan-retinal photocoagulation scars overlying the pigmentary retinopathy; (E) shows leakage (first seen in arterial phase, data not shown) in the venous phase with extensive leakage in the late phase (F). Panel Patient B-2, 10 years old, (G) colour fundus images showing patchy areas of nummular pigmentary retinopathy; (H) FFA shows hyperfluorescence in areas of retinopathy with an area of hypofluorescence at the macula which coincides with delineated area of chorioretinal atrophy (choroidal vessels can be seen), but no evidence of leakage at any phase (I). Images were provided by Professor Michael Gorin from the Jules Stein Eye Institute, UCLA.

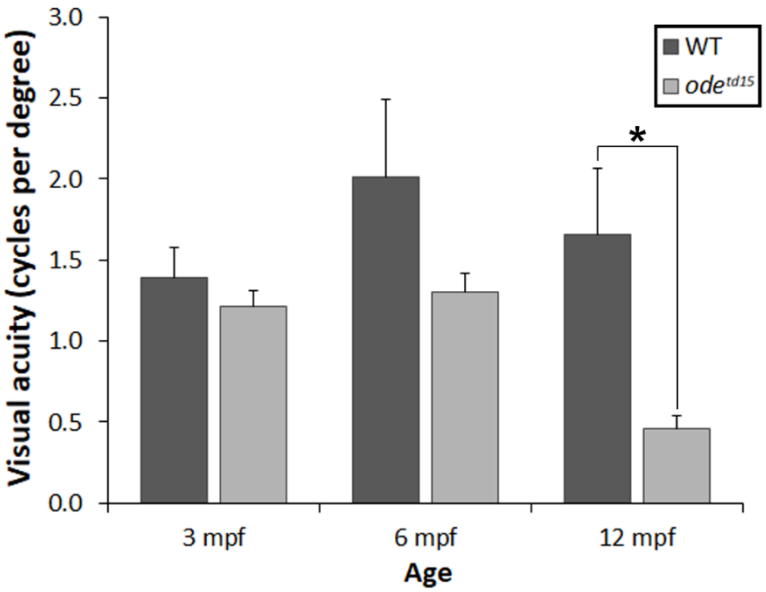

Figure 3-10. Visual function in *obe*^{td15} zebrafish.
Bar chart showing visual acuity (cycles per degree) of wild-type (WT) and *obe*^{td15} zebrafish at 3 months post fertilisation (mpf), 6 mpf and 12 mpf assessed using the optokinetic response assay (n≤4, mean ± SEM). *p<0.05.

injected fish.

3.1.8 Opsin localisation in the *obe*^{td15} retina

To examine opsin localisation in the *obe*^{td15} zebrafish, the 1D4 antibody was used to label retinal sections at 3 mpf and 12 mpf, which detects rhodopsin in most species tested except zebrafish where it has been found to recognise the red cone opsin (323). At 3 mpf, red opsin was detected in the outer segments of the long double cones and there did not appear to be any differences in localisation between the WT and *obe*^{td15} retinas (**Figure 3-11**). There was a clear reduction in red opsin detection in the mutant retina at 12 mpf. Rhodopsin localisation was assessed using the 4D2 antibody. Typical rhodopsin expression defined the rod outer segments in the WT and *obe*^{td15} retina at both timepoints. The labelled rod outer segments had a more disordered appearance in the mutant retina at 12 mpf compared to WT.

3.1.9 Apoptosis and Müller cell activation in the *obe*^{td15} retina

Levels of apoptotic cell death in the retina at 6 and 12 mpf were examined using a TUNEL assay (**Figure 3-12**). This method was not effective at detecting apoptosis in the mutant at either age, suggesting that the degeneration in this model is not slowly progressive and may occur rapidly between these time points. The glial fibrillary acidic protein (GFAP) is known to be upregulated by glial cells in response to retinal injury or stress (324). Immunostaining of GFAP (detected using anti-ZRF1) showed expression in the Müller cell endfeet and processes in both WT and *obe*^{td15} retinas (**Figure 3-13**). By 6 mpf, GFAP expression became increased further along the processes in the mutant retina and at 12 mpf expression was highly irregular and extended into the ONL. The WT retina maintained a similar expression pattern at all ages

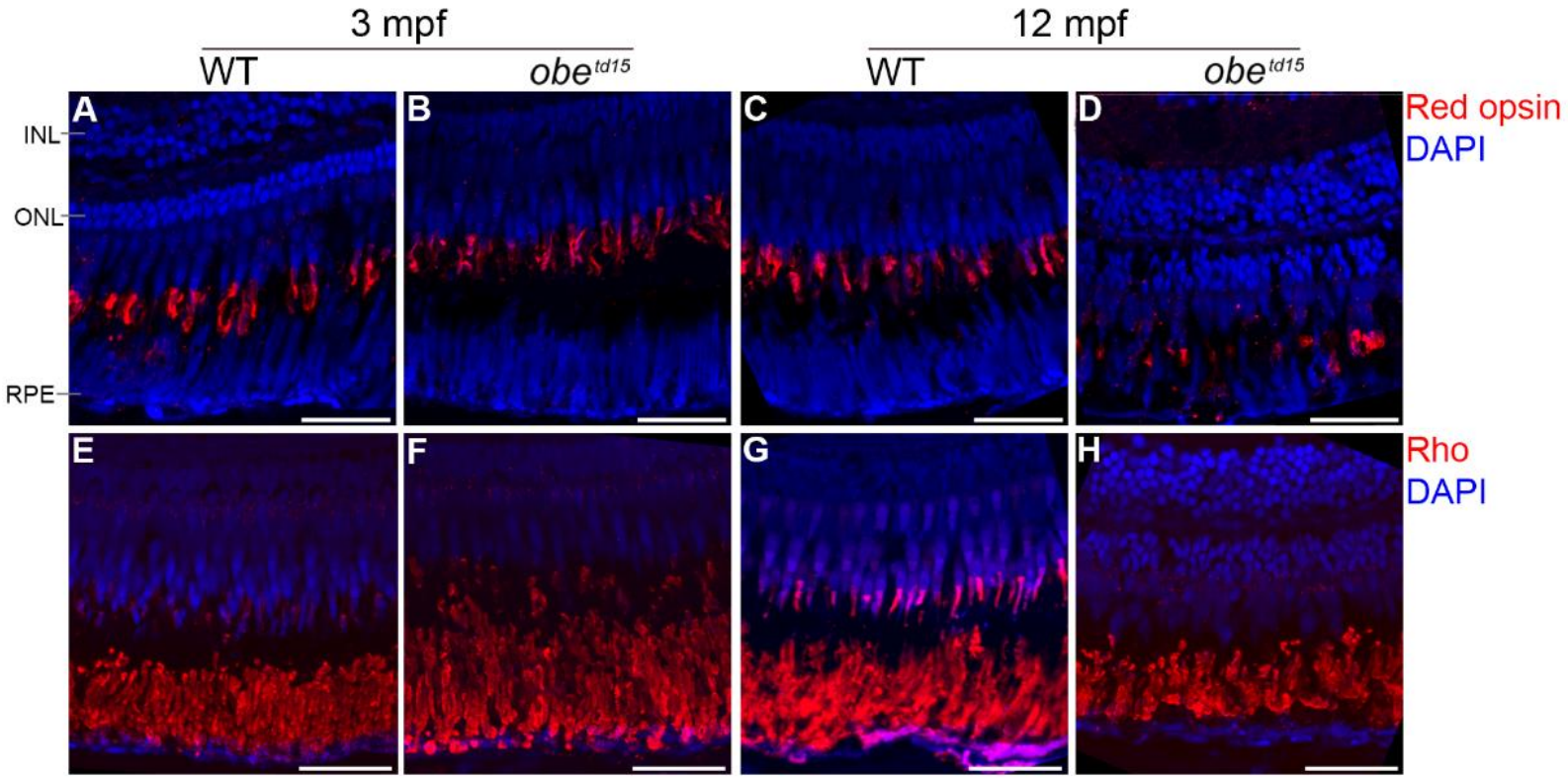

Figure 3-11. Rhodopsin and red opsin localisation in the *obe*^{td15} retina.
Red opsin was detected in the wild-type (WT) and *obe*^{td15} retina at 3 months post fertilisation (mpf) (A, B), and 12 mpf (C, D) by immunostaining with the 1D4 antibody (red). Notably less red opsin was detected in the in the mutant retina at 12 mpf. Rhodopsin was detected in the WT and *obe*^{td15} retina at 3 mpf (E, F) and 12 mpf (G, H) by immunostaining with the 4D2 antibody (red). Rhodopsin was detected in the rod outer segments at all timepoints. The rod outer segments appeared to be more disordered in the mutant retina at 12 mpf. Representative images are shown from two retinas per timepoint for WT and mutant fish. DAPI nucleic acid stain was used as a counterstain (blue). INL, inner nuclear layer; ONL, outer nuclear layer; RPE, retinal pigment epithelium. Scale bar = 25 µm.

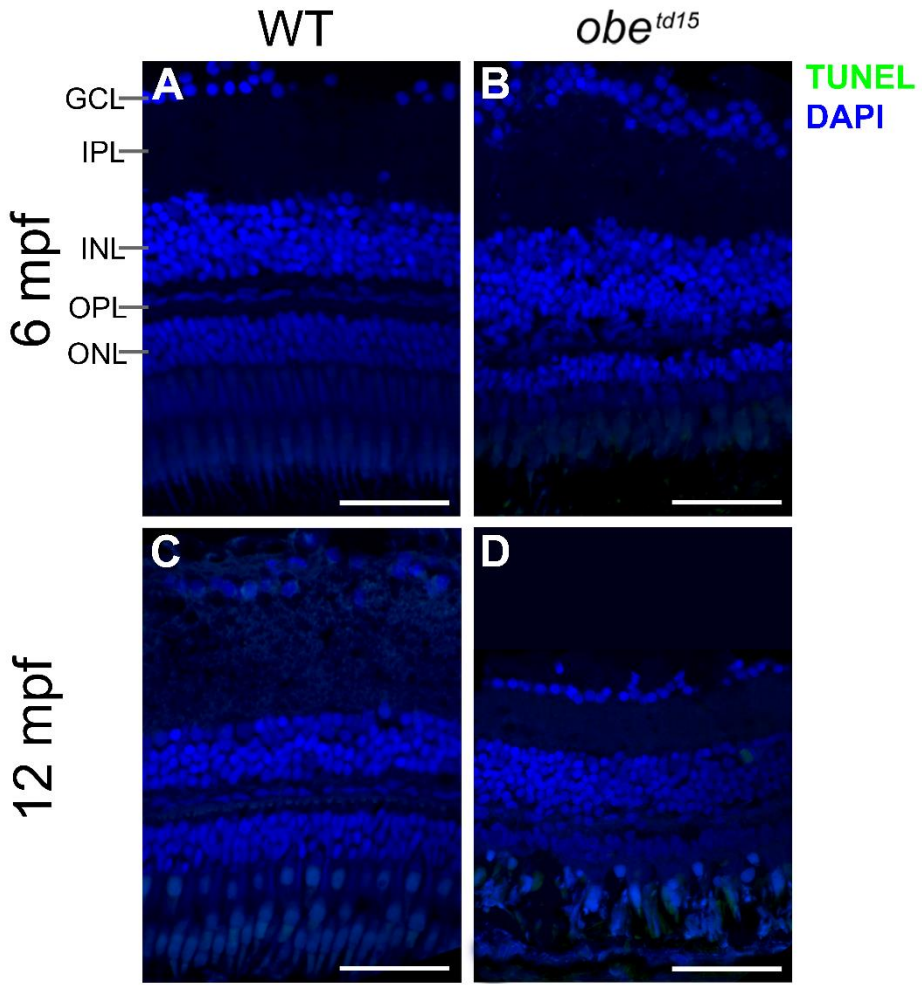

Figure 3-12. Apoptosis in the *obe*^{td15} zebrafish.
TUNEL assays were used to detect apoptotic cells in the wild-type (WT) and *obe*^{td15} retinas at 6 months post fertilisation (mpf) (A, B) and 12 mpf (C, D). Apoptosis was not noted in the WT and mutant retinas at either age (n=3). DAPI nucleic acid stain was used as a counterstain (blue). Scale bar = 50 µm.

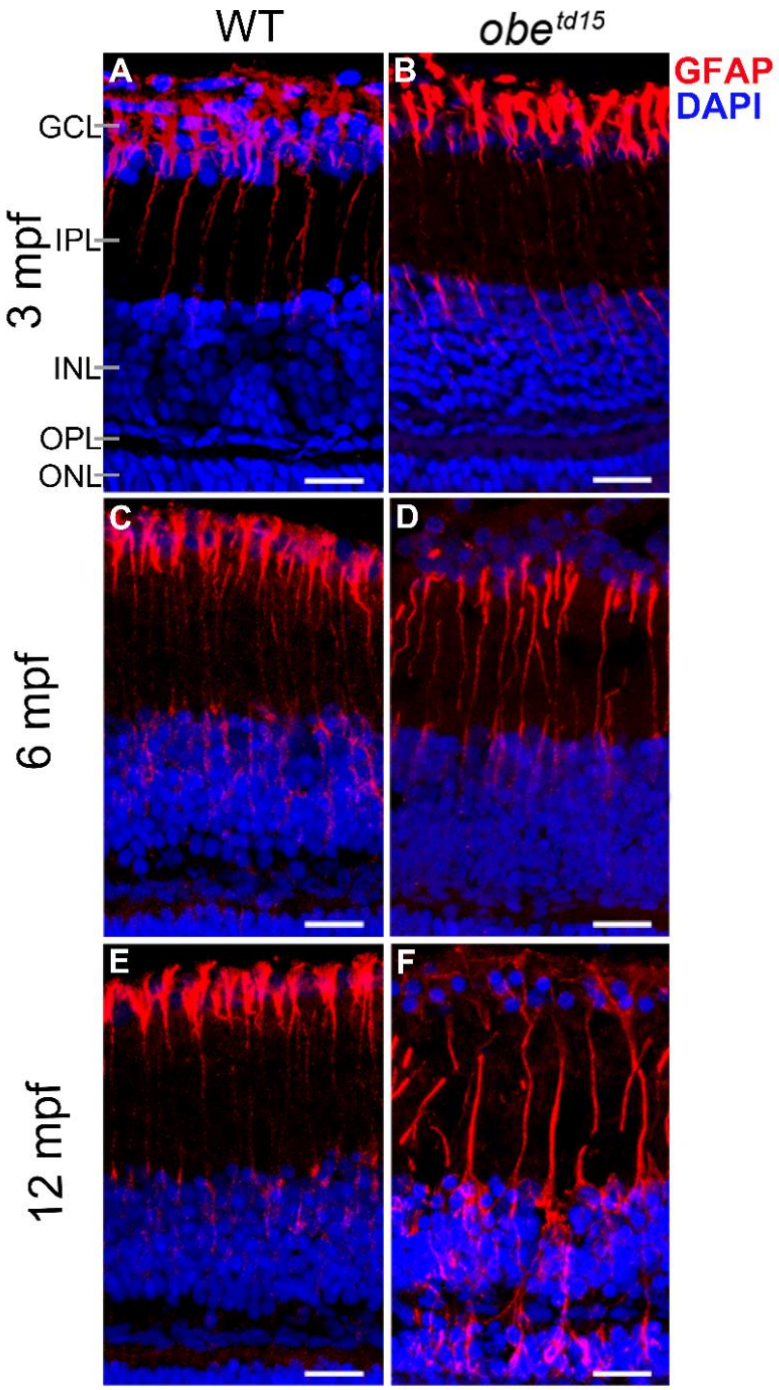

Figure 3-13. Müller cell activation in the *obe*^{td15} retina.
The glial fibrillary acidic protein (GFAP) was detected in the wild-type (WT) and *obe*^{td15} retina at 3 months post fertilisation (mpf) (A, B), 6 mpf (C, D) and 12 mpf (E, F) by immunostaining with the anti-ZRF1 antibody (red). Sections are counterstained with DAPI nuclei acid stain (blue). Increased GFAP was noted in the along the glial processes in the mutant retina at 6 and 12 mpf, and was extended into the ONL at 12 mpf. Representative images are shown from two retinas per timepoint for WT and mutant fish. GCL, ganglion cell layer; IPL, inner plexiform layer; INL, inner nuclear layer; OPL, outer plexiform layer; ONL, outer nuclear layer. Scale bar = 50 µm.

3.1.10 The *obe*^{td15} retinal ultrastructure

Mitochondria and phagosomes

The ultrastructure of *obe*^{td15} RPE was investigated at 3, 6 and 12 mpf using TEM (**Figure 3-14**). This technique allowed subcellular examination of several organelles contained within the RPE, including melanosomes (pigment granules), mitochondria and phagosomes, the latter of which are vesicles containing shed photoreceptor outer segments headed for degradation. The number of mitochondria and phagosomes in the RPE cells were assessed in WT and mutant fish. At 3 mpf, a modest increase in mitochondria per µm was noted in the RPE of *obe*^{td15} zebrafish, with a substantial 4.3-fold increase in phagosomes, indicative of altered phagosome clearance (n=3) ($p<0.001$). At 6 mpf, there was a 5.5-fold increase in mitochondria ($p<0.001$) and a 2.8-fold increase in phagosomes in the mutant RPE compared to WT ($p<0.01$). At 12 mpf, the mitochondria numbers remained high with a 6.4-fold increase ($p<0.001$), but the phagosome number declined to 1.6-fold, with no significant difference between *obe*^{td15} and WT fish at this point. The expansion in numbers of mitochondria and phagosomes in the *obe*^{td15} retinas resulted in a displacement of the cellular organelles from the basal to the apical site of the RPE. The *obe*^{td15} 12 mpf retinas exhibited areas of severe disease containing disordered photoreceptor outer segments with islands of preserved tissue (**Figure 3-15**). This is similar to the pattern of degeneration commonly seen in human retinal disorders and further long-term studies would reveal the late natural history.

Mitochondrial size

Measurement of mitochondrial size revealed a progressive increase in size over time in the *obe*^{td15} zebrafish RPE, with a mean area of 0.10 ±0.008 um^2, 0.19 ±0.018 um^2 and 0.24 ±0.015 um^2 at 3, 6 and 12 mpf respectively (13 mitochondria measured per

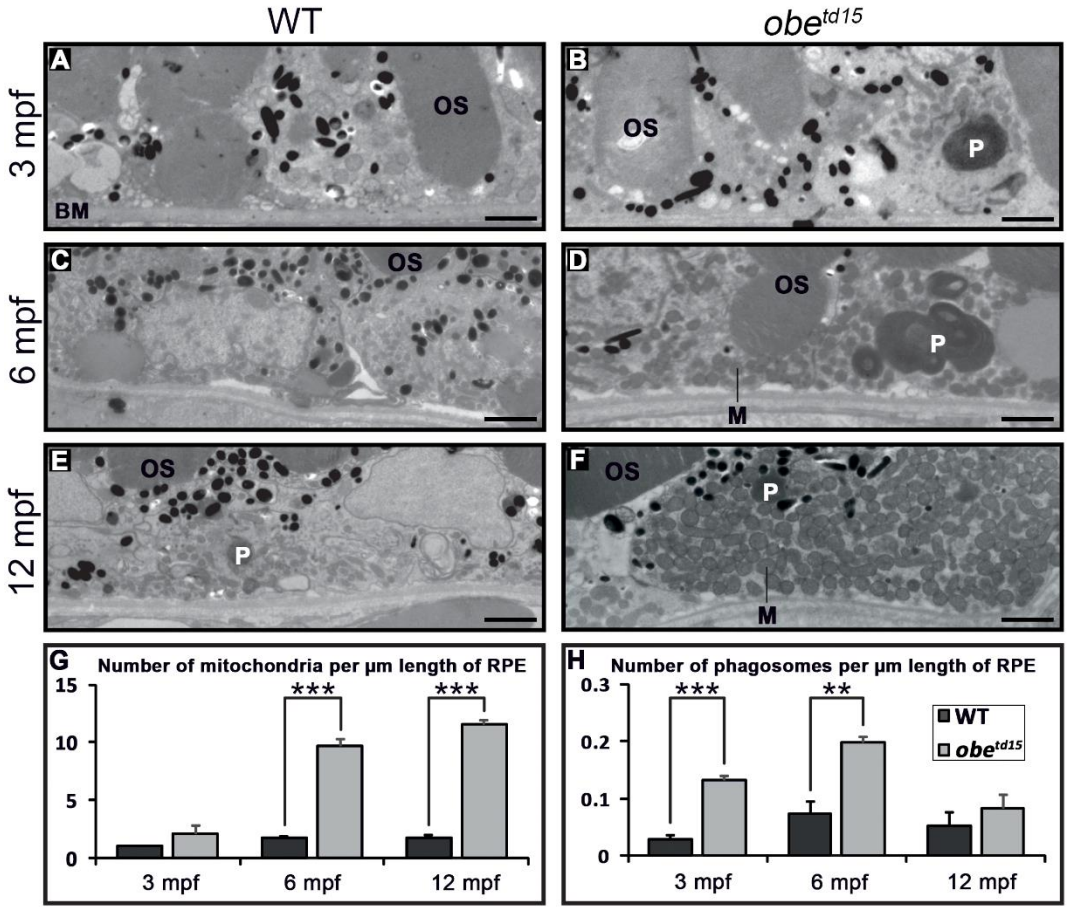

Figure 3-14. Mitochondrial abundance and phagosome clearance in the *obe*^{td15} retinal pigment epithelium (RPE).
Transmission electron microscopy cross-sections of the RPE show little difference between WT and *obe*^{td15} fish at 3 months post fertilisation (mpf) (A, B), while at 6 mpf (C, D) and 12 mpf (E, F) there is a significant increase in the number of mitochondria (M) in *obe*^{td15} compared to WT eyes. Additionally, there is a significant increase in the number of phagosomes (P) in *obe*^{td15} eyes at 3 and 6 mpf. Bar charts displaying numbers of mitochondria and phagosomes per µm length of RPE are shown in (G) and (H). OS, photoreceptor outer segments; BM, Bruch's membrane. Results are means (three eyes) ± SEM. **P<0.01, ***P<0.001. Scale bars = 2 µm.

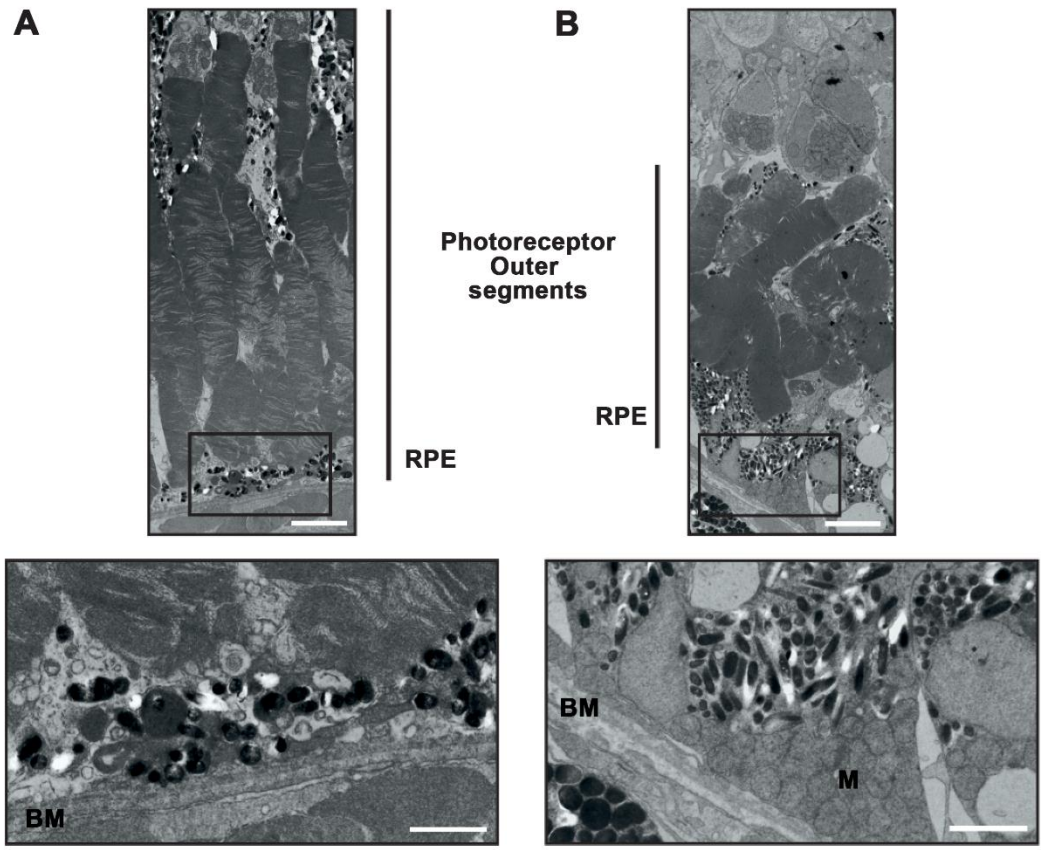

Figure 3-15. *obe*^{td15} retinas exhibit areas of photoreceptor loss with islands of preserved retina.
Transmission electron microscopy images of the photoreceptor outer segment and retinal pigment epithelium (RPE) from a 12 months post fertilisation *obe*^{td15} zebrafish eyes. (A) shows a region displaying preserved retinal tissue whereas (B) is an affected region with disordered photoreceptor outer segments and numerous, large mitochondria in the RPE. BM, basement membrane; M, mitochondria. Scale bars = 5 µm (top) and 2 µm (bottom).

WT and mutant age group) (**Figure 3-16**). Mitochondria in the WT RPE were similar in size to the mutant at 3 mpf and showed an overall decrease in size with age to 0.07 ±0.004 um^2 and 0.05 ±0.006 um^2 at 6 and 12 mpf respectively. The *obe*^{td15} mitochondria were significantly greater than WT at these timepoints, demonstrating a 4.9-fold increase in mean area compared to WT at 12 mpf ($p<0.001$).

Melanosomes

As *obe*^{td15} zebrafish show aberrant melanosome aggregation in their skin resulting in defective skin pattern formation, the melanosomes in the RPE were also investigated. In fish, the melanosomes of the RPE exhibit a redistribution from the basal cell body into the apical processes upon the onset of light, which is reversed in the dark (29). Examination of melanosome distribution in the RPE at 3, 6 and 12 mpf in fully light-adapted fish exposed to normal light:dark cycle did not reveal any significant differences in the percentage of melanosomes localised to the apical photoreceptor region between the WT and *obe*^{td15} RPE (**Figure 3-17**). In order to further assess melanosome function, 12 mpf WT and mutant fish were dark-adapted for 48 hours before collection. This revealed a significantly increased basal aggregation in the RPE of *obe*^{td15} zebrafish over a more distributed apical localisation in the WT ($p<0.05$).

3.1.11 Mitochondrial biogenesis and metabolism

In order to verify the qualitative ultrastructural appearances of the mitochondrial changes in the RPE, qRT-PCR of *polg2* (mitochondrial DNA polymerase subunit gene), *fis1* (fission) and *opa1* (fusion gene) in isolated retinal and RPE tissue of WT and *obe*^{td15} zebrafish at 6 and 12 mpf was conducted (n=3) (**Figure 3-18**). *polg2* expression was upregulated in *obe*^{td15} tissue compared to WT, showing 1.29-fold ±0.32 and 1.62-fold ±0.04 increases at 6 and 12 mpf respectively ($p<0.01$). *fis1* was

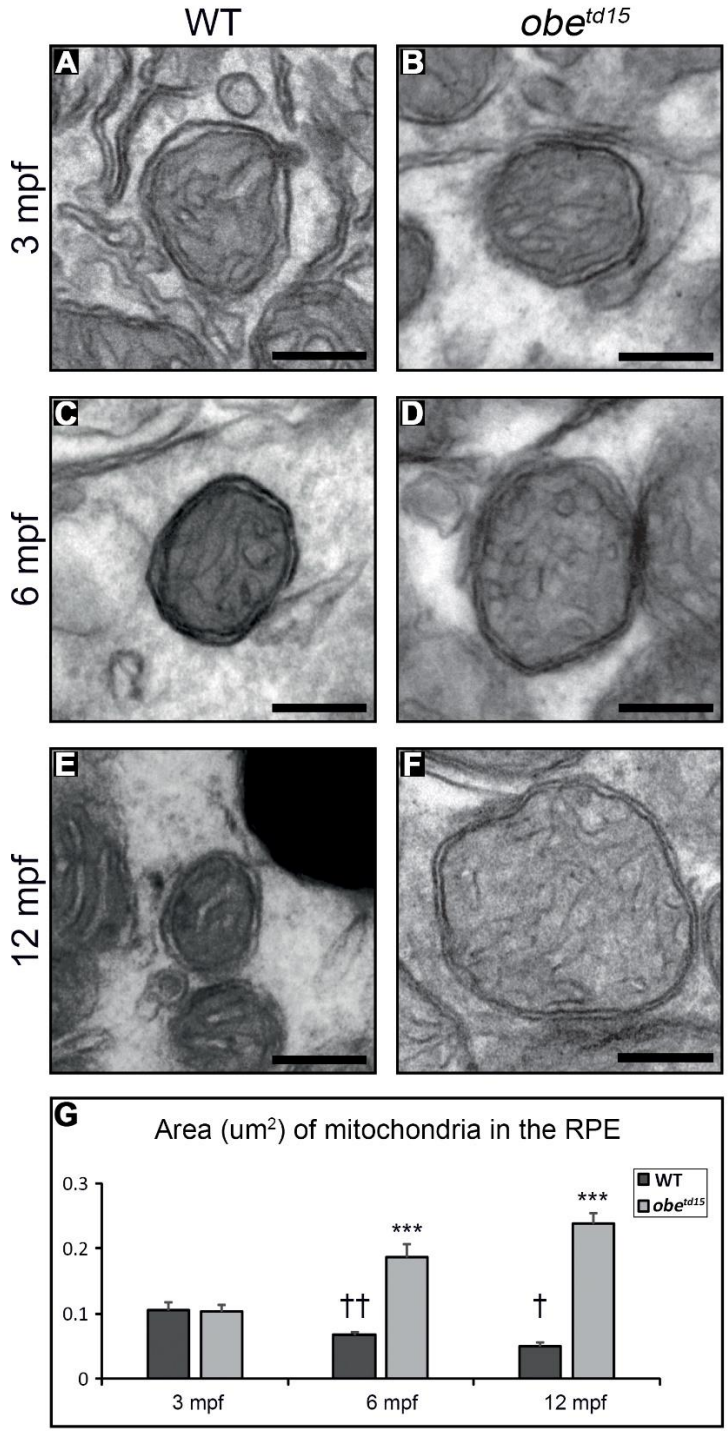

Figure 3-16. Mitochondrial size in *obe*^{td15} retinal pigment epithelium (RPE). Mitochondrial size in the wild-type (WT) RPE at 3 months post-fertilisation (mpf) (A), 6 mpf (C) and 12 mpf (E) shows a decrease with age, while mitochondrial size in the *obe*^{td15} RPE at 3 mpf (B), 6 mpf (D) and 12 mpf (F) shows an increase with age. Mitochondrial area measured from transmission electron micrographs displayed on bar chart (G). Results are mean ± SEM (n=13 from three retinas from per timepoint for WT and mutant fish). Statistical significance relative to WT of different ages †P<0.05, ††P<0.01. Statistical significance relative to WT against *obe*^{td15} of the same age ***P<0.001. Scale bar = 200 nm.

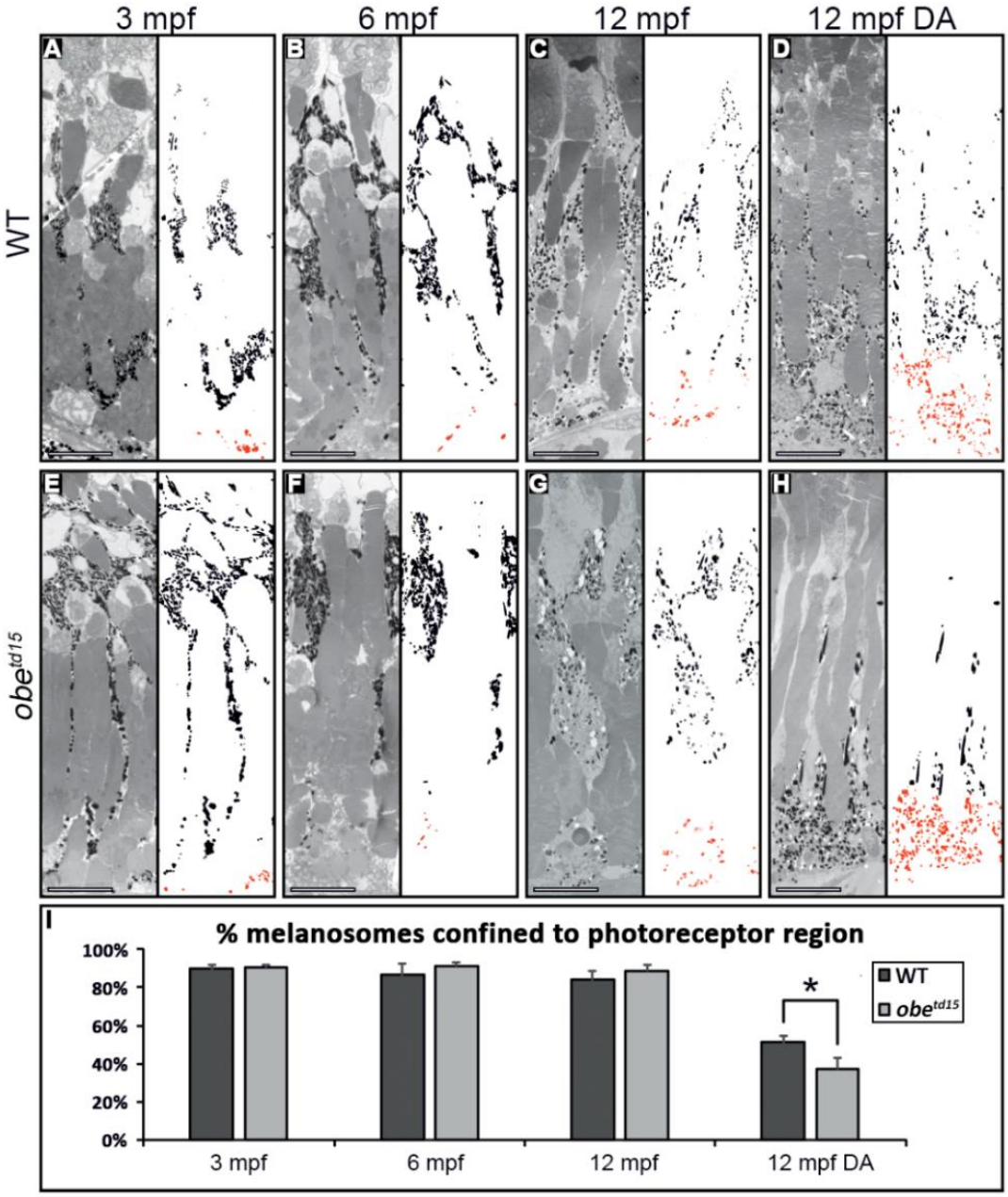

Figure 3-17. Melanosome localisation in the *obe*^{td15} retinal pigment epithelium (RPE) in normal and dark-adapted conditions.
Transmission electron micrographs of wild-type (WT) (A-D) and *obe*^{td15} (E-H) RPE at 3 months post-fertilisation (mpf), 6 mpf and 12 mpf with neighbouring panels showing digitally extracted melanosomes with the basal RPE-localised melanosomes false-coloured in red. Using these extracted melanosomes, the proportion of melanosomes localised to the photoreceptor region was calculated, shown in bar chart (I). There was little difference in the proportion of melanosomes localised to the photoreceptor region in zebrafish exposed to a normal daily light cycle. Whereas, dark-adaptation (DA) of 12 mpf *obe*^{td15} zebrafish (H) caused significantly more melanosomes to localise away from the apical photoreceptor region (inside the RPE) compared to WT zebrafish eyes (D). Results are the means (from three regions from three eyes) ± SEM. *P<0.05. Scale bars = 10 μm.

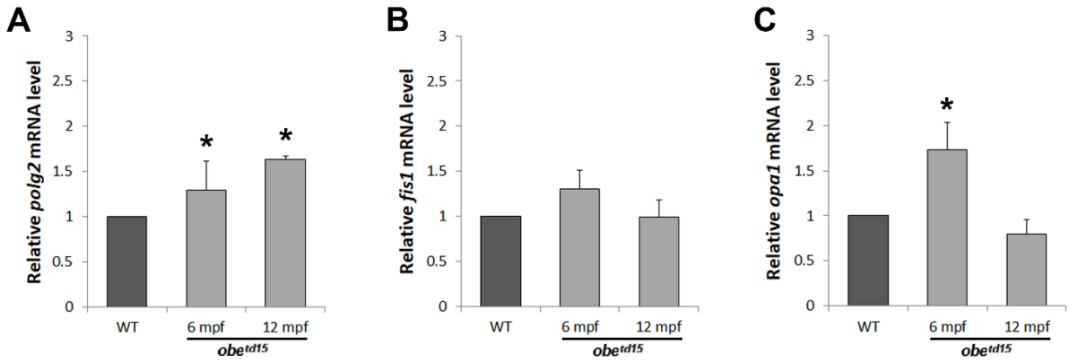

Figure 3-18. Mitochondrial biogenesis in the *obe*^{td15} retina.
Quantitative RT-PCR was used to determine relative mRNA expression levels of (A) *polg2*, (B) *fis1*, (C) *opa1* at 6 and 12 months post fertilisation (mpf) (n=3 for each age, mean ± SEM). *p<0.05.

elevated at 6 mpf with a 1.31-fold increase ±0.31 in expression before declining at 12 mpf to a 0.99-fold change ±0.31 in the mutant compared to WT. A similar trend was observed in *opa1* expression which showed a 1.73-fold ±0.31 increase at 6 mpf ($p<0.01$) before dropping to levels lower than WT at 12 mpf (0.80-fold change ±0.16).

To examine changes in energy production-related genes in the *obe*^{td15} RPE and retina, qRT-PCRs were performed to assess expression levels of genes that encode enzymes involved in glycolysis (*pgk1*) and anaerobic respiration (*ldha*) (**Figure 3-19A-B**). *pgk1* expression increased 1.65-fold ±0.04 and 2.42-fold ±0.35 in *obe*^{td15} fish compared to WT at 6 and 12 mpf respectively. Expression of *ldha* showed 1.12-fold ±0.12 and 1.41-fold ±0.24 increases in the mutant at 6 and 12 mpf respectively. An ATP assay was performed at 6 and 12 mpf (**Figure 3-19C)**. This revealed a 50.1% and a 32.8% reduction in ATP levels at 6 and 12 mpf respectively in the mutant relative to WT ($n=5$, $p<0.001$ and $p<0.01$).

3.1.12 Retinal stress

To examine levels of mitochondrial stress in the *obe*^{td15} RPE and retina, qRT-PCR of *bcl2a, sod1* and *sod2* at 6 and 12 mpf was carried out (n=3) (**Figure 3-20A-C**). The *sod1* and *sod2* genes encode cytoplasmic and mitochondrial superoxide dismutases respectively, which are antioxidant enzymes involved in oxidative stress response (325). At 6 mpf, expression of *sod1* and *sod2* were similar to age-matched WT, showing 0.84-fold ±0.10 and 1.03-fold ±0.08 changes respectively. Levels of both genes were elevated at 12 mpf, with a 2.21-fold ±0.08 increase in *sod1* and a 3.04-fold ±0.16 increase in *sod2* expression in *obe*^{td15} fish versus WT. qRT-PCR of *bcl2a,* an apoptosis regulator in the mitochondrial death pathway, showed that expression was increased 1.66-fold ±0.06 at 6 mpf in the mutant versus WT ($p<0.05$), before

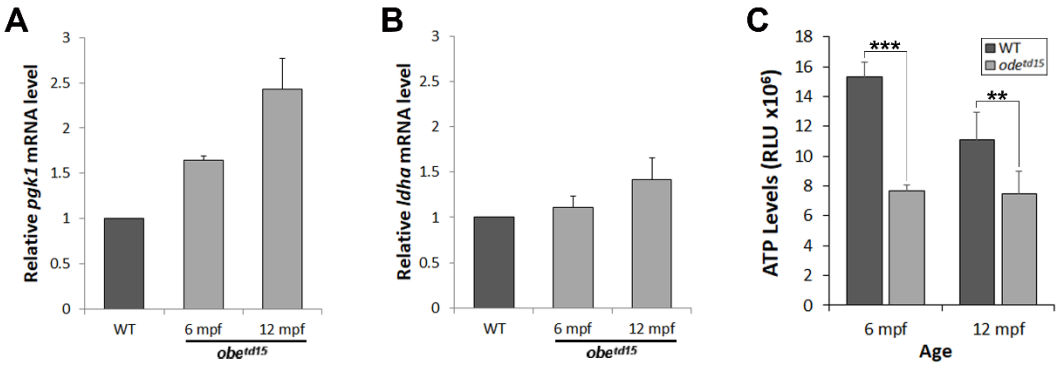

Figure 3-19. Energy metabolism in the *obe*^{td15} retina.
Quantitative RT-PCR was used to determine relative mRNA expression levels of (A) *pgk1* and (B) *ldha* genes at 6 and 12 months post fertilisation (mpf) (n=3 for each age, mean ± SEM). (C) ATP levels (in relative luminescence units, RLU) were examined using a luciferin-luciferase assay in the *obe*^{td15} retina at 6 and 12 months (n=5 for each age, mean ± SEM). **p<0.01, ***p<0.001.

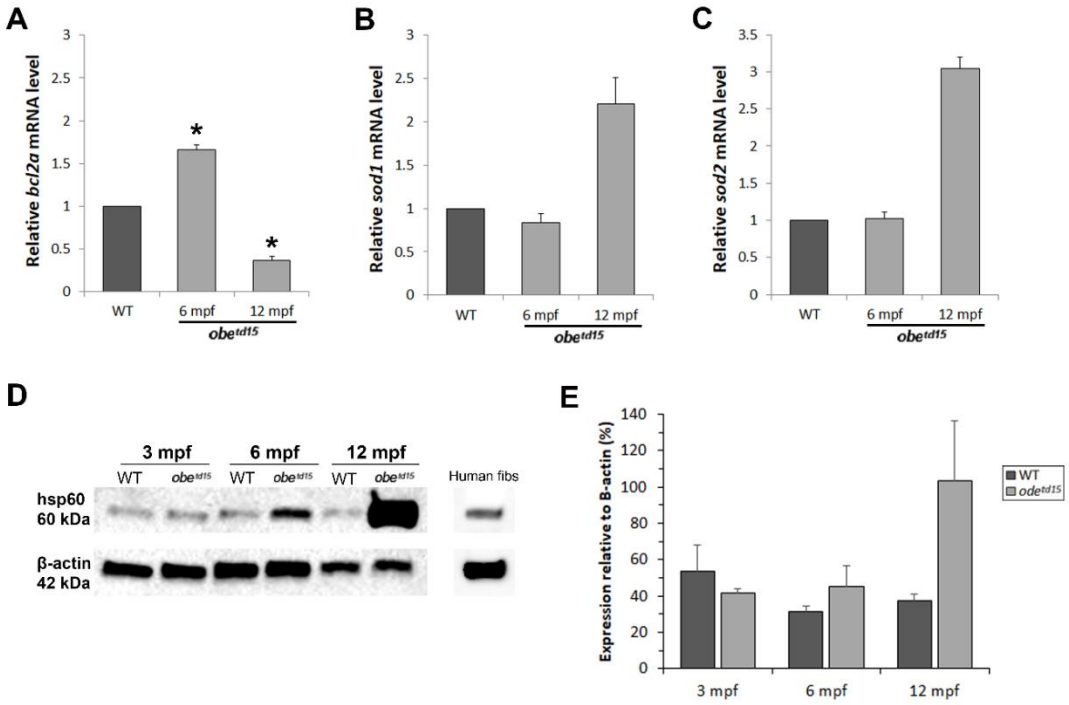

Figure 3-20. Retinal stress in *obe*^{td15} zebrafish.
Quantitative RT-PCR was used to determine relative mRNA expression levels of (A) *sod1*, (B) *sod2* and (C) *bcl2a* genes at 6 and 12 months post-fertilisation (mpf) (n=3 for each age, mean ± SEM). (D) Western blot analysis was used to assess levels of heat shock protein 60 (hsp60) at 3, 6 and 12 mpf. The blot was re-probed with anti-β-actin as a loading control for samples. Bar chart (E) shows mean ± SEM result from three independent experiments. *p<0.05.

showing a decline to 0.36-fold ±0.05 at 12 mpf ($p<0.05$).

To further investigate oxidative stress, a western blot assay was carried out for hsp60, a mitochondrial chaperone involved in stress response (326) (**Figure 3-20D-E**). This revealed comparable levels of protein expression at 3 mpf in WT and *obe*^{td15} RPE and retinal tissue. At 6 and 12 mpf, hsp60 was increased in the mutant by 13.7% and 66.3% respectively.

3.2 Discussion

The Kir7.1 protein is an inwardly rectifying potassium channel linked to two forms of retinal disease, LCA and SVD. Previous mouse work demonstrated the essential function of Kir7.1 in the RPE but was limited by the early lethality of *Kcnj13* homozygous mice (99). Little is known about its role in retinal photoreceptor maintenance and survival. The present study explored the disease pathology using the *obe*^{td15} zebrafish model, which showed a late onset retinal degeneration and visual loss, characterised using both *in vivo* and *ex vivo* assessment. The adult onset disease in these fish allowed investigation of the retinal events that preceded the widespread degeneration, uncovering insightful changes within the retina and RPE.

obe^{td15} zebrafish were originally identified from an ENU mutagenesis screen by their abnormal pigment pattern (101). The *obe*^{td15} mutation was revealed to be a missense change in the *kcnj13* transmembrane helix domain M2, which was found to abolish K^+ conductance (102). In light of findings that *kcnj13* mutations cause early-onset retinal disease in human patients, the previously unexplored *obe*^{td15} retinal phenotype was of interest for investigating the disease pathomechanisms. In the present study, protein sequence comparison showed conservation of the Kir7.1 functional domains between human, mouse and zebrafish sequences and RNAscope confirmed *kcnj13* expression in the zebrafish retina and RPE. Previously, *kcnj13* mRNA has been detected in the retina and RPE tissue in human (78) and mouse (100), however antibody staining showed protein expression specific to the RPE in both species (99, 100, 327). This may also be the case in zebrafish and a zebrafish Kir7.1 antibody (currently available) will be necessary to verify localisation. Alternatively, localisation of fluorescently-tagged Kir7.1 protein (e.g. with GFP) could be examined by injecting a plasmid containing the transgene with a retinal/RPE-specific promoter into the

single-cell stage embryos.

In contrast to the early onset of disease in *KCNJ13* patients, and other LCA zebrafish models that showed developmental phenotypes (93-96), the *obe*^{td15} showed adult onset retinal abnormalities, despite *kcnj13* being expressed from the developmental stages. Both SD-OCT and histological examination revealed retinal thinning and cone cell loss at 12 mpf, while the optokinetic response tests verified functional changes in vision, which could be further investigated using more informative methods such as ERG. Although red cone loss and severe disruption to the cone mosaic organisation was observed in *obe*^{td15} fish, apoptosis was not detected in the retina using TUNEL assays. This may indicate that the retinal degeneration occurs rapidly and unpredictably, and the majority of apoptosis is complete at 12 mpf when widespread destruction is apparent. Testing several timepoints in between 6 and 12 mpf may be necessary to determine the point at which vast retinal cell death occurs. Furthermore, to verify that the TUNEL technique is working, an adult zebrafish retina with an ouabain-induced retinal degeneration could be used as a positive control. Obtaining additional cone opsin antibodies i.e. blue, UV, will also be of interest to examine whether cone subtypes are differentially affected in the *obe*^{td15} retina.

Interestingly, SD-OCT imaging revealed irregular retinovascular changes in the *obe*^{td15} zebrafish at 12 mpf, which have not been noted in *KCNJ13*-related LCA previously (81, 84, 85). However, two brothers from one of the two unreported unrelated families with the same p.Thr153Ile homozygous mutation exhibited extensive vasoproliferative responses in their late teens similar to the changes seen in the zebrafish. This missense change was located in the M2 helix domain coding region of *KCNJ13, c*onsistent with the mutation harboured by *obe*^{td15} fish. The patients' retinovascular abnormalities were unlike vasoproliferative tumours, Coats-

like retinopathy or the SVD phenotype. However, these novel findings suggest that SVD may lie on a clinical spectrum. The variability of the clinical phenotype may be dependent on the position of the mutation in the gene as well as from other modifying genetic factors. For younger affected individuals who share the same mutation, regular monitoring would be recommended for early detection and management, especially since the progression of fibrovascular proliferation was relatively rapid.

These findings suggest that retinovascular changes may be another factor contributing to the *KCNJ13* disease pathology. Pathological vascular growth is observed in other ocular diseases, such as retinopathy of prematurity, diabetic retinopathy, and wet age-related macular degeneration (328). For instance, in diabetic retinopathy, vessel swelling and abnormal growth of new vessels on the retinal surface is associated with metabolic and oxidative stress (329). Patients with RP also occasionally develop Coats-like exudative vasculopathy, characterised by telangiectatic retinovascular abnormalities and extravascular lipid depositions (330). The system of the vascular endothelial growth factor (VEGF) and its receptors plays an important role in pathological ocular angiogenesis, and anti-VEGF agents have been used to treat disorders driven by this process (331). Investigating changes in the expression of these factors and related genes or proteins in the *obe*^{td15} zebrafish will be necessary to determine their involvement in the observed vascular alterations.

In addition to changes in vessel structure, SD-OCT highlighted fibrous material and hyperreflective deposits present in the vitreous surrounding the vessels. The identity of these formations is unknown, and they may or may not be related to the vasculature. Previously, abnormal deposits have been noted on retinal examinations of *KCNJ13* patients; crystalline deposits in the retina and fibrillar degeneration of the vitreous are characteristic in patients with SVD (322), and hyperreflective formations

in the retina were described in an LCA patient, which were thought to be pigment deposits (85). Further investigation is necessary to determine if these structures observed on *obe*^{td15} zebrafish retina are related to those viewed on clinical images.

As obvious changes in gross retinal structure were not notable until 12 mpf, the *obe*^{td15} RPE ultrastructure was examined to look at alterations that may contribute to the degeneration. The RPE plays an essential role in the maintenance of photoreceptors, exchanging nutrients, ions and waste products, phagocytosing shed outer segments and recycling photopigment for the visual cycle (9). In addition, melanosomes in the RPE serve to reduce harmful back-scattered light and remove free radicals produced during these processes. Electron microscopy of the *obe*^{td15} zebrafish RPE revealed changes to the phagosome clearance, mitochondrial number and melanosome movement not previously described. In fish and amphibians, the melanosomes of the RPE exhibit a dramatic redistribution from the basal cell body into the apical processes upon the onset of light, which is reversed in the dark (29). Melanosomes in the mammalian RPE also show modest movement during the light cycle (332). It was found that in dark-adapted *obe*^{td15} fish, the melanosomes were shown to have a more basal aggregation within the RPE cells, indicating an increased motility of these mutant organelles in the absence of light. This relates to previous findings that Kir7.1 is involved in regulating melanosome distribution in the melanophores of the zebrafish skin, resulting in a distinct stripe pattern (102). Defects in melanosome movement have been associated with several human retinal diseases, such as Usher syndrome (243) and choroideremia (38) and this may also be a contributing factor to retinal dysfunction in *obe*^{td15} zebrafish and patients with *KCNJ13* mutations.

Phagosome clearance was an additional process found to be affected in the *obe*^{td15} zebrafish RPE. Daily, the RPE phagocytoses portions of the photoreceptor outer

segments and the resulting phagosomes are required to move from the apical to the basal region in order to mature and acquire the capacity to fuse with lysosomes for degradation (30). In *obe*^{td15} fish at 3 and 6 mpf, there was an increased accumulation of phagosomes in the RPE cells, suggesting that phagosome processing may be disrupted. As the Kir7.1 expression has been localised to the apical RPE (333), the membrane involved in phagocytosis, it is feasible that this protein may play a part in the process. Defects in phagocytosis and phagosome degradation by the RPE are associated with several negative outcomes, such as lipid accumulation, oxidative stress and mitochondrial dysfunction (31-34), and have been found in models of other retinal diseases including age-related macular degeneration (35, 36), Usher syndrome (37) and choroideremia (38, 39). Considering that significant alterations in phagosome clearance were seen by 3 mpf, preceding other notable mitochondrial changes, it is proposed here that the retinal disease in this model is primarily a failure of RPE phagosome physiology with a secondary mitochondrial dysfunction. Phagosome abundance was similar to WT at 12 mpf, which may reflect a different disease phase i.e. gliosis of the retina at this point.

One of the most striking changes observed in the *obe*^{td15} RPE was the vast mitochondrial expansion noted at 6 and 12 mpf, in which significant increases in both mitochondrial number and size were found along with upregulation of *polg2,* an indicator of mitochondrial number, and several other mitochondria-related genes. The outer retina has the greatest metabolic demand in the body, owing largely to the photoreceptor activity, and the RPE has an enriched mitochondrial population to meet the high-energy needs of these cells to ensure function and survival (40). The main role of mitochondria is to provide energy in the form of ATP, in addition to numerous other tasks which include regulation of apoptosis stress response pathways and calcium levels. These organelles are not static and are known to respond to the

energetic needs of their environment. The observed changes in mitochondrial biogenesis in the mutant RPE which precede retinal degeneration may be a compensatory response to unmet energy demands or retinal stress caused by Kir7.1 channel dysfunction. The finding that ATP levels were significantly reduced at 6 and 12 mpf supports this, and also suggests an impairment of mitochondrial function in the mutant retina as there is insufficient ATP production despite their expansion.

Furthermore, glycolysis and anaerobic respiratory cycle genes (*pgk1* and *ldha* respectively) were upregulated in the *obe*^{td15} retina which may reflect a possible feedback loop in which these genes are upregulated in response to reduced cellular energy levels from insufficient mitochondrial aerobic metabolism. The presence of senescent or dysfunctional mitochondria has been found to lead to a metabolic shift from aerobic respiration to glycolytic metabolism resulting in expression changes of the lactate dehydrogenase genes (334). The finding that both genes were most upregulated compared to WT at 12 mpf may be related to levels of metabolic and/or oxidative stress.

In addition to increased abundance, mitochondria in the *obe*^{td15} RPE were greater in size than WT and expanded with age. In several systems, it has been shown that mitochondrial morphology can show changes in size, shape and membrane organisation as a result of ageing or stress. Enlarged mitochondria are typically a sign of pathology and have been found in ageing or dysfunctional cells (335), including muscle (336, 337), cardiomyopathy (338) and by forced senescence in culture (339). In the murine RPE, metabolic or oxidative stress resulted in the formation of large mitochondria produced by activation of the P13/AKT/mTor signaling pathway (340). From the present data, a decrease in mitochondrial size with age appears to be the

normal progression in WT zebrafish, which has also been observed in human RPE cells (341, 342).

To explore whether the abnormal growth in the *obe*^{td15} retina may be related to alterations in the mitochondrial dynamics, the expression of *fis1* and *opa1* was investigated as indicators of fission and fusion, respectively. Mitochondria are able to use these processes in response to metabolic or environmental stress (343). Fusion supports mitochondrial function by mixing contents of partially damaged mitochondria and is stimulated by energy demand and stress, while fission creates new mitochondria and removes those that are damaged. *opa1* and *fis1* were both upregulated at 6 mpf in the mutant retina, albeit significantly for *opa1* only, which may reflect an attempt to compensate for elevated stress and energy demands at this time point and may also contribute to the observed morphological changes. Large mitochondria are autophagocytosed less readily than small ones (336), also potentially causing oversized organelles to accumulate in the mutant. Alternatively, large mitochondria with higher ATP production, known as mega-mitochondria, have been previously described in the zebrafish photoreceptor inner segment ellipsoid (41, 42). It has been found that during development these mitochondria are able to enlarge independently of the fusion process. Although not described in RPE, it could be possible that the mitochondria of *obe*^{td15} fish may enlarge via a similar process to create larger organelles with elevated ATP activity as a compensatory response. Further experimentation will be necessary to determine this. It should be noted that the mitochondrial changes observed in the RPE ultrastructure may not reflect the retina as a whole and the qRT-PCR data may be affected by an inability to completely isolate specific layers; the use of precise techniques, e.g. laser capture microdissection or fluorescence-activated cell sorting, may provide more accurate data in future investigations.

As the mitochondrial alterations in the mutant were indicative of retinal stress events preceding degeneration, the expression of several genes and proteins associated with stress response pathways was examined. At 6 mpf, activation of the Müller cells became apparent through increased expression of GFAP through their retinal processes, a characteristic sign of retinal injury or stress (324). Depleted ATP levels, also noted at 6 mpf, are associated with metabolic and oxidative stress and even moderate reductions have been found to significantly contribute to oxidative stress in RPE cells (32, 344). hsp60 is a highly conserved mitochondrial chaperone that assists protein folding and facilitates proteolytic degradation of denatured proteins and is typically upregulated in response to mitochondrial stress (326). It was found that hsp60 expression was robustly increased at 6 and 12 mpf in the *obe*^{td15} retina. Previously, a premature decline in ATP associated with changes in hsp60 expression was found in the *Cfh*$^{-/-}$ mouse model of retinal degeneration, preceding the phenotype development (345). The expression of an additional stress-related gene *bcl2a* was investigated, which was found to be significantly upregulated at 6 mpf in the *obe*^{td15} retina. This gene is orthologous to *BLC2*, an anti-apoptosis suppressor known to facilitate mitochondrial DNA repair and support cell survival (346). Overexpressing *BCL2* or using compounds that cause its upregulation has been shown to inhibit retinal cell death in several rodent models (347-351) and cellular models (346, 352, 353). Increased expression at 6 mpf in the mutant retina may be a protective response to a stressed environment and contributes to the preservation of retinal structure at this time point.

To investigate oxidative stress, the expression of antioxidant enzymes *sod1* and *sod2* was assessed as a proxy measure of reactive oxygen species (ROS) levels, which were found to be upregulated at 12 mpf in the *obe*^{td15} retina. ROS are generated as by-products of the electron transfer chain and build up can compromise mitochondrial

function by damaging their DNA, implicating mitochondria as both generators and targets of oxidative stress. Elevated levels of ROS in the retina can be induced by environmental factors such as blue light (354) and are associated with ageing and disease (355). Increased expression in the *obe*^{td15} retina at 12 mpf may be a consequence of prolonged mitochondrial dysfunction causing an accumulation of ROS, which may in part trigger widespread degeneration. Additionally, at 12 mpf, a downregulation of *bcl2a* expression was observed, which has been previously reported in oxidative stress-associated retinal cell death (356-359). VEGF has been found to be upregulated in response to oxidative stress (329), which could account for the vascular changes that also occur in the retina *obe*^{td15} retina at this point; further work will be necessary to determine this. Overall, evidence suggests that oxidative stress plays a role in the Kir7.1 pathophysiology.

Several features observed in the *obe*^{td15} retina, such as reduced ATP and oxidative stress, are typically associated with impaired mitochondrial function, one of the hallmarks of ageing (360) and therefore this implicates an altered rate of ageing in this model. This has been found to underlie several age-related neurodegenerative disorders, including Alzheimer's (361), Parkinson's disease (362), age-related macular degeneration, diabetic retinopathy and glaucoma (43). The free radical theory of ageing proposes that the progressive mitochondrial dysfunction that occurs with ageing results in increased production of ROS which in turn causes further mitochondrial deterioration and global cellular damage (360). The elevated metabolic activity and extensive mitochondrial population in the retina and RPE make these tissues particularly vulnerable to these processes, which may be a common mechanism preceding many types of retinal degeneration. Several therapeutic strategies, such as the use of near infrared light (363) or PEDF (357) have shown promise in supporting mitochondrial function in the retina/RPE and may be effective

across a range of disorders, including *KCNJ13*-related retinal degeneration.

Future investigation into Kir7.1 channel function in the zebrafish, using techniques such as patch clamp electrophysiology or ERG, and establishing protein localisation in the retina should aid in shedding light on how Kir7.1 dysfunction induces the various pathological changes observed *obe*^{td15} retina. Potential defects in phagosome processing can be further explored by examining the RPE at multiple timepoints after the onset of light, and immunostaining for early and late phagosome/lysosome markers. Establishing subcellular localisation of Kir7.1 within the RPE, potentially through the use of immunogold labelling on TEM sections, may reveal whether or not the channel is associated with the mitochondrial membranes; this will give more insight into whether the mitochondrial alterations are a primary and secondary dysfunction in this model. The qRT-PCR and ATP data gives limited information on mitochondrial function and damage, which could be further investigated using Seahorse XF analysis and direct measures of ROS and mitochondrial DNA mutations. The late retinal vascular changes seen in the *obe*^{td15} retina are another intriguing feature to explore, which will be examined further in *obe*^{td15} fish crossed with Tg(*fli1a*:GFP), a transgenic line expressing a vascular-specific fluorescent marker.

In summary, longitudinal analysis of the *obe*^{td15} zebrafish retina has been valuable in providing novel insight into disorders caused by Kir7.1 dysfunction, which in this model was characterised by a severe degeneration associated with alterations in the retinal vasculature and activity of phagosomes and mitochondria the zebrafish RPE. The phagosome and mitochondrial changes preceded retinal degeneration, highlighting these organelles as potential therapeutic targets for *KCNJ13*-related disease. Establishing whether similar changes are seen in patient iPSC-derived RPE cells harbouring *KCNJ13* mutations will be an essential next step. The late vascular

changes seen in zebrafish and humans suggest more closer surveillance is required and further work is necessary to understand the vasoproliferative effect seen in some forms of severe retinal degeneration.

4 *USH2A* in the zebrafish

4.1 Results

4.1.1 Structure and conservation of *ush2a* in the zebrafish

According to the Ensembl genome browser GRCz11 assembly (European Bioinformatics Institute), full length zebrafish *ush2a* (transcript ID. ENSDART00000086201.5) is a 72 exon (15711 bp) gene producing the 5236 aa transmembrane protein, usherin (**Figure 4-1**). The *ush2a* gene is not duplicated in the zebrafish genome. Zebrafish usherin is comparable in size to the human and murine full length orthologues, which produce usherin long isoforms of 5202 and 5193 aa in size, respectively. Using NCBI BLASTP, the amino acid sequence of zebrafish usherin was compared with the human and mouse orthologue sequences. The alignments revealed that the zebrafish protein is 52% identical to the human and 49% identical to the mouse sequences. Using UniProtKB (UniProt Consortium) and SMART (EMBL) to examine conserved domains in zebrafish usherin, it was found to possess the same motif arrangements, with a large extracellular domain consisting of laminin globular domains, N-terminal laminin domains, laminin-type epidermal growth factor-like domain (LamEGF), numerous fibronectin III repeats, a membrane-spanning region and a PDZ-binding C terminus. Therefore, zebrafish *ush2a* is structurally highly conserved and likely to be functionally conserved as well.

4.1.2 *ush2a* expression in WT zebrafish

Developmental expression

Using RT-PCR to examine temporal gene expression, *ush2a* mRNA transcripts were detected in whole zebrafish embryos from 48 hpf onwards and in the enucleated eyes of juvenile and adult zebrafish between 28 dpf and 12 mpf (oldest timepoint

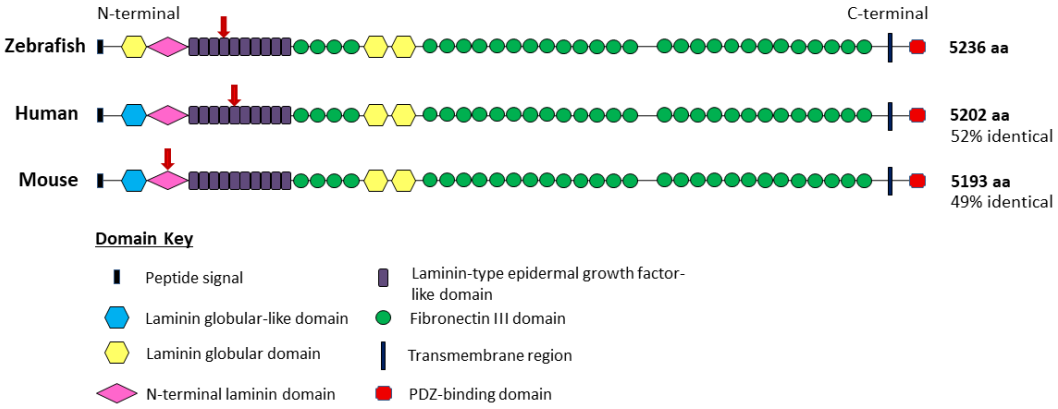

Figure 4-1. Structural conservation of the zebrafish usherin protein.
Comparison of zebrafish usherin with the human and mouse orthologues show similarity in size (amino acids, aa) and structure, demonstrating the conserved motif arrangement between the proteins. NCBI BLASTP alignments were used to analyse homology between the proteins. The red arrows indicate the following: the region of zebrafish *ush2a* targeted using CRISPR/Cas9 in this study; the location of the most common Usher syndrome mutation on human *USH2A* (p.Glu767Serfs); the location of the mutation in the *Ush2a*$^{-/-}$ mutant mouse previously characterised (165).

examined) (**Figure 4-2A, B**). Digoxygenin-labelled RNA probes were produced from the RT-PCR product to examine spatiotemporal expression of *ush2a* using wholemount *in situ* hybridisation in zebrafish embryos (**Figure 4-2C, D**). At 48 hpf, *ush2a* transcripts were detected specifically in the developing eye and ear organs using the antisense probe while the control sense probe showed no specific staining.

Usher 2 gene expression in the adult retina

The RNAscope fluorescent *in situ* assay was used to examine the expression pattern of the three Usher syndrome 2 gene orthologues, *ush2a, gpr98* and *dfnb31a*, in the adult WT zebrafish retina (**Figure 4-3A-E**). Using this assay, individual mRNA transcripts were visualised as spots of fluorescence. Expression in the ONL and photoreceptor inner segments was detected for all three genes. For *ush2a*, expression was exclusive to the ONL/photoreceptors in the retina. While *gpr98* was found to be most strongly expressed in the ONL, transcripts were also detected in the INL. *dfnb31a* expression was the most weakly detected of all the three genes and was localised to the ONL/photoreceptors and INL. The *odc1* positive control probe was detected in all layers except the IPL. The *dapB* negative control probe showed no fluorescence, indicative of absent gene expression. Overall, the spatiotemporal gene expression patterns suggested that *ush2a* expression is well conserved in zebrafish.

Usher 2 gene expression in the zebrafish hair cells

Expression of *ush2a, gpr98* and *dfnb31a* was detected on 6 dpf WT zebrafish inner ear and neuromast sections using the RNAscope assay (**Figure 4-3F-K**). Expression of all three genes was found to be concentrated in the anterior macula of the inner

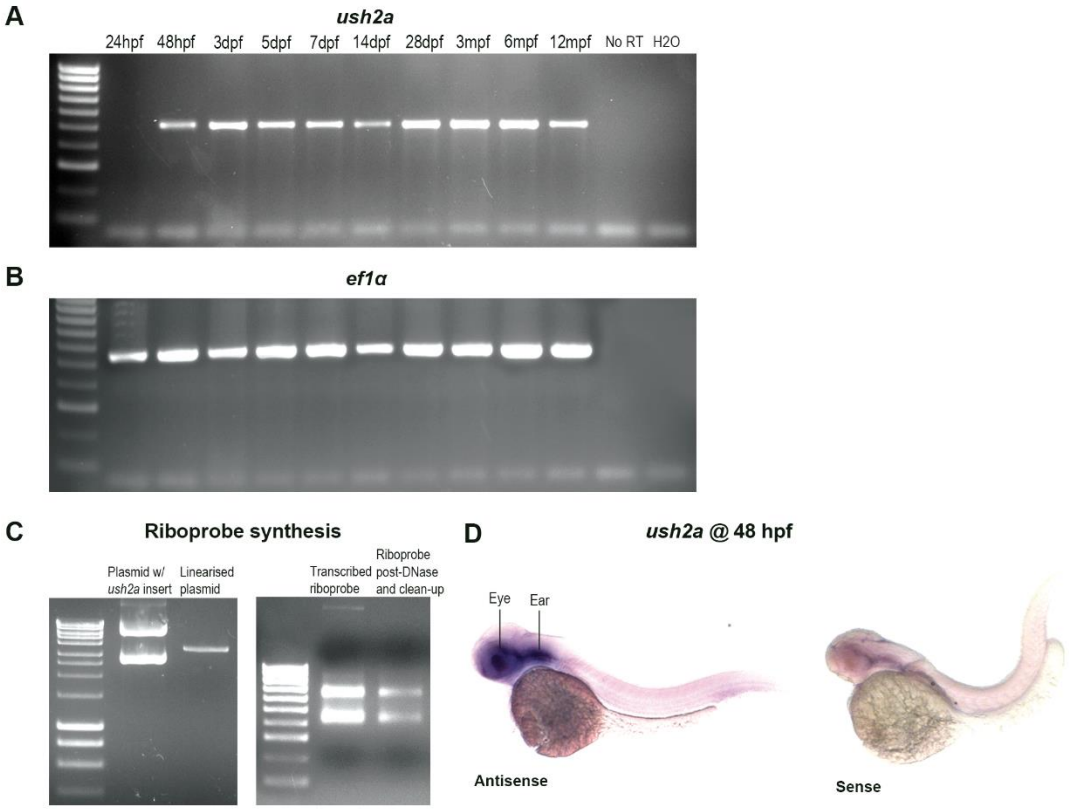

Figure 4-2. Spatiotemporal expression of *ush2a* in the zebrafish.
(A) *ush2a* mRNA expression was detected in whole wild-type zebrafish from 48 hours post-fertilisation (hpf) and in zebrafish eyes from 28 days post-fertilisation (dpf) to 12 months post-fertilisation (mpf). (B) ***ef1α*** expression was used as a control gene. (C) To produce the *in situ* hybridisation probes, the 520 base pair *ush2a* RT-PCR product was cloned into a vector with flanking T7 and SP6 promoters. Using linearised plasmid as a template, T7 or SP6 transcription was used to produce the antisense and sense riboprobes. (D) The *ush2a* antisense riboprobe shows specific eye and ear staining in the wholemount 48 hpf zebrafish embryos. The sense probe did not show strong specific staining.

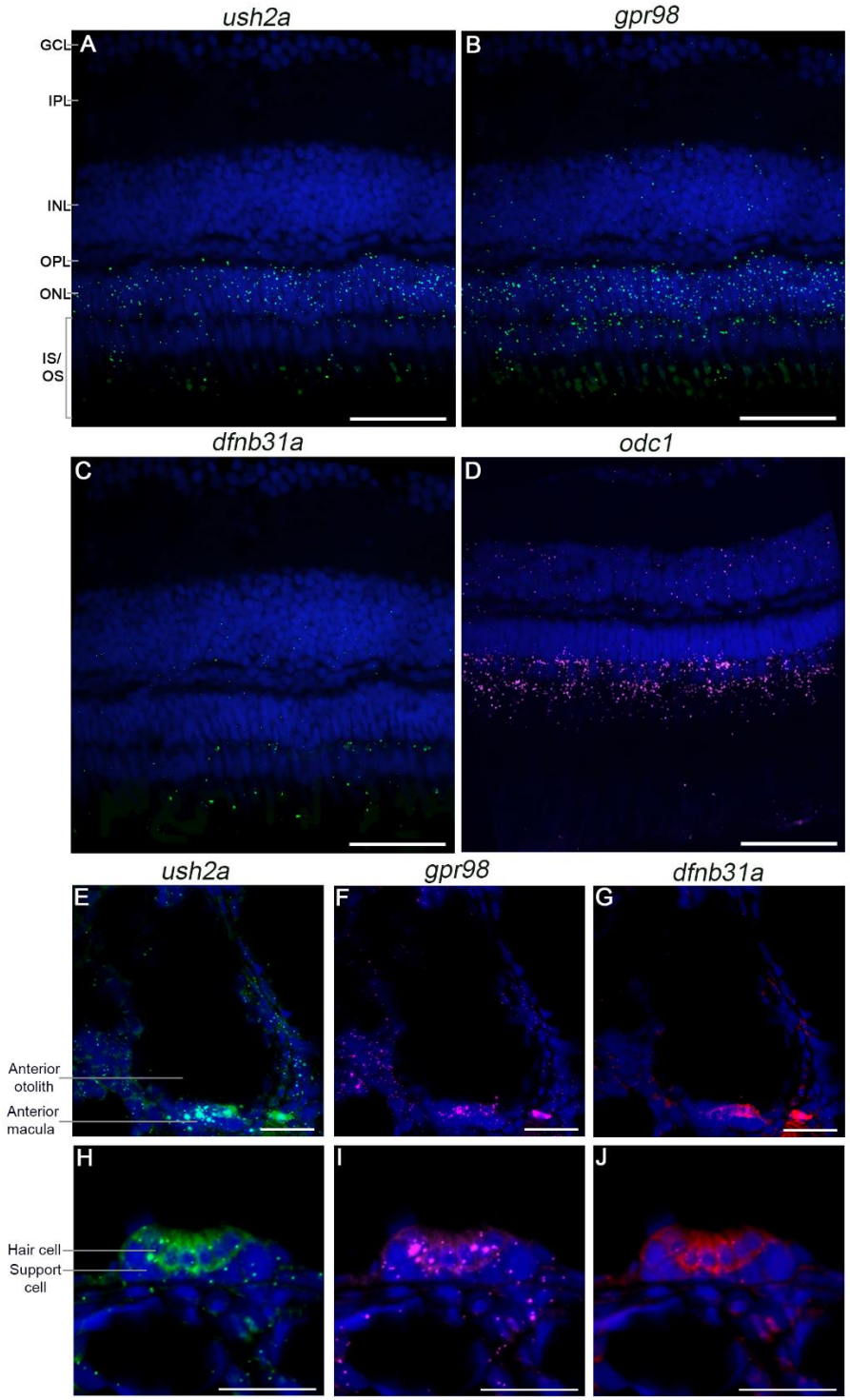

Figure 4-3. Expression of the Usher 2 genes in the zebrafish retina and hair cells. The RNAscope assay was used to detect mRNA expression of the following Usher 2 gene orthologues in the wild-type adult retina: *ush2a* (A), *gpr98* (B) and *dfnb31a* (C) (all shown as green). *odc1* (magenta) was used as a positive control (D). Expression of *ush2a* (green) *gpr98* (magenta) and *dfnb31a* (red) was detected on inner ear (E-G) and neuromast (H-J) transverse sections from wild-type zebrafish at 6 days post-fertilisation. DAPI nucleic acid stain was used as a counterstain (blue). GCL, ganglion cell layer; IPL, inner plexiform layer; INL, inner nuclear layer; OPL, outer plexiform layer; ONL, outer nuclear layer; IS/OS, inner/outer segments. Scale bars = 50 µm (A-E) and 25 µm (F-K).

ear and the hair cells of the neuromast.

4.1.3 Mutagenesis of *ush2a* in the zebrafish

CRISPR/Cas9-mediated mutagenesis was used with the aim of disrupting the *ush2a* gene by inducing indel mutations at a chosen target site and ultimately leading to the production of a zebrafish *ush2a*-null mutant line. In human patients, a range of different mutations identified throughout the whole length of the gene have been found to cause Usher syndrome, although the presence of two truncating mutations is associated with Usher syndrome and not isolated RP (207, 208). According to the Ensembl Zv9 assembly, there are three predicted protein-coding *ush2a* transcripts in the zebrafish, one of which does not include the first 10 exons. Taking this into consideration, the sgRNA was designed to target a sequence within exon 11, which codes for a relatively well conserved region (79% identical between human and zebrafish protein sequence) forming part of a LamEGF domain. Subsequent to the original sgRNA design, the zebrafish GRCz11 genome assembly has been released which predicts two protein-coding transcripts for the *ush2a* gene; a full length isoform including exon 11 and a very short transcript which if translated would produce a protein of only 117 aa.

To assess the mutagenesis efficiency of the chosen sgRNA, the DNA of 11 embryos co-injected with Cas9 mRNA and sgRNA (and one un-injected) was collected at 24 hpf and Sanger sequenced (**Figure 4-4**). The sequencing trace of 9 of the 11 embryos (viewed using SnapGene Viewer, GSL Biotech) indicated the presence of induced mutations (multiple amplicons) at the PAM site and target sequence. This indicated that the generated sgRNA was an effective guide for Cas9-mediated mutagenesis in

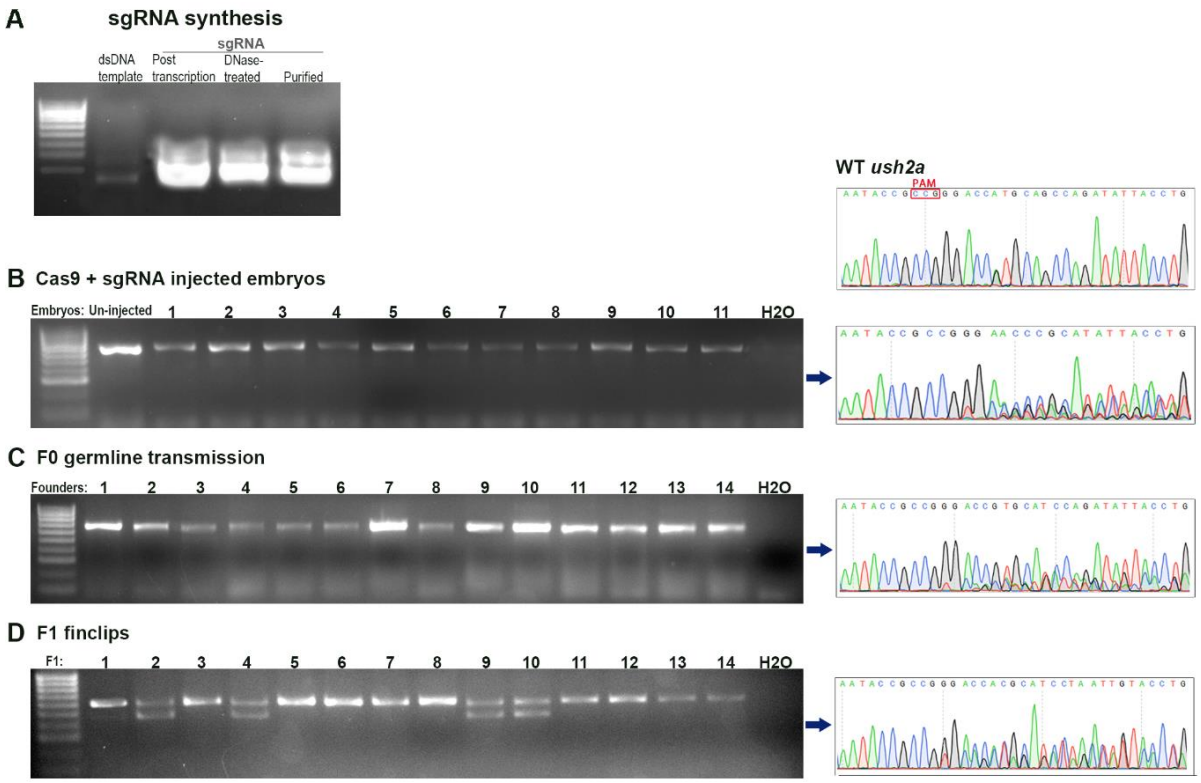

Figure 4-4. CRISPR/Cas9 mutagenesis of *ush2a* in the zebrafish.
(A) sgRNA was transcribed in *vitro* from a double-stranded DNA (dsDNA) template produced by annealing single strand oligonucleotides, which were designed for the targeting of exon 11 of *ush2a*. The presence of mutations was analysed by PCR amplification of a 652 bp DNA sequence containing the CRISPR target region followed by Sanger sequencing of (B) Cas9 mRNA and sgRNA-injected embryos collected at 24 hpf, (C) pooled 24 hpf embryos produced by founder and wild-type breeding (assessment of germline transmission) and (D) finclips from F1 generation adult fish. The Sanger sequencing traces shown are examples of those where mutations were detected. The protospacer adjacent motif (PAM) is highlighted in red on the *ush2a* wild-type (WT) sequence.

this region.

Embryos injected with Cas9 and sgRNA were raised to adulthood (~3 months) and were individually bred with WT zebrafish to assess the presence of germline mutations. For each founder, extracted DNA from 10 pooled embryos was PCR-amplified and analysed through Sanger sequencing. Of 14 founder fish examined, 5 were found to transmit mutations to their embryos. Three of the transmitters were outcrossed with WT to produce the F1 generation, which were finclipped when they reached maturation. Finclip DNA was PCR-amplified and Sanger sequenced to identify heterozygous mutation carriers.

In the heterozygous F1 fish, mutagenic lesions were inferred from the Sanger sequencing traces. 7 different mutations were identified, which included two in-frame deletions (6 bp) and 5 frameshift mutations (**Figure 4-5**). Carriers of the following two *ush2a* mutations were outcrossed with WT fish: a 4 bp deletion (c.2137_2141delACCG p.Thr713Cysfs), and a larger 140 bp lesion resulting from deletion of a portion of exon 11 and the corresponding intron, and a 6 bp insertion (c.2131_2203+73delinsCGGCGG p.Ala711Argfs). Both mutations are predicted to cause frameshifts, leading to premature termination codons. If translated, the usherin protein is predicted to be severely truncated, with loss of LamEGF, laminin globular, fibronectin III, transmembrane and PDZ-binding domains, most likely rendering it non-functional. The resulting F2 generation, a mix of WT and heterozygous fish, were finclipped and sequenced upon maturation. Individuals identified as heterozygous were incrossed with fish carrying the same mutation. For each mutant allele, 25% of the resulting F3 progeny were homozygous and viable. The *ush2a* line with the mutation c.2131_2203+73delinsCGGCGG p.Ala711Argfs was used for subsequent breeding and phenotyping (hereafter referred to as *ush2a* zebrafish). Homozygous

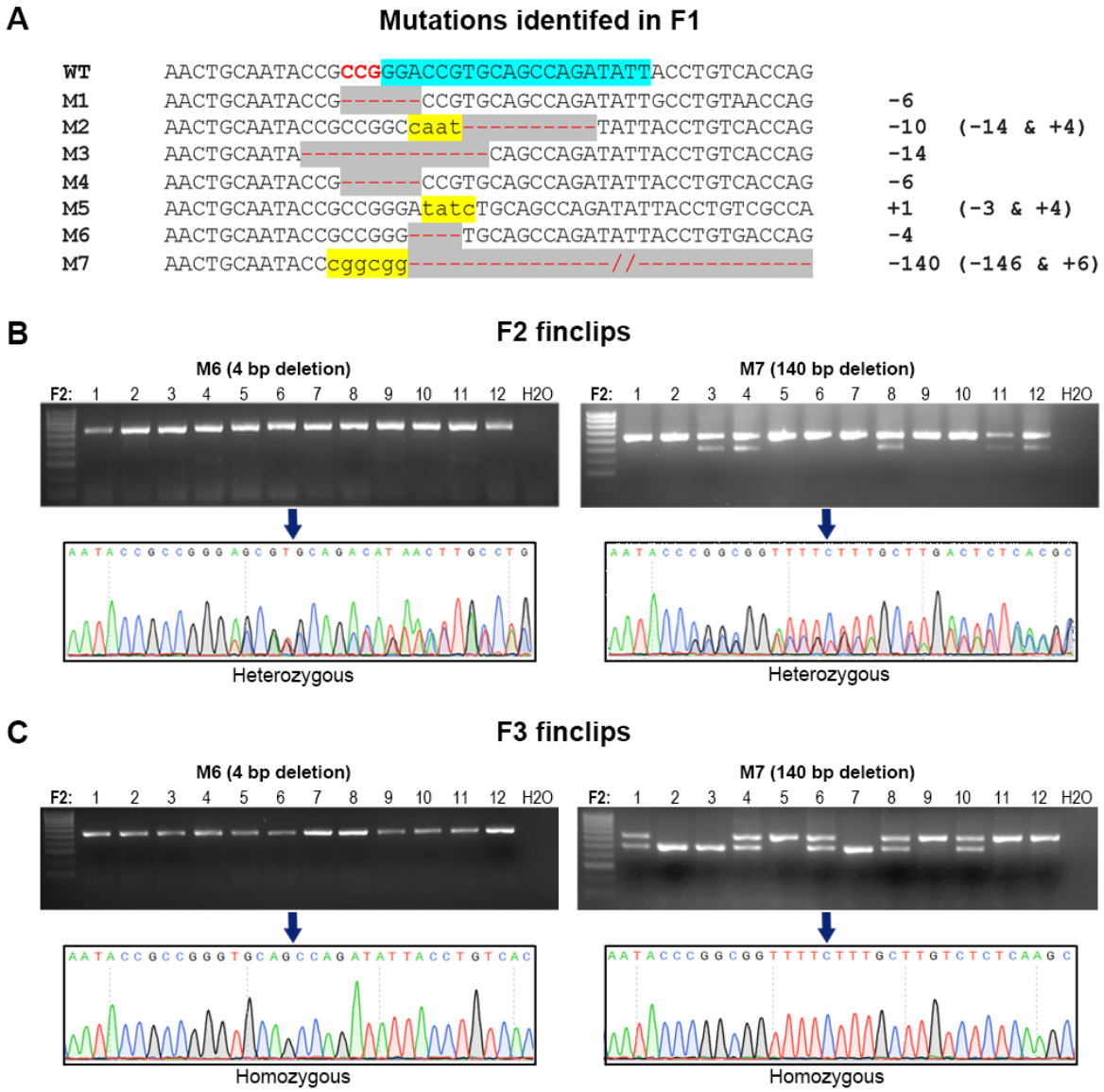

Figure 4-5. Identification of *ush2a* mutant alleles.
(A) DNA from F1 adult finclips was Sanger sequenced and *ush2a* mutations were inferred from heterozygous fish. Seven different mutant alleles were identified. On the wild-type sequence, the protospacer adjacent motif (PAM) is in red and the target sequence is highlighted in blue. (B) Carriers of two different mutations, a 4 base pair (bp) deletion and a 140 bp deletion, were outcrossed with wild-type fish. F2 heterozygous fish were identified from finclip sequencing and carriers of the same mutation were incrossed. (C) The F3 homozygous fish were identified from finclip sequencing.

ush2a zebrafish were compared to their age-matched WT siblings (*ush2a*$^{+/+}$).

4.1.4 General morphology and retinal histology of *ush2a* zebrafish

ush2a zebrafish showed overall normal development with a body morphology comparable to that of WT in the larval and adult stages (**Figure 4-6**). The size and shape of the developing inner ear organs (saccule and utricle otoliths) appeared to be typical in the *ush2a* larvae at 6 dpf. Eye shape, size and pigmentation (iridophores) were normally formed in the larval and adult mutant zebrafish. The adult *ush2a* zebrafish were viable, fertile and similar to WT in body size. To assess changes in *ush2a* expression in the mutant zebrafish, the RNAscope assay was applied to the adult *ush2a* retina (**Figure 4-7**). The mutant retina exhibited notably reduced levels of *ush2a* probe fluorescence in the ONL/photoreceptors compared to WT, suggesting that *ush2a* mRNA has been subject to nonsense-mediated decay due to the CRISPR-induced mutation. The WT and *ush2a* retinas showed similar levels of positive control expression.

The retinal morphology of *ush2a* zebrafish at different ages was examined using histological evaluation (**Figure 4-8**). Transverse retinal sections revealed normal formation of all retinal layers in the mutant at 8 dpf and 1 mpf. From 3 mpf to 12 mpf, the adult retinal morphology of *ush2a* fish showed no gross abnormalities compared to WT.

Retinal thickness and cone mosaic organisation in ush2a zebrafish

Longitudinal live imaging of the *ush2a* retina from 3 mpf to 12 mpf using SD-OCT showed general preservation of retinal structure and distinguishable layers at all ages (**Figure 4-9**). Measurement of mean retinal thickness (GCL-ELM) from SD-OCT

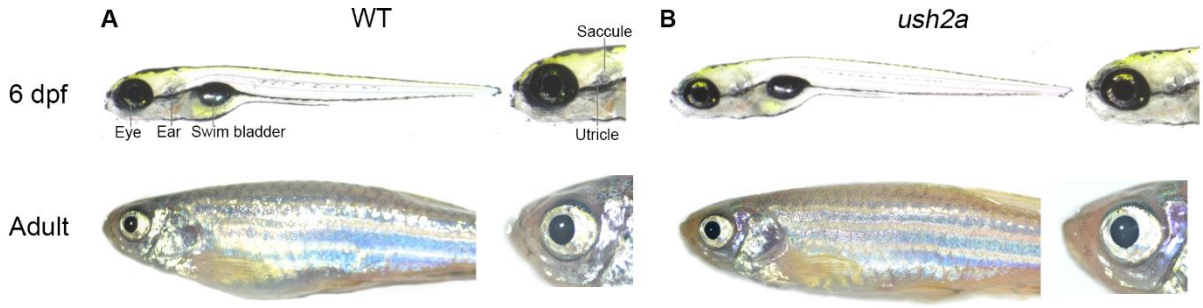

Figure 4-6. Wholemount morphology of *ush2a* zebrafish.
Comparison of general wholemount morphology of wild-type (A) and *ush2a* (B) zebrafish at 6 days post fertilisation (dpf) and in adulthood. *ush2a* zebrafish have a normal appearance at both timepoints.

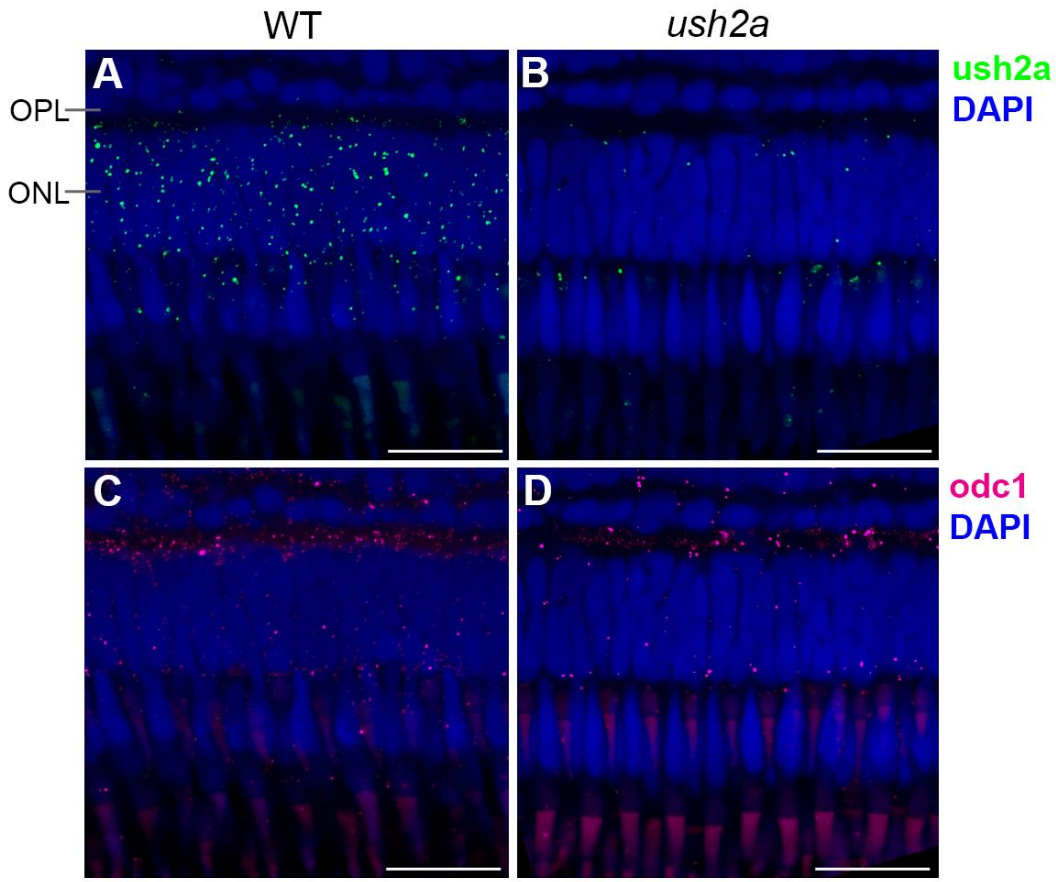

Figure 4-7. Expression of *ush2a* in the adult mutant retina.
The RNAscope fluorescent *in situ* assay was used to compare *ush2a* mRNA expression in the adult retinas of wild-type (WT) (A) and *ush2a* (B) fish (n=2). Notably less *ush2a* transcripts were detected in the mutant retina. The positive control *odc1* showed similar expression levels in both (C, D). DAPI nucleic acid stain was used as a counterstain (blue). OPL, outer plexiform layer; ONL, outer nuclear layer. Scale bar = 25 µm.

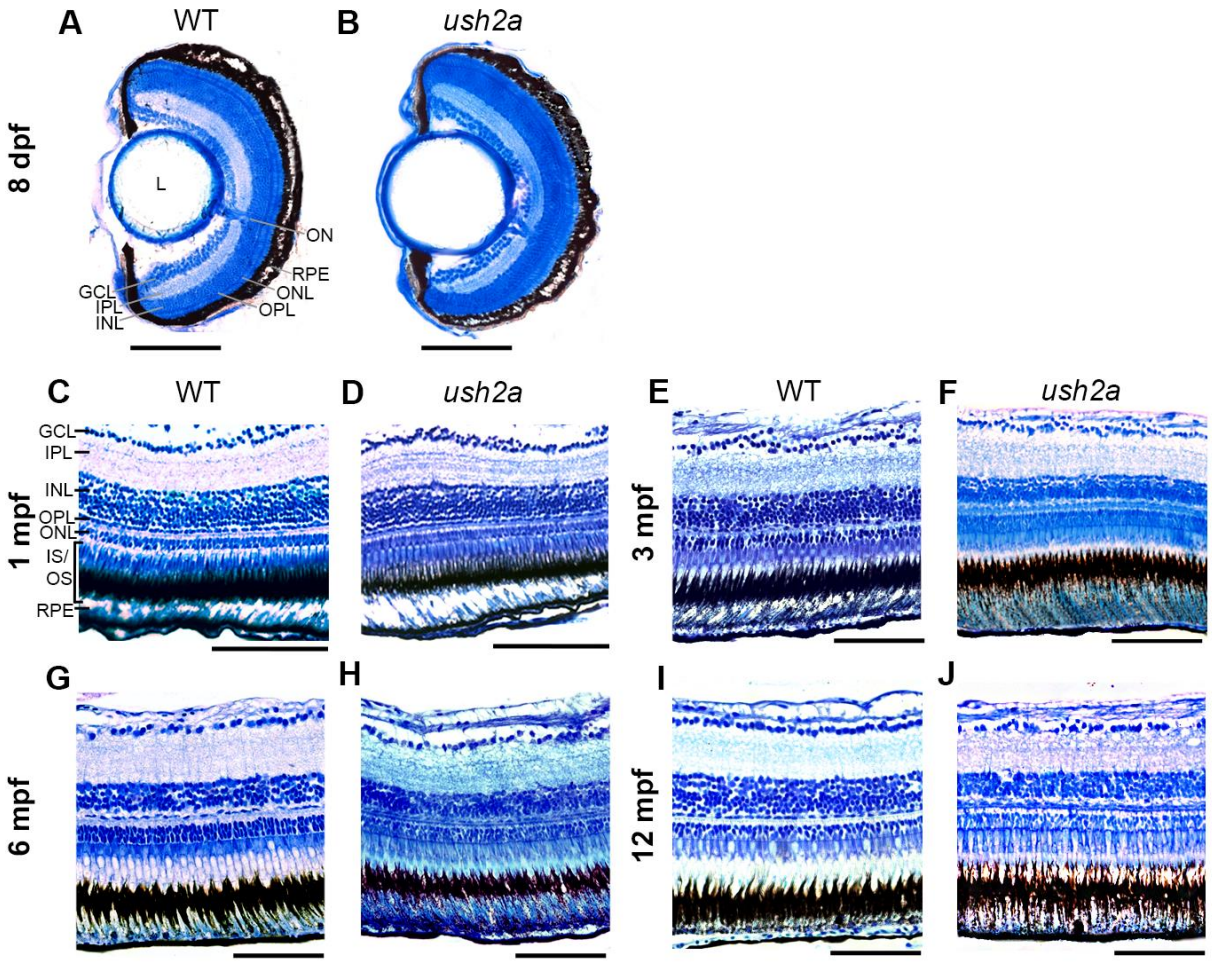

Figure 4-8. Retinal histology of *ush2a* zebrafish.
Transverse retinal sections with optic nerve were stained with 1% toluidine blue to compare wild-type (WT) and *ush2a* retinas at 8 days post fertilisation (dpf) (A, B), 1 month post fertilisation (mpf) (C, D), 3 mpf (E, F), 6 mpf (G, H) and 12 mpf (I, J). Representative sections are shown from two retinas per timepoint for WT and mutant fish. GCL, ganglion cell layer; IPL, inner plexiform layer; INL, inner nuclear layer; OPL, outer plexiform layer; ONL, outer nuclear layer; ON, optic nerve; IS/OS, inner/outer segments; RPE, retinal pigment epithelium. Scale bar = 50 µm.

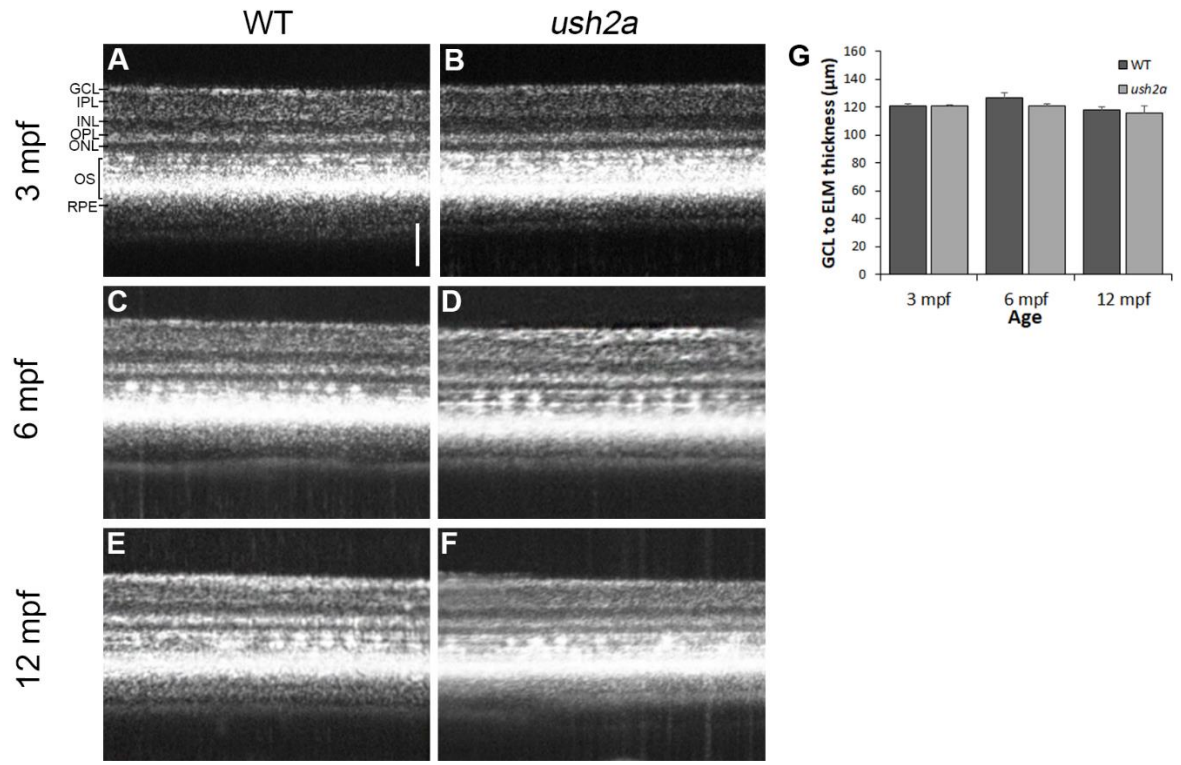

Figure 4-9. Longitudinal *in vivo* imaging of the *ush2a* retinal structure.
SD-OCT was used to image the retinas in live wild-type (WT) and *ush2a* zebrafish at 3 months post fertilisation (mpf) (A, B), 6 mpf (C, D) and 12 mpf (E, F). Bar chart (G) shows retinal thickness measurements (GCL-ELM) at each timepoint, measured using Bioptigen Diver (n≤3 for each age, mean ± SEM). GCL, ganglion cell layer; IPL, inner plexiform layer; INL, inner nuclear layer; OPL, outer plexiform layer; ONL, outer nuclear layer; OS, outer segments; RPE, retinal pigment epithelium. Scale bar = 50 µm.

images revealed similar values between WT and *ush2a* at 3 mpf (121 ±1.2 μm and 121 ±0.7 μm, respectively) (n≥3). At 6 mpf, the *ush2a* retina did not show a change in thickness but was mildly reduced compared to WT, measuring at 121 ±1.5 μm versus 127 ±3.9 μm in WT. At 12 mpf, the *ush2a* retina was 116 ±4.8 μm in thickness compared to 118 ±2.0 μm in WT.

Voronoi domain analysis was used to assess UV cone mosaic regularity from *en face* SD-OCT images, which showed a slight reduction in the regular triangular arrangement of 6-sided polygons in *ush2a* retinas compared to age-matched WT (**Figure 4-10**). At 3, 6 and 12 mpf, the mean percentage of cones with 6 neighbours in the *ush2a* fish was 67.9 ±1.2%, 73.3 ±6.6% and 68.9 ±5.7%, respectively, compared to WT fish at the corresponding ages; 76.1 ±2.1%, 76.8 ±0.97% and 75.6 ±3.2% respectively (n=3).

4.1.5 Visual function in *ush2a* zebrafish

In order to determine the visual function in *ush2a* zebrafish, optokinetic response testing was undertaken at 3, 6 and 12 mpf (**Figure 4-11**). It was found that the *ush2a* zebrafish had a similar visual acuity to WT fish at 3 mpf (1.61 ±0.32 cpd in WT, 1.42 ±0.41 cpd in mutant fish). At 6 mpf, WT fish showed a greater increase in visual acuity than *ush2a* (2.13 ±0.41 cpd in WT, 1.77 ±0.35 cpd in mutant fish. At 12 mpf, mean visual acuity of *ush2a* zebrafish was mildly decreased at 1.89 ±0.40 cpd compared to 2.27 ±0.35 cpd in age-matched WT. The differences in visual acuity between WT and *ush2a* zebrafish were not found to be significant at any age.

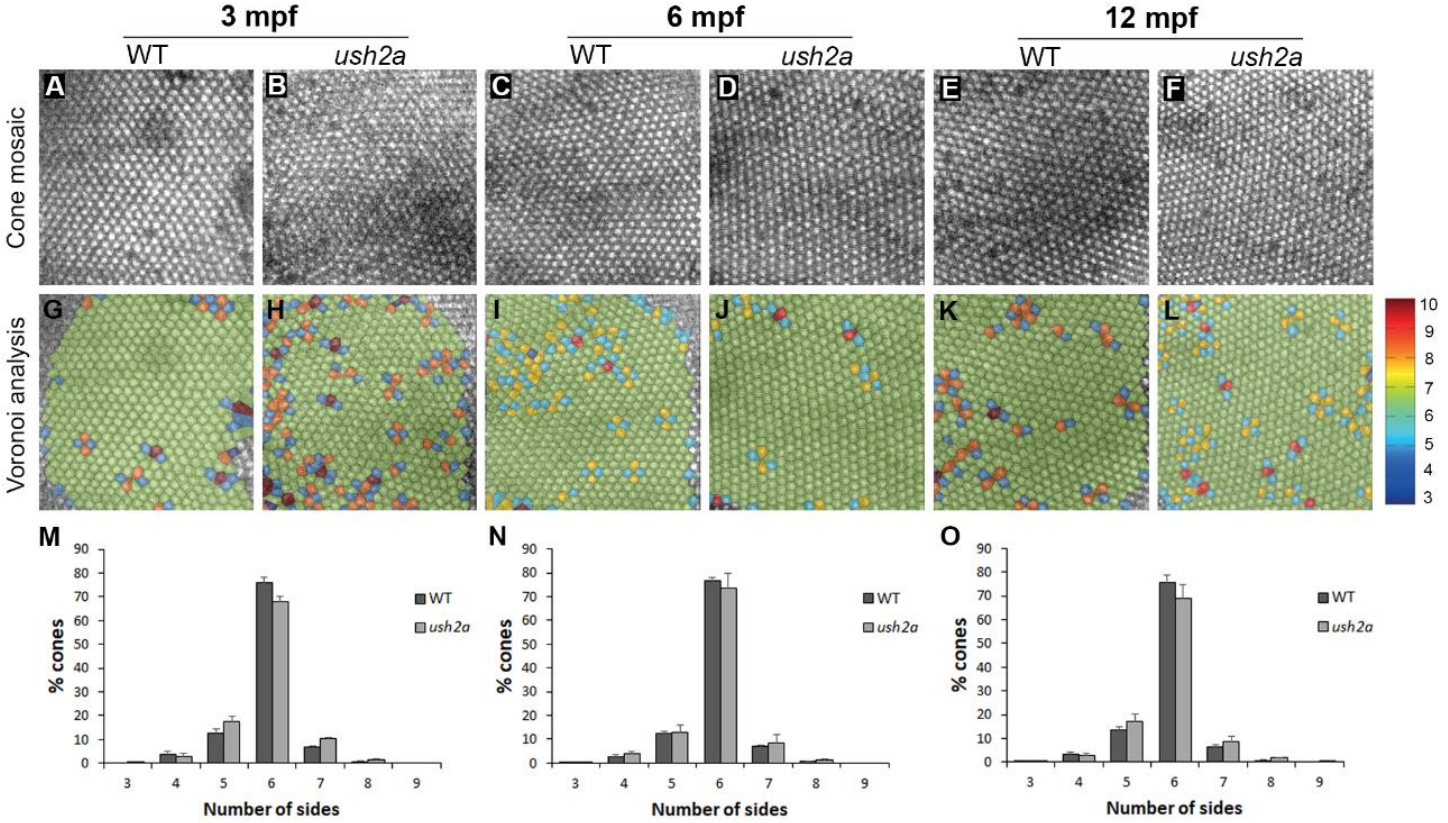

Figure 4-10. Cone photoreceptor mosaic in *ush2a* zebrafish.
SD-OCT was used at fig3, 6 and 12 months post fertilisation (mpf) to image the *en face* cone photoreceptor mosaics (A-F) from which the corresponding Voronoi domain diagrams were produced (G-L) in which a Voronoi polygon is associated with each cone photoreceptor and colour-coded according to the number of sides it possesses (colour key shown on right). Bar charts show the mean percentage of three- to nine-sided Voronoi domains in wild-type (WT) and *ush2a* zebrafish at 3 mpf (M), 6 mpf (N), and 12 mpf (O) (n=3 for each age, mean ± SEM).

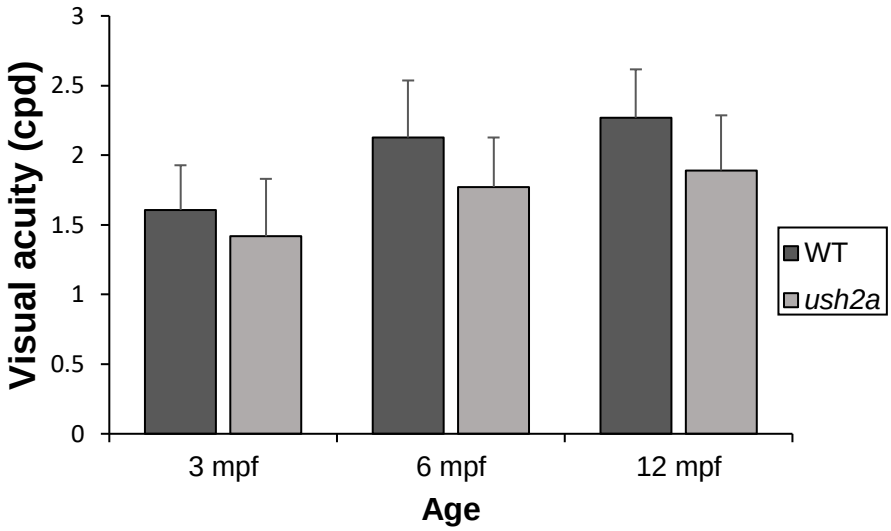

Figure 4-11. Visual function in *ush2a* zebrafish.
Bar chart showing visual acuity (cycles per degree, cpd) of wild-type (WT) and *ush2a* zebrafish at 3 months post fertilisation (mpf), 6 mpf and 12 mpf, assessed using the optokinetic response assay (n≥4, mean ± SEM).

4.1.6 Photoreceptor cell death in the *ush2a* retina

Adult degeneration

Apoptotic cell death in the *ush2a* adult retina was investigated using the TUNEL assay, which works by labelling the 3′-hydroxyl termini in the double-strand DNA breaks generated during apoptosis. At 6 mpf and 12 mpf, fluorescent signal was detected specifically in the photoreceptor nuclei of *ush2a* retinas. At 6 mpf, a mean of 0.73 ±0.18 apoptotic nuclei per 14 μm retinal section (n=15) could be detected in the ONL of the *ush2a* retina, indicative of rod cell death (**Figure 4-12**). At 12 mpf, the number of apoptotic photoreceptor nuclei was increased to 1.92 ±0.46 per section (n=13) and in addition to the ONL, fluorescent nuclei were occasionally detected in the cone nuclei. In WT retinas, apoptosis was not detected at 6 mpf and a negligible amount was detected in the ONL at 12 mpf (0.22 ±0.22 apoptotic nuclei per section, n=10).

Dark- and light-induced photoreceptor degeneration in larvae

In order to accelerate photoreceptor degeneration, WT and *ush2a* zebrafish were raised in either constant dark or constant light conditions from fertilisation up to 8 dpf (**Figure 4-13**). Numbers of apoptotic photoreceptor nuclei were detected per 14 um retinal section using the TUNEL assay. Approximately three sections per individual fish were examined. Apoptosis was not detected in the larvae raised under normal conditions (14:10 light:dark cycle). For dark- reared *ush2a* larvae, a mean of 2.65 ±0.25 apoptotic photoreceptors per retinal section was detected (n=91 from 24 zebrafish), compared to 0.40 ±0.11 apoptotic photoreceptors in WT retinas (n=68 from 24 zebrafish) ($p=0.0001$). Contrastingly, light-reared 8 dpf WT fish had a mean of 4.15 ±0.49 apoptotic photoreceptors per section (n=39 from 12 zebrafish), compared to 2.66 ±0.33 apoptotic photoreceptors per *ush2a* retinal section (n=38 from 12 zebrafish) ($p<0.05$).

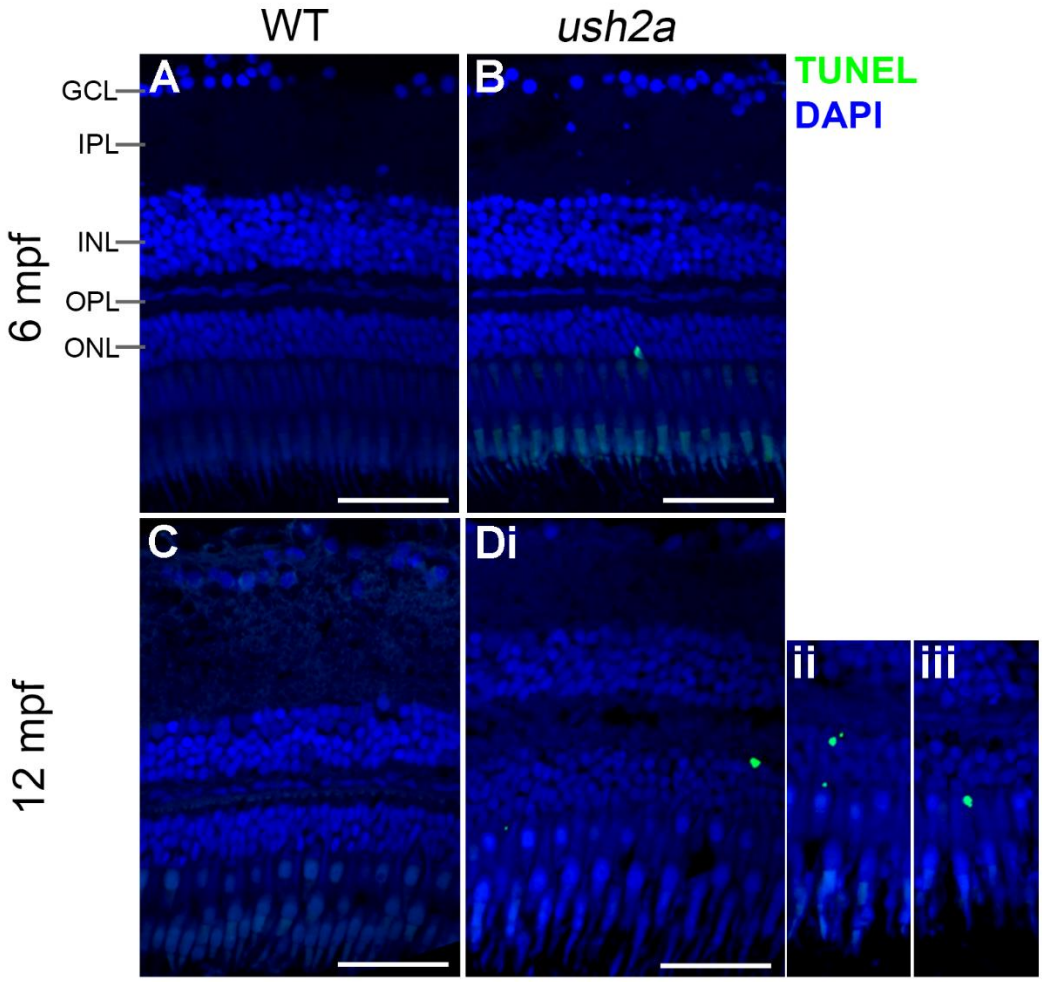

Figure 4-12. Photoreceptor cell death in the adult *ush2a* retina.
TUNEL assays were used to detect apoptotic photoreceptors in the wild-type (WT) and *ush2a* retinas at 6 months post fertilisation (mpf) (A, B) and 12 mpf (C, D). In the 6 mpf *ush2a* retina, apoptotic nuclei (green) could be observed occasionally in the ONL (B). In the 12 mpf *ush2a* retina, apoptotic nuclei were more frequent and could be detected in the ONL (Di, ii) and more rarely in the cone nuclei (Diii). Apoptosis was negligible in the WT retinas at both ages (A, C). Representative images are shown from ≥12 retinal sections from two fish per timepoint for WT and mutant fish. DAPI nucleic acid stain was used as a counterstain (blue). Scale bar = 50 µm.

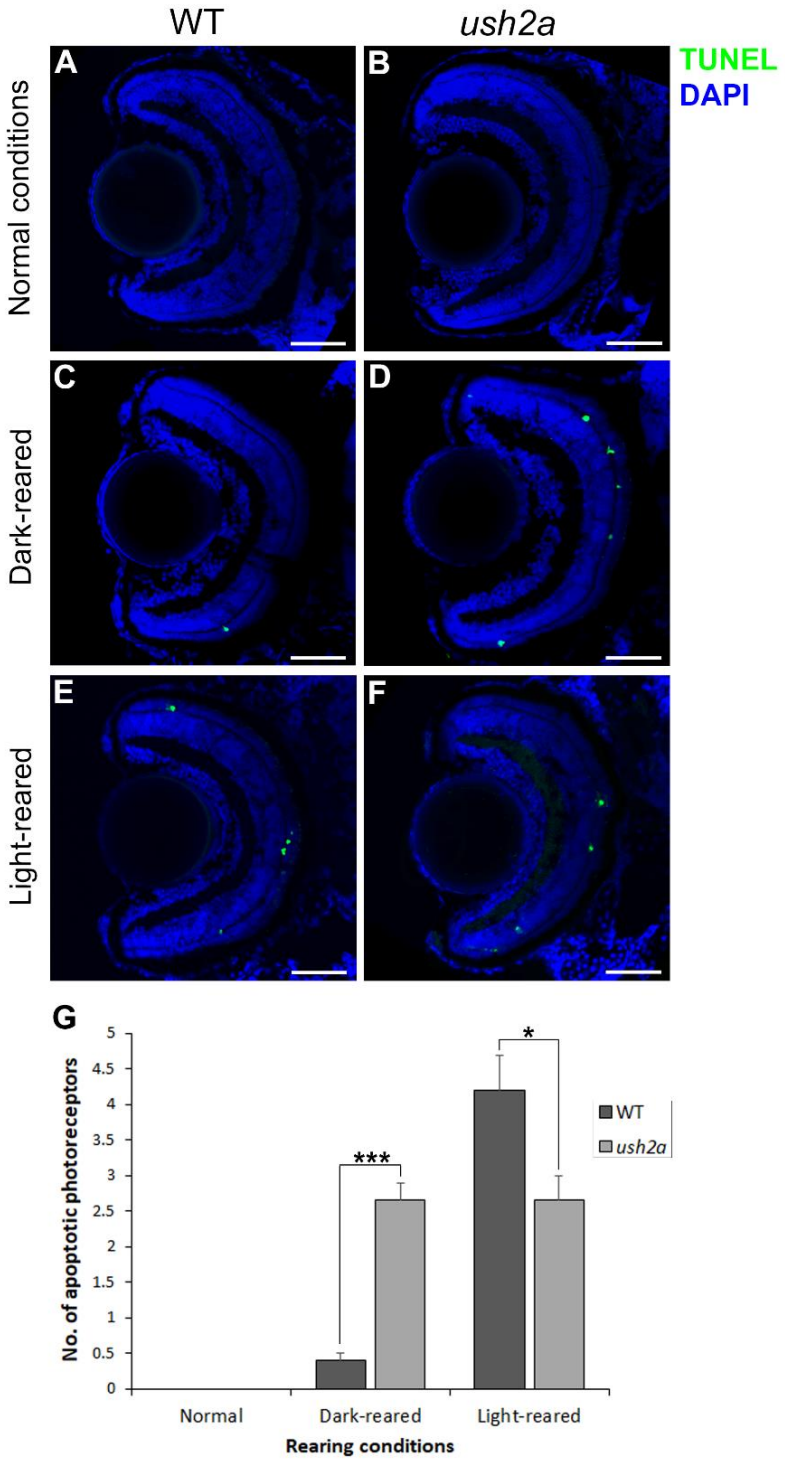

Figure 4-13. Dark- and light-induced photoreceptor degeneration in larval zebrafish.
TUNEL assays were used to detect apoptotic photoreceptors (green) in 8 days post fertilisation wild-type (WT) and *ush2a* larvae raised under normal conditions (A, B), constant dark (C, D) or constant light (E, F). Sections are counterstained with DAPI nuclei acid stain (blue). Bar chart (G) shows the mean number of apoptotic photoreceptors per 14 µm retinal section in WT and *ush2a* zebrafish reared under the three conditions (mean ±SEM), (dark-reared WT: n=68; dark-reared *ush2a*: n=91; light-reared WT: n=39; light-reared *ush2a*: n=38). *p<0.05, **p=0.0001. Scale bar = 25 µm.

4.1.7 Müller cell activation in the *ush2a* retina

To investigate Müller cell activity, the anti-ZRF1 antibody was used to detect retinal expression of GFAP, a protein known to be upregulated by glial cells in response to retinal injury or stress (324). GFAP was expressed in the Müller cell endfeet and processes in both mutant and age-matched WT retinas at 3, 6 and 12 mpf (**Figure 4-14**). The expression levels were mostly similar between WT and *ush2a,* with the exception of 12 mpf where increased GFAP was noted in the Müller cell bodies in the INL of the *ush2a* retina (**Figure 4-14F**).

4.1.8 The *ush2a* retinal ultrastructure

Rod degeneration in the ush2a retina

TEM was used to examine the ultrastructure of the *ush2a* zebrafish retina at 6 and 12 mpf (n=3 per timepoint) (**Figure 4-15**). In the WT adult retina, TEM cross-sectional images revealed Bruch's membrane, the innermost layer of the choroid, lying adjacent to the melanosome-containing RPE monolayer whose apical projections interdigitate with the rod outer segments. The photoreceptor outer segments were seen as relatively electron-dense structures adjoining mitochondria-filled inner segments. The rods formed the outermost layer of photoreceptors with the red-green cone outer segments forming the tier above. At 6 mpf, patches of rod photoreceptor loss and cellular debris were noted among mostly preserved tissue in the *ush2a* retina (**Figure 4-15B**). At 12 mpf, larger regions of rod loss were observed along with the presence of large apoptotic bodies (**Figure 4-15D**).

Lysosomal vesicles in the ush2a photoreceptors

In the 6 mpf *ush2a* retina, the atypical presence of spherical vesicular structures was noted around the photoreceptor inner and outer segment boundary and ribbon

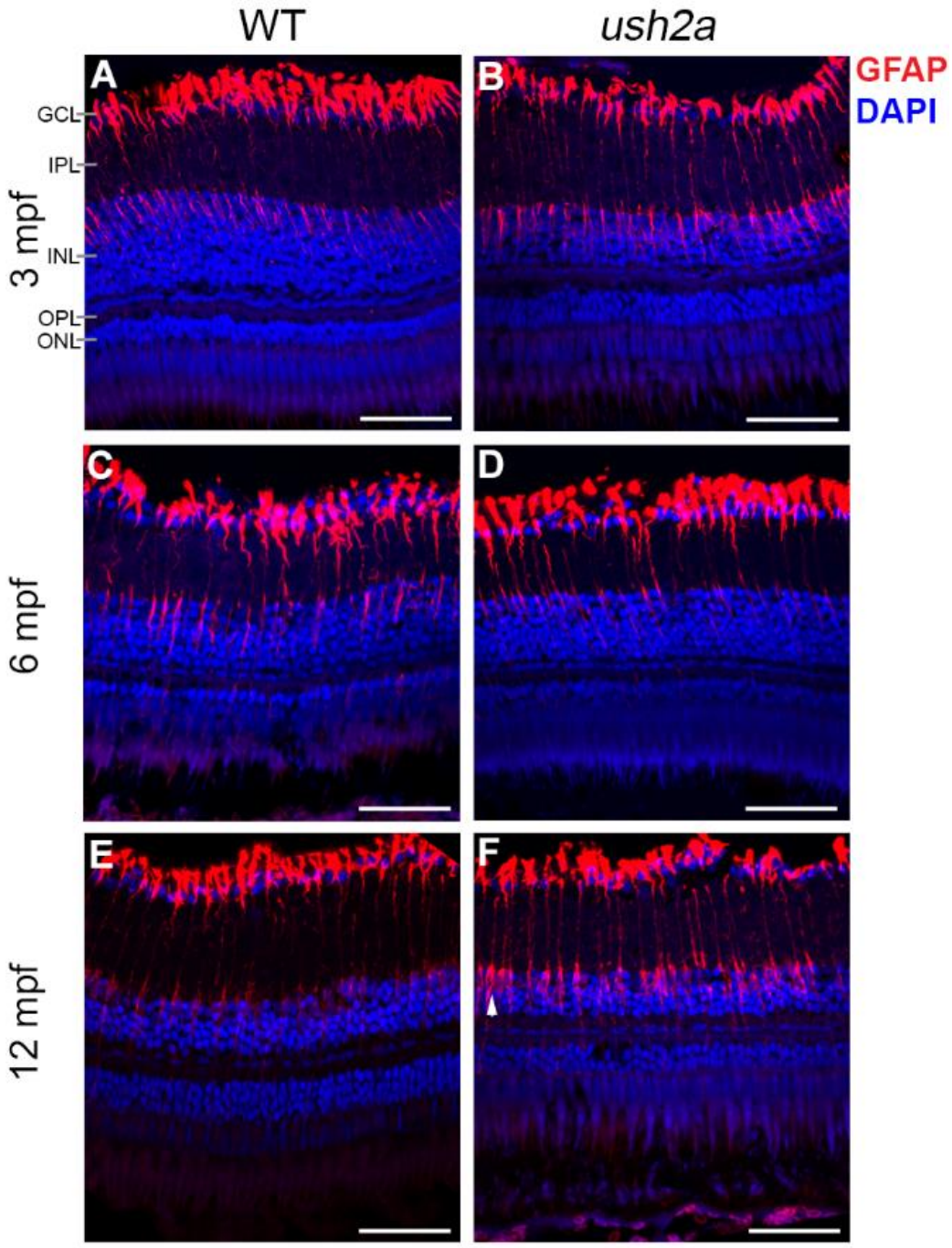

Figure 4-14. Müller cell activation in the *ush2a* retina.
The glial fibrillary acidic protein (GFAP) was detected in the wild-type (WT) and *ush2a* retina at 3 months post fertilisation (mpf) (A, B), 6 mpf (C, D) and 12 mpf (E, F) by immunostaining with the anti-ZRF1 antibody (red). Sections are counterstained with DAPI nuclei acid stain (blue). GFAP was expressed in the Müller cell endfeet and processes in both mutant and WT retinas. Increased GFAP was noted in the Müller cell bodies in the INL of the 12 mpf *ush2a* retina (white arrow). Representative images are shown from two retinas per timepoint for WT and mutant fish. GCL, ganglion cell layer; IPL, inner plexiform layer; INL, inner nuclear layer; OPL, outer plexiform layer; ONL, outer nuclear layer. Scale bar = 50 µm.

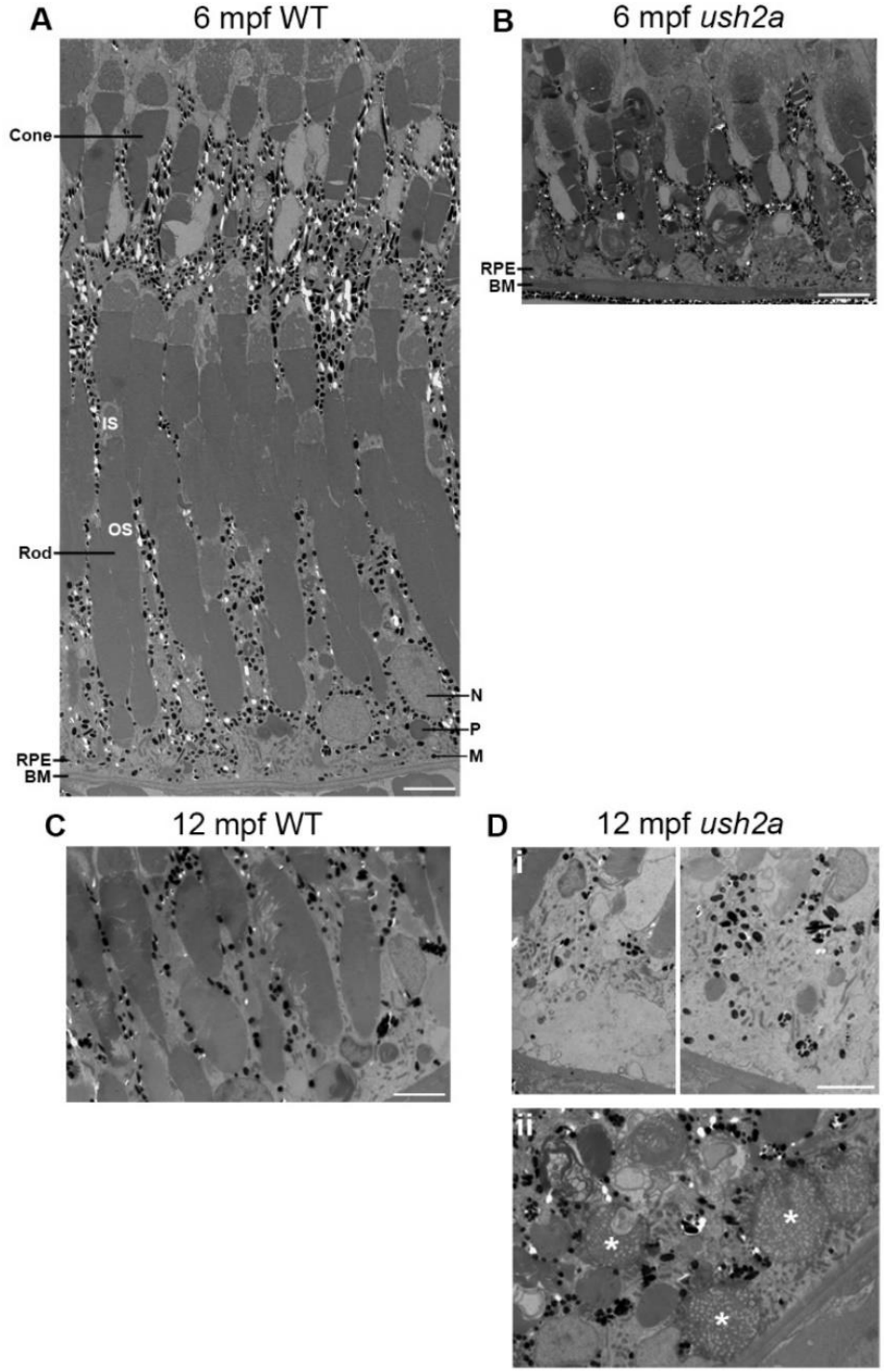

Figure 4-15. Retinal ultrastructure of *ush2a* zebrafish.
Transmission electron microscopy was used to examine the wild-type (WT) and *ush2a* retinal ultrastructure at 6 and 12 months post fertilisation (mpf) (n=3). The WT retina showed tiers of morphologically distinct cone and rod photoreceptors and overlying retinal pigment epithelium (RPE) with long apical projections that interdigitated with the photoreceptors (A). Among mostly preserved tissue, regions of rod loss could be observed in the *ush2a* retina at 6 mpf (B). Larger voids of rod loss were seen in the mutant retina at 12 mpf (D), along with the presence of large apoptotic bodies (highlighted with * in Dii). IS, inner segment; OS, outer segment; RPE, retinal pigment epithelium; BM, Bruch's membrane; N, nucleus; P, phagosome; M, melanosome. Scale bars = 5 µm.

synapses where the photoreceptors synapse with the bipolar and horizontal cells (**Figure 4-16**)**.** These vesicles were not in observed in the WT retina at any age. Although the identity of these structures was not confirmed they most resemble lysosomes, which are vesicles formed from the Golgi complex.

Structure of the connecting cilium

In photoreceptors, the light-sensitive outer segment is linked to the inner segment via a specialised non-motile cilium, the connecting cilium. The connecting cilium represents an elongated transition zone, and along with the basal body complex, forms the photoreceptor ciliary apparatus. Ciliary axonemal microtubules project from the connecting cilium into the outer segment. As usherin has been localised to the connecting cilium in both mammalian and fish photoreceptors (258, 364), the structure of connecting cilia in *ush2a* fish was examined on TEM images (**Figure 4-17**). Generally, the connecting cilia appeared to be relatively intact in the mutant fish when compared to WT. Measurement of the width of the cilia 'shoulders' in 12 mpf WT and *ush2a* photoreceptors revealed an increase in the mutant, measuring 557.1 ±83.7 nm in *ush2a* fish compared to 441.2 ±77.0 nm in WT ($n \geq 7$, $p < 0.05$).

4.1.9 Rhodopsin localisation in the *ush2a* retina

To examine rhodopsin localisation in the *ush2a* zebrafish, the 4D2 antibody was used to label rhodopsin on retinal sections (**Figure 4-18**). At 6 dpf, the expression patterns in the WT and mutant retinas were comparable, indicating normal development of the rod photoreceptors in *ush2a* fish*.* In the adult retina at 3 mpf, typical rhodopsin expression clearly defined the rod outer segments in both the WT and *ush2a* retina. In the 6 mpf *ush2a* retina, rhodopsin was found to be mislocalised in small regions of the retina where it was detected in the presumptive inner segments or axons of the

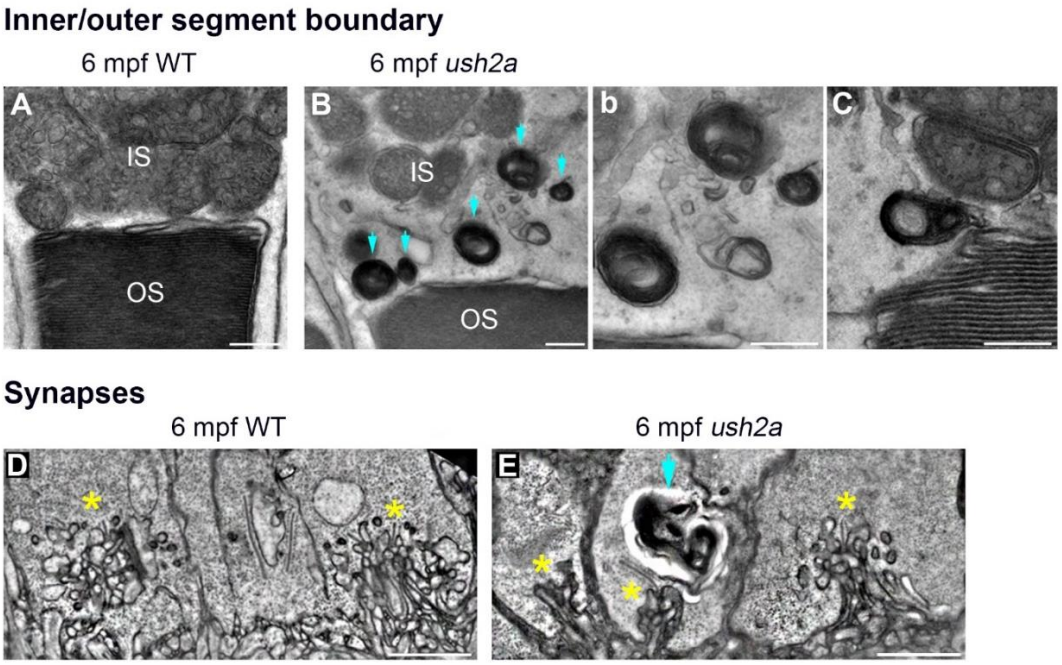

Figure 4-16. Lysosomes in the *ush2a* photoreceptors.
Using transmission electron microscopy, presumptive lysosomal structures (blue arrows) were noted at the inner and outer segment boundary (A-C) and at the synapses (D, E) of the *ush2a* photoreceptors at 6 months post-fertilisation (mpf) (n=3). Ribbon synapses are indicated by *****. These vesicles were not observed in WT retinas. IS, inner segment; OS, outer segment. Scale bars = 500 nm (A-C), 5 µm (D, E).

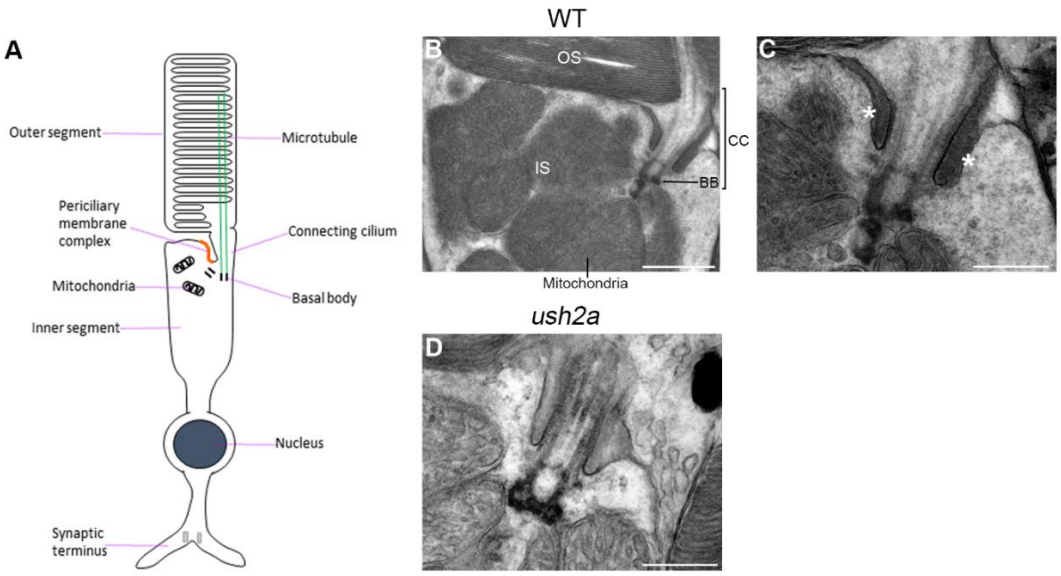

Figure 4-17. The connecting cilium in *ush2a* photoreceptors.
Schematic diagram of a photoreceptor showing the connecting cilium (A). Transmission electron micrographs of the photoreceptor connecting cilium in WT fish (B) (higher magnification shown in (C) and *ush2a* fish (D). * represent points used for cilia width measurements on (C) (n≥7). OS, outer segment; IS, inner segment; BB, basal body; CC, connecting cilium. Scale bars = 1 µm (B), 500 nm (C, D).

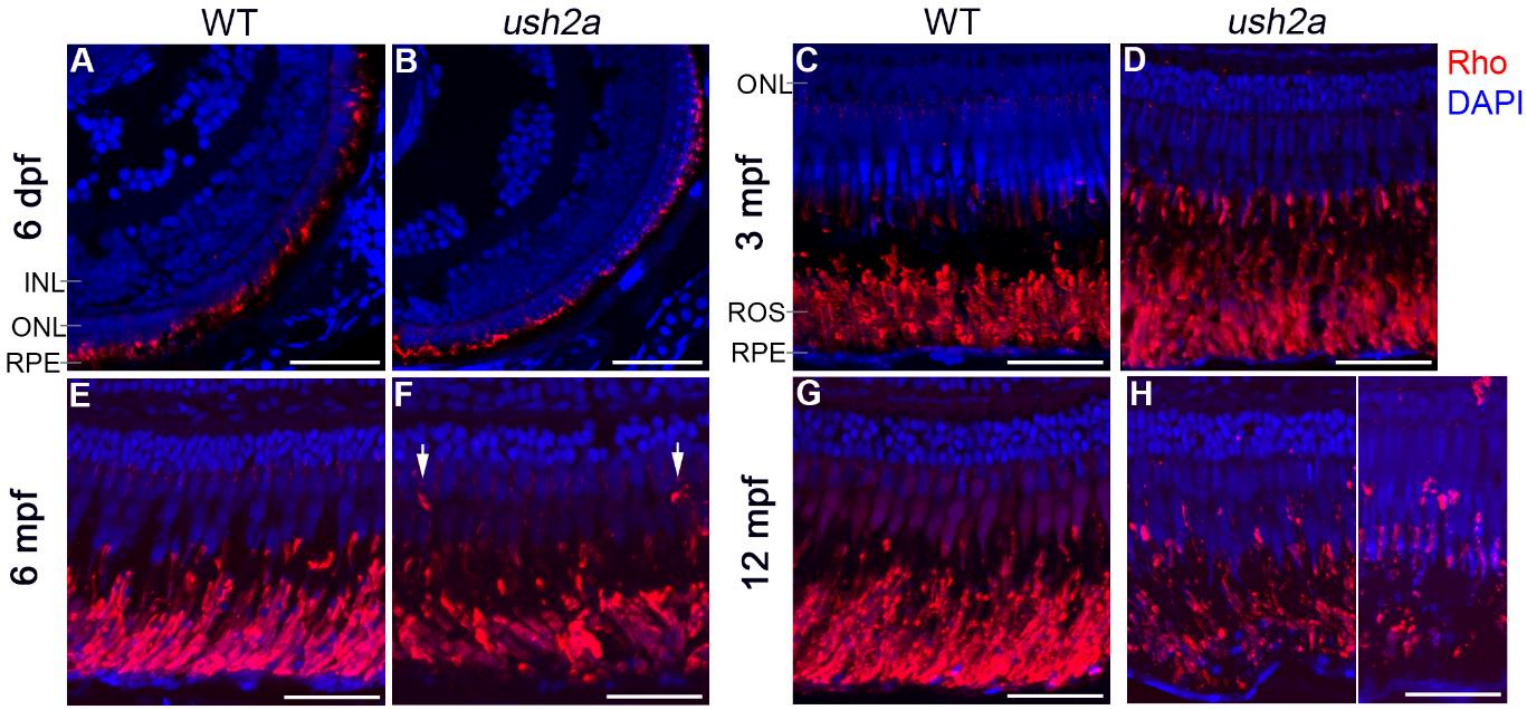

Figure 4-18. Rhodopsin localisation in the *ush2a* retina.
Rhodopsin was detected in the wild-type (WT) and *ush2a* retina at 6 days post fertilisation (dpf) (A, B), 3 months post fertilisation (mpf) (C, D), 6 mpf (E, F) and 12 mpf (G, H) by immunostaining with the 4D2 antibody (red). Sections are counterstained with DAPI nuclei acid stain (blue). In the 6 mpf *ush2a* retina, rhodopsin was found to be mislocalised in small regions of the retina (arrows in F). In the 12 mpf *ush2a* retina, rhodopsin staining showed mislocalisation in most parts of the retina and expression in the rod outer segments (ROS) appears to be abnormal compared to WT. Representative images are shown from two retinas per timepoint for WT and mutant fish. INL, inner nuclear layer; ONL, outer nuclear layer; RPE, retinal pigment epithelium. Scale bar = 25 µm.

rods (**Figure 4-18F**). By 12 mpf, rhodopsin staining showed mislocalisation in most parts of the *ush2a* retina and could be detected in the ONL. In addition, rhodopsin expression in the rod outer segments was grossly abnormal compared to age-matched WT.

4.1.10 Red opsin localisation in the *ush2a* retina

Red cone opsin localisation in *ush2a* fish was assessed using the 1D4 antibody (**Figure 4-19**). At 3, 6 and 12 mpf, red opsin expression was detected in the outer segments of the long double cones and there did not appear to be any differences in localisation between the WT and *ush2a* retinas.

4.1.11 Hair cell development in *ush2a* zebrafish

The zebrafish has two mechanosensory organs, the inner ear and lateral line, both of which contain sensory cells which are morphologically and physiologically similar to hair cells in higher vertebrates. As the cochlear hair cells of mice with Usher 2 gene mutations show defective development, thought to underlie sensorineural deafness in *USH2A* patients, the hair cells of larval *ush2a* zebrafish were assessed for abnormalities.

Neuromasts

In fish and amphibians, the lateral line is a mechanosensory system used in prey detection, predatory avoidance and schooling behaviour. It consists of small sensory organs, known as neuromasts, distributed in a stereotyped pattern along the head and trunk surface. Each neuromast is made up of a rosette-like cluster of stereociliary hair cells with kinocilia at the centre surrounded by a gelatinous cupula

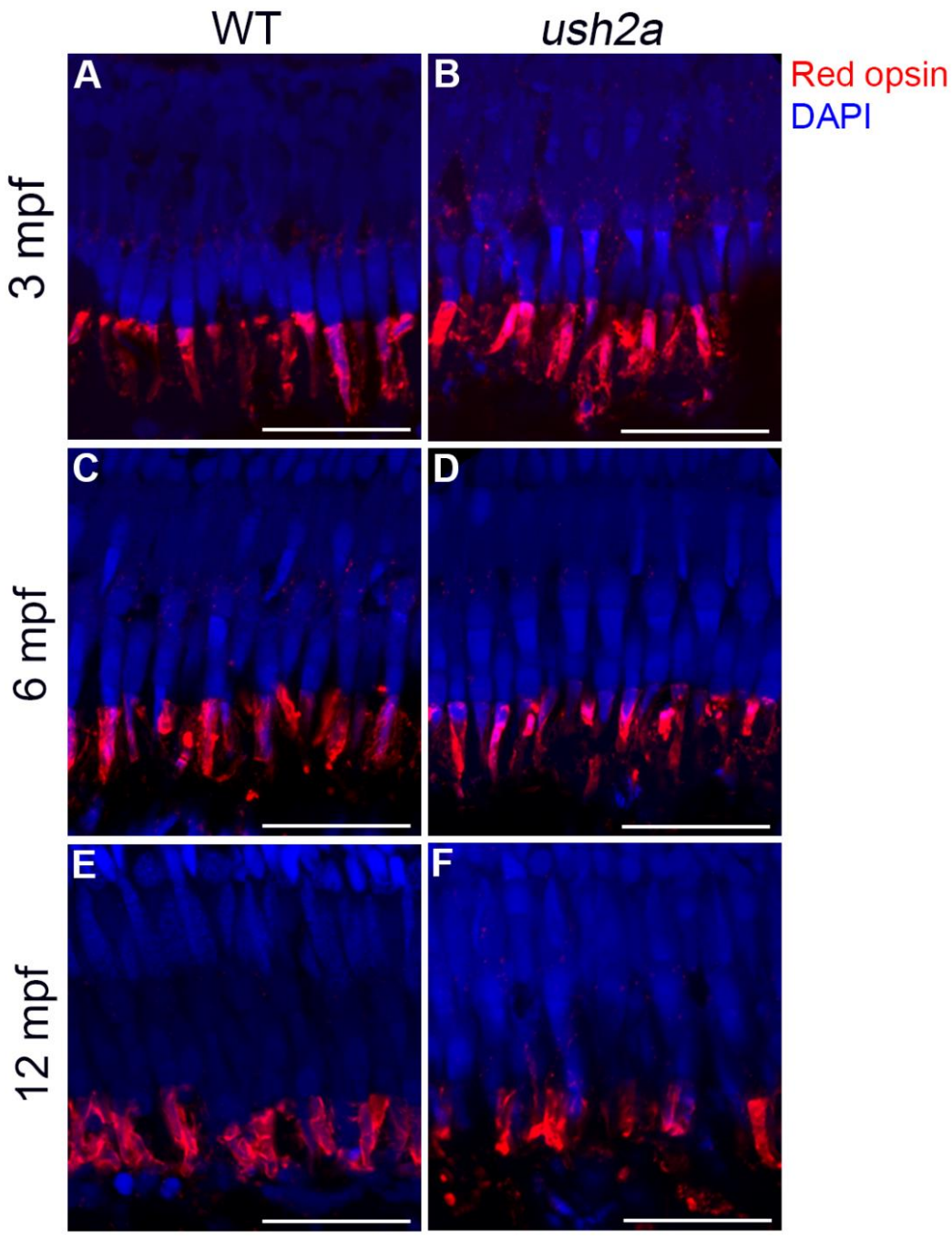

Figure 4-19. Red opsin localisation in the *ush2a* retina.
Red opsin was detected in the wild-type (WT) and *ush2a* retina at 3 months post fertilisation (mpf) (A, B), 6 mpf (C, D) and 12 mpf (E, F) by immunostaining with the 1D4 antibody (red). Sections are counterstained with DAPI nuclei acid stain (blue). Red opsin was detected in the double cone outer segments and showed normal localisation at all timepoints. Representative images are shown from two retinas per timepoint for WT and mutant fish. Scale bar = 25 µm.

(**Figure 4-20A**). Water flow causes the cupula to deflect, which is transduced into graded receptor potentials by the hair cell stereocilia. In WT and *ush2a* 6 dpf zebrafish, the neuromast morphology was examined by staining with an acetylated tubulin antibody, which labels the kinocilia and hair cell bodies, and Alexa Fluor 647 Phalloidin which labels the stereocilia (**Figure 4-20B-D**). The otic and middle neuromasts of the cranial region (according to Harris et al. 2003 grouping (365)) were examined. It was found that the neuromasts of 6 dpf *ush2a* more frequently showed abnormalities i.e. absent or shortened kinocilia or reduced numbers of hair cell bundles. The mean number of stereociliary bundles per neuromast was found to be 14.2 ±0.70 in *ush2a* zebrafish compared to 17.2 ±0.76 in WT larvae (mean ±SEM, n=40) ($p<0.01$).

Inner ear sensory maculae

In the zebrafish embryonic stage, there are two sensory maculae contained within the otic capsules: the anterior utricule macula and the posterior saccule macula which are thought to have primarily vestibular and auditory roles, respectively. Each macula is made up of sensory epithelia containing numerous mechanosensory hair cells, each with a ciliary bundle of multiple stereocilia and a kinocilium. In 6 dpf WT and *ush2a* larvae, the hair cell bundles of the anterior macula were examined by immunostaining with Alexa Fluor 647 Phalloidin (**Figure 4-21**). WT hair bundles had a characteristic cone-shaped appearance with tapering at the tips and projected more or less orthogonally from the plane of each cuticular plate. While the individual stereociliary bundles appeared to be intact in the mutant fish, the hair bundles appeared reduced in number and differently organised within the macula patch. In *ush2a* larvae, the mean number of hair bundles per anterior macula was 67 ±1.1, compared to 60.3 ±1.6 in WT larvae (n=8, $p<0.01$). A tapping-induced vibrational startle reflex test was used to test hair cell function in the larvae at 6 dpf. In WT, only

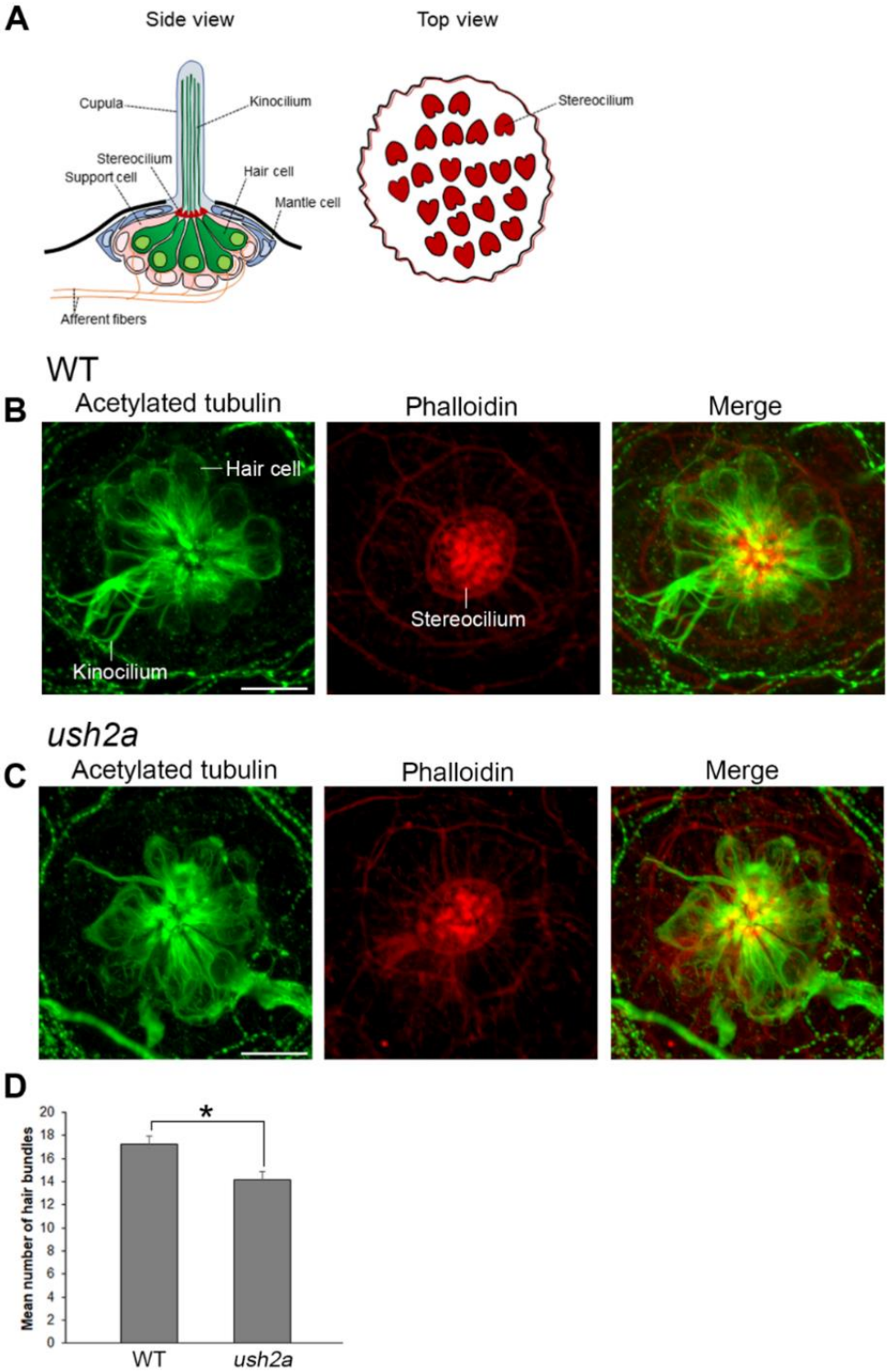

Figure 4-20. Neuromast development in *ush2a* larval zebrafish.
A schematic diagram of a neuromast is shown in (A). The neuromasts of wild-type (WT) and *ush2a* at 6 days post fertilisation were immunostained with anti-acetylated tubulin (green), which labels the kinocilia and hair cell bodies, and phalloidin (red) which labels the stereocilia. A representative WT neuromast is shown in (B). An abnormal *ush2a* neuromasts is shown in (C), where kinocilia and hair cells are missing. Bar chart (D) shows the mean number (±SEM) of hair bundles per neuromast in WT and *ush2a* larvae (n=40). *p<0.01. Scale bar = 10 µm.

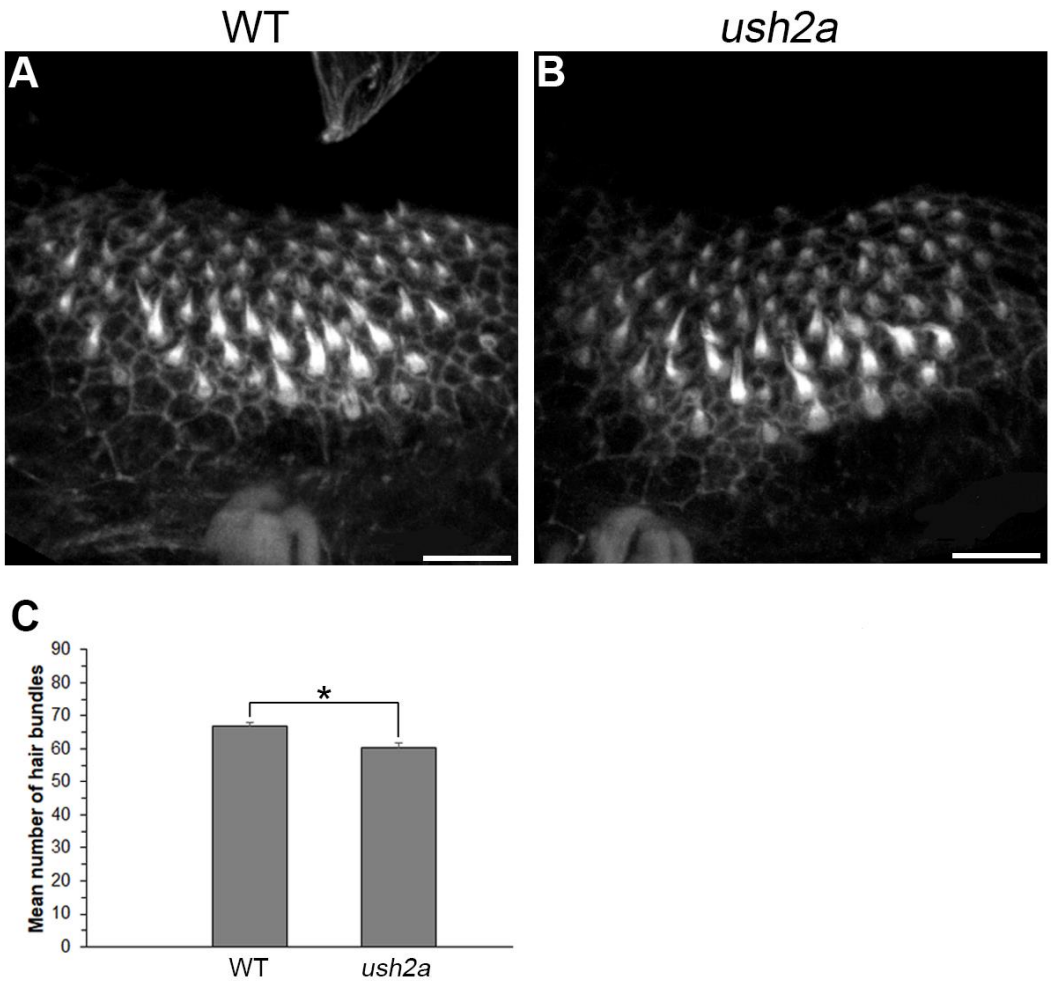

Figure 4-21. Sensory macula development in *ush2a* larval zebrafish.
Stereociliary hair bundles of the anterior macula in wild-type (WT) (A) and *ush2a* (B) zebrafish at 6 days post fertilisation (dpf), immunostained with Alexa Fluor 647 Phalloidin. Bar chart (C) shows the mean number (±SEM) of hair bundles per anterior macula in WT and *ush2a* larvae (n=8). *p<0.01. Scale bar = 10 µm.

18.9% of larvae were classed as ‘non-responders’ compared to 47.1% of *ush2a* fish (n=80).

4.2 Discussion

USH2A is the most prevalent gene associated with Usher syndrome, the commonest deaf-blindness disorder, and is also significant cause of isolated autosomal recessive RP. Although an *Ush2a* mutant mouse has been previously characterised, the development of additional more time- and cost-efficient disease models will aid progress towards further understanding the *USH2A*-associated retinal pathology and developing suitable treatments. The current study aimed to explore the zebrafish as a model of Usher syndrome through the phenotypic characterisation an *ush2a* mutant line generated using CRISPR/Cas9-based gene targeting.

Initially, structural and functional conservation of *ush2a* was assessed by examining the protein sequence and expression patterns in the zebrafish. Sequence comparison between species revealed a relatively high level of similarity between the zebrafish protein with the human and mouse orthologues. The predicted proteins of all three species are comparable in size with the same basic functional domain composition, including several domains common to extracellular matrix proteins and cell adhesion proteins, and a transmembrane region, supporting a conserved function between species.

In human and mouse, there are two usherin isoforms (short secreted and long transmembrane), the latter of which is found to be expressed predominantly in the retina and developing cochlea (138, 165, 366). Usherin has been detected in many other human tissues, although early studies did not distinguish between isoforms (140, 367). A short secreted isoform has not been identified for zebrafish. Previously, usherin has been localised to the anterior macula and retina in 5 dpf zebrafish using a now discontinued antibody (364, 368). It should be noted that zebrafish *ush2a*

antibodies are not currently available commercially and custom *ush2a* antibodies were purchased for this project but were not effective at detecting the usherin when tested. As discussed in Chapter 3, a fluorescently-tagged usherin protein could be used to determine localisation in the zebrafish in future experiments. Alternatively, RT-PCR and *in situ* hybridisation analysis were used to examine *ush2a* expression in the present study, which confirmed presence in the developing zebrafish eye and ear. Transcripts were detected from 48 hpf and showed strong expression in the adult eye at all timepoints examined. In the adult zebrafish retina, *ush2a* was found to be specifically expressed in the photoreceptors along with two Usher 2 gene orthologues, *gpr98* and *dfnb31a*, consistent with previous mouse work showing co-localisation in these cells (169, 258). Overall, the species similarity in expression patterns provided additional support for a conserved role of *ush2a* in zebrafish, highlighting it as a potentially effective model for further investigating the role of *ush2a*.

An *ush2a* line (c.2131_2203+73delinsCGGCGG p.Ala711Argfs) was produced using the CRISPR/Cas9 system, which has in recent years become a popular tool for rapid and efficient gene targeting in zebrafish. In this study, the technique has been used to generate disruptive frameshift alleles in a well-conserved N-terminal region of the zebrafish *ush2a* gene. If translated, the protein is predicted to be truncated and non-functional. As protein knockout could not be qualified with antibody staining the RNAscope assay was used, which showed significant reduction in *ush2a* mRNA transcripts in the adult mutant retina, likely as a result of nonsense-mediated decay in which mRNA transcripts harbouring premature stop codons are degraded as a mechanism of quality control (369). Human *USH2A* is associated with a diverse mutation spectrum, including nonsense, missense, frameshift, splice-affecting mutations, although the presence of two truncating mutations where no viable protein

is likely to be produced is more often associated with Usher syndrome and a worse visual prognosis (207, 208). The mutations generated in the *ush2a* zebrafish line resemble the severity of those found in Usher syndrome patients.

Initial characterisation of the *ush2a* mutant zebrafish by examining the general morphology showed normal formation of the eye and ear structures in larvae with development into viable adults, consistent with the corresponding mouse model (165). The retinal structure was examined using histological evaluation and longitudinal SD-OCT up to 12 mpf, which was the oldest timepoint examined due to the time limitation of the study. This revealed normal retinal development with no gross abnormalities in the adult retinal morphology. Retinal thickness measurements and cone mosaic organisation, along with visual function, showed mild reductions in the *ush2a* zebrafish compared to WT at all ages, however these differences were not significant. In *Ush2a* mice, retinal degeneration only begins to become apparent by 12 months of age at the earliest due to subtle thinning of the ONL and severe disruption of the cone cells occurs at a much later timepoint (~20 months) (165, 246). Similarly, the *Whrn* knockout mouse showed a late onset degeneration (28+ months of age) (169), while other Usher 2 mouse models *Gpr98* and *whirler* did not show a degeneration (167, 170). The *ush2a* zebrafish retina may show similar disease progression with severe widespread loss of photoreceptors apparent on histological sections at a later timepoint than investigated so far. As the zebrafish retina is cone-dominated, the degeneration may not manifest as rapidly due to the preponderance of cones over rods.

Further evidence for a slowly progressive photoreceptor degeneration in the *ush2a* zebrafish was provided by the detection of apoptotic cell death in the photoreceptor nuclei at 6 mpf, which increased at 12 mpf. Apoptosis was predominantly detected

in the ONL, which is mostly made up of rod photoreceptor nuclei, and accordingly TEM was able to confirm small regions of rod loss at 6 mpf. These findings are consistent with the development of RP in Usher syndrome patients, which typically first presents as night blindness and loss of peripheral vision caused by rod degeneration (121). This may account for minimal changes in optokinetic responses and cone mosaic organisation in the *ush2a* zebrafish; these examinations may be more effective at later stages of degeneration. In larval zebrafish, it is known that the optokinetic response is cone-mediated as mature rod responses are not elicited until 15 dpf (370); however, the retinal cells that make the key contributions towards the optokinetic response in adult zebrafish have not been well studied. Such investigations would be useful for providing further insight into the responses observed in *ush2a* zebrafish. Visual function may be better assayed using the optokinetic response under different light conditions, or using a sensitive and informative investigation such as ERG.

It is unclear why the rod photoreceptors are primarily affected in *ush2a* mutant fish, or *USH2A* patients, as rod-exclusive expression of usherin has not been described (165, 247, 364). Typically, rod apoptosis in RP is due to rod-specific molecular defects and secondary cone loss is believed to occur as a result of either 1) loss of rod-derived cone viability factor (RdCVF) (371) or 2) increased exposure to oxygen, inducing oxidative stress (372). Usher syndrome as a whole differs from most other forms of RP because expression of the mutated Usher genes is not limited to rods but is also present in cones (247, 373), and clarifying the mechanisms underlying the rod/cone degeneration in the various Usher subtypes will be essential for the development of therapeutic treatments. The evidence from several Usher 1 (167, 250) and Usher 2 (165, 246) mouse mutants indicates that cone dysfunction is not solely a secondary effect to rod loss as cone subtypes are most affected in these models. In *myo7aa*

mutant fish, although only rod loss was evident, altered ERG responses were also indicative of cone dysfunction (255). A similar condition may exist in the *ush2a* fish; the present findings demonstrate that the function of *ush2a* in zebrafish cone photoreceptors is less critical for their survival than its function in rods and further work will be necessary to determine these differences; this will be discussed more below.

In contrast to the *Ush2a* mutant mouse, which showed GFAP upregulation as early as p80 (246), the *ush2a* zebrafish retina did not show notable changes in Müller cell activity prior to degeneration. In the mammalian retina, Müller cell activation is an early unspecific but sensitive indicator of a wide variety of retinal diseases and injuries (324). Upon damage, Müller glial cells respond with reactive gliosis, indicated by cell hypertrophy and upregulation of GFAP. In contrast to the mammalian response, adult zebrafish Müller glia exhibit reactive gliosis immediately following retinal injury then down-regulate the gliotic response and become stem cells which regenerate the appropriate retinal cells (374). Normal GFAP expression in the zebrafish retina differs from that of mice as it is expressed along the Müller glial processes in the WT retina in an unstressed state, as demonstrated here. In the *ush2a* retina, there was a mild increase in GFAP in the INL at 12 mpf, but this did not precede observable changes in the photoreceptors. Unlike in *Ush2a* mice, GFAP expression will not be an effective indicator of early retinal stress in the *ush2a* zebrafish for potential therapeutic studies.

As the *ush2a* retinal degeneration was slow and late onset, the use of constant light or dark exposure was employed to accelerate photoreceptor cell death, which has been effective in other models of Usher syndrome (248, 249, 255). Firstly, it was observed that rearing in constant light or constant dark elicited photoreceptor apoptosis in both WT and *ush2a* larvae. The mechanisms involved in light-induced

photoreceptor death have been characterised in rodent retinas and is believed to occur as result of repetitive bleaching of the visual pigment rhodopsin, which causes an accumulation of retinoid intermediates that ultimately induce apoptosis (375). The processes underlying constant dark-induced apoptosis have been less well characterised and constant dark exposure has produced varied results in different models; for instance, the effect was more severe than prolonged light exposure in salamander (376) and frogs (377), while in other cases it had either no effect or a protective effect on cell survival (250, 378-380). In the absence of light, cyclic guanine monophosphate (cGMP) concentration is high and bound to a cyclic nucleotide-gated channel that allows the passage of Na^+ and Ca^{2+} into the photoreceptor for a depolarised resting state. The photoreceptors continuously release the neurotransmitter glutamate. Prolonged maintenance in this state may cause accumulation of cGMP, disrupted channel permeability, and depletion of the cells resources. It has been found that dark-rearing in zebrafish can cause changes in photoreceptor morphology by inhibiting the shedding of rod outer segments and shortening the inner segments (381), factors that may render them vulnerable to apoptosis. In the present study, constant dark exposure was shown to cause a minimal amount of photoreceptor death in WT, which was substantially increased in the *ush2a* retinas, suggesting that loss of *ush2a* compromises the photoreceptor viability under these conditions.

The use of constant light-rearing was found to have a more profound effect on WT photoreceptor survival than light deprivation. Intriguingly, this effect was significantly attenuated in the *ush2a* larvae. Although unexpected, a similar phenomenon has been previously observed in *Rpe65* L450M (382) and *Myo7a* (USH1B) mice (245). The protection against light-induced death in these models was attributed to reduced activity of RPE65, an essential enzyme in the visual cycle, resulting in slower

regeneration of rhodopsin which is thought to be a trigger for apoptosis. Consistent with this observation, it has also been found that zebrafish ventral rod photoreceptors which contain lesser amounts of rhodopsin are less vulnerable to light damage (383). Reduced levels of light-induced apoptosis in the *ush2a* retina may be related to the process being rhodopsin-mediated, as findings from the present study suggest that rhodopsin content in the outer segments may be affected in these zebrafish (discussed in more detail below) and therefore could make *ush2a* rod photoreceptors less responsive to constant light conditions. However, these findings are inconsistent with a previous study in *myo7aa*$^{-/-}$ zebrafish, where constant light-rearing exacerbated retinal cell death (255) in the mutant and did not appear to affect WT fish. There may be several factors that contribute to the discrepancy between the investigations; for instance, in the *myo7aa*$^{-/-}$ zebrafish cell death was assessed by histological examination rather than TUNEL analysis and unlike *ush2a* fish, m*yo7aa*$^{-/-}$ fish showed a pronounced developmental phenotype with early onset retinal degeneration.

In mouse photoreceptors, usherin forms a complex with the other two Usher 2 proteins at the PMC, a structure thought to be involved in transport vesicle docking and trafficking through the connecting cilium (258). Zebrafish usherin has also been found to co-localise with centrin, a connecting cilium marker (364) so likely performs a similar function in zebrafish photoreceptors. Considering this, the morphology of the photoreceptor connecting cilia in the *ush2a* zebrafish retina were examined on electron micrographs and measurement of the cilia widths from each shoulder suggested that there may be some structural changes in the mutant. Among the previous Usher syndrome models, morphological defects have been observed around the connecting cilium in a small percentage of *Whrn* knockout mouse photoreceptor, which included vacuole accumulation and abnormal distance and membrane fusion between the apical inner segment and the connecting cilium (169).

However, the structures observed on TEM are easily affected by alterations in section orientation and further specimens need to be examined to confirm cilia abnormalities in the *ush2a* zebrafish.

In addition to cilia-related observations, examining the *ush2a* retinal ultrastructure revealed the presence of vesicular structures around the photoreceptor inner and outer segment boundary and at the synaptic termini. Although the use of immunogold labelling will be necessary to confirm the identity of these structures, they have the appearance of lysosomes which are hydrolytic enzyme-containing vesicles that can break down many kinds of biomolecules (384). In addition to polymer degradation, lysosomes are involved in various cell processes, including secretion, plasma membrane repair, cell signalling, and energy metabolism. The presence of these organelles within the *ush2a* photoreceptors is atypical and may be related to defective protein trafficking and altered autophagy. Interestingly, the vesicles were noted at 6 mpf and not 12 mpf, suggesting that they are a transient feature of the retinal pathology. Similar observations were previously reported in *ninl* and *dzank1* morphant zebrafish, which are two cilia-related genes known to interact with *ush2a* (364). The morphant photoreceptors were found to accumulate vesicles including lysosomal structures, which were occasionally noted in the inner segment and were very reminiscent of the structures observed in the present study. Importantly, usherin was also found to be mislocalised in these zebrafish, further suggesting that the appearance of these organelles may be related to loss of *ush2a* and its interacting partners that are involved in trafficking through the connecting cilium.

To further explore potential protein trafficking defects in the *ush2a* retina, the localisation of two photopigments, rhodopsin and red opsin, was examined at various ages. In the photoreceptors, rod and cone opsins undergo maturation and packaging in the Golgi

complex in the inner segment, then are transported to the outer segment through the connecting cilium (385). In the *ush2a* retina, while red opsin showed normal labelling at the double cone outer segments at all ages examined, rhodopsin occasionally showed mislocalisation to parts of the rod cells other than the outer segment from 6 mpf. By 12 mpf, the rhodopsin labelling in the rod outer segments had an abnormal appearance which may be a result of prolonged mistrafficking. The finding that rhodopsin and not cone opsin localisation was affected may contribute to primary rod degeneration in the *ush2a* retina. It is also possible that mislocalised rhodopsin may be a consequence of degenerating rod cells rather than the cause of apoptosis, and further work is required to determine the mechanisms. This will include generating a new line of *ush2a* mutants crossed with transgenic fish that express a rod-specific fluorescent marker Tg(*rho*:YFP). Considering that very modest levels of apoptosis were detected at 12 mpf when extensive rhodopsin mislocalisation was observed, it could be postulated that it contributes to apoptosis. Defective rhodopsin trafficking is consistent with the proposed function of the PMC, which was originally identified in frog photoreceptors (386). Numerous rhodopsin-containing vesicles were found in the surrounding cytoplasm of the frog PRC, the structure analogous to the PMC, suggesting that the PRC may be a docking site of vesicles transporting newly synthesised rhodopsin from the Golgi. Immunogold labelling will be necessary to further examine subcellular rhodopsin localisation on electron micrographs of the *ush2a* retina.

Consistent with the findings of the present study, defective photopigment transport has been identified in several IRD models, including those of non-syndromic RP, LCA and Usher syndrome (385). In *whirler* photoreceptors, rhodopsin was found to be mislocalised (249), and mislocalisation of both rhodopsin and cone opsin has been observed in the USH1B mutant mice (242, 249) and zebrafish (255). The proteins

encoded by these mutant genes, whirlin and myosin VIIA, are among several Usher syndrome proteins found to interact with usherin at the mouse PMC (169, 258), making phenotypic similarities between these models likely. However, in contrast to the *ush2a* zebrafish retina, the *Ush2a* mouse was found to have normal rhodopsin labelling while red cone opsin staining showed mislocalisation by p80 (246). The reason for this species discrepancy is unknown. In zebrafish, rhodopsin mislocalisation was also observed in *ninl* and *dzank1* morphant photoreceptors, in which usherin was also mislocalised, supporting a role for usherin and its interacting proteins in rhodopsin transport in fish (364). While the majority of IRD zebrafish models characterised to date have shown developmental phenotypes, disruption of another cilia gene *ahi1* (Joubert syndrome) caused a similar retinal phenotype to the *ush2a* fish showing an adult onset degeneration associated with rhodopsin mislocalisation by 5 mpf (387). Considering that rod cells are the first to be lost in Usher syndrome patients, rhodopsin transport may also be defective in human photoreceptors. Examining patient iPSc-derived retinal cups may provide further insight into these changes.

In addition to retinal disease, Usher syndrome 2 features sensorineural deafness caused by abnormal development of the cochlear hair cells, and therefore the sensory hair cells of the *ush2a* zebrafish were examined. In mammals, usherin forms part of the ankle links that form between the hair cell stereocilia, thought to be essential for regulating growth and organisation postnatally (263). *Ush2a* mice showed morphological defects in their cochlear stereociliary bundles including distorted shapes and mislocalised kinocilia (263). The developing zebrafish inner ear possesses two sensory patches involved in hearing and balance, the anterior macula (utricle) and posterior macula (saccule), which contain hair cells that are homologous to those of the mammalian mechanosensory system (251). In zebrafish, usherin

expression has been detected in the stereocilia and kinocilia of the anterior macula hair cells (368). Upon examination at 6 dpf, the developing anterior macula in *ush2a* zebrafish had fewer stereociliary hair bundles within the macula patch. Previously, splayed stereociliary bundles have been observed in the sensory hair cells of zebrafish Usher models *myo7aa* (144), *cdh23* (154), *ush1c* (149) and *clrn1* (174) and reduced hair bundle numbers were found in the anterior and/or posterior macula of *myo7aa*, *cdh23* and *ush1c* zebrafish larvae (149, 368). The stereociliary bundle morphology appeared to be relatively intact in the *ush2a* zebrafish, indicating a milder phenotype compared to Usher 1 and 3 models. The reduction in vibrational startle reflexes in *ush2a* larvae suggested that hair cell function may be affected but this was only a very crude and rapid behavioural assay. Investigating hair cell function using more sensitive behavioural or electrophysiological experiments will provide more information on the severity of the dysfunction.

In addition to the audiovestibular organs, aquatic vertebrates possess a mechanosensory lateral line system for detecting water movements, which is made up of numerous hair cell clusters known as neuromasts (388). Expression of several Usher genes or proteins have been localised to the neuromasts, including *myo7aa* (144), *cdh23* (154), *pcdh15a* (252), *ush1c* (149), *cib2 (127)* and *clrn1* (174) and examination of their respective mutant phenotypes has yielded varying results. In *myo7aa* and *cdh23* zebrafish, the number of hair bundles per neuromast showed a similar reduction to that in *ush2a* zebrafish reported here (~20%) (252). The neuromasts of *clrn1* larvae were functionally defective with a slight decrease in hair bundle number (174), and the corresponding morphants also showed shortening of the kinocilia, defective vesicular turnover, mislocalisation of the synaptic components (220). Most recently, the neuromasts of *pcdh15a* mutant zebrafish were well characterised, showing a reduction in kinociliary length as well as in the number of

kinocilia per neuromast and revealing a role for *pcdh15a* in ciliary cargo transport (389). As the neuromast abnormalities observed in *ush2a* fish in the present study i.e reduced hair bundles and kinocilia resemble those seen in the other Usher mutants, *ush2a* may also be involved in cilia development and function in the zebrafish lateral line. To explore this further, determining localisation within the neuromasts using an usherin specific antibody will be essential before examining functional changes such as microphonic potential recordings or FM1-43 uptake.

In summary, the findings of the present study suggest that the *USH2A* gene and protein is generally well conserved in the zebrafish in both structure and function. CRISPR/Cas9 proved to be an effective technique in producing an *ush2a* mutant zebrafish line for investigating the *USH2A*-associated disease pathophysiology. Initial phenotypic analysis of the *ush2a* retina provided new insight into the disorder, revealing rhodopsin mislocalisation and subcellular changes on the ultrastructure potentially associated with trafficking defects, in line with other models of Usher syndrome. The adult onset retinal degeneration predominantly affecting rod photoreceptors in the *ush2a* zebrafish is consistent with the *USH2A* patient clinical symptoms, supporting this mutant as an informative model. In addition, assessment of the mechanosensory hair cells implicated developmental defects which have been previously described in *Ush2a* mutant mice. Overall, the findings highlight the *ush2a* zebrafish as a promising model for further analysis and preclinical therapeutic studies.

5 Conclusion

In this thesis, investigating the pathophysiology of retinopathies caused by *KCNJ13* and *USH2A* mutations using zebrafish has contributed towards understanding the mechanisms of these blinding disorders. Both zebrafish mutant lines examined showed an adult onset degeneration, adding to the growing resource of adult zebrafish disease models. Aside from this, the disease progression was notably different between these models; in *ush2a,* the photoreceptor loss showed a slow progression primarily affecting rods while the *obe*^{td15} fish showed a rapid, severe and widespread retinal degeneration, which is relatively consistent with their respective clinical phenotypes. Each investigation benefited largely from the use of electron microscopy to uncover informative subcellular changes in the retinal ultrastructure. SD-OCT, a relatively recently established technique for zebrafish imaging, was also invaluable for efficient longitudinal monitoring of retinal structure in both zebrafish lines and revealed previously undescribed retinovascular changes in the *obe*^{td15} zebrafish. These studies have highlighted avenues for further experimentation both within the zebrafish mutants and relevant cellular models. These zebrafish lines offer cost-effective non-mammalian alternatives to their corresponding mouse models, which were either embryonic lethal or showed a very late onset degeneration, and have further reinforced the value of this organism for modelling retinal diseases.

5.1 Overview of study

KCNJ13 mutations cause rare but early-onset and severe retinal disease, highlighting a strong need for therapeutic interventions. In this thesis, the retinal pathophysiology was examined by characterising the previously unexplored retinal phenotype in the pre-existing zebrafish model *obe*^{td15} through the use of histology, SD-OCT, electron

microscopy and optokinetic testing. Severe retinal degeneration was notable at 12 mpf in *obe*^{td15} fish with changes in visual function. An important observation was the phagosome and mitochondrial alterations in the RPE of *obe*^{td15} fish before degeneration, supported by qRT-PCR and ATP data, which have not been described previously. Gene and protein expression changes, including that of GFAP, hsp60, *bcla2*, also suggested that the retina was under stress, likely due to oxidative changes. It is interesting that similar alterations in the RPE are associated with age-related macular degeneration and this may implicate common mechanisms between the disorders. In this study, the inner retinal vasculature and vitreous of the *obe*^{td15} zebrafish was also examined using SD-OCT and revealed irregular retinovascular changes with vitreal deposits, showing some resemblance to both the SVD and LCA phenotype. In addition, examination of previously unreported patients from two unrelated *KCNJ13*-related LCA families harbouring the same missense mutation showed differences in the presence of retinovascular abnormalities, with two affected members of one family showing a severe fibrovascular proliferation that was not apparent in younger affected members of a second family. The variability of the clinical phenotype among *KCNJ13* patients may be dependent on the position of the mutation in the gene as well as from other modifying genetic factors, plus age of onset, highlighting the need for regular monitoring.

The *USH2A* gene is associated with a significant amount of syndromic and non-syndromic RP cases and understanding these disorders will have a substantial effect on visual loss in the population. In this thesis, CRISPR/Cas9 was used to generate an *ush2a* mutant zebrafish in which to explore the pathophysiology of the *USH2A* retinopathy. The retinal phenotype was assessed using histological evaluation, SD-OCT, electron microscopy and retinal immunostaining. This revealed an adult onset slowly progressive rod photoreceptor degeneration, with apparent preservation of

cone cells. In *USH2A*-related RP, the disease follows a similar course with initial rod death (peripheral vision loss), and the macula (cones) affected last. The reason for this pattern of photoreceptor loss is unclear, as usherin expression has been detected at the PMC in both rod and cone photoreceptors. In the zebrafish, the differences could be related to the predominance of cones in the retina, with the critical mass of cones over rods producing a slower degeneration. Furthermore, *ush2a* may be involved in processes within the cone cells that are less critical to their survival. Immunohistochemistry and examination of the *ush2a* retinal ultrastructure suggested that disruption of *ush2a* led to trafficking-related defects in the rod photoreceptors, apparent by incomplete transport of the photopigment rhodopsin and the presence of lysosomal vesicles at the connecting cilium. This is consistent with the proposed function of usherin in mammalian photoreceptors and the phenotype of other Usher syndrome models. Overlap with the phenotypes of other Usher models suggests this will be informative for the pathophysiology of not only *USH2A* retinopathies but other Usher syndrome subtypes.

5.2 Future work

The findings on the *KCNJ13* retinal pathophysiology have provided a focus for future investigations on patient iPSC-derived cellular models; iPSCs have already been produced from a homozygous nonsense (p.Arg66*) patient fibroblasts, which will be converted to RPE cells. Using these cells, phagosome-related defects could be assessed using RPE phagocytosis assays. In addition, mitochondrial function will be investigated using Seahorse XF analysis. If mitochondrial function is affected in the patient RPE cells, the use of antioxidant treatments or exposure to near-infrared light to support ATP levels may be suitable options for preclinical therapeutic studies. These treatments can also be tested alongside in the *obe*^{td15} zebrafish to further

assess efficacy in an *in vivo* preclinical model. Using the *obe*^{td15} fish, retinovascular changes will also be further explored. The mutants have already been crossed with transgenic zebrafish with a vascular fluorescent marker to generate a double line (*obe*^{td15};Tg[*fli1a*:GFP]), which will aid visualisation of the vasculature in future experiments. Possible alterations in the expression of VEGF-related proteins in the mutant retina will be examined using either immunostaining or western blot to determine if they are involved in the retinal vessel abnormalities. This may highlight another avenue for treatment in certain *KCNJ13*-LCA patients through the use of anti-VEGF therapy.

Another key research question is why different mutations in *KCNJ13* cause such variability in clinical phenotype. To address this, RPE and retinal morphology can be examined using different mutation-specific cellular models, within which Kir7.1 function can also be assessed using electrophysiological methods such as patch clamping. In addition, these models could be used to investigate genotype-specific molecular alterations, potentially using RNA-seq, which will aid in determining the mechanisms underlying clinical phenotypic variability.

For future *USH2A* studies, further immunolabelling experiments will be necessary to establish alterations in subcellular localisation of usherin and potential interacting proteins, including opsins, in the *ush2a* zebrafish, and the potential downstream consequences of these changes that contribute to apoptosis e.g. endoplasmic reticulum stress. Longer follow up will be necessary to examine cone changes that may be forthcoming. Future experiments will also focus on why rods and not cones are affected initially. A *ush2a* mutant line with a rod-specific marker (*ush2a*;Tg[*rho*:YFP]) has been produced for further investigation of the rod photoreceptors; generating additional transgenic lines with cone specific markers e.g.

lws1/lws2 reported with a fluorescent protein for red cones, will aid in isolating photoreceptor subtypes for single cell RNA-seq analysis.

A key purpose of producing an *ush2a* zebrafish line was for use in future therapeutic studies. As the *USH2A* gene is too large for traditional viral gene therapy, our lab is interested in developing a non-viral gene therapy for treating *USH2A*-related RP. The *USH2A* gene will be cloned into scaffold/matrix-attached region (S/MAR)-containing vectors, which are non-viral episomal vectors with an unlimited carrying capacity, with the aim of restoring gene expression in the *ush2a* zebrafish retina, likely via intravitreal injection. Establishing the best method of transfection into the juvenile or adult zebrafish retina with DNA vectors will be necessary, as this has not been achieved previously. In this thesis, the identification of phenotypic changes in the *ush2a* retina e.g. apoptotic photoreceptor numbers, rhodopsin mislocalisation, has highlighted measurable outcomes for evaluating for therapeutic efficacy. In addition, iPSCs have been generated from fibroblasts taken from a patient with *USH2A*-related Usher syndrome; these will be used to produce retinal organoids to both continue investigation into the *USH2A* pathophysiology and transfect with the non-viral vectors to restore *USH2A* expression. If successful, this could develop into a promising treatment for many affected individuals with RP.

6 References

1. Liew G, Michaelides M, Bunce C. A comparison of the causes of blindness certifications in England and Wales in working age adults (16-64 years), 1999-2000 with 2009-2010. *BMJ open*. 2014;4(2):e004015.
2. Mitry D, et al. Causes of certifications for severe sight impairment (blind) and sight impairment (partial sight) in children in England and Wales. *Br J Ophthalmol*. 2013;97(11):1431-6.
3. Daiger S, Sullivan L, Bowne S, Rossiter B. RetNet, the Retinal Information Network. *University of Texas Houston Health Science Center*. [Accessed 15 December 2017]. Available from: http://www.sph.uth.tmc.edu/RetNet/.
4. Richardson R, Tracey-White D, Webster A, Moosajee M. The zebrafish eye-a paradigm for investigating human ocular genetics. *Eye (Lond)*. 2016.
5. Sung CH, Chuang JZ. The cell biology of vision. *J Cell Biol*. 2010;190(6):953-63.
6. Wright AF, Chakarova CF, Abd El-Aziz MM, Bhattacharya SS. Photoreceptor degeneration: genetic and mechanistic dissection of a complex trait. *Nat Rev Genet*. 2010;11(4):273-84.
7. Hoon M, Okawa H, Della Santina L, Wong RO. Functional architecture of the retina: development and disease. *Prog Retin Eye Res*. 2014;42:44-84.
8. Slijkerman RW, et al. The pros and cons of vertebrate animal models for functional and therapeutic research on inherited retinal dystrophies. *Prog Retin Eye Res*. 2015;48:137-59.
9. Strauss O. The retinal pigment epithelium in visual function. *Physiol Rev*. 2005;85(3):845-81.
10. Carlson BM. Chapter 13 - Sense Organs. Human Embryology and Developmental Biology (Fifth Edition). Philadelphia: W.B. Saunders; 2014. p. 269-93.
11. Wong ROL. Introduction – from eye field to eyesight. In: Sernagor E, Eglen S, Harris B, Wong R, editors. Retinal Development:: Cambridge University Press; 2006. p. 1-7.
12. Graw J. Eye development. *Curr Top Dev Biol*. 2010;90:343-86.
13. Hufnagel RB, Brown NL. Chapter 27 - Specification of Retinal Cell Types A2 - Rubenstein, John L.R. In: Rakic P, editor. Patterning and Cell Type Specification in the Developing CNS and PNS. Oxford: Academic Press; 2013. p. 519-36.
14. Yang X-J. Roles of cell-extrinsic growth factors in vertebrate eye pattern formation and retinogenesis. *Semin Cell Dev Biol*. 2004;15(1):91-103.

15. Broadgate S, Yu J, Downes SM, Halford S. Unravelling the genetics of inherited retinal dystrophies: Past, present and future. *Prog Retin Eye Res*. 2017;59:53-96.

16. Landau K, Kurz-Levin M. Retinal disorders. *Handb Clin Neurol*. 2011;102:97-116.

17. Dias MF, et al. Molecular genetics and emerging therapies for retinitis pigmentosa: Basic research and clinical perspectives. *Prog Retin Eye Res*. 2017.

18. Moore NA, Morral N, Ciulla TA, Bracha P. Gene therapy for inherited retinal and optic nerve degenerations. *Expert Opin Biol Ther*. 2017:1-13.

19. Wiley LA, et al. Patient-specific induced pluripotent stem cells (iPSCs) for the study and treatment of retinal degenerative diseases. *Prog Retin Eye Res*. 2015;44:15-35.

20. Zrenner E, et al. Subretinal electronic chips allow blind patients to read letters and combine them to words. *Proc Biol Sci*. 2011;278(1711):1489-97.

21. Fadool JM, Dowling JE. Zebrafish models of retinal development and disease. In: Sernagor E, Eglen S, Harris B, Wong R, editors. Retinal Development:: Cambridge University Press; 2006. p. 342-70.

22. Branchek T, Bremiller R. The development of photoreceptors in the zebrafish, Brachydanio rerio. I. Structure. *J Comp Neurol*. 1984;224(1):107-15.

23. Tarboush R, Chapman GB, Connaughton VP. Ultrastructure of the distal retina of the adult zebrafish, Danio rerio. *Tissue Cell*. 2012;44(4):264-79.

24. Chhetri J, Jacobson G, Gueven N. Zebrafish--on the move towards ophthalmological research. *Eye (Lond)*. 2014;28(4):367-80.

25. Okinawa Institute of Science and Technology. Zebrafish retinal development. 19 August 2014. [Accessed 15 December 2017]. Available from: https://www.oist.jp/news-center/photos/zebrafish-retina-development.

26. Hodel C, et al. Myosin VIIA is a marker for the cone accessory outer segment in zebrafish. *Anatomical Record-Advances in Integrative Anatomy and Evolutionary Biology*. 2014;297(9):1777-84.

27. Yacob A, Wise C, Kunz YW. The accessory outer segment of rods and cones in the retina of the guppy, Poecilia reticulata P. (Teleostei). An electron microscopical study. *Cell Tissue Res*. 1977;177(2):181-93.

28. Hodel C, Neuhauss SC, Biehlmaier O. Time course and development of light adaptation processes in the outer zebrafish retina. *Anat Rec A Discov Mol Cell Evol Biol*. 2006;288(6):653-62.

29. Burnside B. Light and circadian regulation of retinomotor movement. *Prog Brain Res*. 2001;131:477-85.

30. Bosch E, Horwitz J, Bok D. Phagocytosis of outer segments by retinal pigment epithelium: phagosome-lysosome interaction. *J Histochem Cytochem*. 1993;41(2):253-63.

31. Jiang M, et al. Microtubule motors transport phagosomes in the RPE, and lack of KLC1 leads to AMD-like pathogenesis. *J Cell Biol*. 2015;210(4):595-611.

32. Schutt F, Aretz S, Auffarth GU, Kopitz J. Moderately reduced ATP levels promote oxidative stress and debilitate autophagic and phagocytic capacities in human RPE cells. *Invest Ophthalmol Vis Sci*. 2012;53(9):5354-61.

33. Kuny S, Cho WJ, Dimopoulos IS, Sauve Y. Early onset ultrastructural and functional defects in RPE and photoreceptors of a Stargardt-Like macular dystrophy (STGD3) transgenic mouse model. *Invest Ophthalmol Vis Sci*. 2015;56(12):7109-21.

34. Reyes-Reveles J, Dhingra A, Alexander D, Bragin A, Philp NJ, Boesze-Battaglia K. Phagocytosis-dependent ketogenesis in retinal pigment epithelium. *J Biol Chem*. 2017;292(19):8038-47.

35. Park SW, et al. Dry age-related macular degeneration like pathology in aged 5XFAD mice: Ultrastructure and microarray analysis. *Oncotarget*. 2017;8(25):40006-18.

36. Karan G, et al. Lipofuscin accumulation, abnormal electrophysiology, and photoreceptor degeneration in mutant ELOVL4 transgenic mice: a model for macular degeneration. *Proc Natl Acad Sci U S A*. 2005;102(11):4164-9.

37. Gibbs D, Kitamoto J, Williams DS. Abnormal phagocytosis by retinal pigmented epithelium that lacks myosin VIIa, the Usher syndrome 1B protein. *Proc Natl Acad Sci U S A*. 2003;100(11):6481-6.

38. Wavre-Shapton ST, Tolmachova T, Lopes da Silva M, Futter CE, Seabra MC. Conditional ablation of the choroideremia gene causes age-related changes in mouse retinal pigment epithelium. *PLoS One*. 2013;8(2):e57769.

39. Gordiyenko NV, Fariss RN, Zhi C, MacDonald IM. Silencing of the CHM gene alters phagocytic and secretory pathways in the retinal pigment epithelium. *Invest Ophthalmol Vis Sci*. 2010;51(2):1143-50.

40. Lefevere E, Toft-Kehler AK, Vohra R, Kolko M, Moons L, Van Hove I. Mitochondrial dysfunction underlying outer retinal diseases. *Mitochondrion*. 2017.

41. Kim J, et al. The presence of megamitochondria in the ellipsoid of photoreceptor inner segment of the zebrafish retina. *Anat Histol Embryol*. 2005;34(6):339-42.

42. Masuda T, Wada Y, Kawamura S. ES1 is a mitochondrial enlarging factor contributing to form mega-mitochondria in zebrafish cones. *Sci Rep*. 2016;6:22360.
43. Barot M, Gokulgandhi MR, Mitra AK. Mitochondrial dysfunction in retinal diseases. *Curr Eye Res*. 2011;36(12):1069-77.
44. Howe K, et al. The zebrafish reference genome sequence and its relationship to the human genome. *Nature*. 2013;496(7446):498-503.
45. Link BA, Collery RF. Zebrafish models of retinal disease. *Annual Review of Vision Science*. 2015;1(1):125-53.
46. Haffter P, et al. The identification of genes with unique and essential functions in the development of the zebrafish, Danio rerio. *Development*. 1996;123:1-36.
47. Malicki J, et al. Mutations affecting development of the zebrafish retina. *Development*. 1996;123:263-73.
48. Gross JM, et al. Identification of zebrafish insertional mutants with defects in visual system development and function. *Genetics*. 2005;170(1):245-61.
49. Brockerhoff SE, Hurley JB, Janssen-Bienhold U, Neuhauss SC, Driever W, Dowling JE. A behavioral screen for isolating zebrafish mutants with visual system defects. *Proc Natl Acad Sci U S A*. 1995;92(23):10545-9.
50. Doyon Y, et al. Heritable targeted gene disruption in zebrafish using designed zinc-finger nucleases. *Nat Biotechnol*. 2008;26(6):702-8.
51. Meng X, Noyes MB, Zhu LJ, Lawson ND, Wolfe SA. Targeted gene inactivation in zebrafish using engineered zinc-finger nucleases. *Nat Biotechnol*. 2008;26(6):695-701.
52. Sander JD, et al. Targeted gene disruption in somatic zebrafish cells using engineered TALENs. *Nat Biotechnol*. 2011;29(8):697-8.
53. Huang P, Xiao A, Zhou M, Zhu Z, Lin S, Zhang B. Heritable gene targeting in zebrafish using customized TALENs. *Nat Biotechnol*. 2011;29(8):699-700.
54. Hwang WY, et al. Efficient genome editing in zebrafish using a CRISPR-Cas system. *Nat Biotechnol*. 2013;31(3):227-9.
55. Sander JD, Joung JK. CRISPR-Cas systems for editing, regulating and targeting genomes. *Nat Biotechnol*. 2014;32(4):347-55.
56. Moore FE, et al. Improved somatic mutagenesis in zebrafish using transcription activator-like effector nucleases (TALENs). *PLoS One*. 2012;7(5):e37877.
57. Li T, et al. TAL nucleases (TALNs): hybrid proteins composed of TAL effectors and FokI DNA-cleavage domain. *Nucleic Acids Res*. 2011;39(1):359-72.
58. Bedell VM, et al. In vivo genome editing using a high-efficiency TALEN system. *Nature*. 2012;491(7422):114-8.

59. Horvath P, Barrangou R. CRISPR/Cas, the immune system of bacteria and archaea. *Science*. 2010;327(5962):167-70.

60. Fu Y, et al. High-frequency off-target mutagenesis induced by CRISPR-Cas nucleases in human cells. *Nat Biotechnol*. 2013;31(9):822-6.

61. Auer TO, Duroure K, De Cian A, Concordet JP, Del Bene F. Highly efficient CRISPR/Cas9-mediated knock-in in zebrafish by homology-independent DNA repair. *Genome Res*. 2014;24(1):142-53.

62. Hruscha A, et al. Efficient CRISPR/Cas9 genome editing with low off-target effects in zebrafish. *Development*. 2013;140(24):4982-7.

63. Liu D, et al. Efficient gene targeting in zebrafish mediated by a zebrafish-codon-optimized Cas9 and evaluation of off-targeting effect. *J Genet Genomics*. 2014;41(1):43-6.

64. Thomas HR, Percival SM, Yoder BK, Parant JM. High-throughput genome editing and phenotyping facilitated by high resolution melting curve analysis. *PLoS One*. 2014;9(12):e114632.

65. Li J, Zhang BB, Ren YG, Gu SY, Xiang YH, Du JL. Intron targeting-mediated and endogenous gene integrity-maintaining knockin in zebrafish using the CRISPR/Cas9 system. *Cell Res*. 2015;25(5):634-7.

66. Shah AN, Davey CF, Whitebirch AC, Miller AC, Moens CB. Rapid reverse genetic screening using CRISPR in zebrafish. *Nature methods*. 2015;12(6):535-40.

67. Varshney GK, et al. High-throughput gene targeting and phenotyping in zebrafish using CRISPR/Cas9. *Genome Res*. 2015;25(7):1030-42.

68. Nasevicius A, Ekker SC. Effective targeted gene 'knockdown' in zebrafish. *Nat Genet*. 2000;26(2):216-20.

69. Raghupathy RK, McCulloch DL, Akhtar S, Al-mubrad TM, Shu X. Zebrafish model for the genetic basis of X-linked retinitis pigmentosa. *Zebrafish*. 2013;10(1):62-9.

70. Koenekoop RK. An overview of Leber congenital amaurosis: a model to understand human retinal development. *Surv Ophthalmol*. 2004;49(4):379-98.

71. Kumaran N, Moore AT, Weleber RG, Michaelides M. Leber congenital amaurosis/early-onset severe retinal dystrophy: clinical features, molecular genetics and therapeutic interventions. *Br J Ophthalmol*. 2017;101(9):1147-54.

72. Chacon-Camacho OF, Zenteno JC. Review and update on the molecular basis of Leber congenital amaurosis. *World journal of clinical cases*. 2015;3(2):112-24.

73. Perrault I, et al. Spectrum of retGC1 mutations in Leber's congenital amaurosis. *Eur J Hum Genet*. 2000;8(8):578-82.

74. Krapivinsky G, Medina I, Eng L, Krapivinsky L, Yang Y, Clapham DE. A novel inward rectifier K+ channel with unique pore properties. *Neuron*. 1998;20(5):995-1005.

75. Partiseti M, Collura V, Agnel M, Culouscou JM, Graham D. Cloning and characterization of a novel human inwardly rectifying potassium channel predominantly expressed in small intestine. *FEBS Lett*. 1998;434(1-2):171-6.

76. Doring F, et al. The epithelial inward rectifier channel Kir7.1 displays unusual K+ permeation properties. *J Neurosci*. 1998;18(21):8625-36.

77. Hibino H, Inanobe A, Furutani K, Murakami S, Findlay I, Kurachi Y. Inwardly rectifying potassium channels: their structure, function, and physiological roles. *Physiol Rev*. 2010;90(1):291-366.

78. Yang D, Swaminathan A, Zhang X, Hughes BA. Expression of Kir7.1 and a novel Kir7.1 splice variant in native human retinal pigment epithelium. *Exp Eye Res*. 2008;86(1):81-91.

79. Hejtmancik JF, et al. Mutations in KCNJ13 cause autosomal-dominant snowflake vitreoretinal degeneration. *Am J Hum Genet*. 2008;82(1):174-80.

80. Nakamura N, Suzuki Y, Sakuta H, Ookata K, Kawahara K, Hirose S. Inwardly rectifying K+ channel Kir7.1 is highly expressed in thyroid follicular cells, intestinal epithelial cells and choroid plexus epithelial cells: implication for a functional coupling with Na+,K+-ATPase. *Biochem J*. 1999;342 (Pt 2):329-36.

81. Sergouniotis PI, et al. Recessive mutations in KCNJ13, encoding an inwardly rectifying potassium channel subunit, cause leber congenital amaurosis. *Am J Hum Genet*. 2011;89(1):183-90.

82. Yang D, Pan A, Swaminathan A, Kumar G, Hughes BA. Expression and localization of the inwardly rectifying potassium channel Kir7.1 in native bovine retinal pigment epithelium. *Invest Ophthalmol Vis Sci*. 2003;44(7):3178-85.

83. Hughes BA, Takahira M. Inwardly rectifying K+ currents in isolated human retinal pigment epithelial cells. *Invest Ophthalmol Vis Sci*. 1996;37(6):1125-39.

84. Pattnaik BR, et al. A novel KCNJ13 nonsense mutation and loss of Kir7.1 channel function causes Leber congenital amaurosis (LCA16). *Hum Mutat*. 2015;36(7):720-7.

85. Perez-Roustit S, et al. Leber congenital amaurosis with large retinal pigment clumps caused by compound heterozygous mutations in *KCNJ13*. *Retin Cases Brief Rep*. 2017;11(3):221-6.

86. Khan AO, Bergmann C, Neuhaus C, Bolz HJ. A distinct vitreo-retinal dystrophy with early-onset cataract from recessive KCNJ13 mutations. *Ophthalmic Genet*. 2015;36(1):79-84.

87. Yang RB, Robinson SW, Xiong WH, Yau KW, Birch DG, Garbers DL. Disruption of a retinal guanylyl cyclase gene leads to cone-specific dystrophy and paradoxical rod behavior. *J Neurosci*. 1999;19(14):5889-97.

88. Redmond TM, et al. Rpe65 is necessary for production of 11-cis-vitamin A in the retinal visual cycle. *Nat Genet*. 1998;20(4):344-51.

89. Mehalow AK, et al. CRB1 is essential for external limiting membrane integrity and photoreceptor morphogenesis in the mammalian retina. *Hum Mol Genet*. 2003;12(17):2179-89.

90. Maeda A, et al. Retinol dehydrogenase (RDH12) protects photoreceptors from light-induced degeneration in mice. *J Biol Chem*. 2006;281(49):37697-704.

91. Acland GM, et al. Gene therapy restores vision in a canine model of childhood blindness. *Nat Genet*. 2001;28(1):92-5.

92. Lheriteau E, et al. Successful gene therapy in the RPGRIP1-deficient dog: a large model of cone-rod dystrophy. *Mol Ther*. 2014;22(2):265-77.

93. Omori Y, Malicki J. oko meduzy and related crumbs genes are determinants of apical cell features in the vertebrate embryo. *Curr Biol*. 2006;16(10):945-57.

94. Schonthaler HB, et al. Evidence for RPE65-independent vision in the cone-dominated zebrafish retina. *Eur J Neurosci*. 2007;26(7):1940-9.

95. Baye LM, et al. The N-terminal region of centrosomal protein 290 (CEP290) restores vision in a zebrafish model of human blindness. *Hum Mol Genet*. 2011;20(8):1467-77.

96. Stiebel-Kalish H, et al. Gucy2f zebrafish knockdown--a model for Gucy2d-related leber congenital amaurosis. *Eur J Hum Genet*. 2012;20(8):884-9.

97. Pellikka M, et al. Crumbs, the Drosophila homologue of human CRB1/RP12, is essential for photoreceptor morphogenesis. *Nature*. 2002;416(6877):143-9.

98. Villanueva S, et al. Cleft palate, moderate lung developmental retardation and early postnatal lethality in mice deficient in the Kir7.1 inwardly rectifying K+ channel. *PLoS One*. 2015;10(9):e0139284.

99. Zhong H, Chen Y, Li Y, Chen R, Mardon G. CRISPR-engineered mosaicism rapidly reveals that loss of Kcnj13 function in mice mimics human disease phenotypes. *Sci Rep*. 2015;5:8366.

100. Shahi PK, et al. Abnormal electroretinogram after Kir7.1 channel suppression suggests role in retinal electrophysiology. *Sci Rep*. 2017;7(1):10651.

101. Haffter P, et al. Mutations affecting pigmentation and shape of the adult zebrafish. *Dev Genes Evol*. 1996;206(4):260-76.

102. Iwashita M, et al. Pigment pattern in jaguar/obelix zebrafish is caused by a Kir7.1 mutation: implications for the regulation of melanosome movement. *PLoS Genet*. 2006;2(11):e197.

103. Weleber RG, et al. Results at 2 years after gene therapy for RPE65-deficient Leber congenital amaurosis and severe early-childhood-onset retinal dystrophy. *Ophthalmology*. 2016;123(7):1606-20.

104. Bainbridge JW, et al. Long-term effect of gene therapy on Leber's congenital amaurosis. *N Engl J Med*. 2015;372(20):1887-97.

105. Testa F, et al. Three-year follow-up after unilateral subretinal delivery of adeno-associated virus in patients with Leber congenital Amaurosis type 2. *Ophthalmology*. 2013;120(6):1283-91.

106. Jacobson SG, et al. Improvement and decline in vision with gene therapy in childhood blindness. *N Engl J Med*. 2015;372(20):1920-6.

107. Usher C. On the inheritance of retinitis pigmentosa, with notes of cases. *R Lond Ophthalmol Hosp Rep*. 1914;19:130-236.

108. Vernon M. Usher's syndrome--deafness and progressive blindness. Clinical cases, prevention, theory and literature survey. *J Chronic Dis*. 1969;22(3):133-51.

109. Fortnum HM, Summerfield AQ, Marshall DH, Davis AC, Bamford JM. Prevalence of permanent childhood hearing impairment in the United Kingdom and implications for universal neonatal hearing screening: questionnaire based ascertainment study. *Br Med J*. 2001;323(7312):536-9.

110. Marazita ML, Ploughman LM, Rawlings B, Remington E, Arnos KS, Nance WE. Genetic epidemiologic studies of early-onset deafness in the United States school-age population. *Am J Med Genet*. 1993;46(5):486-91.

111. Rosenberg T, Haim M, Hauch AM, Parving A. The prevalence of Usher syndrome and other retinal dystrophy-hearing impairment associations. *Clin Genet*. 1997;51(5):314-21.

112. Spandau UHM, Rohrschneider K. Prevalence and geographical distribution of Usher syndrome in Germany. *Graefes Arch Clin Exp Ophthalmol*. 2002;240(6):495-8.

113. Boughman JA, Vernon M, Shaver KA. Usher syndrome - definition and estimate of prevalence from two high-risk populations. *J Chronic Dis*. 1983;36(8):595-603.

114. Grondahl J. Estimation of prognosis and prevalence of retinitis pigmentosa and Usher syndrome in Norway. *Clin Genet*. 1987;31(4):255-64.

115. Von Graefe A. Vereinzelte Beobachtungen und Bemerkungen. Exceptionelles Verhalten des Gesichtsfeldes bei Pigmententartung des Netzhaut. *Albrecht Graefes Arch Klin Ophthalmol*. 1858;4:250-3.

116. Petit C. Usher syndrome: From genetics to pathogenesis. *Annual Review of Genomics and Human Genetics*. 2001;2:271-97.

117. Reiners J, Nagel-Wolfrum K, Juergens K, Maerker T, Wolfrum U. Molecular basis of human Usher syndrome: deciphering the meshes of the Usher protein network provides insights into the pathomechanisms of the Usher disease. *Exp Eye Res*. 2006;83(1):97-119.

118. El-Amraoui A, Petit C. The retinal phenotype of Usher syndrome: Pathophysiological insights from animal models. *Comptes Rendus Biologies*. 2014;337(3):167-77.

119. Pakarinen L, Karjalainen S, Simola KO, Laippala P, Kaitalo H. Usher's syndrome type 3 in Finland. *Laryngoscope*. 1995;105(6):613-7.

120. Ness SL, et al. Genetic homogeneity and phenotypic variability among Ashkenazi Jews with Usher syndrome type III. *J Med Genet*. 2003;40(10):767-72.

121. Mathur P, Yang J. Usher syndrome: Hearing loss, retinal degeneration and associated abnormalities. *Biochim Biophys Acta*. 2014;1852(3):406-20.

122. Cohen M, Bitner-Glindzicz M, Luxon L. The changing face of Usher syndrome: Clinical implications. *Int J Audiol*. 2007;46(2):82-93.

123. Liu XZ, et al. Mutations in the myosin VIIA gene cause a wide phenotypic spectrum, including atypical Usher syndrome. *Am J Hum Genet*. 1998;63(3):909-12.

124. Ahmed ZM, et al. PCDH15 is expressed in the neurosensory epithelium of the eye and ear and mutant alleles are responsible for both USH1F and DFNB23. *Hum Mol Genet*. 2003;12(24):3215-23.

125. Ahmed ZM, et al. Nonsyndromic recessive deafness DFNB18 and Usher syndrome type IC are allelic mutations of USHIC. *Hum Genet*. 2002;110(6):527-31.

126. Schultz JM, et al. Allelic hierarchy of CDH23 mutations causing non-syndromic deafness DFNB12 or Usher syndrome USH1D in compound heterozygotes. *J Med Genet*. 2011;48(11):767-75.

127. Riazuddin S, et al. Alterations of the CIB2 calcium- and integrin-binding protein cause Usher syndrome type 1J and nonsyndromic deafness DFNB48. *Nat Genet*. 2012;44(11):1265-71.

128. Rivolta C, Berson EL, Dryja TP. Paternal uniparental heterodisomy with partial isodisomy of chromosome 1 in a patient with retinitis pigmentosa mutation in without hearing loss and a missense the usher syndrome type II gene USH2A. *Arch Ophthalmol*. 2002;120(11):1566-71.

129. Nakayama J, et al. A nonsense mutation of the MASS1 gene in a family with febrile and afebrile seizures. *Ann Neurol*. 2002;52(5):654-7.

130. Ebermann I, et al. A novel gene for Usher syndrome type 2: mutations in the long isoform of whirlin are associated with retinitis pigmentosa and sensorineural hearing loss. *Hum Genet*. 2007;121(2):203-11.

131. Schneider E, et al. Homozygous disruption of PDZD7 by reciprocal translocation in a consanguineous family: a new member of the Usher syndrome protein interactome causing congenital hearing impairment. *Hum Mol Genet*. 2009;18(4):655-66.

132. Oonk AMM, et al. Nonsyndromic hearing loss caused by USH1G mutations: widening the USH1G disease spectrum. *Ear Hear*. 2015;36(2):205-11.

133. Yang T, Wei X, Chai Y, Li L, Wu H. Genetic etiology study of the non-syndromic deafness in Chinese Hans by targeted next-generation sequencing. *Orphanet J Rare Dis*. 2013;8:85.

134. Khan MI, et al. CLRN1 mutations cause nonsyndromic retinitis pigmentosa. *Ophthalmology*. 2011;118(7):1444-8.

135. Wolfrum U, Liu XR, Schmitt A, Udovichenko IP, Williams DS. Myosin VIIa as a common component of cilia and microvilli. *Cell Motil Cytoskeleton*. 1998;40(3):261-71.

136. Scanlan MJ, et al. Isoforms of the human PDZ-73 protein exhibit differential tissue expression. *Biochimica Et Biophysica Acta-Gene Structure and Expression*. 1999;1445(1):39-52.

137. Overlack N, Maerker T, Latz M, Nagel-Wolfrurn K, Wolfrum U. SANS (USH1G) expression in developing and mature mammalian retina. *Vision Res*. 2008;48(3):400-12.

138. van Wijk E, et al. Identification of 51 novel exons of the Usher syndrome type 2A (USH2A) gene that encode multiple conserved functional domains and that are mutated in patients with Usher syndrome type II. *Am J Hum Genet*. 2004;74(4):738-44.

139. Vastinsalo H, et al. Alternative splice variants of the USH3A gene Clarin 1 (CLRN1). *Eur J Hum Genet*. 2011;19(1):30-5.

140. Bhattacharya G, Miller C, Kimberling WJ, Jablonski MM, Cosgrove D. Localization and expression of usherin: a novel basement membrane protein defective in people with Usher's syndrome-type IIa. *Hear Res*. 2002;163(1-2):1-11.

141. Weil D, et al. Defective myosin VIIA gene responsible for Usher syndrome type 1B. *Nature*. 1995;374(6517):60-1.

142. Liu XZ, et al. Autosomal dominant non-syndromic deafness caused by a mutation in the myosin VIIA gene. *Nat Genet*. 1997;17(3):268-9.

143. Weil D, et al. The autosomal recessive isolated deafness, DFNB2, and the Usher 1B syndrome are allelic defects of the myosin-VIIA gene. *Nat Genet*. 1997;16(2):191-3.

144. Ernest S, Rauch GJ, Haffter P, Geisler R, Petit C, Nicolson T. Mariner is defective in myosin VIIA: a zebrafish model for human hereditary deafness. *Hum Mol Genet*. 2000;9(14):2189-96.

145. Bitner-Glindzicz M, et al. A recessive contiguous gene deletion causing infantile hyperinsulinism, enteropathy and deafness identifies the Usher type 1C gene. *Nat Genet*. 2000;26(1):56-60.

146. Verpy E, et al. A defect in harmonin, a PDZ domain-containing protein expressed in the inner ear sensory hair cells, underlies Usher syndrome type 1C. *Nat Genet*. 2000;26(1):51-5.

147. Lefevre G, et al. A core cochlear phenotype in USH1 mouse mutants implicates fibrous links of the hair bundle in its cohesion, orientation and differential growth. *Development*. 2008;135(8):1427-37.

148. Lentz JJ, et al. Deafness and retinal degeneration in a novel USH1C knock-in mouse model. *Dev Neurobiol*. 2010;70(4):253-67.

149. Phillips JB, et al. Harmonin (Ush1c) is required in zebrafish Muller glial cells for photoreceptor synaptic development and function. *Dis Model Mech*. 2011;4(6):786-800.

150. Grillet N, et al. Harmonin mutations cause mechanotransduction defects in cochlear hair cells. *Neuron*. 2009;62(3):375-87.

151. Johnson KR, et al. Mouse models of USH1C and DFNB18: phenotypic and molecular analyses of two new spontaneous mutations of the Ush1c gene. *Hum Mol Genet*. 2003;12(23):3075-86.

152. Tian C, et al. Ush1c gene expression levels in the ear and eye suggest different roles for Ush1c in neurosensory organs in a new Ush1c knockout mouse. *Brain Res*. 2010;1328:57-70.

153. Bolz H, et al. Mutation of CDH23, encoding a new member of the cadherin gene family, causes Usher syndrome type 1D. *Nat Genet*. 2001;27(1):108-12.

154. Sollner C, et al. Mutations in cadherin 23 affect tip links in zebrafish sensory hair cells. *Nature*. 2004;428(6986):955-9.

155. Chaib H, et al. A newly identified locus for usher syndrome type I, USH1E, maps to chromosome 21q21. *Hum Mol Genet*. 1997;6(1):27-31.

156. Ahmed ZM, et al. Mutations of the protocadherin gene PCDH15 cause Usher syndrome type 1F. *Am J Hum Genet*. 2001;69(1):25-34.

157. Alagramam KN, et al. Mutations in protocadherin 15 and cadherin 23 affect tip links and mechanotransduction in mammalian sensory hair cells. *PLoS One*. 2011;6(4).

158. Weil D, et al. Usher syndrome type I G (USH1G) is caused by mutations in the gene encoding SANS, a protein that associates with the USH1C protein, harmonin. *Hum Mol Genet*. 2003;12(5):463-71.

159. Ahmed ZM, Riazuddin S, Khan SN, Friedman PL, Friedman TB. USH1H, a novel locus for type I Usher syndrome, maps to chromosome 15q22-23. *Clin Genet*. 2009;75(1):86-91.

160. Giese APJ, et al. CIB2 interacts with TMC1 and TMC2 and is essential for mechanotransduction in auditory hair cells. *Nature communications*. 2017;8(1):43.

161. Michel V, et al. CIB2, defective in isolated deafness, is key for auditory hair cell mechanotransduction and survival. *EMBO Mol Med*. 2017.

162. Jaworek TJ, Bhatti R, Latief N, Khan SN, Riazuddin S, Ahmed ZM. USH1K, a novel locus for type I Usher syndrome, maps to chromosome 10p11.21-q21.1. *J Hum Genet*. 2012;57(10):633-7.

163. Eudy JD, et al. Mutation of a gene encoding a protein with extracellular matrix motifs in usher syndrome type IIa. *Science*. 1998;280(5370):1753-7.

164. Rivolta C, Sweklo EA, Berson EL, Dryja TP. Missense mutation in the USH2A gene: association with recessive retinitis pigmentosa without hearing loss. *Am J Hum Genet*. 2000;66(6):1975-8.

165. Liu X, et al. Usherin is required for maintenance of retinal photoreceptors and normal development of cochlear hair cells. *Proc Natl Acad Sci U S A*. 2007;104(11):4413-8.

166. Weston MD, Luijendijk MWJ, Humphrey KD, Moller C, Kimberling WJ. Mutations in the VLGR1 gene implicate G-protein signaling in the pathogenesis of Usher syndrome type II. *Am J Hum Genet*. 2004;74(2):357-66.

167. McGee J, et al. The very large G-protein-coupled receptor Vlgr1: A component of the ankle link complex required for the normal development of auditory hair bundles. *J Neurosci*. 2006;26(24):6543-53.

168. Michalski N, et al. Molecular characterization of the ankle-link complex in cochlear hair cells and its role in the hair bundle functioning. *J Neurosci*. 2007;27(24):6478-88.

169. Yang J, et al. Ablation of Whirlin Long Isoform Disrupts the USH2 Protein Complex and Causes Vision and Hearing Loss. *Plos Genetics*. 2010;6(5).

170. Mburu P, et al. Defects in whirlin, a PDZ domain molecule involved in stereocilia elongation, cause deafness in the whirler mouse and families with DFNB31. *Nat Genet*. 2003;34(4):421-8.

171. Adato A, et al. USH3A transcripts encode clarin-1, a four- transmembrane-domain protein with a possible role in sensory synapses. *Eur J Hum Genet*. 2002;10(6):339-50.

172. Geng R, et al. Usher syndrome IIIA gene clarin-1 is essential for hair cell function and associated neural activation dagger. *Hum Mol Genet*. 2009;18(15):2748-60.

173. Geller SF, et al. CLRN1 Is Nonessential in the Mouse Retina but Is Required for Cochlear Hair Cell Development. *Plos Genetics*. 2009;5(8).

174. Gopal SR, et al. Zebrafish models for the mechanosensory hair cell dysfunction in usher syndrome 3 reveal that clarin-1 is an essential hair bundle protein. *J Neurosci*. 2015;35(28):10188-201.

175. Alagramam KN, et al. A small molecule mitigates hearing loss in a mouse model of Usher syndrome III. *Nat Chem Biol*. 2016;12(6):444-51.

176. Geng R, et al. Modeling and preventing progressive hearing loss in Usher Syndrome III. *Sci Rep*. 2017;7(1):13480.

177. Gerber S, et al. USH1A: Chronicle of a slow death. *Am J Hum Genet*. 2006;78(2):357-9.

178. Le Quesne Stabej P, et al. Comprehensive sequence analysis of nine Usher syndrome genes in the UK National Collaborative Usher Study. *J Med Genet*. 2012;49(1):27-36.

179. Heissler SM, Manstein DJ. Functional characterization of the human myosin-7a motor domain. *Cell Mol Life Sci*. 2012;69(2):299-311.

180. Liu XZ, et al. Mutations in the myosin VIIA gene cause non-syndromic recessive deafness. *Nat Genet*. 1997;16(2):188-90.

181. Riazuddin S, et al. Mutation spectrum of MYO7A and evaluation of a novel nonsyndromic deafness DFNB2 allele with residual function. *Hum Mutat*. 2008;29(4):502-11.

182. Lenassi E, et al. Natural history and retinal structure in patients with Usher syndrome type 1 owing to MYO7A mutation. *Ophthalmology*. 2014;121(2):580-7.

183. Ouyang XM, et al. Mutations in the alternatively spliced exons of USH1C cause non-syndromic recessive deafness. *Hum Genet*. 2002;111(1):26-30.

184. Reiners J, et al. Differential distribution of harmonin isoforms and their possible role in Usher-1 protein complexes in mammalian photoreceptor cells. *Invest Ophthalmol Vis Sci*. 2003;44(11):5006-15.

185. Sheng M, Sala C. PDZ domains and the organization of supramolecular complexes. *Annu Rev Neurosci*. 2001;24:1-29.

186. Adato A, et al. Interactions in the network of Usher syndrome type 1 proteins. *Hum Mol Genet*. 2005;14(3):347-56.

187. Boeda B, et al. Myosin VIIa, harmonin and cadherin 23, three Usher I gene products that cooperate to shape the sensory hair cell bundle. *EMBO J*. 2002;21(24):6689-99.

188. Kalay E, et al. A novel D458V mutation in the SANS PDZ binding motif causes atypical Usher syndrome. *Journal of Molecular Medicine-Jmm*. 2005;83(12):1025-32.

189. Bashir R, Fatima A, Naz S. A frameshift mutation in SANS results in atypical Usher syndrome. *Clin Genet*. 2010;78(6):601-3.

190. Lagziel A, Overlack N, Bernstein SL, Morell RJ, Wolfrum U, Friedman TB. Expression of cadherin 23 isoforms is not conserved: implications for a mouse model of Usher syndrome type 1D. *Mol Vis*. 2009;15(196-99):1843-57.

191. Reiners J, Marker T, Jurgens K, Reidel B, Wolfrum U. Photoreceptor expression of the Usher syndrome type 1 protein protocadherin 15 (USH1F) and its interaction with the scaffold protein harmonin (USH1C). *Mol Vis*. 2005;11(40-41):347-55.

192. Ahmed ZM, et al. The tip-link antigen, a protein associated with the transduction complex of sensory hair cells, is protocadherin-15. *J Neurosci*. 2006;26(26):7022-34.

193. Sotomayor M, Weihofen WA, Gaudet R, Corey DP. Structural determinants of cadherin-23 function in hearing and deafness. *Neuron*. 2010;66(1):85-100.

194. Bork JM, et al. Usher syndrome 1D and nonsyndromic autosomal recessive deafness DFNB12 are caused by allelic mutations of the novel cadherin-like gene CDH23. *Am J Hum Genet*. 2001;68(1):26-37.

195. Doucette L, et al. Profound, prelingual nonsyndromic deafness maps to chromosome 10q21 and is caused by a novel missense mutation in the Usher syndrome type IF gene PCDH15. *Eur J Hum Genet*. 2009;17(5):554-64.

196. Blazejczyk M, et al. Biochemical characterization and expression analysis of a novel EF-hand Ca2+ binding protein calmyrin2 (Cib2) in brain indicates its function in NMDA receptor mediated Ca2+ signaling. *Arch Biochem Biophys*. 2009;487(1):66-78.

197. Ahmed ZM, Frolenkov GI, Riazuddin S. Usher proteins in inner ear structure and function. *Physiol Genomics*. 2013;45(21):987-9.

198. Booth KT, et al. Variants in CIB2 cause DFNB48 and not USH1J. *Clin Genet*. 2017.

199. Hmani-Aifa M, et al. Identification of two new mutations in the GPR98 and the PDE6B genes segregating in a Tunisian family. *Eur J Hum Genet*. 2009;17(4):474-82.

200. Weston MD, et al. Genomic structure and identification of novel mutations in Usherin, the gene responsible for Usher syndrome type IIa. *Am J Hum Genet*. 2000;66(4):1199-210.

201. Dreyer B, et al. Spectrum of USH2A mutations in Scandinavian patients with Usher syndrome type II. *Hum Mutat*. 2008;29(3):451-.

202. Yan D, Ouyang X, Patterson DM, Du LL, Jacobson SG, Liu X-Z. Mutation analysis in the long isoform of USH2A in American patients with Usher Syndrome type II. *J Hum Genet*. 2009;54(12):732-8.

203. Pearsall N, Bhattacharya G, Wisecarver J, Adams J, Cosgrove D, Kimberling W. Usherin expression is highly conserved in mouse and human tissues. *Hear Res*. 2002;174(1-2):55-63.

204. Bhattacharya G, Kalluri R, Orten DJ, Kimberling WJ, Cosgrove D. A domain-specific usherin/collagen IV interaction may be required for stable integration into the basement membrane superstructure. *J Cell Sci*. 2004;117(2):233-42.

205. Dreyer B, et al. A common ancestral origin of the frequent and widespread 2299delG USH2A mutation. *Am J Hum Genet*. 2001;69(1):228-34.

206. Lenassi E, Saihan Z, Bitner-Glindzicz M, Webster AR. The effect of the common c.2299delG mutation in USH2A on RNA splicing. *Exp Eye Res*. 2014;122:9-12.

207. Lenassi E, et al. A detailed clinical and molecular survey of subjects with nonsyndromic USH2A retinopathy reveals an allelic hierarchy of disease-causing variants. *Eur J Hum Genet*. 2015;23(10):1318-27.

208. Pierrache LH, et al. Visual Prognosis in USH2A-Associated Retinitis Pigmentosa Is Worse for Patients with Usher Syndrome Type IIa Than for Those with Nonsyndromic Retinitis Pigmentosa. *Ophthalmology*. 2016;123(5):1151-60.

209. Hartel BP, et al. A combination of two truncating mutations in USH2A causes more severe and progressive hearing impairment in Usher syndrome type IIa. *Hear Res*. 2016;339:60-8.

210. Rosenbaum DM, Rasmussen SGF, Kobilka BK. The structure and function of G-protein-coupled receptors. *Nature*. 2009;459(7245):356-63.

211. Paavola KJ, Hall RA. Adhesion G protein-coupled receptors: signaling, pharmacology, and mechanisms of activation. *Mol Pharmacol*. 2012;82(5):777-83.

212. Hu Q-X, et al. Constitutive G alpha(i) coupling activity of very large G protein-coupled receptor 1 (VLGR1) and its regulation by PDZD7 protein. *J Biol Chem*. 2014;289(35):24215-25.

213. Shin D, Lin ST, Fu YH, Ptacek LJ. Very large G protein-coupled receptor 1 regulates myelin-associated glycoprotein via Galphas/Galphaq-mediated protein kinases A/C. *Proc Natl Acad Sci U S A*. 2013;110(47):19101-6.

214. van Wijk E, et al. The DFNB31 gene product whirlin connects to the Usher protein network in the cochlea and retina by direct association with USH2A and VLGR1. *Hum Mol Genet*. 2006;15(5):751-65.

215. Audo I, et al. A novel DFNB31 mutation associated with Usher type 2 syndrome showing variable degrees of auditory loss in a consanguineous Portuguese family. *Mol Vis*. 2011;17(178):1598-606.

216. Tlili A, et al. Identification of a novel frameshift mutation in the DFNB31/WHRN gene in a Tunisian consanguineous family with hereditary non-syndromic recessive hearing loss. *Hum Mutat*. 2005;25(5):503-.

217. Joensuu T, et al. Mutations in a novel gene with transmembrane domains underlie Usher syndrome type 3. *Am J Hum Genet*. 2001;69(4):673-84.

218. Fields RR, et al. Usher syndrome type III: Revised genomic structure of the USH3 gene and identification of novel mutations. *Am J Hum Genet*. 2002;71(3):607-17.

219. Hemler ME. Tetraspanin functions and associated microdomains. *Nature Reviews Molecular Cell Biology*. 2005;6(10):801-11.

220. Ogun O, Zallocchi M. Clarin-1 acts as a modulator of mechanotransduction activity and presynaptic ribbon assembly. *J Cell Biol*. 2014;207(3):375-91.

221. Zallocchi M, et al. Role for a Novel Usher Protein Complex in Hair Cell Synaptic Maturation. *PLoS One*. 2012;7(2).

222. Zallocchi M, et al. Localization and expression of clarin-1, the Clrn1 gene product, in auditory hair cells and photoreceptors. *Hear Res*. 2009;255(1-2):109-20.

223. Tian G, et al. Clarin-1, encoded by the Usher Syndrome III causative gene, forms a membranous microdomain: possible role of clarin-1 in organizing the actin cytoskeleton. *J Biol Chem*. 2009;284(28):18980-93.

224. Ebermann I, et al. PDZD7 is a modifier of retinal disease and a contributor to digenic Usher syndrome. *J Clin Invest*. 2010;120(6):1812-23.

225. Vona B, et al. Confirmation of PDZD7 as a nonsyndromic hearing loss gene. *Ear Hear*. 2016;37(4):e238-46.

226. Khateb S, et al. A homozygous nonsense CEP250 mutation combined with a heterozygous nonsense C2orf71 mutation is associated with atypical Usher syndrome. *J Med Genet*. 2014;51(7):460-9.
227. Fu Q, et al. CEP78 is mutated in a distinct type of Usher syndrome. *J Med Genet*. 2016.
228. Puffenberger EG, et al. Genetic mapping and exome sequencing identify variants associated with five novel diseases. *PLoS One*. 2012;7(1).
229. Skradski SL, Clark AM, Jiang H, White HS, Fu YH, Ptacek LJ. A novel gene causing a mendelian audiogenic mouse epilepsy. *Neuron*. 2001;31(4):537-44.
230. Kros CJ, et al. Reduced climbing and increased slipping adaptation in cochlear hair cells of mice with Myo7a mutations. *Nat Neurosci*. 2002;5(1):41-7.
231. Michalski N, et al. Harmonin-b, an actin-binding scaffold protein, is involved in the adaptation of mechanoelectrical transduction by sensory hair cells. *Pflugers Archiv-European Journal of Physiology*. 2009;459(1):115-30.
232. Caberlotto E, et al. Usher type 1G protein sans is a critical component of the tip-link complex, a structure controlling actin polymerization in stereocilia. *Proc Natl Acad Sci U S A*. 2011;108(14):5825-30.
233. Johnson KR, Zheng QY, Weston MD, Ptacek LJ, Noben-Trauth K. The Mass1(frings) mutation underlies early onset hearing impairment in BUB/BnJ mice, a model for the auditory pathology of Usher syndrome IIC. *Genomics*. 2005;85(5):582-90.
234. Holme RH, Kiernan BW, Brown SDM, Steel KP. Elongation of hair cell stereocilia is defective in the mouse mutant whirler. *J Comp Neurol*. 2002;450(1):94-102.
235. Mogensen MM, Rzadzinska A, Steel KR. The deaf mouse mutant whirler suggests a role for whirlin in actin filament dynamics and stereocilia development. *Cell Motil Cytoskeleton*. 2007;64(7):496-508.
236. Geng R, et al. The mechanosensory structure of the hair cell requires clarin-1, a protein encoded by Usher syndrome III causative gene. *J Neurosci*. 2012;32(28):9485-98.
237. Yao L, et al. The time course of deafness and retinal degeneration in a Kunming mouse model for Usher syndrome. *PLoS One*. 2016;11(5):e0155619.
238. Libby RT, Steel KP. Electroretinographic anomalies in mice with mutations in Myo7a, the gene involved. in human Usher syndrome type 1B. *Invest Ophthalmol Vis Sci*. 2001;42(3):770-8.

239. Libby RT, Kitamoto J, Holme RH, Williams DS, Steel KP. Cdh23 mutations in the mouse are associated with retinal dysfunction but not retinal degeneration. *Exp Eye Res*. 2003;77(6):731-9.

240. Haywood-Watson RJL, et al. Ames waltzer deaf mice have reduced electroretinogram amplitudes and complex alternative splicing of Pcdh15 transcripts. *Invest Ophthalmol Vis Sci*. 2006;47(7):3074-84.

241. Tian G, Lee R, Ropelewski P, Imanishi Y. Impairment of vision in a Mouse Model of Usher Syndrome Type III. *Invest Ophthalmol Vis Sci*. 2016;57(3):866-75.

242. Liu XR, Udovichenko IP, Brown SDM, Steel KP, Williams DS. Myosin VIIa participates in opsin transport through the photoreceptor cilium. *J Neurosci*. 1999;19(15):6267-74.

243. Liu XR, Ondek B, Williams DS. Mutant myosin VIIa causes defective melanosome distribution in the RPE of shaker-1 mice. *Nat Genet*. 1998;19(2):117-8.

244. Gibbs D, Kitamoto J, Williams DS. Abnormal phagocytosis by retinal pigmented epithelium that lacks myosin Vila, the Usher syndrome 1B protein. *Proc Natl Acad Sci U S A*. 2003;100(11):6481-6.

245. Lopes VS, et al. The Usher 1B protein, MYO7A, is required for normal localization and function of the visual retinoid cycle enzyme, RPE65. *Hum Mol Genet*. 2011;20(13):2560-70.

246. Lu B, et al. Cell transplantation to arrest early changes in an ush2a animal model. *Invest Ophthalmol Vis Sci*. 2010;51(4):2269-76.

247. Sahly I, et al. Localization of Usher 1 proteins to the photoreceptor calyceal processes, which are absent from mice. *J Cell Biol*. 2012;199(2):381-99.

248. Peng YW, Zallocchi M, Wang WM, Delimont D, Cosgrove D. Moderate light-induced degeneration of rod photoreceptors with delayed transducin translocation in shaker1 mice. *Invest Ophthalmol Vis Sci*. 2011;52(9):6421-7.

249. Tian M, et al. Photoreceptors in whirler mice show defective transducin translocation and are susceptible to short-term light/dark changes-induced degeneration. *Exp Eye Res*. 2014;118:145-53.

250. Trouillet A, et al. Cone degeneration is triggered by the absence of USH1 proteins but prevented by antioxidant treatments. *Sci Rep*. 2018;8(1):1968.

251. Monroe JD, Rajadinakaran G, Smith ME. Sensory hair cell death and regeneration in fishes. *Front Cell Neurosci*. 2015;9:131.

252. Seiler C, et al. Duplicated genes with split functions: independent roles of protocadherin15 orthologues in zebraf ish hearing and vision. *Development*. 2005;132(3):615-23.

253. Glover G, Mueller KP, Sollner C, Neuhauss SC, Nicolson T. The Usher gene cadherin 23 is expressed in the zebrafish brain and a subset of retinal amacrine cells. *Mol Vis*. 2012;18:2309-22.

254. Phillips JB, Vaestinsalo H, Wegner J, Clement A, Sankila E-M, Westerfield M. The cone-dominant retina and the inner ear of zebrafish express the ortholog of CLRN1, the causative gene of human Usher syndrome type 3A. *Gene Expression Patterns*. 2013;13(8):473-81.

255. Wasfy MM, Matsui JI, Miller J, Dowling JE, Perkins BD. myosin 7aa(-/-) mutant zebrafish show mild photoreceptor degeneration and reduced electroretinographic responses. *Exp Eye Res*. 2014;122:65-76.

256. Toro S, Phillips J, Westerfield M. Whirlin proteins localize at the outer limiting membrane and subapical region of zebrafish retina. *Invest Ophthalmol Vis Sci*. 2013;54(6):287-.

257. Reiners J, et al. Scaffold protein harmonin (USH1C) provides molecular links between Usher syndrome type 1 and type 2. *Hum Mol Genet*. 2005;14(24):3933-43.

258. Maerker T, et al. A novel Usher protein network at the periciliary reloading point between molecular transport machineries in vertebrate photoreceptor cells. *Hum Mol Genet*. 2008;17(1):71-86.

259. Senften M, et al. Physical and functional interaction between protocadherin 15 and myosin VIIa in mechanosensory hair cells. *J Neurosci*. 2006;26(7):2060-71.

260. Siemens J, et al. Cadherin 23 is a component of the tip link in hair-cell stereocilia. *Nature*. 2004;428(6986):950-5.

261. Kazmierczak P, et al. Cadherin 23 and protocadherin 15 interact to form tip-link filaments in sensory hair cells. *Nature*. 2007;449(7158):87-U59.

262. Bahloul A, et al. Cadherin-23, myosin VIIa and harmonin, encoded by Usher syndrome type I genes, form a ternary complex and interact with membrane phospholipids. *Hum Mol Genet*. 2010;19(18):3557-65.

263. Zou J, et al. Individual USH2 proteins make distinct contributions to the ankle link complex during development of the mouse cochlear stereociliary bundle. *Hum Mol Genet*. 2015;24(24):6944-57.

264. Zou J, et al. The roles of USH1 proteins and PDZ domain-containing USH proteins in USH2 complex integrity in cochlear hair cells. *Hum Mol Genet*. 2017;26(3):624-36.

265. Hunter DG, Fishman GA, Mehta RS, Kretzer FL. Abnormal sperm and photoreceptor axonemes in Usher's syndrome. *Arch Ophthalmol*. 1986;104(3):385-9.

266. Bonneau D, Raymond F, Kremer C, Klossek JM, Kaplan J, Patte F. Usher syndrome type I associated with bronchiectasis and immotile nasal cilia in two brothers. *J Med Genet*. 1993;30(3):253-4.

267. Aparisi MJ, et al. Study of USH1 splicing variants through minigenes and transcript analysis from nasal epithelial cells. *PLoS One*. 2013;8(2):e57506.

268. Ribeiro JC, et al. Accelerated age-related olfactory decline among type 1 Usher patients. *Sci Rep*. 2016;6:28309.

269. Jansen F, et al. Impact of the Usher syndrome on olfaction. *Hum Mol Genet*. 2016;25(3):524-33.

270. Gillespie PG, Muller U. Mechanotransduction by hair cells: models, molecules, and mechanisms. *Cell*. 2009;139(1):33-44.

271. Kelly M, Chen P. Shaping the mammalian auditory sensory organ by the planar cell polarity pathway. *Int J Dev Biol*. 2007;51(6-7):535-47.

272. Goodyear RJ, Marcotti W, Kros CJ, Richardson GP. Development and properties of stereociliary link types in hair cells of the mouse cochlea. *J Comp Neurol*. 2005;485(1):75-85.

273. Michel V, et al. Cadherin 23 is a component of the transient lateral links in the developing hair bundles of cochlear sensory cells. *Dev Biol*. 2005;280(2):281-94.

274. Zou J, et al. Deletion of PDZD7 disrupts the Usher syndrome type 2 protein complex in cochlear hair cells and causes hearing loss in mice. *Hum Mol Genet*. 2014;23(9):2374-90.

275. Yagi H, et al. Vlgr1 is required for proper stereocilia maturation of cochlear hair cells. *Genes Cells*. 2007;12(2):235-50.

276. Kazmierczak P, Mueller U. Sensing sound: molecules that orchestrate mechanotransduction by hair cells. *Trends Neurosci*. 2012;35(4):220-9.

277. Grati Mh, Kachar B. Myosin VIIa and sans localization at stereocilia upper tip-link density implicates these Usher syndrome proteins in mechanotransduction. *Proc Natl Acad Sci U S A*. 2011;108(28):11476-81.

278. Zallocchi M, Delimont D, Meehan DT, Cosgrove D. Regulated vesicular trafficking of specific PCDH15 and VLGR1 variants in auditory hair cells. *J Neurosci*. 2012;32(40):13841-59.

279. Gregory FD, Bryan KE, Pangrsic T, Calin-Jageman IE, Moser T, Lee A. Harmonin inhibits presynaptic Cav1.3 Ca(2)(+) channels in mouse inner hair cells. *Nat Neurosci*. 2011;14(9):1109-11.

280. Gregory FD, Pangrsic T, Calin-Jageman IE, Moser T, Lee A. Harmonin enhances voltage-dependent facilitation of Ca(v)1.3 channels and synchronous

exocytosis in mouse inner hair cells. *Journal of Physiology-London*. 2013;591(13):3253-69.

281. Hasson T, Heintzelman MB, Santos-Sacchi J, Corey DP, Mooseker MS. Expression in cochlea and retina of myosin VIIa, the gene product defective in Usher syndrome type 1B. *Proc Natl Acad Sci U S A*. 1995;92(21):9815-9.

282. Cosgrove D, Zallocchi M. Usher protein functions in hair cells and photoreceptors. *Int J Biochem Cell Biol*. 2014;46:80-9.

283. Kersten FFJ, et al. Association of whirlin with Ca(v)1.3 (alpha(1D)) channels in photoreceptors, defining a novel member of the Usher protein network. *Invest Ophthalmol Vis Sci*. 2010;51(5):2338-46.

284. Williams DS, et al. Harmonin in the murine retina and the retinal phenotypes of Ush1c-mutant mice and human USH1C. *Invest Ophthalmol Vis Sci*. 2009;50(8):3881-9.

285. Schietroma C, et al. Usher syndrome type 1-associated cadherins shape the photoreceptor outer segment. *J Cell Biol*. 2017;216(6):1849-64.

286. Jatana KR, Thomas D, Weber L, Mets MB, Silverman JB, Young NM. Usher syndrome: characteristics and outcomes of pediatric cochlear implant recipients. *Otol Neurotol*. 2013;34(3):484-9.

287. Pietola L, et al. Speech recognition and communication outcomes with cochlear implantation in Usher syndrome type 3. *Otol Neurotol*. 2012;33(1):38-41.

288. Colella P, et al. Myosin7a deficiency results in reduced retinal activity which is improved by gene therapy. *PLoS One*. 2013;8(8):e72027.

289. Lopes VS, et al. Retinal gene therapy with a large MYO7A cDNA using adeno-associated virus. *Gene Ther*. 2013;20(8):824-33.

290. Trapani I, et al. Effective delivery of large genes to the retina by dual AAV vectors. *EMBO Mol Med*. 2014;6(2):194-211.

291. Dyka FM, Boye SL, Chiodo VA, Hauswirth WW, Boye SE. Dual adeno-associated virus vectors result in efficient in vitro and in vivo expression of an oversized gene, MYO7A. *Human Gene Therapy Methods*. 2014;25(2):166-77.

292. Zou J, et al. Whirlin replacement restores the formation of the USH2 protein complex in whirlin knockout photoreceptors. *Invest Ophthalmol Vis Sci*. 2011;52(5):2343-51.

293. Dinculescu A, et al. AAV-Mediated clarin-1 expression in the mouse retina: implications for USH3A gene therapy. *PLoS One*. 2016;11(2):e0148874.

294. Colella P, et al. Efficient gene delivery to the cone-enriched pig retina by dual AAV vectors. *Gene Ther*. 2014;21(4):450-6.

295. Hashimoto T, et al. Lentiviral gene replacement therapy of retinas in a mouse model for Usher syndrome type 1B. *Gene Ther*. 2007;14(7):584-94.
296. Zallocchi M, et al. EIAV-Based Retinal Gene Therapy in the shaker1 Mouse Model for Usher Syndrome Type 1B: Development of UshStat. *PLoS One*. 2014;9(4).
297. Benedetti S, Hoshiya H, Tedesco FS. Repair or replace? Exploiting novel gene and cell therapy strategies for muscular dystrophies. *The FEBS journal*. 2013;280(17):4263-80.
298. Pan B, et al. Gene therapy restores auditory and vestibular function in a mouse model of Usher syndrome type 1c. *Nat Biotechnol*. 2017;35(3):264-72.
299. Emptoz A, et al. Local gene therapy durably restores vestibular function in a mouse model of Usher syndrome type 1G. *Proc Natl Acad Sci U S A*. 2017;114(36):9695-700.
300. Isgrig K, et al. Gene therapy restores balance and auditory functions in a mouse model of Usher syndrome. *Mol Ther*. 2017;25(3):780-91.
301. Birch DG, Weleber RG, Duncan JL, Jaffe GJ, Tao W. Randomized trial of ciliary neurotrophic factor delivered by encapsulated cell intraocular implants for retinitis pigmentosa. *Am J Ophthalmol*. 2013;156(2):283-92.e1.
302. Tao W, et al. Encapsulated cell-based delivery of CNTF reduces photoreceptor degeneration in animal models of retinitis pigmentosa. *Invest Ophthalmol Vis Sci*. 2002;43(10):3292-8.
303. Rebibo-Sabbah A, Nudelman I, Ahmed ZM, Baasov T, Ben-Yosef T. In vitro and ex vivo suppression by aminoglycosides of PCDH15 nonsense mutations underlying type 1 Usher syndrome. *Hum Genet*. 2007;122(3-4):373-81.
304. Nudelman I, et al. Development of novel aminoglycoside (NB54) with reduced toxicity and enhanced suppression of disease-causing premature stop mutations. *J Med Chem*. 2009;52(9):2836-45.
305. Nudelman I, Glikin D, Smolkin B, Hainrichson M, Belakhov V, Baasov T. Repairing faulty genes by aminoglycosides: development of new derivatives of geneticin (G418) with enhanced suppression of diseases-causing nonsense mutations. *Bioorg Med Chem*. 2010;18(11):3735-46.
306. Goldmann T, et al. Beneficial read-through of a USH1C nonsense mutation by designed aminoglycoside NB30 in the retina. *Invest Ophthalmol Vis Sci*. 2010;51(12):6671-80.
307. Goldmann T, et al. A comparative evaluation of NB30, NB54 and PTC124 in translational read-through efficacy for treatment of an USH1C nonsense mutation. *EMBO Mol Med*. 2012;4(11):1186-99.

308. Li M, Suzuki K, Kim NY, Liu GH, Izpisua Belmonte JC. A cut above the rest: targeted genome editing technologies in human pluripotent stem cells. *J Biol Chem*. 2014;289(8):4594-9.

309. Overlack N, Goldmann T, Wolfrum U, Nagel-Wolfrum K. Gene repair of an Usher syndrome causing mutation by zinc-finger nuclease mediated homologous recombination. *Invest Ophthalmol Vis Sci*. 2012;53(7):4140-6.

310. Fuster-Garcia C, et al. USH2A Gene Editing Using the CRISPR System. *Molecular therapy Nucleic acids*. 2017;8:529-41.

311. Lentz JJ, et al. Rescue of hearing and vestibular function by antisense oligonucleotides in a mouse model of human deafness. *Nat Med*. 2013;19(3):345-50.

312. Depreux FF, et al. Antisense oligonucleotides delivered to the amniotic cavity in utero modulate gene expression in the postnatal mouse. *Nucleic Acids Res*. 2016.

313. Slijkerman RW, et al. Antisense oligonucleotide-based splice correction for USH2A-associated retinal degeneration caused by a frequent deep-intronic mutation. *Molecular therapy Nucleic acids*. 2016;5(10):e381.

314. Westerfield M. The Zebrafish Book. A Guide for the Laboratory Use of Zebrafish (Danio rerio). 4th ed. Eugene: University of Oregon Press; 2000.

315. Kimmel CB, Ballard WW, Kimmel SR, Ullmann B, Schilling TF. Stages of embryonic development of the zebrafish. *Dev Dyn*. 1995;203(3):253-310.

316. Gagnon JA, et al. Efficient mutagenesis by Cas9 protein-mediated oligonucleotide insertion and large-scale assessment of single-guide RNAs. *PLoS One*. 2014;9(5):e98186.

317. Toms M, Tracey-White D, Muhundhakumar D, Sprogyte L, Dubis AM, Moosajee M. Spectral domain optical coherence tomography: an in vivo imaging protocol for assessing retinal morphology in adult zebrafish. *Zebrafish*. 2017;14(2):118-25.

318. Baraas RC, et al. Adaptive optics retinal imaging reveals S-cone dystrophy in tritan color-vision deficiency. *J Opt Soc Am A Opt Image Sci Vis*. 2007;24(5):1438-47.

319. Kram YA, Mantey S, Corbo JC. Avian cone photoreceptors tile the retina as five independent, self-organizing mosaics. *PLoS One*. 2010;5(2):e8992.

320. Cameron DJ, et al. The optokinetic response as a quantitative measure of visual acuity in zebrafish. *Journal of visualized experiments : JoVE*. 2013(80):50832.

321. Fimbel SM, Montgomery JE, Burket CT, Hyde DR. Regeneration of inner retinal neurons after intravitreal injection of ouabain in zebrafish. *J Neurosci*. 2007;27(7):1712-24.

322. Lee MM, Ritter R, 3rd, Hirose T, Vu CD, Edwards AO. Snowflake vitreoretinal degeneration: follow-up of the original family. *Ophthalmology*. 2003;110(12):2418-26.
323. Yin J, et al. The 1D4 antibody labels outer segments of long double cone but not rod photoreceptors in zebrafish. *Invest Ophthalmol Vis Sci*. 2012;53(8):4943-51.
324. Bringmann A, Reichenbach A. Role of Muller cells in retinal degenerations. *Front Biosci*. 2001;6:E72-92.
325. Miao L, St Clair DK. Regulation of superoxide dismutase genes: implications in disease. *Free Radic Biol Med*. 2009;47(4):344-56.
326. Pellegrino MW, Nargund AM, Haynes CM. Signaling the mitochondrial unfolded protein response. *Biochim Biophys Acta*. 2013;1833(2):410-6.
327. Zhang W, Zhang X, Wang H, Sharma AK, Edwards AO, Hughes BA. Characterization of the R162W Kir7.1 mutation associated with snowflake vitreoretinopathy. *Am J Physiol Cell Physiol*. 2013;304(5):C440-9.
328. Saint-Geniez M, D'Amore PA. Development and pathology of the hyaloid, choroidal and retinal vasculature. *Int J Dev Biol*. 2004;48(8-9):1045-58.
329. Yang Y, Hayden MR, Sowers S, Bagree SV, Sowers JR. Retinal redox stress and remodeling in cardiometabolic syndrome and diabetes. *Oxid Med Cell Longev*. 2010;3(6):392-403.
330. Khan JA, Ide CH, Strickland MP. Coats'-type retinitis pigmentosa. *Surv Ophthalmol*. 1988;32(5):317-32.
331. Campochiaro PA, Aiello LP, Rosenfeld PJ. Anti-vascular endothelial growth factor agents in the treatment of retinal disease: from bench to bedside. *Ophthalmology*. 2016;123(10s):S78-s88.
332. Futter CE, Ramalho JS, Jaissle GB, Seeliger MW, Seabra MC. The role of Rab27a in the regulation of melanosome distribution within retinal pigment epithelial cells. *Mol Biol Cell*. 2004;15(5):2264-75.
333. Kusaka S, et al. Functional Kir7.1 channels localized at the root of apical processes in rat retinal pigment epithelium. *J Physiol*. 2001;531(Pt 1):27-36.
334. Ross JM, et al. High brain lactate is a hallmark of aging and caused by a shift in the lactate dehydrogenase A/B ratio. *Proc Natl Acad Sci U S A*. 2010;107(46):20087-92.
335. Terman A, Kurz T, Navratil M, Arriaga EA, Brunk UT. Mitochondrial turnover and aging of long-lived postmitotic cells: the mitochondrial-lysosomal axis theory of aging. *Antioxidants & redox signaling*. 2010;12(4):503-35.
336. Navratil M, Terman A, Arriaga EA. Giant mitochondria do not fuse and exchange their contents with normal mitochondria. *Exp Cell Res*. 2008;314(1):164-72.

337. Holtze S, et al. Study of age-dependent structural and functional changes of mitochondria in skeletal muscles and heart of naked mole rats (Heterocephalus glaber). *Biochemistry (Mosc)*. 2016;81(12):1429-37.

338. Tandler B, Dunlap M, Hoppel CL, Hassan M. Giant mitochondria in a cardiomyopathic heart. *Ultrastruct Pathol*. 2002;26(3):177-83.

339. Yoon YS, et al. Formation of elongated giant mitochondria in DFO-induced cellular senescence: involvement of enhanced fusion process through modulation of Fis1. *J Cell Physiol*. 2006;209(2):468-80.

340. Zhao C, et al. mTOR-mediated dedifferentiation of the retinal pigment epithelium initiates photoreceptor degeneration in mice. *J Clin Invest*. 2011;121(1):369-83.

341. Feher J, Kovacs I, Artico M, Cavallotti C, Papale A, Balacco Gabrieli C. Mitochondrial alterations of retinal pigment epithelium in age-related macular degeneration. *Neurobiol Aging*. 2006;27(7):983-93.

342. Bianchi E, et al. Retinal pigment epithelium, age-related macular degeneration and neurotrophic keratouveitis. *Int J Mol Med*. 2013;31(1):232-42.

343. Youle RJ, van der Bliek AM. Mitochondrial fission, fusion, and stress. *Science*. 2012;337(6098):1062-5.

344. Cano M, et al. Oxidative stress induces mitochondrial dysfunction and a protective unfolded protein response in RPE cells. *Free Radic Biol Med*. 2014;69:1-14.

345. Calaza KC, Kam JH, Hogg C, Jeffery G. Mitochondrial decline precedes phenotype development in the complement factor H mouse model of retinal degeneration but can be corrected by near infrared light. *Neurobiol Aging*. 2015;36(10):2869-76.

346. Godley BF, Jin GF, Guo YS, Hurst JS. Bcl-2 overexpression increases survival in human retinal pigment epithelial cells exposed to H(2)O(2). *Exp Eye Res*. 2002;74(6):663-9.

347. Nir I, Kedzierski W, Chen J, Travis GH. Expression of Bcl-2 protects against photoreceptor degeneration in retinal degeneration slow (rds) mice. *J Neurosci*. 2000;20(6):2150-4.

348. Zhang T, Wei Y, Jiang X, Li J, Qiu S, Zhang S. Protection of photoreceptors by intravitreal injection of the Y-27632 Rho-associated protein kinase inhibitor in Royal College of Surgeons rats. *Mol Med Rep*. 2015;12(3):3655-61.

349. Zhou X, Wei Y, Qiu S, Xu Y, Zhang T, Zhang S. Propofol decreases endoplasmic reticulum stress-mediated apoptosis in retinal pigment epithelial cells. *PLoS One*. 2016;11(6):e0157590.

350. Rocco ML, Balzamino BO, Esposito G, Petrella C, Aloe L, Micera A. NGF/anti-VEGF combined exposure protects RCS retinal cells and photoreceptors that underwent a local worsening of inflammation. *Graefes Arch Clin Exp Ophthalmol*. 2017;255(3):567-74.

351. Wang R, et al. Methane rescues retinal ganglion cells and limits retinal mitochondrial dysfunction following optic nerve crush. *Exp Eye Res*. 2017;159:49-57.

352. Arend N, Wertheimer C, Laubichler P, Wolf A, Kampik A, Kernt M. Idebenone prevents oxidative stress, cell death and senescence of retinal pigment epithelium cells by stabilizing BAX/Bcl-2 ratio. *Ophthalmologica*. 2015;234(2):73-82.

353. Guo X, et al. Matrigel and Activin A promote cell-cell contact and anti-apoptotic activity in cultured human retinal pigment epithelium cells. *Exp Eye Res*. 2016;147:37-49.

354. King A, Gottlieb E, Brooks DG, Murphy MP, Dunaief JL. Mitochondria-derived reactive oxygen species mediate blue light-induced death of retinal pigment epithelial cells. *Photochem Photobiol*. 2004;79(5):470-5.

355. Nita M, Grzybowski A. The role of the reactive oxygen species and oxidative stress in the pathomechanism of the age-related ocular diseases and other pathologies of the anterior and posterior eye segments in adults. *Oxid Med Cell Longev*. 2016;2016:3164734.

356. Jin GF, Hurst JS, Godley BF. Hydrogen peroxide stimulates apoptosis in cultured human retinal pigment epithelial cells. *Curr Eye Res*. 2001;22(3):165-73.

357. He Y, Leung KW, Ren Y, Pei J, Ge J, Tombran-Tink J. PEDF improves mitochondrial function in RPE cells during oxidative stress. *Invest Ophthalmol Vis Sci*. 2014;55(10):6742-55.

358. Tringali G, Sampaolese B, Clementi ME. Expression of early and late cellular damage markers by ARPE-19 cells following prolonged treatment with UV-A radiation. *Mol Med Rep*. 2016;14(4):3485-9.

359. Cai X, Chen L, McGinnis JF. Correlation of ER stress and retinal degeneration in tubby mice. *Exp Eye Res*. 2015;140:130-8.

360. Lopez-Otin C, Blasco MA, Partridge L, Serrano M, Kroemer G. The hallmarks of aging. *Cell*. 2013;153(6):1194-217.

361. Moreira PI, Carvalho C, Zhu X, Smith MA, Perry G. Mitochondrial dysfunction is a trigger of Alzheimer's disease pathophysiology. *Biochim Biophys Acta*. 2010;1802(1):2-10.

362. Keane PC, Kurzawa M, Blain PG, Morris CM. Mitochondrial dysfunction in Parkinson's disease. *Parkinsons Dis*. 2011;2011:716871.

363. Sivapathasuntharam C, Sivaprasad S, Hogg C, Jeffery G. Aging retinal function is improved by near infrared light (670 nm) that is associated with corrected mitochondrial decline. *Neurobiol Aging*. 2017;52:66-70.

364. Dona M, et al. NINL and DZANK1 co-function in vesicle transport and are essential for photoreceptor development in zebrafish. *PLoS Genet*. 2015;11(10):e1005574.

365. Harris JA, Cheng AG, Cunningham LL, MacDonald G, Raible DW, Rubel EW. Neomycin-induced hair cell death and rapid regeneration in the lateral line of zebrafish (Danio rerio). *Journal of the Association for Research in Otolaryngology : JARO*. 2003;4(2):219-34.

366. Adato A, et al. Usherin, the defective protein in Usher syndrome type IIA, is likely to be a component of interstereocilia ankle links in the inner ear sensory cells. *Hum Mol Genet*. 2005;14(24):3921-32.

367. Pearsall N, Bhattacharya G, Wisecarver J, Adams J, Cosgrove D, Kimberling W. Usherin expression is highly conserved in mouse and human tissues. *Hear Res*. 2002;174(1-2):55-63.

368. Blanco-Sanchez B, Clement A, Fierro J, Jr., Washbourne P, Westerfield M. Complexes of Usher proteins preassemble at the endoplasmic reticulum and are required for trafficking and ER homeostasis. *Dis Model Mech*. 2014;7(5):547-59.

369. Miller JN, Pearce DA. Nonsense-mediated decay in genetic disease: friend or foe? *Mutation research Reviews in mutation research*. 2014;762:52-64.

370. Bilotta J, Saszik S, Sutherland SE. Rod contributions to the electroretinogram of the dark-adapted developing zebrafish. *Dev Dyn*. 2001;222(4):564-70.

371. Ait-Ali N, et al. Rod-derived cone viability factor promotes cone survival by stimulating aerobic glycolysis. *Cell*. 2015;161(4):817-32.

372. Yu DY, Cringle S, Valter K, Walsh N, Lee D, Stone J. Photoreceptor death, trophic factor expression, retinal oxygen status, and photoreceptor function in the P23H rat. *Invest Ophthalmol Vis Sci*. 2004;45(6):2013-9.

373. Millan JM, Aller E, Jaijo T, Blanco-Kelly F, Gimenez-Pardo A, Ayuso C. An update on the genetics of Usher syndrome. *Journal of Ophthalmology*. 2011.

374. Thomas JL, Ranski AH, Morgan GW, Thummel R. Reactive gliosis in the adult zebrafish retina. *Exp Eye Res*. 2016;143:98-109.

375. Wenzel A, Grimm C, Samardzija M, Reme CE. Molecular mechanisms of light-induced photoreceptor apoptosis and neuroprotection for retinal degeneration. *Prog Retin Eye Res*. 2005;24(2):275-306.

376. Besharse JC, Brandon RA. Effects of continuous light and darkness on the eyes of the troglobitic salamander Typhlotriton spelaeus. *J Morphol*. 1976;149(4):527-46.

377. Hollyfield JG, Rayborn ME, Medford D. Damaging Effects of Constant Light and Darkness on the Retina of the Frog. In: Williams TP, Baker BN, editors. The Effects of Constant Light on Visual Processes. Boston, MA: Springer US; 1980. p. 401-7.

378. Naash ML, et al. Light-induced acceleration of photoreceptor degeneration in transgenic mice expressing mutant rhodopsin. *Invest Ophthalmol Vis Sci*. 1996;37(5):775-82.

379. Rascher K, et al. Light deprivation slows but does not prevent the loss of photoreceptors in taurine transporter knockout mice. *Vision Res*. 2004;44(17):2091-100.

380. Fan J, Woodruff ML, Cilluffo MC, Crouch RK, Fain GL. Opsin activation of transduction in the rods of dark-reared Rpe65 knockout mice. *J Physiol*. 2005;568(Pt 1):83-95.

381. Campbell LJ, Jensen AM. Phosphodiesterase inhibitors sildenafil and vardenafil reduce zebrafish rod photoreceptor outer segment shedding. *Invest Ophthalmol Vis Sci*. 2017;58(13):5604-15.

382. Wenzel A, Reme CE, Williams TP, Hafezi F, Grimm C. The Rpe65 Leu450Met variation increases retinal resistance against light-induced degeneration by slowing rhodopsin regeneration. *J Neurosci*. 2001;21(1):53-8.

383. Thomas JL, Nelson CM, Luo X, Hyde DR, Thummel R. Characterization of multiple light damage paradigms reveals regional differences in photoreceptor loss. *Exp Eye Res*. 2012;97(1):105-16.

384. Settembre C, Fraldi A, Medina DL, Ballabio A. Signals for the lysosome: a control center for cellular clearance and energy metabolism. *Nature reviews Molecular cell biology*. 2013;14(5):283-96.

385. Hollingsworth TJ, Gross AK. Chapter one - Defective Trafficking of Rhodopsin and Its Role in Retinal Degenerations. In: Jeon KW, editor. Int Rev Cell Mol Biol. 293: Academic Press; 2012. p. 1-44.

386. Papermaster DS. The birth and death of photoreceptors :The Friedenwald lecture. *Invest Ophthalmol Vis Sci*. 2002;43(5):1300-9.

387. Lessieur EM, Fogerty J, Gaivin RJ, Song P, Perkins BD. The ciliopathy gene ahi1 is required for zebrafish cone photoreceptor outer segment morphogenesis and survival. *Invest Ophthalmol Vis Sci*. 2017;58(1):448-60.

388. Lush ME, Piotrowski T. Sensory hair cell regeneration in the zebrafish lateral line. *Dev Dyn*. 2014;243(10):1187-202.
389. Goodman L, Zallocchi M. Integrin alpha8 and Pcdh15 act as a complex to regulate cilia biogenesis in sensory cells. *J Cell Sci*. 2017;130(21):3698-712.